DEFORMATION OF CONTINENTAL LITHOSPHERE: STUDIES IN THE URAL MOUNTAINS, THE ADRIATIC REGION, AND THE WESTERN UNITED STATES

BY

SARAH ELIZABETH KRUSE

B.S., UNIVERSITY OF WISCONSIN (1984)

SUBMITTED TO THE DEPARTMENT OF
EARTH, ATMOSPHERIC, AND PLANETARY SCIENCES
IN PARTIAL FULFILLMENT OF THE REQUIREMENTS
FOR THE DEGREE OF

DOCTOR OF PHILOSOPHY

AT THE

MASSACHUSETTS INSTITUTE OF TECHNOLOGY
AUGUST 1989

© MASSACHUSETTS INSTITUTE OF TECHNOLOGY

SIGNATURE OF AUTHOR _____
DEPARTMENT OF EARTH, ATMOSPHERIC, AND PLANETARY SCIENCES

CERTIFIED BY _____
MARCIA K. MCNUTT, THESIS SUPERVISOR

CERTIFIED BY _____
LEIGH H. ROYDEN, THESIS SUPERVISOR

ACCEPTED BY _____
THOMAS H. JORDAN, CHAIRMAN, DEPARTMENTAL COMMITTEE

MASSACHUSETTS INSTITUTE OF TECHNOLOGY
NOV 06 1989
LIBRARIES

DEFORMATION OF CONTINENTAL LITHOSPHERE: STUDIES IN THE URAL MOUNTAINS, THE ADRIATIC REGION, AND THE WESTERN UNITED STATES

BY

SARAH ELIZABETH KRUSE

SUBMITTED TO THE DEPARTMENT OF EARTH, ATMOSPHERIC, AND PLANETARY SCIENCES ON AUGUST 23, 1989 IN PARTIAL FULFILLMENT OF THE REQUIREMENTS FOR THE DEGREE OF DOCTOR OF PHILOSOPHY IN GEOPHYSICS

ABSTRACT

Geophysical and geological observations from the Ural Mountains have been compiled to test whether the surficial similarities of the Appalachian and Ural orogenic belts extend to include deep lithospheric structure and compensation mechanism. The combined data suggest support of the mountains by a stiff continental slab which is depressed by an effective subcrustal load in addition to the topography. The model preferred in this study which fits the geophysical data and predicts the presence and shape of the Ural foredeep to the west of the mountains requires eastward-directed underthrusting of the Russian platform behaving as an elastic plate more than 50-km thick. It is unlikely that an elastic plate this stiff could have resulted from conductive cooling of a thermal plate only 125-km thick. The weight of the existing mountains on such an elastic plate is insufficient to produce the deflection of the Moho inferred from seismic and gravity data. An additional load on the elastic plate may be provided by a buried mass of similar origin to surface outcrops of dense mafic and ultramafic rocks in the eastern Urals. Alternatively, the load may represent the effect of a shallowing of the Moho east of the mountains which is a remnant of a buried passive continental margin. Seismic data and Bouguer gravity anomalies suggest that the effect of the subsurface mass anomaly is at least as great as the present-day topography and that the Russian plate flexurally underthrusts the Urals for more than 100 km. We speculate that similar effective subsurface loads may exist at younger continental orogens but are obscured by the topographic load in less eroded mountain belts.

Geometric reconstruction of foredeep basins overlying the continental Adriatic lithosphere shows its changing deflection beneath the Dinaride, Southern Alp, and Apennine thrust belts throughout Cenozoic time. Basin reconstructions are based on backstripping techniques using well log data, biostratigraphy, and seismic stratigraphy of the foredeep basin fill. Growth of the foredeep basins occurred coevally with the maximum convergent tectonic activity in adjacent thrust belts. Lithospheric deflections beneath the Apennine and Dinaride foredeep basins in the central Adriatic and beneath the Apennine and Southern Alp basins of northern Italy can be modeled as two–sided flexure of a thin elastic plate with uniform thickness. Basin reconstructions are compatible with an effective plate thickness of 10 to 20 kilometers (flexural rigidity of ??) that is roughly constant both during individual convergent events and between the Eocene development of the Dinaride foredeep basin and the Pliocene development of the Apennine foredeep basin. In particular, the data in the central Adriatic are incompatible with models for significant weakening of the lithosphere subsequent to the Dinaride convergent event. Reconstructions suggest that the basement beneath the Eocene–Oligocene Dinaride and Pliocene–Quaternary Apennine foredeep basins may have dipped more steeply toward the thrust belts at the time of the cessation of major tectonic activity than it does at present. The underlying Adriatic lithosphere may have 'unflexed' as rates of convergence diminished in

these settings. Flexural modeling of the Adriatic foredeep suggests that erosion of topographic load, reduction in regional stresses, or lithospheric weakening in regions of highest plate curvature may each in themselves be insufficient to explain the inferred post–tectonic 'unflexing'. The deflection data may be better explained by a combination of these processes with changes in forces acting at depth within the convergence zone.

The conditions are examined under which ductile flow of lower crustal material is effective in explaining the small variations in gravity anomalies and elevations observed between neighboring areas that have undergone highly variable amounts of upper crustal extension. This study addresses in particular the transition zone between the unextended Colorado Plateau and the extended eastern Basin and Range province near Lake Mead, Nevada, where Bouguer gravity and topography data suggest that both present and pre–extensional variations in crustal thickness between the unextended and extended regions are small. In addition several proposed mechanisms for producing uniform crustal thickness across the transition zone, such as overthickening of subsequently extended areas and crustal thinning in the footwall of low–angle normal faults are inviable in the Lake Mead area. The viscosities required for ductile flow in a lower crustal channel to reduce discontinuities in crustal thickness associated with variable amounts of extension are found to be highly dependent on the channel thickness and on the length scale of flow required. Finite element modeling shows that flow over 700 kilometers across the eastern Basin and Range and western Colorado Plateau under the extension rates estimated near Lake Mead requires effective viscosities less than 10^{18} to 10^{20} Pa·s for ductile channels 5 to 25 kilometers in thickness. Flow over shorter length scales appropriate to metamorphic core complexes may be accommodated with effective viscosities as high as 10^{21} Pa·s. These effective viscosities may be sustained by lower crustal material deforming at laboratory–extrapolated power law creep rates. The longer–scale flow may require elevated crustal temperatures (more than 700°C) depending on the composition assumed for the ductile channel. Thus ductile flow in the lower crust appears to be a viable mechanism for preventing large variations in total crustal thickness between highly extended and less extended regions, thereby explaining the relative uniformity in gravity and topography between such regions.

ACKNOWLEDGEMENTS

The enthusiasm, support, and insight of my advisors Marcia McNutt and Wiki Royden made the process of learning how to do my own research an enjoyable one. Marcia's obvious pleasure in tackling geophysical problems, which she expresses so well in the classroom, was instrumental in drawing me into geophysics. I am grateful to both Marcia and Wiki for giving me the freedom to explore a variety of subjects on my way to this thesis, and then for being accessible and helpful about any aspects of these projects.

Jim Elliot was a very supportive, attentive advisor who helped boost my confidence as I began graduate school. I appreciate his continued support even after I left his field of planetary science for the greener pastures of geophysics.

For my study of the Ural mountains I am grateful to Michel Diament, who held interesting conversations and dispensed insight even while seasick aboard the *Thomas Washington*. Paolo Scandone and Etta Patacca and their associates in Pisa introduced me to the regional geology of the Apennine mountains, and together with Wiki afforded me the opportunity to visit one of the places I was writing about. Paolo and his library are an imcomparable source of information on Italian geology. Brian Wernicke, together with Marcia, encouraged me to pursue my ideas that became the third chapter. Brian and Gary Axen were an invaluable resource for the geological observations that stimulated this work. Roger Buck, Matt Cordery, and in particular Jason Phipps Morgan were generous with their time, ideas and finite element programs, and the work in the third chapter could not have been completed without them.

Carolyn Ruppel, Geoff Abers, and Steve Hickman were constant sources of help, constructive criticism, and ideas, as well as friendship. Many of the ideas that worked their way into this thesis developed through conversations with them.

Jim Knapp, Beth Robinson, Alan Leinbach, Don Hickmott, Cathy Rocke, and Karen Garrison made these years in Boston rich in friendship, warmth, and humor. Laura Hastings and Anne Mast reminded me that friendships can weather great changes and survive intact.

My family, my in-laws, and especially my parents, gave me love and a sense of balance through my ups and downs. Their diverse perspectives on life helped me keep my own perspective. Extra thanks go to my grandmothers: my mother's mother, who reminded me that life is often best lived one day at a time, and my father's mother, who got her Ph.D. long before it was common for women, and who after many years can still empathize with the problems of finishing a thesis.

A brief acknowledgement cannot do justice to the love and support given by my husband Tom Juster through our years together in graduate school. His sense of humor and adventure has sustained me through rough periods and added immeasurable pleasure to my life.

TABLE OF CONTENTS

INTRODUCTION

The three chapters of this thesis address the mechanics of the deformation of continental lithosphere, the first two in convergent settings where the deflection of one plate beneath another is recorded in a foredeep basin and an adjacent thrust belt, and the third in a region where continental lithosphere has undergone significant extension.

There is some overlap in the goals of Chapters One and Two, which describe the deflection of the downgoing lithosphere at convergence zones in terms of a simple model treating the lithosphere as a thin elastic plate. Application of this technique to the lithospheric deformation recorded in and near the Ural mountains of the Soviet Union (Chapter One) was motivated by a desire to enhance understanding of both the long–term mechanical properties of cratonic lithosphere and, on a local scale, the geometry of the convergence of the Russian and Siberian plates that resulted in the formation of the Ural mountain belt. Prior modeling of the deflection of continental lithosphere that occurred during Paleozoic time was limited to a single study in the Appalachian mountains of the eastern United States [Karner and Watts, *J. Geophys. Res.*, *88*, 1983]. These authors found that (1) the present mass of the Appalachian mountains is insufficient to maintain the deflection of lithosphere that is recorded in the foredeep basins adjacent to the mountains, (2) the 'missing' mass required to produce the observed deflection may be mass anomalies embedded at depth within the downgoing lithosphere, and (3) the wavelength of the deflection of the downgoing plate implies a very large flexural rigidity (effective elastic plate thickness) for the deflected lithosphere. An immediate goal of the work presented in Chapter One was to establish whether these features are unique to the Appalachian belt, or are exhibited in the Ural mountain region as well. If also present in the Ural region, these features may be interpreted as common to, or perhaps inherent to, the convergence and flexure of cratonic lithosphere. A secondary goal of the Ural study was to establish whether the principal direction of underthrusting beneath the mountain belt could be inferred from the geological observations and from analogies drawn with the Appalachian convergence zone, where the geometry of underthrusting is better understood.

The application of the thin elastic plate model to the deflection of the Adriatic lithosphere near Italy and Yugoslavia was motivated by a question posed not only in the Ural study but long associated with modeling of lithospheric deflections in both continental and oceanic settings, namely what are the physical sources of the forces often required in flexural models to act on the downgoing plate, from locations external to the region where plate deflection can be observed? The answer to this question is of interest as the magnitudes of subsurface forces associated with subduction zone processes, such as the

negative buoyancy of the downgoing slab and shear stresses on the plate associated with asthenospheric flow, are quite difficult to estimate from near–surface geophysical observations. The paired question of nature of the mechanical response of the lithosphere to applied forces is also addressed in the Adriatic study (Chapter Two), where the ability to reconstruct past as well as present deflections of the lithosphere in this region allows examination of changes through time of both the effective flexural rigidity of the lithosphere and the forces necessary to sustain the reconstructed deflections.

The work presented in the third chapter attempts to explain the puzzling observation that highly extended (and hence presumably thinned) lithosphere in the Basin and Range province of the western United States lies at elevations comparable to those of the adjacent unextended Colorado Plateau. The third chapter, like the first two, poses the question of what kind of deformation in the lithosphere could potentially explain the geophysical data. The focus of this study, however, is on a simple model treating the crust as a combination of a brittle upper layer and a deeper ductile channel. As in the first two chapters we impose any direct observations of lithospheric deformation (in this case the surface extension) as a boundary condition on the mechanical model, and establish the range of model parameters that are compatible with the data. Because the model developed in Chapter Three has not been as widely used as the thin elastic plate model, the third chapter addresses more closely the conditions under which the Lake Mead ductile flow model is compatible with experimental data on deformation of crustal rocks.

The thin elastic plate model used in Chapters One and Two and the ductile flow model applied to the Lake Mead area in Chapter Three differ in their assumptions about the process of lithospheric deformation responsible for the observed topography, gravity, and near–surface deformation. These models, however, are not mutually exclusive. Both models can be used to describe lithosphere that deforms at shallow depths by brittle failure (Byerlee's Law) and by ductile failure at greater depths, with greatest deviatoric stresses maintained at intermediate depths near the brittle–ductile transition (see Figure 7a of Chapter Three). Because the depth range and integrated strength of the brittle and ductile zones of deformation are highly dependent on the lithospheric temperature structure, the magnitude of applied stresses, and the rates of strain, the thin elastic plate model and ductile flow models may each be appropriate for describing lithospheric deformation under a limited range of temperature, stress, and strain rate conditions.

Because the geotherms beneath the relatively cold Russian and Adriatic lithospheres are normal, the crust–mantle boundary in these areas lies within the strong intermediate layer, above the depths at which deformation occurs primarily by ductile flow. Bouguer gravity anomalies, assumed to arise primarily from deflections of the crust mantle boundary, will

thus reflect the deflections of the strong layer. The deformation of this strong layer can be modeled as the deflection of a thin elastic plate. Ductile deformation will certainly also be present at greater depths, but because ductile deformation occurs within mantle material of relatively uniform density, it will leave a significantly smaller effect on the gravity field. In contrast, the elevated crustal temperatures in the Basin and Range may enable ductile deformation to occur at shallow depths above the crust–mantle boundary. In this region Bouguer gravity anomalies may reflect depths to the base of a ductile layer, and will directly record shallower brittle or elastic deformation only if there are significant density contrasts within the crust.

Thus in regions underlain by relatively cold continental lithosphere such as the Urals and Adriatic, the gravity and basement deflection data record the deformation of the strongest portion of the lithosphere, and may be appropriately modeled as corresponding to the deflections of a thin elastic plate. In the much warmer Lake Mead region, the depths to the crust–mantle boundary recorded in the Bouguer gravity anomalies and seismic data reflect the combined thicknesses of brittle, intermediate, and ductile layers. The higher temperatures which reduce the depth of the brittle–ductile transition also have the effect of reducing the integrated strength of the shallower lithosphere such that the mechanical strength of the shallow brittle layer may have little impact on ductile flow deeper in the crust. This may be observed in the Lake Mead area, where combined topography and gravity data suggest the lithosphere has a small flexural rigidity. The geophysical and geological observations in this area therefore result from the combined effects of local brittle deformation and variations in the thickness of the deeper ductile layer, and are better explained by the ductile flow model than the thin elastic plate model.

The applicability of the thin elastic plate model to the Ural and Adriatic convergence zones is also a consequence of the relatively small amount of strain undergone by the downgoing lithosphere directly beneath the foredeep basins and thrust belts. Within the lithosphere near the neutral plane of the bending there should exist a range of depths where stresses induced by bending do not exceed the yield stress of the material. The success of the thin elastic plate model in simultaneously fitting both gravity and basement deflection data suggests that neither brittle deformation at shallower depths nor ductile deformation at greater depths in the downgoing plate introduces major differences between plate deflections inferred from basement deflections and those inferred from deflections of the crust–mantle boundary.

The style of lithospheric deformation depends not only on the temperature and stress conditions, but also on the rates of strain. The success of the thin elastic plate model in describing the deformational history in the Adriatic region with an approximately

constant flexural rigidity (see Chapter Two) suggests that the strength of the lithosphere does not decrease significantly over the 2 to 50 million year time periods modeled in this study. Thus viscoelastic relaxation over these time scales in the portions of the lithosphere maintaining the observed deflection cannot be detected in this study. Viscoelastic relaxation may, however, be a significant process over shorter or longer time scales. The success of the ductile flow model in explaining the Lake Mead observations suggests that significant ductile flow in the lower crust may occur under applied stresses on time scales of 10 million years or less. This result appears to be compatible with the extrapolation of laboratory flow laws for lower crustal material to the strain rate and stress conditions of the Lake Mead area.

CHAPTER 1
COMPENSATION OF PALEOZOIC OROGENS: A COMPARISON OF THE URALS TO THE APPALACHIANS

INTRODUCTION

The mechanism by which mountain ranges are isostatically compensated reflects the rheological properties of the continental lithosphere and the tectonic processes responsible for orogeny. The well-accepted view that mountains are supported by crustal thickening has been recently challenged by a radically different concept in which fold belts are underthrust by rigid continental plates which support effective subcrustal loads in the orogenic hinterland as well as the topography. Stockmal and Beaumont (1987) propose that the leading edge of the underthrusting plate is a passive continental margin. In this case the apparent subcrustal load is in fact mantle material beneath thinned crust. In the particular case of the Appalachians, Karner and Watts (1983) have proposed that the mountains are compensated by the North American craton behaving like a fractured elastic plate 80-130-km thick which also supports a buried load, 5 times as massive as the topography, beneath the Piedmont province. If the presence of effective deep loads proves to be generally valid for old and inactive orogens, it implies that: 1) tectonic models for continental orogeny must be revised to explain the presence of significant buried mass anomalies loading the downgoing plate which cannot be dynamic or thermal in nature due to their long-term persistence; 2) the asymptotic thickness of continental lithosphere must be greater than that of oceanic lithosphere; and 3) the vertical rebound of the Earth's crust in response to erosion of mountainous topography is modified by the finite rigidity of the elastic plate and the invulnerability of the buried loads to erosion.

Here we test the model applied to the Appalachians (Karner and Watts, 1983) at another Paleozoic orogen, the Ural Mountains. The Urals formed during Permian time due to the collision of the Russian and Siberian plates (Hamilton, 1970; Zonenshain et al., 1984). The fact that the lithospheric structure in the vicinity of the Urals, unlike the Appalachians, has not been modified by post-Hercynian tectonic events (e.g., the opening of the Atlantic) allows for a more straightforward interpretation of the data in terms of the collisional process. While the poor signal-to-noise ratio in the gravity data precludes quantitative constraints on a compensation mechanism, we are able to address several unanswered questions concerning the formation of the Urals, such as: How has the convergence of the Russian and Siberian plates been accomodated at depth? Has

there been significant underthrusting of a plate beneath the mountains, and if so, what is the orientation? Is the load of the mountains maintained by the Russian plate, the Siberian plate, or both?

GEOLOGIC SETTING

The Ural Mountains extend for more than 2000 km from the Barents Sea in the north nearly to the Caspian Sea in the south and separate the Russian Platform from the West Siberian Lowlands (Figure 1). Paleomagnetic poles from the Russian Platform and East Siberia are distinctly different during Paleozoic time and merge by Permian time (Khramov and Rodinov, 1981). The timing of folding and thrust faulting also indicates convergence and final collision of the Russian and Siberian plates occurred during Permian time (Hamilton, 1970; Zonenshain et al., 1984).

A transect of the southern Urals across strike from west to east (Fig. 2) reveals the following features: (a) the Russian Platform; (b) the Ural foredeep; (c) the western Urals; (d) the Main Uralian Deep Fault (MUDF), a thrust fault dipping 40 to 60 degrees to the east; (e) the eastern Urals; and (f) the West Siberian Lowlands bounded on the east by the Siberian platform.

The Precambrian basement and lower Paleozoic carbonates of the Russian Platform dip eastward beneath the Ural foredeep (Bally and Snelson, 1980). An interface traced by deep seismic sounding and interpreted as the Russian Platform basement extends from the platform beneath the folded western Urals to the MUDF (Aleinikov et al., 1980).

In the foredeep west of the Urals lower Paleozoic carbonates are overlain by Devonian through Triassic platform carbonates which grade eastward to thicker terrigenous clastics derived from the east (Hamilton, 1970; Dymkin et al, 1984). The surface width of the foredeep deposits ranges from 0 to approximately 100 km (Fig. 2) (Dymkin and Puchkov, 1984) although Bally and Snelson's (1980) cross-section in the southern Urals suggests a basin width in this region of approximately 150 km. The foredeep appears to extend perhaps 20 km or more eastward beneath the Urals (Bally and Snelson, 1980; Zonenshain et al., 1984; Dymkin et al., 1984).

In the western Urals, late Precambrian basement is conformably overlain by folded and sheared Paleozoic continental shelf and deep-water sediments up to 6-7 km thick (Dymkin et al., 1984; Dymkin and Puchkov, 1984; Zonenshain et al., 1984). Structural relationships are complex: allochthonous Paleozoic volcanics and ultramafic intrusions are juxtaposed against Precambrian and early Paleozoic continental basement extending

east of the foredeep beneath the Urals to the MUDF (Hamilton, 1970; Dymkin and Puchkov, 1984; Zonenshain et al, 1984; Ivanov and Rusin, 1986). Nappes derived from the east appear to have been translated at least a few tens of kilometers (Dymkin et al., 1984), and decrease in age to the east (Kazantseva and Kamaletdinov, 1986).

The MUDF separating the western and eastern Urals is a zone of serpentinite melange including high pressure metamorphic rocks (glaucophane- and kyanite-schists, and eclogite (Hamilton, 1970; Dymkin et al., 1984)), from a few to 20 km wide and bounded on the east by sheets of ultramafic rocks (Hamilton, 1970). Seismic data indicate the fault dips 40 to 60° to the east, although it may flatten with depth (Dymkin and Puchkov, 1984). The melange zone may extend more than 200 km beneath the eastern Urals (Zonenshain et al., 1984). K-Ar geochronology of the mafic and ultramafic rocks yields Ordovician and Silurian ages (Hamilton, 1970).

The Urals east of the MUDF include Paleozoic island-arc type volcanic complexes. The youngest complexes are of Middle Carboniferous age (310 Ma) (L. Zonenshain, pers. comm.). Igneous rocks include ultramafics and mafics of ophiolite sequences bounded by eastward dipping faults (Dymkin and Puchkov, 1984; Savelyev and Savelyeva, 1977) and radiometrically dated 450 to 280 Ma granitic gneiss domes predominantly in the east (Zonenshain et al., 1984). Large faults show late stage motions that become progressively younger to the east (Hamilton, 1970).

Drilling in the West Siberian Lowlands on the eastern flank of the Urals indicates Upper Devonian and Carboniferous shallow-water limestone and terrigenous sediments and volcanic sequences arranged in simple linear folds beneath Mesozoic and Cenozoic sediments (Dymkin et al., 1984). Following Late Permian and Early-Middle Triassic uplift and graben and rift formation, the West Siberian Lowlands underwent generally uninterrupted subsidence throughout Mesozoic time (Nesterov et al., 1984; Rudkevich, 1976). The crust in the region is anomalously thin (less than 35 - 40 km) relative to the crust of the surrounding Russian and Siberian cratons (greater than 40 km) (Tamrazyan, 1971; Nesterov et al., 1984).

GEOLOGIC CONSTRAINTS ON CONVERGENCE STYLE

Despite the wealth of geologic data described above, the orientation and extent of lithospheric underthrusting in the Urals remain unresolved. Several partially conflicting tectonic interpretations exist. Hamilton (1970) has proposed an Ordovician and Silurian subduction zone that dipped east away from the Russian platform beneath an island arc. (Throughout this paper convergence geometries are described in terms of the present day

orientation with the Russian Platform to the west and the West Siberian Lowlands to the east of the orogenic belt.) The early east-dipping subduction zone is now represented by the MUDF. In Early Devonian time the continent collided with the island arc, and the orientation of subduction changed during Devonian time from east-dipping to west-dipping due to the resistance of the lighter, more buoyant continental crust of the Russian platform until the Siberian and Russian platforms collided in the Permian. Hamilton's preferred final polarity of subduction is westward dipping.

Murray (1972) uses the observation of parallel early Paleozoic and Devonian metamorphic and igneous belts to argue for west-dipping subduction, although this may only pertain to motions prior to the Permian continent-continent collision.

In their analysis of the southern Urals, Zonenshain et al. (1984) have proposed that the eastern border of the Russian Platform was a passive margin as the Uralian paleo-ocean formed to the east during Early Ordovician time. Early Paleozoic sediments were deposited on the margin of the platform. Subsequent formation of island arcs in the ocean basin and the closure of the basin from Silurian through Carboniferous time resulted in the obduction of ophiolites and the formation of the igneous nappes in the western Urals and the folded arc-type volcanics in the eastern Urals. Deposition of foredeep sediments, continued westward thrusting, and the closure of the ocean occurred in the final stages of collision in the southern Urals (310-220 m.y. ago). While earlier subduction within the ocean basin may have been west-dipping, the primary thrusting orientation was of the Russian platform beneath the nappes to the east. Thus Zonenshain et al. (1984) propose a primary underthrusting polarity opposite to that of Hamilton (1970) and Murray (1972).

There is clearly disagreement in the literature over the collisional process and lithospheric deformation in the Urals. We believe the strongest evidence in the geologic literature points to an east-dipping underthrusting of crust. The westward displacement of nappes over the Russian Platform, the eastward dip of major faults, the preserved asymmetric shape of the foredeep, and the seismic reflectors extending from the Ural foredeep eastward to the MUDF all point to east-dipping subduction of crust.

A second line of evidence arises if we suppose the gross geological similarities between Urals and the Appalachians reflect similarities in subduction polarities. Comparing the two orogenic belts, the Appalachian Piedmont province with granitic plutons and scattered ultramafics is comparable to the eastern Urals; the folded and faulted sediments and complex structure of the Blue Ridge and Valley and Ridge are analogous to features of the western Urals; the Brevard zone separating the Piedmont from the sedimentary Appalachians may correspond to the MUDF, and the Appalachian

foreland area to the Ural foredeep. Therefore Karner and Watts' (1983) model for an elastic plate flexing eastward beneath the Appalachian foreland and mountains corresponds to the Russian Platform plate dipping eastward beneath the Urals. We have used topography and gravity data and information on the depth to the Moho to test the validity of this model in the Urals.

GEOPHYSICAL DATA

Topography

We averaged the dbdb5 5 minute topography data set obtained from the Defense Mapping Agency to 15 minute intervals and projected the data in the region of interest (Fig. 3). Although the source data interpolated by dbdb5 appear sparse in the northern area of the West Siberian Lowlands, coverage over the topographic high of the Urals appears complete.

Gravity

We compiled gravity anomalies in the region from the data sets of Bowin et al. (1981) and Zakatov (1953) and the map of Artemyev et al. (1973) and converted these values to Bouguer anomalies, assuming a crustal density of 2670 kg/m^3. Long wavelengths in the gravity field were removed using Gem9 coefficients to degree and order 10. This does not affect gravity features reflecting loading of the lithosphere by the Ural Mountains, as these have wavelengths on the order of several hundred kilometers or less, as described below. Fig. 4 shows Bouguer anomalies averaged along strike.

Moho depth

Large scale contour maps of Moho depth for the entire USSR (Tamrazyan, 1971; Smyslov et al., 1984) and for the Russian platform (Nalivkin, 1976) are available although the control is not given. These maps suggest depression of the Moho from a mean level of 40 km to 45 to 50 km beneath the Urals. Berlyand (1983) reports Moho depths of 33-45 km beneath the Russian Platform margin, Ural foredeep and western Urals, and deeper values of 45-50 km and 35-45 km underlying the western and eastern parts of the eastern Urals, respectively. The best data come from a cross-strike continuous deep seismic sounding profile at approximately 55°N (Volvovskii and

Volvovskii, 1975) (Fig. 5) that shows depths we estimate accurate to within 6 km. The location of this profile is shown on Fig. 3. An approximately 3-10 km deep depression of the Moho is centered beneath the eastern flank of the Urals.

ELASTIC PLATE MODELS

A model that treats the lithosphere as an elastic plate overlying an inviscid fluid and supporting topographic and subsurface loads (Fig. 6) can explain the observed deflection of downwarped crust at oceanic subduction zones (Hanks, 1971 and others) and has been applied to the compensation of sediment loads on continental lithosphere (Walcott, 1970). More recently, it has been used at diverse continental orogenic belts such as the Appalachians and Alps (Karner and Watts, 1983), Himalaya (Karner and Watts, 1983; Lyon-Caen and Molnar, 1983, 1985), Carpathians (Royden and Karner, 1984), Apennines (Royden and Karner, 1984; Royden et al., 1987), the Tarim Basin (Lyon-Caen and Molnar, 1984), Bolivian Andes (Lyon-Caen et al., 1985), Transverse Ranges, CA (Sheffels and McNutt, 1986), Zagros (Snyder and Barazangi, 1986), and other Eurasian mountain belts (McNutt and Kogan, 1986; McNutt et al., 1988). By applying this model in the Urals we can compare the implied mechanical behavior of the Ural collisional belt with that of the Appalachians and other diverse orogenic zones.

In this study we use the standard equation describing flexure of a thin elastic plate in two dimensions:

$$\frac{d^2}{dx^2}\left(D\frac{d^2w}{dx^2}\right) - \frac{d}{dx}\left(t\frac{dw}{dx}\right) = q\,(x)$$

where w(x) is the vertical deflection of the plate, q(x) the vertical load, t(x) the horizontal stress, and D(x) the flexural rigidity at location x along the profile. The flexural rigidity is related to the effective elastic plate thickness T_e via the relation

$$D = \frac{E\,T_e^3}{12\,(1-\nu^2)}$$

where E is Young's modulus and ν is Poisson's ratio. We point out the classic Airy compensation mechanism (Airy, 1855), in which the mass of the mountains is locally isostatically balanced by a thickening of the crust, is the special case of an elastic plate with zero thickness. The differential equation is solved using a finite difference method; back substitution is performed on a 5-band matrix (Sheffels and McNutt, 1986).

Boundary conditions allow us to specify a bending moment (equivalent to a torque) on the fractured end of the plate. We calculate the flexure of the plate for the desired loads and boundary conditions. We then compute the gravity anomalies resulting from equivalent flexure of the lithosphere and compare these with the observed gravity field.

Of the parameters needed in our modeling, only the topography is known precisely. We assume fixed crustal (2670 kg/m^3) and mantle (3300 kg/m^3) densities. This density structure is obviously an oversimplification, as several seismic refraction studies in the Ural region (Sokolov et al., 1974; Druzhinin et al., 1983; Volvovskii and Volvovskii, 1975) reveal refracting interfaces at 10 to 20 km that indicate material properties vary with depth within the crust. However, more complicated modeling is unjustified for several reasons. First, if the lithosphere flexes coherently (as one plate) at the depths where density contrasts exist, then the plate deflection of lithosphere with a more complicated density profiles will be the same as the deflection calculated for the simple model with the same upper-crustal and mantle densities. The parallel warpings of refracting interfaces (Sokolov et al., 1974; Druzhinin et al., 1983) suggest coherent flexing in the Urals. Secondly, we lack any direct data on deep crustal densities on which to base a more accurate density model. Any forward gravity modeling is inherently nonunique, and an infinite number of density structures may result in the same gravity signature. Finally, the long wavelengths in the flexure of plates in our models discussed below means that the depth assumed for lithospheric density contrasts has a relatively small effect on the model gravity field. In the regions where the plates are more sharply bent the model gravity is determined in general by postulated (non-unique) excess subsurface mass (Fig. 7). We set values for the bulk modulus (70 GPa), Poisson's ratio (0.25), and the crust-mantle boundary depth determined from seimic refraction studies (40km) (Volvovskii and Volvovskii, 1975; Smyslov et al., 1984). For simplicity, the elastic thickness is assumed to be constant throughout the plate and the horizontal stress is presumed to be negligible. We then derive the elastic plate thickness, terminal bending moment, and possible subsurface loads by fitting the predicted gravity and Moho deflections to the observations.

We stacked the gravity data into two cross-strike profiles trending approximately east-west. Because cross-strike variations in topography, gravity, and geologic features are much greater than along-strike variations in the Urals, two-dimensional analysis of profiles averaged along-strike is a good approximation to the 3-dimensional structure. Profile 1 consists of data averaged over 400 km along strike through the central Urals; Profile 2 is derived from averaging over 600 km through the southern Urals. On both

profiles topography data were interpolated to 33 km intervals, Bouguer gravity anomalies to 67 km intervals.

We also require a successful model to predict a minimum of 2 km of depression of the Moho beneath the mountains (to agree with sismic profiling) and at least 1 km of depression on the western flank of the mountains (to predict the presence of the Ural foredeep). In the southern profile, we also require the maximum depression be located east of the topographic high, as shown on the profile of Volvovskii and Volvovskii (1975).

Following work in the Appalachians (Karner and Watts, 1983), we assume the elastic plate extends from the west beneath the Urals, with a free end beneath or east of the mountains. Before comparing the calculated gravity field produced by such a plate with the data, two modifications are made to the model gravity field computed directly from the deflection of the crust-mantle boundary and postulated subsurface loads. First, we assume that topographic mass east of the end of the elastic plate is locally compensated and add the resulting Bouguer anomalies to our model anomalies. Secondly, we note that the Russian Platform is not exactly in regional isostatic equilibrium. Our elastic plate model assumes the plate as a whole is isostatically compensated; therefore to model plates in this region we must assume the presence of a long wavelength gravity anomaly in the regional field. For the purpose of fitting the models to the data we added 16 and 52 gu to Profiles 1 and 2, respectively, on the Russian plate.

RESULTS

Figs. 7a and b show the Bouguer anomalies expected for elastic plates of thickness 0, 50 100, and 150 km and the observed anomalies for Profiles 1 and 2. Along each profile there are significant differences between observed and predicted gravity for all plate thicknesses. In particular, on both profiles the observed gravity low slightly west of, and the gravity high to the east of the mountain peak are not predicted. Furthermore, the load of the topography acting on even extremely weak plates fails to depress the plate more than 2 km. Thus, this simple model fails to predict the geophysical observations for a wide range of plate thicknesses.

We examine possible crustal sources of gravity anomalies that could explain the discrepancy between the observed and predicted gravity anomalies and could produce greater plate deflections. We model the effect on the predicted Bouguer gravity field of a strip of dense material along the strike of the Urals of given width and depth, assuming

this load is supported by the elastic plate. Figs 6c and d show the result of the addition of a band of material of density 3100 kg/m^3, 100 km wide acting on the elastic plates in combination with the bending moment that produces the most desirable fit over the Russian Platform. The band of excess mass in each case in Fig. 7 (approximately 8 x 10^{11} N/m) is roughly the minimum mass which depresses the crust at least 2 km. With this strip of high density material the model can successfully predict a significant Moho depression and provides an adequate fit to the gravity anomalies. We note that the mafic and ultramafic rocks and ore deposits observed on the eastern Urals are roughly coincident with the short wavelength gravity high, suggesting that similar dense material within the crust is the source of this anomaly.

The sediment basins on the Russian Platform and foredeep basin west of the Urals may also have a significant gravity signature. Although sediment isopachs for the Russian Platform are given by Nalivikin (1976), gravity observations over these sediments indicate they are of variable density, so we cannot make precise predictions for their gravitational effect. Furthermore, even complete surface mapping of sediments will probably not reveal all shallow density variations, as Lyon-Caen and Molnar (1983; 1985) have suggested in the Himalaya that sediments extend toward the mountains beneath thrust sheets. We neglect any direct modeling of the gravity and loading effects of sediments, but note that the gravity low west of the mountains may arise in part from the presence of shallow sediments.

We cannot find a maximum value for the eastward extent of an elastic plate from the gravity data. For a given elastic plate deflection profile, increasing the length of the plate is equivalent to changing the force and bending moment acting on the end of the plate, and models for plates that extend further east may yield equivalent deflections and gravity signatures over the Russian Platform. The data suggest, however, that the plate extends at least beneath the mountain load. The presence of the asymmetric foredeep basin is explained by the depression of plates with non-zero thickness beneath the Urals, and the continuity of reflectors from the Russian Platform to the MUDF (Aleinikov et al., 1980) indicates that the basement is continuous from the Russian Platform eastward beneath the mountains. We find models for east-dipping elastic plates terminating directly beneath the mountain peaks are acceptable and require approximately equivalent subsurface loads as those depicted in Fig. 7. Simple models for a Russian plate with non-zero thickness that does not extend beneath the mountains do not predict the gravity low observed west of the topographic high in both the southern and central Urals. Although the failure of these gravity models is not conclusive, as this discrepancy may be due in part to the presence of low density sediments west of the Urals, the gravity and

geological data taken together strongly suggest the elastic plate extends eastward to the MUDF.

Because of the low signal-to-noise ratio in the gravity data in Figs. 7c and d, this data set is not an effective constraint on an elastic plate thickness. The shape and location of the Ural foredeep basin therefore provide the most important constraint on plate thickness. Only plates with thickness greater than 50 km predict a depression of the elastic plate beneath the observed foredeep basin. Thus we have a lower bound on the effective plate thickness. We also note that the gravity bulge in the southern profile over the central Russian Platform correlates spatially with the Tatar Swell, a shallowing of the Precambrian basement (Bally and Snelson, 1980; Artyushkov and Bear, 1986). This suggests that the basement shallowing in the Tatar swell is primarily not locally compensated, and therefore that the Russian Platform does indeed have flexural strength.

To confirm our suspicions on the polarity of subduction, we tested two other sets of plate geometries (Figures 8 and 9). In the first, we assumed a plate extends from the West Siberian Lowlands west beneath the Urals to their eastern flank. This corresponds to the subduction orientation proposed by Hamilton (1970). Even with the inclusion of a subsurface load such a model fails to predict gravity observations over the West Siberian Lowlands and the mountains in the southern Urals (Fig. 8b) and provides a rough fit to the gravity data in the central Urals (Fig. 8a) only assuming weak (0 or 50 km) plates. Application of a bending moment on the end of the plate does not improve the fit of the models for thicker plates. Although a west-dipping, weak plate model does not contradict the gravity data, this scenario is unappealing for two reasons. (1) this compensation mechanism fails to explain the presence of the Ural foredeep, and (2), a very weak plate is inconsistent with elastic plate parameters for the Ural region derived from admittance and coherence data (McNutt and Kogan, 1986; McNutt et al., 1988). If, however, the West Siberian plate does not extend (and is not depressed) beneath the mountains, models assuming a stiffer West Siberian plate may reproduce the relatively flat gravity field over the West Siberian Lowlands. To quantify the thickness of such a plate with forward modeling would require detailed knowledge of anomalous crustal masses in the West Siberian Lowlands, as no distinct topographic loads on the plate are present. In any case the tectonic implication of the modeling shown in Fig. 8 is that west-dipping subduction beneath the Urals did not occur to an extent that a West Siberian plate with significant elastic strength maintains the load of the mountains.

In the final set of models discussed, we assumed a continuous elastic plate extends from the Russian Platform to the West Siberian Lowlands beneath the Urals (Fig. 9). Such a model would imply that the Russian and Siberian plates have sutured and thus

behave mechanically as a single plate. The case of zero elastic plate thickness corresponds to the traditional model for support of the mountain load by local crustal thickening. The continuous plate model can produce agreement with the geophysical observations only assuming subsurface loads act on an extremely thin plate, so that loads are effectively locally compensated. Our objections to this model are equivalent to those stated for the weak west-dipping plate model above. We conclude that of these three sets of models, only an east-dipping plate geometry adequately predicts the observed Moho depths, gravity anomalies, and presence of the foredeep basin.

DISCUSSION

The Elastic Plate Thickness

From the shape of the Ural foredeep we can infer that an elastic plate supporting the Urals is at least 50-km thick. Elastic plates with thicknesses up to 100-150 km are compatible with the geophysical data. These thicknesses lie within the range observed at other continental thrust belts, which extends from 8 km in the Apennines (Royden and Karner, 1984) to approximately 100 km in the Appalachians (Karner and Watts, 1983). The elastic strength of the thickest continental plates such as the Appalachians, and perhaps the Urals, is incompatible with accepted models for the oceanic lithosphere that predict maximum elastic plate thicknesses of 40 km (Watts et al., 1980) and 55 km (McNutt and Menard, 1982) for a 125-km thick thermal plate. If the relationships between elastic and thermal plate thicknesses found for oceanic lithosphere are valid in continental settings, then a 100-km thick elastic plate implies that the thickness of cratonic continental lithosphere must be greater than old oceanic lithosphere. McNutt et al. (1988) suggest that on continental plates the range of observed elastic thickness reflect to a great extent variations in the lithospheric stress regime. In light of their hypothesis a thicker Russian plate has presumably withstood less compressive stress and probably dips more gently than most continental plates underthrust at orogenic zones.

McNutt et al. (1988) derive a 85-km elastic plate thickness for the Russian plate using coherence data and a simple forward model. McNutt and Kogan (1986) predict a 124 km plate, converting a value derived from regional admittance data to a fractured plate thickness. Their estimate could be revised downward by assuming that the fractured plate does not end exactly beneath the mountains, but continues farther to the east. Our model incorporating an east-dipping Russian plate supporting the mountain

load places no constraints on an acceptable effective elastic plate thickness for the adjacent West Siberian Plate.

Direction of Underthrusting

Gravity data is incompatible with simple models of continuous or west-dipping elastic plate (with nonzero thickness) mechanisms for compensation of the Urals. Thus, if westward subduction beneath the Urals did occur during their formation, the plate does not transmit the load of the mountains eastward. The only mechanically significant underthrusting beneath the Urals allowed by our modeling is eastward directed underthrusting of the Russian plate.

There are several important geological implications of this result. An eastern underthrusting or subduction orientation implies that the Ural foredeep is truly a foredeep basin, as its asymmetric east-thickening shape suggests. The Paleozoic Russian Platform basement extending beneath the mountains is presumably part of the underthrust plate. The eastern dip of the MUDF and faults surrounding ophiolitic blocks and the westward transport of nappes are perhaps surficial manifestations of larger scale plate subduction.

The Subsurface Load

The loads modeled in Fig. 7 are the minimum required to produce the smallest plate deflection (2 km) we consider compatible with the Moho data described above. Although larger loads explaining greater than 2 km of Moho deflection are more likely because several maps show Moho depressions of more than 5 km (Tamrazyan, 1971; Smyslov et al., 1984) we cannot distinguish these models from the minimum load models on the basis of the gravity data. The minimum loads for the southern and central regions (Fig. 7) are 1-2 times the topographic load. Thus in the Urals the effective subsurface load is at least half the external load on the plate, and is probably the dominant feature controlling the elastic flexure.

It is encouraging to note that the ratio of our minimum effective subsurface load to topographic load (approximately one) is equal to the value derived by McNutt et al. (1988) with a very different method. They used admittance and coherence calculated from Bouguer gravity and topography data (Forsyth, 1985) to estimate an elastic plate thickness in the region of the Urals. To make the elastic plate thickness computed by each method agree, they require a ratio of internal to surficial load of one. Their method yields no information however on the location of loads within the plate.

Several lines of evidence suggest that the subsurface load required in the Urals is a compositional feature, and a remnant of the convergence process. It may have been emplaced in a process similar to the obduction of crustal flakes onto the underthrusting plate proposed in continental orogenic belts by Karner and Watts (1983). The ophiolitic and volcanic-arc type sequences in the eastern Urals are an indication preexisting dense material was blocked from subduction during convergence. The subsurface load could also represent the shallowing of the Moho where thinned continental crust at a passive margin was buried by advancing thrust sheets (Stockmal and Beaumont, 1987). The Moho, however, appears slightly deeper, rather that shallower, on the eastern flank of the mountains in the region of the gravity high (Fig. 5) (although this section of the profile seems to be very noisy). At any rate, several alternative explanations proposed for such forces are unlikely in this old orogenic belt. We expect the dynamic forces associated with the convergence that formed the mountains to have dissipated, since active convergence ceased in the beginning of the Mesozoic. Another suggestion, proposed in active convergence zones such as the Transverse Ranges (Sheffels and McNutt, 1986) and the Himalaya (Lyon-Caen and Molnar, 1983), is that the projection of the subducting slab under the mountain belt maintains a thermal (and hence density) anomaly which produces a force and bending moment on the end of the elastic plate. The Urals are too old to retain a significant thermal anomaly of this kind. Furthermore, both of the latter hypotheses predict a gravity low over the depressed region of the Moho, which is not observed in the Urals.

While substantial subsurface loads have been proposed in the Appalachians and Alps (Karner and Watts, 1983) and in the Zagros (Snyder and Barazangi, 1986), no such crustal subsurface loads are required in several active orogenic belts resulting from continental-continental collision such as the Himalaya (Lyon-Caen and Molnar, 1983, 1985) and the Transverse Ranges (CA) (Sheffels and McNutt, 1986). We speculate that anomalously dense subsurface material exists at many continental orogenic belts, but is obscured by the larger topography at young and active subduction zones. In older or quickly eroding regions the subsurface load, which remains intact, becomes the dominant load over time. This load, whatever its origin, then limits the vertical rebound of the lithosphere and serves to preserve the foredeep basin.

The Bending Moment

Application of a bending moment of 1 to 3 x 10^{17} N slightly improves the fit of the thicker east-dipping fractured plate models (Figs. 7c,d). Because of the time elapsed

since active convergence in the Urals, the nature of such a bending moment on the fractured plate end, if present, is presumably neither dynamic or thermal. A simple explanation for a bending moment is that it arises from the distribution of loads acting on the plate

The West Siberian Lowlands

Our gravity modeling over the subducting Russian Platform does not place any constraints on the mechanical behavior of the West Siberian Lowlands. The trend of the gravity data in West Siberia is remarkably flat (after the removal of very long wavelengths), supporting our preferred conclusion that the Urals indeed have little effect on this plate at present. The occurrence of post-collisional West Siberian uplift and graben formation (Artyushkov and Bear, 1986; Nesterov et al., 1984, Rudkevich, 1976) suggests to us that following the collisional event this region may have been an elevated plateau that formed adjacent to a subducting plate. This scenario is perhaps analogous to the present-day Tibetan Plateau, which is undergoing some extension (for example Mercier et al., 1987). The widespread basins of the West Siberian Lowlands (Kulikov et al., 1972) may represent a later stage of such extension. The extent of the Mesozoic subsidence and work by Aplonov (1986) showing that some Triassic rifts developed into a narrow oceanic-type basin further suggest that West Siberia eventually evolved into a highly extended region. The Mesozoic setting is perhaps comparable to the initial stages of development of a back-arc-type basin. In any case, the present-day thin crust and uniform elevation of the West Siberian Lowlands indicate the lithosphere has been extended and thinned, and we note that both of the above tectonic analogies for West Siberian extension are compatible only with an east-dipping subduction orientation in the Urals.

Gordon and Hempton (1986) have postulated a somewhat different genetic relationship between the Urals and the grabens in West Siberia. They propose the grabens are pull-apart basins forming on preexisting planes of weakness as a result of the compression which formed the Urals. We believe that such a mechanism is unlikely to yield the great amount of extension implied by the evolution of some West Siberian rifts into an oceanic-type basin, as Aplonov (1986) suggests. However, further analysis of the structure of the West Siberian grabens and the relative timing of compression in the Urals and extension on the West Siberian plate is needed to test these hypotheses.

CONCLUSIONS

The apparently contradictory observations of a Moho depression of several kilometers beneath the Urals and lack of significant corresponding negative gravity anomaly may be resolved by the assumption of a substantial subsurface crustal load. The geophysical observations are compatible with a model that assumes the Russian plate flexes downward to the east beneath the mountains. The presence of subsurface loads on a thick plate also explains the east-thickening shape of the Ural foredeep basin and its preservation despite considerable erosion of the topographic load. This excess crustal load may be composed of material, similar to the mafic and ultramafic outcrops in the eastern Urals, that was trapped within the crust rather than subducted during the collisional process that created the Urals. We suggest on the basis of an east-dipping underthrusting geometry and the observations of post-collisional uplift and extension in the West Siberian Lowlands that West Siberia may possibly represent the future state of present-day elevated plateaus at continental collisional zones such as the Tibetan Plateau.

We have tested a compensation mechanism proposed for the Appalachians, in the Urals. We find a combination of Bouguer gravity data, seismic profiles, and a knowledge of the location and shape of the Ural foredeep basin support the analogous Appalachian model. These results suggest the common geological characteristics of the Urals and Appalachians are the surficial manifestation of similar lithospheric deformation upon convergence and comparable compensation mechanisms. If this model for a thin elastic plate depressed by the weight of topographic and subsurface masses is found to have more general validity, several important implications follow. The great elastic plate thickness derived for the lithosphere at these Paleozoic orogens could not exist within oceanic lithosphere, thermally 125 km thick. Thus cratonic continental lithosphere must be thicker than oceanic lithosphere, or possess inherently greater flexural strength at comparable temperatures. Effective subsurface loads such as those discussed here should modify the extent the crust isostatically rebounds as mountain belts erode. We suggest these loads are not unique to Precambrian or Paleozoic orogens, but may occur in many continental-continental subduction zones, where their effect on plate behavior and the gravity field is obscured by the topographic signal at young uneroded mountain belts.

Finally, we note that the gravity data alone allowed us only to verify that a loaded thin elastic plate model could be applicable to the Urals. Due to the poor signal-to-noise ratio in the data we are unable to impose quantitative constraints on an effective elastic

plate thickness. It has been suggested that the scientific requirements for accuracy and resolution of gravity data are less stringent for mountain belts due to the large amplitude and the long wavelength of gravity anomalies produced by flexure of a stiff plate (Geopotential Research Mission Science Steering Group, 1985). After examining the available data from the Urals, we conclude that gravity data accurate to a few mgals at wavelengths of less than 100 km are desirable even in regions of high plate strength in order to distinguish flexurally-induced mass deficits from crustal loads.

REFERENCES

Airy, G.B., 1855. On the computation of the effect of the attraction of mountain masses. Philos. Trans. R. Soc. London, 145: 101-104.

Aleinikov, A.L., Bellavin, O.V., Bulashevich, Yu.P., Tavrin, I.F., Maksimov, E.M., Rudkevich, M.Ya., Nalivkin, V.D., Shablinskaya, N.V. and Surkov, V.S., 1980. Dynamics of the Russian and West Siberian Platforms. In: A.W. Bally, P.L. Bender, T.R. McGetchin and R.I. Walcott (Editors), Dynamics of Plate Interiors. Geodyn. Ser. Vol. 1, AGU, Washington, D.C., pp. 53-71.

Aplonov, S.V., 1986. A hypothetical Early Mesozoic paleoocean in the northern part of the West Siberian Lowlands. Okeanologiia, 26: 467-473.

Artemyev, M.E., H. Kambarov, and A. Dacimov, 1973. Isostatic state of the southern area of the USSR. In: M.E. Artemyev (Editor), Isostasy. Scientific council for complex investigations of the Earth's crust and upper mantle, USSR Academy of Sciences, Nauka, Moscow.

Artyushkov, E.V., and Bear, M.A., 1986. Mechanism of formation of hydrocarbon basins: The West Siberia, Volga-Urals, Timan-Pechora Basins and the Permian Basin of Texas. Tectonophysics, 122: 247-281.

Bally, A.W. and Snelson, S., 1980. Realms of subsidence. In: A.D. Miall (Editor), Facts and Principles of World Petroleum Occurrence. Can. Soc. Petr. Geol., Calgary, Alberta, Canada, pp. 9-94.

Berlyand, N.G., 1983. Classification of the Urals by type of crustal structure. Internat. Geology Rev., 25: 1365-1374.

Bowin, C., Warsi, W. and Milligan, J., 1981. Free-air gravity anomaly map of the world. Geol. Soc. Am. Map and Chart Series, MC-46.

Druzhinin, V.S. et al., 1983. Probable section of the Earth's crust in the region of the projected Uralian ultra-deep drill hole. Internat. Geology Rev., 25: 463-469.

Dymkin, A.M., Ivanov, S.N., Kamaletdinov, M.A., Popov, B.A., Puchkov, V.N., Zoloev, K.K. and Fishman, M.V., 1984. Geology of the Urals. In: Geology of the USSR. 27th Int. Geol. Congress, Colloquium 1, Vol. 1, Nauka, Moscow, pp. 61-71.

Dymkin, A.M. and Puchkov, V.N., 1984. Ancient Urals - new problems. Episodes, 7: 33-37.

Forsyth, D.W., 1985. Subsurface loading and estimates of the flexural rigidity of continental lithosphere. J. Geophys. Res., 90: 12,623-12,632.

Geopotential Research Mission Science Steering Group, 1985. Geopotential Research Mission-Scientific Rationale.

Gordon, M.B. and Hempton, M.R., 1986. Collision-induced rifting: The Grenville Orogeny and the Keweenawan Rift of North America. Tectonophysics, 127: 1-25.

Hamilton, W., 1970. The Uralides and the motion of the Russian and Siberian Platforms. Geol. Soc. Am. Bull., 81: 2553-2576.

Hanks, T.C., 1971. The Kuril Trench - Hokkaido Rise system: Large shallow earthquakes and simple models of deformation. Geophys. J. R. Astron. Soc., 23: 173-189.

Ivanov, S.N. and Rusin, A.I., 1986. Model for the evolution of the linear fold belt in the continents: Example of the Urals. Tectonophysics, 127: 383-397.

Karner, G.D., and Watts, A.B., 1983. Gravity anomalies and flexure of the lithosphere at mountain ranges. J. Geophys. Res., 88: 10,449-10,477.

Kazantseva, T.T. and Kamaletdinov, M.A., 1986. The geosynclinal development of the Urals. Tectonophysics, 127: 371-181.

Khramov, A.N. and Rodinov, V.P., 1981. Paleomagnetism and reconstruction of paleogeographic positions of the Siberian and Russian Plates during the Late Proterozoic and Palaeozoic. In: M.W. McElhinny, A.N. Khramov, M. Ozima and D.A. Valencia (Editors), Global Reconstruction and the Geomagnetic Field During the Palaeozoic. Adv. Earth Plan. Sci. 10, Proc. IUGG Symp. Dec., 1979, 23-37.

Kulikov, P.K., Belousov, A.P. and Latypov, A.A., 1972. West Siberian Triassic Rift System. Geotectonics, 7: 367-371.

Lyon-Caen, H. and Molnar, P., 1983. Constraints on the structure of the Himalaya from an analysis of gravity anomalies and a flexural model of the lithosphere. J. Geophys. Res., 88: 8171-8191.

Lyon-Caen, H. and Molnar, P., 1985. Gravity anomalies, flexure of the Indian Plate, and the structure, support and evolution of the Himalaya and Ganga Basin. Tectonics, 4: 513-538.

Lyon-Caen, H., Molnar, P. and Suarez, G., 1985. Gravity anomalies and flexure of the Brazilian Shield beneath the Bolivian Andes. Earth Planet. Sci. Lett., 75: 81-92.

McNutt, M.K. and Menard, H.W., 1982. Constraints on yield strength in the oceanic lithosphere derived from observations of flexure. Geophys. J. R. Astr. Soc., 71: 363-394.

McNutt, M.K. and Kogan, M.G., 1987. Isostasy in the USSR, II, Interpretation of admittance data. In: K. Fuchs and C. Froidevaux (Editors), The Composition, Structure, and Dynamics of Lithosphere-Asthenosphere System. Geodyn. Ser. Vol. 16, AGU, Washington, D.C.

McNutt, M.K., Diament, M. and Kogan, M.G., 1988. Variations of elastic plate thickness at continental thrust belts, J. Geophys. Res., accepted.

Mercier, J.-L., Armijo, R., Tapponnier, P., Carey-Gailhardis, E.and Lin, H.T., 1987. Change from Late Tertiary compression to Quaternary extension in southern Tibet during the India-Asia collision. Tectonics, 6: 275-304.

Murray, C.G., 1972. Zoned ultramafic complexes of the Alaskan type: Feeder pipes of andesitic volcanoes. In: R. Shagam, R.B. Hargraves, W.J. Morgan, F.B. Von Houten, C.A. Burk and H.D. Holland and L.C. Hollister (Editors), Studies in Earth and Space Sciences. GSA Memoir 132, Boulder, CO, pp. 313-335.

Nalivkin, V.D., 1976. Dynamics of the development of the Russian Platform structures. Tectonophysics, 36: 247-262.

Nesterov, I.I., Rudkevich, M.Ya. and Trofimuk, A.A., 1984. Geology of West Siberian Platform. In: Geology of the USSR. 27th Int. Geol. Congress, Colloquium 1, Vol. 1, Nauka, Moscow, pp. 52-66.

Royden, L. and Karner, G.D., 1984. Flexure of lithosphere beneath Apennine and Carpathian foredeep basins: Evidence of an insufficient topographic load. Am. Assoc. Petr. Geol. Bull., 68: 704-712.

Royden, L., Patacca, E. and Scandone, P., 1987. Segmentation and configuration of subducted lithosphere in Italy: An important control on thrust-belt and foredeep-basin evolution. Geology, 15: 714-717.

Rudkevich, M.Ya., 1976. The history and the dynamics of the development of the West Siberian Platform. Tectonophysics, 36: 275-287.

Savalyev, A.A. and Savelyeva, G.N., 1977. Ophiolites of the Voykar-Syninsk Massif (Polar Urals). Geotectonics, 11: 427-437.

Sheffels, B. and McNutt, M., 1986. Role of subsurface loads and regional compensation in the isostatic balance of the Transverse Ranges, California: Evidence for intracontinental subduction. J. Geophys. Res., 91: 6419-6431.

Smyslov, A.A., Yanshin, A.L., Zaichenko, V.Yu., Karus, E.V., Surkov, V.S., Puzyrev, N.N., Erkhov, V.A. and Shchukin, Yu.K., 1984. Deep crustal structure and geodynamics of the lithosphere of the USSR territory. In: Geology of the USSR. 27th Int. Geol. Congress, Colloquium 1, Vol. 1, Nauka, Moscow, pp. 18-31.

Sokolov, V.B., Kozyrev, Ye.I., Rybalka, V.M. and Chudakova, L.N., 1974. Crustal structure in the central Urals (from seismic data). Doklady Akad. Nauk SSSR, 215: 84-86.

Snyder, D.B. and Barazangi, M., 1986. Deep crustal structure and flexure of the Arabian plate beneath the Zagros collisional mountain belt as inferred from gravity observations. Tectonics, 5: 361-373.

Stockmal, G.S. and C. Beaumont, 1987. Geodynamic models of convergent margin tectonics: the sourthern Canadian Cordillera and the Swiss Alps. Manuscript prepared for the symposium "Basins of Eastern Canada and Worldwide Analogues", August 13-15, 1986, Halifax, Nova Scotia.

Tamrazyan, G.P., 1971. Siberian continental drift. Tectonophysics, 11: 433-460.

Walcott, R.I., 1970. Flexural rigidity, thickness, and viscosity of the lithosphere. J. Geophys. Res., 75: 3941-3954.

Watts, A.B., Bodine. J.H. and Ribe, N.R., 1980. Observations of flexure and the geological evolution of the Pacific ocean basin. Nature, 238: 532-537.

Volvovskii, I.S. and Volvovskii, B.S., 1975. Cross-section of the Earth's crust in the territory of the USSR, plotted from deep seismic soundings, Sovestkoe radio, Moscow.

Zakatov, P.S., 1953. A course in higher geodesy. Translated from Russian for NSF by Israel Program for Scientific Translations, Jerusalem, 1962.

Zonenshain, L.P., Korinevsky, V.G., Kazmin, V.G., Pechersky, D.M., Khain, V.V. and Matveenkov, V.V., 1984. Plate tectonic model of the South Urals development. Tectonophysics, 109: 95-135.

FIGURE CAPTIONS

Figure 1. The Urals and neighboring orogenic belts (stippled areas) and adjacent platforms plotted in a conic conformal projection. The box shows the location of the topography map in Fig. 3. The dashed line marks the approximate eastern boundary of the West Siberian Lowlands.

Figure 2. Schematic geologic map of the Urals after Dymkin and Puchkov (1984). The Russian Platform lies to the west; West Siberia lies to the east. Descriptions of the labeled geologic provinces are given in the text.

Figure 3. Topography map of the Urals and adjacent platforms in a conic conformal projection. Elevations given in meters. The location of this map is plotted on Fig. 1. The thick black line indicates the location of the deep seismic sounding profile shown in Fig. 5. The solid circle shows the approximate location of a depression in the Moho marked with an arrow on the seismic profile of Fig. 5 and marks the location of the city of Sverdlovsk. The open circle shows the location of the city of Perm.

Figure 4. Bouguer gravity anomalies and topography averaged along strike in the region of the box shown in Fig. 1. The asymmetry in the gravity about the topographic peak suggests the mountain load is not supported simply by local thickening of the crust.

Figure 5. Moho depths across the Urals from a deep seismic sounding profile (Volvovskii and Volvovskii, 1975) and schematic cross-section through the southern Urals (Zonenshain et al., 1984). The location of the Moho profile is indicated on Fig. 3. The arrow marks the location of a depression in the Moho centered beneath the eastern Urals.

Figure. 6. Schematic diagram of lithosphere treated as a thin elastic plate and deflected beneath a topographic load near the end of the elastic plate. T_e indicates elastic plate thickness, ρ_c and ρ_m the crust and mantle densities, respectively. The dotted region represents the foredeep basin. The deflection of the crust-mantle boundary and the gravity anomalies arising from the crust-mantle density contrast are calculated and compared with observations.

Figure 7. Topography and theoretical gravity and plate deflection profiles for a thin elastic plate compensating the Russian Platform and Ural topographic and crustal loads. The free end of the plate lies beneath the Urals' eastern flank. Solid circles represent observed Bouguer gravity data stacked along strike. (a) and (b) show profiles with no postulated subsurface loads. In (c) and (d) boxes beneath the topography profiles mark the horizontal location and width (but not the true depth or vertical extent) of assumed subsurface bands of high-density material. The loads of the excess subsurface mass acting on the plates is given in each figure. The load acting on the plates with zero thickness is one that yields a reasonable fit to the gravity data. The load acting on each plate with nonzero thickness is approximately the minimum load required to depress the plate at least 2 km. The bending moment acting on the end of the plate is zero unless specified in the figure. Note the magnitudes of the moment and subsurface load vary with the elastic plate thickness.

Figure 8. Similar to Fig. 7, for a thin elastic plate model assuming a plate dipping west beneath the mountains with the plate end beneath the Urals' eastern flank. The solid circles mark Bouguer gravity data stacked along strike. The boxes beneath the mountain topography mark the location (but not the true depth or vertical thickness) of postulated subsurface high-density loads. The load acting on the plates with zero thickness is one that yields a reasonable fit to the gravity data. The load acting on each plate with nonzero thickness is approximately the minimum load required to depress the plate at least 2 km.

Figure 9. Similar to Fig. 8, assuming a continuous thin elastic plate extends from the Russian Platform beneath the Urals to the West Siberian Lowlands. No subsurface loads are applied. Zero elastic plate thickness corresponds to the traditional model for compensation of the mountain load by local crustal thickening.

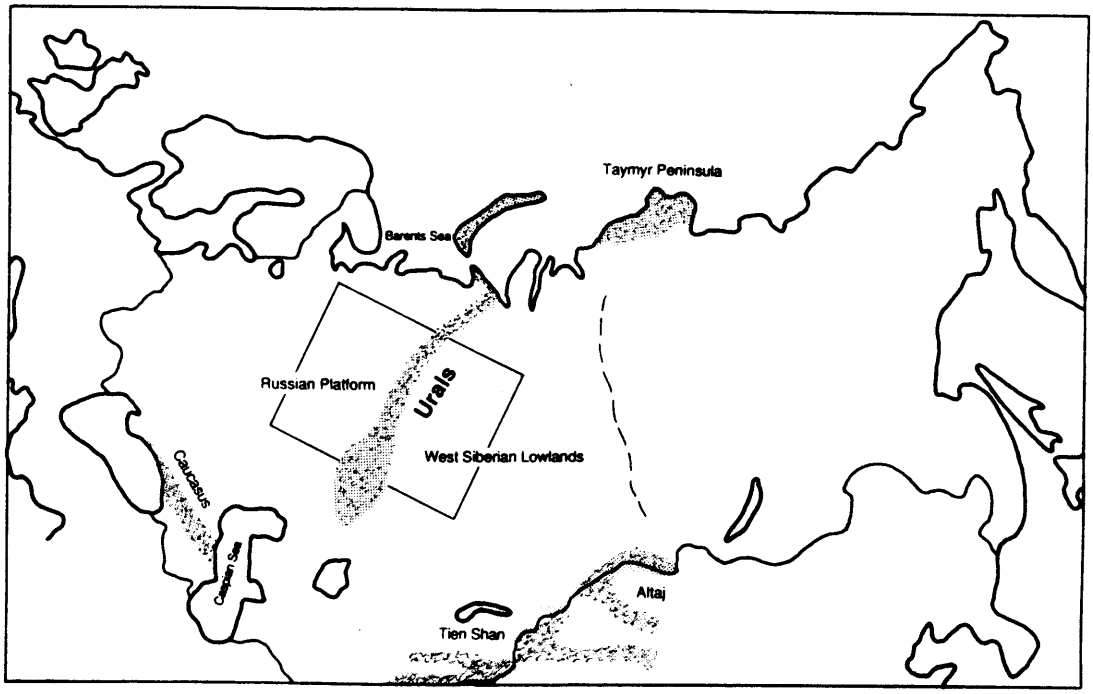
Taymyr Peninsula
Barents Sea
Russian Platform
Urals
West Siberian Lowlands
Caucasus
Caspian Sea
Altaj
Tien Shan

Figure 1

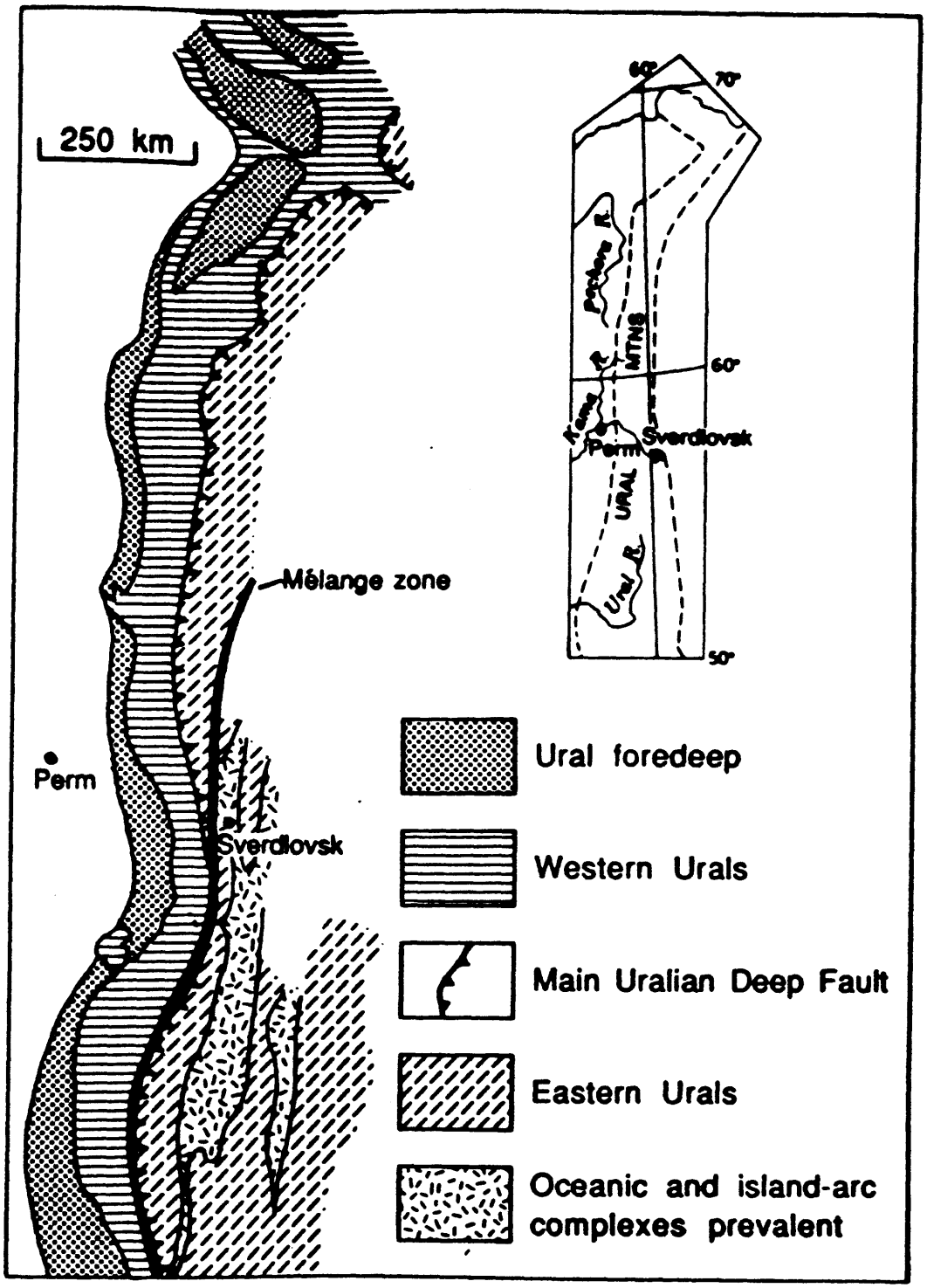
250 km
Mélange zone
Perm
Sverdlovsk
60°
70°
50°
MTNS
URAL
Perm
Sverdlovsk
Ural foredeep
Western Urals
Main Uralian Deep Fault
Eastern Urals
Oceanic and island-arc complexes prevalent

Figure 2

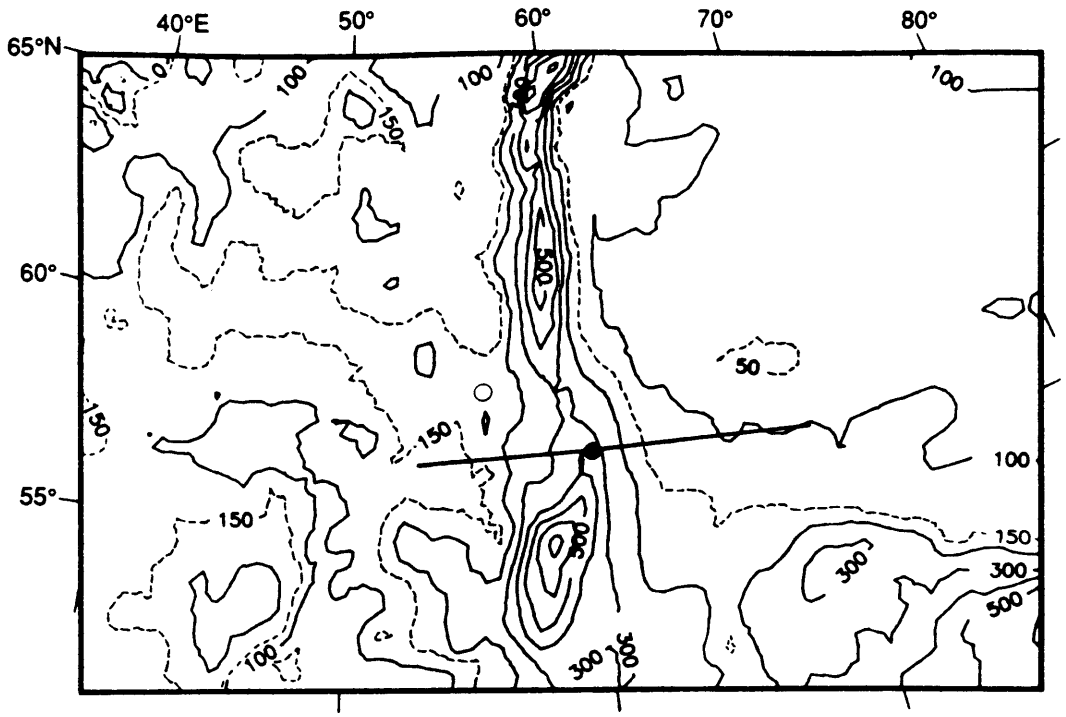

Figure 3

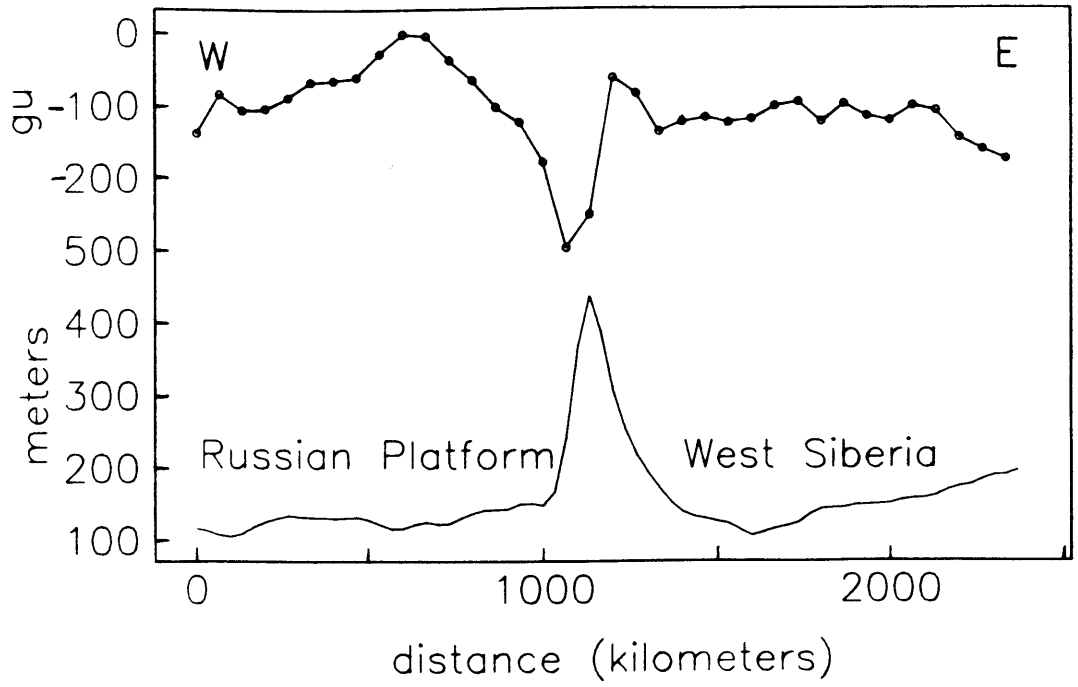
0
-100
-200
500
400
300
200
100
gu
meters
W
E
Russian Platform
West Siberia
0
1000
2000
distance (kilometers)

Figure 4

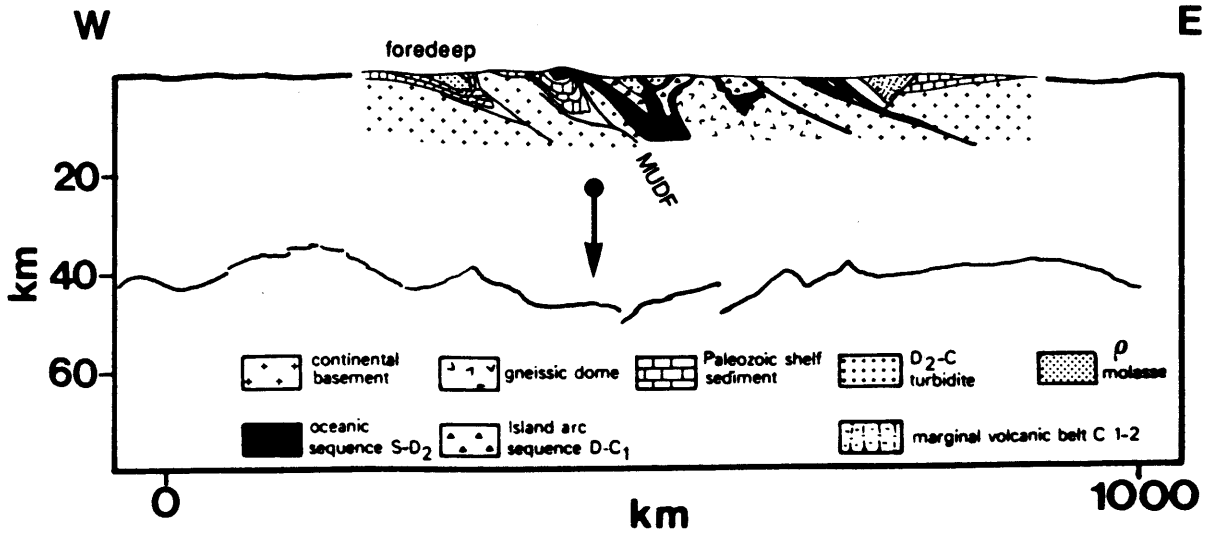
W
E
foredeep
MUDF
20
40
60
km
continental basement
gneissic dome
Paleozoic shelf sediment
D2-C turbidite
ρ molasse
oceanic sequence S-D2
Island arc sequence D-C1
marginal volcanic belt C 1-2
0
1000
km

Figure 5

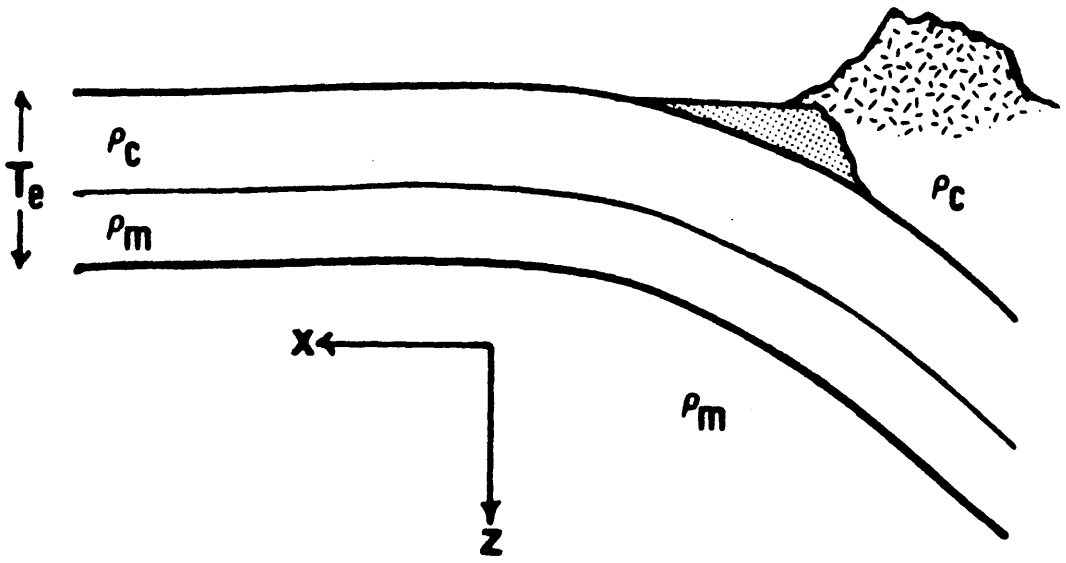

Figure 6

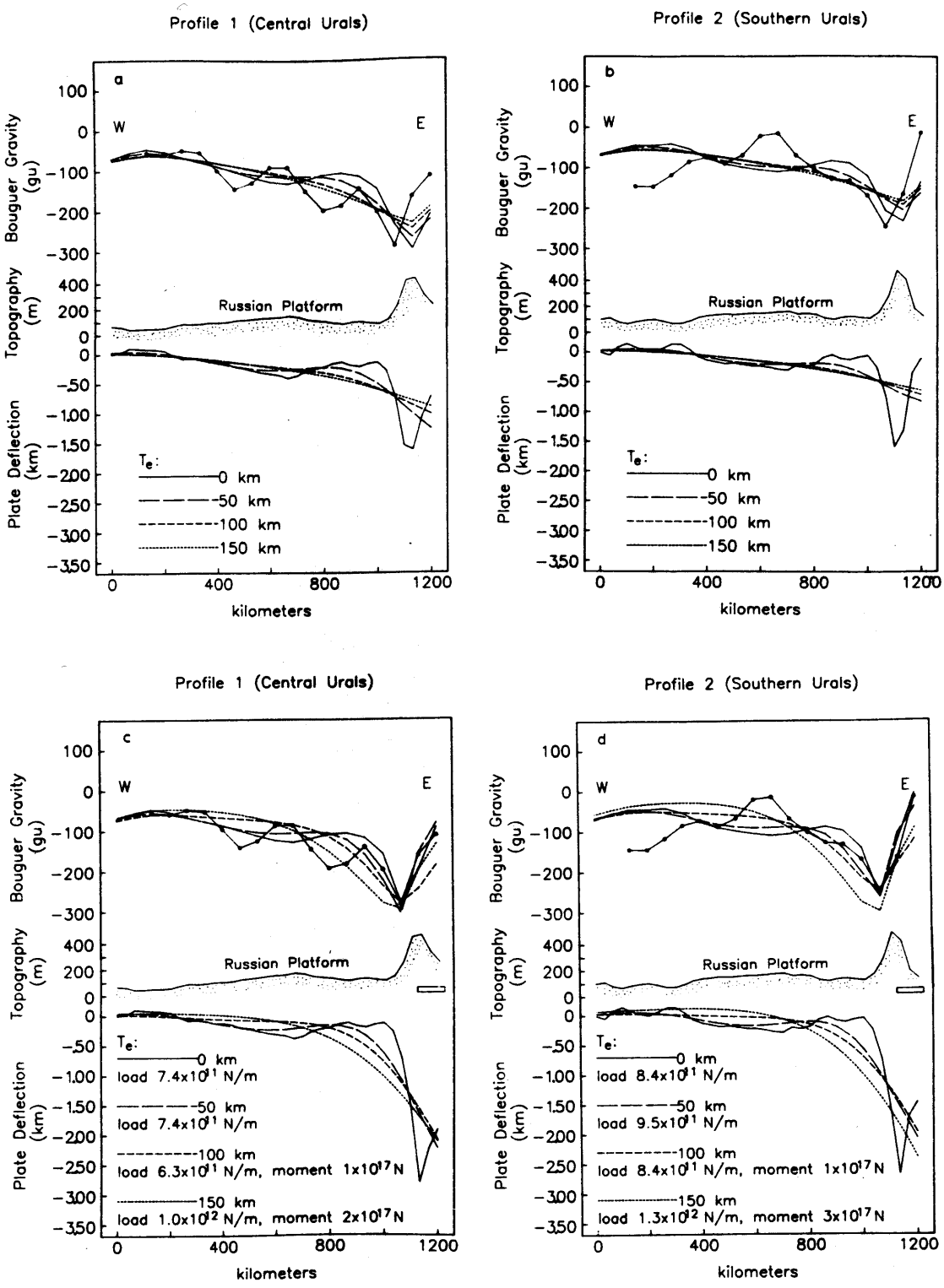
Profile 1 (Central Urals)
Profile 2 (Southern Urals)
Profile 1 (Central Urals)
Profile 2 (Southern Urals)
a
b
c
d
W
E
Bouguer Gravity (gu)
Topography (m)
Plate Deflection (km)
Russian Platform
Te:
0 km
-50 km
-100 km
-150 km
load 7.4x10^11 N/m
load 6.3x10^11 N/m, moment 1x10^17 N
load 1.0x10^12 N/m, moment 2x10^17 N
load 8.4x10^11 N/m
load 9.5x10^11 N/m
load 8.4x10^11 N/m, moment 1x10^17 N
load 1.3x10^12 N/m, moment 3x10^17 N
kilometers

Figure 7

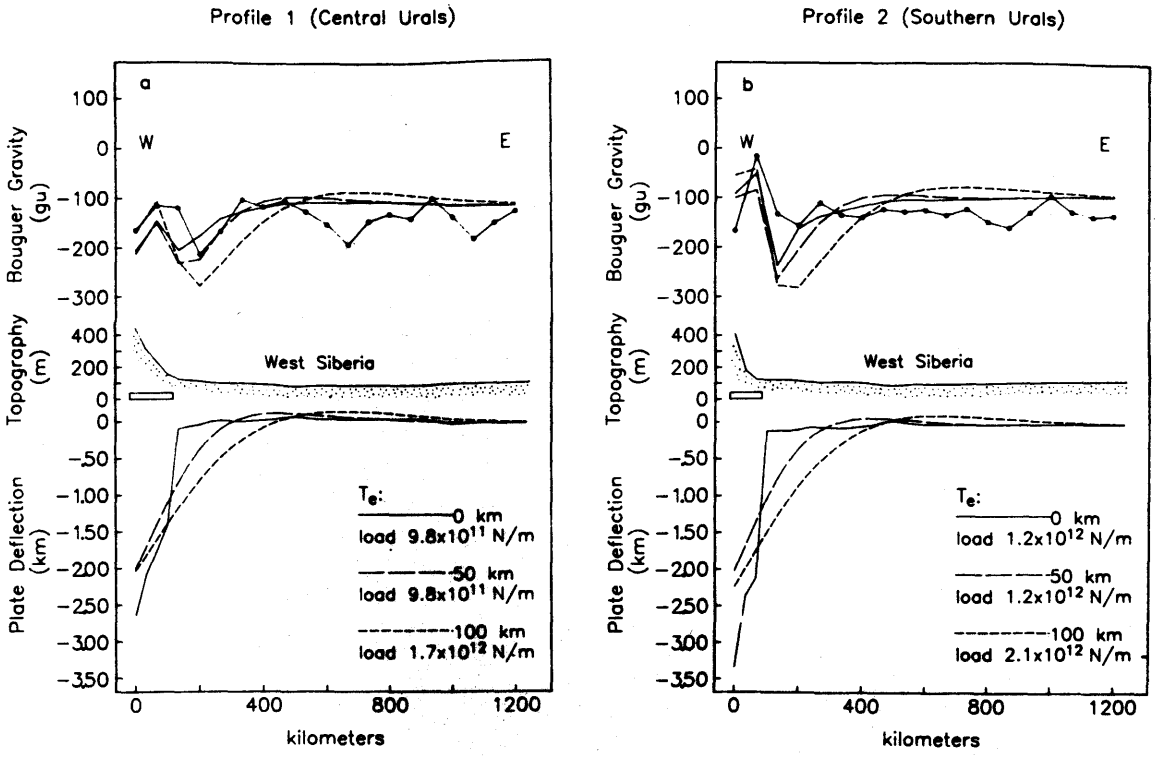
Profile 1 (Central Urals)
Profile 2 (Southern Urals)
a
b
W
E
Bouguer Gravity (gu)
Topography (m)
Plate Deflection (km)
West Siberia
T_e:
0 km
load 9.8x10^11 N/m
50 km
load 9.8x10^11 N/m
100 km
load 1.7x10^12 N/m
load 1.2x10^12 N/m
load 2.1x10^12 N/m
kilometers

Figure 8

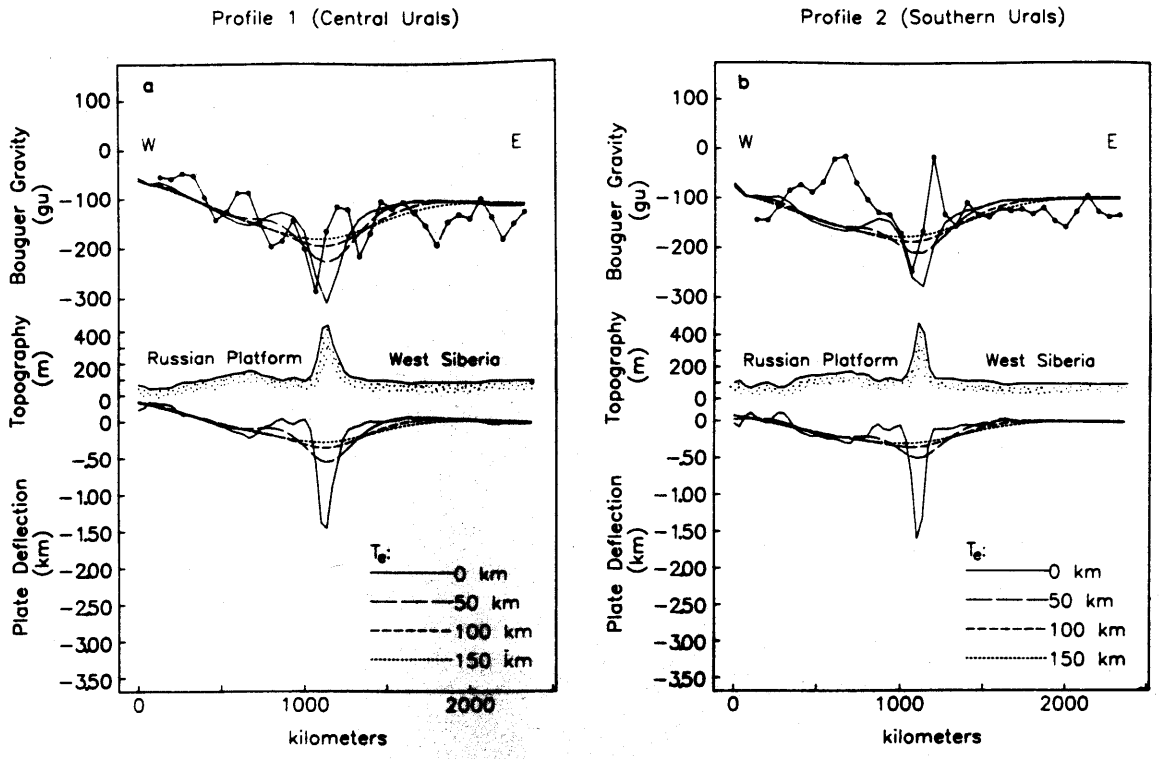
Profile 1 (Central Urals)
Profile 2 (Southern Urals)
a
b
W
E
Bouguer Gravity (gu)
Topography (m)
Plate Deflection (km)
Russian Platform
West Siberia
T_e:
0 km
50 km
100 km
150 km
kilometers

Figure 9

CHAPTER 2
FLEXURE OF THE ADRIATIC LITHOSPHERE (ITALY) THROUGH TIME

INTRODUCTION

The nature and evolution of forces acting at convergent plate boundaries and their relationship to lithospheric and upper crustal deformation are fundamental but poorly understood phenomena. One expression of these forces is the deflection of the subducting lithosphere, which can be observed directly in the bathymetry of oceanic trenches and in the geometry of foredeep basins similarly produced at continental convergent zones (e.g. Hanks, 1971; Parsons and Molnar, 1976; Beaumont, 1978; Beaumont, 1981]. Gravity anomalies over the convergence zone provide an additional indirect expression of the shape of the subducting lithosphere as the lower–density crust of the downgoing plate is deflected into higher–density mantle material. Combinations of gravity anomalies and direct observations of plate deflections have been used determine the downgoing plate shape in a variety of oceanic and continental convergent zones (for example Watts and Talwani, 1974; Lyon–Caen and Molnar, 1985; Nunn, 1987).

Insight into the convergent zone processes controlling the deflection of the downgoing plate and the mechanical response of the lithosphere can be obtained from the deflection of the lithosphere. The shape of the deflected lithosphere in convergent settings has been adequately described in terms of elastic [Hanks, 1971], viscoelastic [Beaumont, 1978], or elastic–plastic behavior [McAdoo, 1978], suggesting that although lithospheric deflections may be approximated by simple models, true lithospheric rheology is certainly more complex than any one model and may be quite variable. Nevertheless, these flexural models often demonstrate the necessity for significant subsurface forces acting on the downgoing plate in order to explain the observed deflection and associated gravity anomalies in both continental and oceanic settings [Karner and Watts, 1983; Lyon–Caen and Molnar, 1983; Royden and Karner, 1984]. However, many studies, particularly those in oceanic trenches where the trench bathymetry reflects only the present state of the convergence zone, have had limited success in elucidating the nature of these forces, which may represent the weight of the deeper parts of the downgoing plate, regional compressive stresses, or mantle drag on the downgoing plate.

In this study of the Cenozoic convergent zones on the margins of the northern Adriatic Sea and Po Basin of Italy (Figure 1), we seek to estimate the relative importance of the topographic load, subsurface forces, and compressive stresses acting on the downgoing plate and to evaluate their relation to surficial deformation. At the same time we examine

variations in the response of the plate to applied forces through time. The Adriatic setting is advantageous because foredeep basin geometries and Bouguer gravity data provide two direct constraints on the deflection of the downgoing plate. In addition, we can recover information on the evolution of convergent zone forces and plate response through reconstructions of past plate deflections using seismic stratigraphy and biostratigraphy of the foredeep basins. In particular, the timing of the convergent events in this region allows us to study the deflection of the continental lithosphere which floors the Adriatic Sea and the Po Plain of Italy during and following separate episodes of convergence in Eocene–Oligocene and Pliocene time. The reconstructed deflection subsequent to the cessation of the major thrusting events may reflect fundamental changes occurring as convergence ceases in the northern Adriatic.

TECTONIC SETTING

The Dinaride, Southern Alpine, and Apennine mountain belts formed in response to north–south convergence and shortening between the Eurasian and African plates during Cenozoic time. During the growth of the thrust belts, the continental lithosphere in the region bounded by these mountain belts was deflected downward beneath the thrust belts, resulting in the development of a series of asymmetric foredeep basins. This segment of continental lithosphere underlies the northern Adriatic Sea and the Po Plain of Italy and is referred to here as the Adriatic lithosphere or Adriatic fragment. It is often referred to as the Apulian fragment, particularly in discussion of southern Alpine tectonics. The Moho lies at 25–35 km depth in the northern Adriatic Sea and deepens to the west [Finetti et al., 1966; Geise and Morelli, 1975; Cermak, 1978]. There are no geophysical indications of discontinuities in the lithosphere between the northern Adriatic Sea and Po Plain [Stock, unpublished manuscript], so that it appears reasonable to assume the lithosphere was relatively homogeneous across this region prior to deflections along its boundaries. Cenozoic sedimentary rocks overlying the Adriatic basement form a pair of northwest trending basin systems on the margins of the Adriatic fragment, while the basement forms a central high and deepens in opposing directions toward the thrust belts.

Dinaride–Adriatic System

The foredeep basin along the northeastern side of the Adriatic sea developed contemporaneously with the Dinaride thrust belt of Yugoslavia in Eocene–Oligocene time. Southwest–vergent thrusting in the Dinaride mountains involved Mesozoic and Paleozoic

sedimentary rocks and the Cenozoic sedimentary rocks in the internal (northeastern) parts of the foredeep basin. The amount of shortening recorded in the Dinaride thrust belt increases southward and palinspastic restorations require hundreds of kilometers of convergence involving continental crust in the southern Dinarides [Burchfiel, 1980].

Thick upper Cretaceous deposits and late Cretaceous and perhaps early Eocene reefs grew in a very shallow water environment external to the Dinaride thrust belt. These carbonate rocks are overlain by Eocene to Miocene clastic foredeep deposits that thicken northeast to a maximum of 5 to 6 kilometers. The coeval growth of the foredeep basin and the Dinaride orogenic belt suggests a genetic link as Adriatic lithosphere was subducted to the northeast in Eocene time. Basin growth and thrusting ceased probably by Oligocene time. Eocene to Miocene sedimentary rocks in the foredeep are overlain by Pliocene sedimentary rocks associated with the development of the Apennine foredeep basin and are discussed below.

Southern Alpine–Northern Po Basin System

The Southern Alps evolved through compressive deformation of Mediterranean continental and oceanic fragments during the north-south convergence of the Eurasian and African plates. The collision of the Eurasian plate with the continental Adriatic fragment in Eocene time is recorded both in north and northwest-vergent compressional structures within the northern and central Alps and in a region of south-vergent thrusts in the Southern Alps (Figure 1). The direction of subduction is inferred to have been mainly to the south through Eocene time but is less clear in Miocene time. The south-vergent thrusts within the Southern margin of the Alps are probably antithetic to the Eurasian plate subduction [Laubscher, 1985].

Sediments within the Po basin, which is underlain by the Adriatic lithosphere, reflect two episodes of asymmetric foredeep basin development. The first episode was characterized by the growth of a north–thickening Miocene sedimentary trough up to 4 km deep. These Miocene sedimentary strata are partly deformed by a series of south–vergent thrust faults which form the southernmost expression of thrusting in the Southern Alps. This Miocene trough records a downwarping of Po Plain lithosphere towards the north. Palinspastic reconstructions showing northward–increasing deflection of basement beneath the Southern Alps [Laubscher, 1985] and data suggesting a north–dipping Moho [Giese and Morelli, 1975] support this interpretation. The second episode of basin development in Miocene and Pliocene time involved deposition of a south–thickening sedimentary wedge reaching a maximum thickness of more than 5 kilometers. The thinner northern margin of

this Pliocene sediment package unconformably overlies the older north–thickening sedimentary rocks [Pieri and Groppi, 1981]. This younger package of rocks is part of the Apennine–Adriatic system described below. Structures within the Po Plain are predominantly compressional, indicating that subsidence of the plate beneath these basins has occurred in response to convergence and, presumably, to loading during emplacement of advancing thrusts sheets.

Apennine–Adriatic System

Pliocene development of the Apennine thrust belt and western Adriatic foredeep basin postdates tectonic activity in the Dinarides and Southern Alps. Northeast–directed thrusting in the Apennine thrust belt occurred throughout Miocene and Pliocene time in response to southwestward subduction of the Adriatic lithosphere beneath the mountain belt [Civetta et al., 1978]. The thrust belt migrated to the east throughout middle and late Miocene time, transporting sedimentary rocks originally deposited on the Adriatic plate and stripped from their basement during thrusting (for example, Ogniben et al., 1975; Bally et al., 1986). At least 60–170 km of shortening is estimated to have occurred across the central Apennines in Pliocene–Quaternary time [Bally et al., 1986]. An active Benioff zone in the Calabrian arc records more than 500 km of subduction that may be associated with Miocene to Recent shortening in the southern Apennines [Gasparini et al., 1985]. West of the Apennine mountains, late Miocene–Pliocene back–arc–type extension generated oceanic crust in the Tyrrhenian Sea [Malinverno and Ryan, 1986; Kastens et al., 1988] while Pliocene–Quaternary extension affected onshore areas in western Italy. The separation of extensional and compressional regions is quite narrow: the eastern limit of Pliocene Quaternary grabens is less than 100 km from the Pliocene thrust front, and young normal faults are found within the Apennine mountains [Bally et al., 1986; Malinverno and Ryan, 1986]. Seismicity along the Italian peninsula occurs at shallow depths with focal mechanisms that suggest east–west extension [Gasparini et al., 1985].

The present Apennine–Po foredeep basin was formed in Pliocene–Quaternary time, but remnants of older foredeep basins can be found within the thrust belt itself [Scandone and Patacca, unpublished manuscript, 1987]. The present basin thickens uniformly to the southwest, containing up to 8 km of Pliocene–Quaternary sediments [Pieri and Groppi, 1981; Ogniben et al., 1975]. The arcuate shape of the basin in map view as it wraps westward onshore to the north under the Po Plain and to the south under southern Italy is apparently the result of division into sub–parallel offset segments. Royden et al. [1987] have identified four distinct segments, each exhibiting a 'typical' foredeep basin shape

which deepens to the southwest beneath the Apennine thrust sheets and shallows in a flexural high in the central Adriatic.

The late Miocene salt deposits that covered much of the Mediterranean area effectively mark the base of the Apennine foredeep basin. The excellent reflective properties of this layer make the contact easy to identify on reflection seismic lines. The overlying Pliocene sediments contain marly shales and pelites intercalated with turbiditic sandstones characteristic of a low–energy offshore depositional environment [open file well logs; Ori et al., 1986]. Quaternary deposits are primarily sands and clays. Bio– and lithostratigraphic analyses suggest the depositional environment shallowed from outer neritic to littoral between lower and upper Pleistocene sequences [Dondi et al., 1985]. Younger Quaternary deposits show foreset structures characteristic of a deltaic system, perhaps modified by eustatic oscillations [Ori et al., 1986; Dondi et al., 1985].

A series of thrust faults associated with northeast–vergent Apennine thrusting have disturbed Pliocene, and to a lesser extent Quaternary, strata in the internal part of the basin. Where undisturbed, the angle of the southwestward dip of upper Pliocene and Quaternary horizons decreases up section. Lowermost Quaternary horizons in the central Adriatic basin segments shallow over the internal parts of the foredeep forming a broad synclinal axis in the western part of the Adriatic Sea. Marine Quaternary horizons are uplifted along the northeastern coast of central of Italy [Crescenti et al., 1980].

TOPOGRAPHY AND BOUGUER GRAVITY DATA

Topography data used in this study (Figure 2a) were compiled from the dbdb5 data set [Defense Mapping Agency] and from regional topographic maps.

Bouguer gravity anomalies over the study area compiled from Morelli [1969], Giese and Morelli [1975] and [Klingele, 1976] are shown in Figure 2b. In general, Bouguer gravity anomalies are positive over the shallow external parts of the foredeep basins and more negative over the deeper internal sections and over the mountains. The trends of Bouguer anomalies in the northern Adriatic and central Italy also follow the segmentation characteristic of the Apennine foredeep basin system. West of the Italian peninsula, Bouguer gravity anomalies become increasingly positive over the Tyrrhenian Sea that implies the existence of a substantial volume of locally uncompensated high–density material [Royden, 1988]. Unfortunately, no gravity anomalies were available to the east of the northern and central portions of the Adriatic Sea. Thus, information on the depression of a downgoing plate beneath the Dinarides is restricted to depth–to–basement data.

The northern portion of Profile E–E' modeled in this paper (see Figure 2) crosses the edge of the Ivrea Zone, a region of a large positive gravity anomaly inferred to reflect local crustal doubling [Lyon–Caen and Molnar, 1989]. To avoid the effects of this feature in our gravity modeling we compiled gravity data along Profile E–E' by extrapolating gravity anomalies from 50 km to the east of the profile for profile locations more than 175 kilometers north of the Italian coastline . The extrapolated gravity data are part of the broad region of smoothly varying east–west trending Bouguer gravity contours (Figure 2b). Topography data were compiled along the profile itself.

RECONSTRUCTIONS OF FOREDEEP BASIN GEOMETRY

Method

The geometry of the Adriatic foredeep basins can be reconstructed from the seismic stratigraphic record at a given time t by restoring the sediment fill deposited prior to t to its position at time t (Figure 3). This is done by subtracting the thickness of sediments deposited since t from the total basin thickness. The depth to the basement at t is then simply the sum of the thickness of the remaining sediment package (sediments older than t) plus the water depth in which the sedimentary horizon was deposited at time t. In addition, we correct for the compaction of sediments deposited before time t. This reconstruction technique requires horizons in the seismic record for which (a) the present depth, (b) the age of deposition, and (c) the depositional water depth (referred to hereafter as water depth) are known.

In this study, we applied the backstripping technique to reconstructions of the Adriatic foredeep basins along profiles striking perpendicular to the trend of the basins and the associated thrust belts. Present depth, age, and water depth of deposition for a number of strata were compiled from reflection seismic profiles [Marine Seismic Survey, Adriatic Sea, Geophysical Service International Limited, London, 1967], the paleontological record of open–file well logs in the Adriatic Sea, existing interpretations of seismic stratigraphic data in the Po Plain [Pieri and Groppi, 1981] and in the Adriatic Sea [Scandone and Patacca, unpublished map, 1987; Dondi et al., 1985, Ori et al., 1986, Bally et al., 1986], and some confidential industry data (seismic and drilling).

The largest uncertainties in the reconstructions are associated with the estimates of the water depth in which the sediments were deposited. For most of the horizons used in this study there were few or no biostratigraphic or sedimentological constraints on the water depths except that these horizons were deposited in more than about 200 meters of water. These reconstructions were completed under the assumption that the depositional water

depth was uniform, but unknown, across the foredeep basin. The ramifications of this assumption are addressed by Royden [1988] and below. Uncertainties in the present depths of identified horizons arise primarily from velocity–to–depth conversions and these uncertainties increase with depth. Verification of velocity-to-depth conversion factors through well control suggests depth data are accurate to 500 meters at 5 kilometers depth, and are more accurate at shallower depths.

To minimize uncertainties in the age of seismically reflective layers and lateral variations in the ages of the layers across of the foredeep basins, we used seismically reflective horizons that coincided closely with paleontological markers. As a result we estimate that absolute ages of post–Miocene rocks should be accurate to several hundred thousand years or less (Iaccarino, 1985). This age uncertainty is less than 20% of the absolute age of the youngest horizon studied (1.8 m.y.) and is therefore judged sufficiently small for the purposes of this study. Lateral variations in age should be less than or on the order of uncertainties in absolute age.

Limited knowledge of the porosity and compaction characteristics of the foredeep sediments introduces additional uncertainties into reconstructions of past basin geometries. To estimate the possible importance of sediment compaction as these basins formed, we reconstructed the foredeep basin geometries assuming first that sediments did not compact at all during basin growth, and secondly that sediments compacted according to compaction parameters for shale, which is the most highly compacting material in these foredeep basins. Differences between reconstructions based on the first and second assumptions may be interpreted as a conservative estimate of the uncertainties associated with sediment compaction properties. We used the method of Sclater and Christie [1980] to decompact older sediments under the second assumption, with an exponential decrease in sediment porosity ϕ with depth, $\phi = \phi_0 e^{-az}$, where z is depth, positive downward, $\phi_0 = 80\%$, and a $= 0.4\ km^{-1}$. Sediment properties were assumed to be uniform throughout the basin.

We tried to recover flexurally induced changes in the depth of the foredeep horizons by avoiding locations where thrusting or salt–related doming had obviously disturbed otherwise smoothly dipping reflecting horizons. Where thrusting has pervasively distorted the sedimentary fill, as in portions of the northern Po basin, we based our reconstructions of basement motions on palinspastic restorations.

Results

Figures 4 through 7 and Tables 1 through 4 show the present and reconstructed depths to reflecting layers compiled along four profiles across the Adriatic lithosphere. Profiles B-B', C-C' and D-D' are centered on the northernmost three segments of the

Apennine foredeep basin system (Figure 2). (Profiles are labeled in accordance with the study of Royden [1988].) Profile B-B' extends into the Dinaride foredeep basin as well. Profile E-E' crosses the northwesternmost portion of the Apennine foredeep and the basin associated with deformation in the Southern Alps. The profiles strike approximately perpendicular to the trend of the thrust belts and to contours of Bouguer gravity anomalies and foredeep basin isopachs. Depths to the base Pliocene reflecting horizon along profiles B-B', C-C' and D-D' are those compiled by Royden [1988].

Profile B–B' (Dinaride and Apennine foredeeps). Figure 4a shows the present depth to the lowermost Tertiary, lowermost Pliocene, middle Pliocene, and lowermost Quaternary horizons along a profile perpendicular to the strike of the Apennine and Dinaride foredeep basins through the central Adriatic Sea (Figure 4a). The base of the Dinaride and Apennine foredeep basins coincides with the contact between a Mesozoic carbonate sequence and the base of Tertiary strata. This basal Tertiary layer thus reflects the composite shape of these two overlapping foredeep basins. The structure and faunal associations of the Mesozoic carbonate sequence suggest that it was deposited at depths less than 100 meters in the eastern Adriatic. A shelf break located at $x \approx 290$ km along B–B' (see Figure 4a) separates these shallow water deposits from carbonate rocks of the same age deposited in the western Adriatic in water depths greater than 1 kilometer.

The Pliocene sequence is marked by a highly reflective Messinian salt layer. In the western half of the Adriatic Sea, pre–Pliocene Tertiary rocks are only a few hundred meters thick. The thickness of pre–Pliocene Tertiary rocks increases as the base Pliocene layer shallows northeastward to a depth of less than one kilometer. An 800 meter change in base Pliocene depth between $x = 250$ km and $x = 300$ km on profile B–B' may reflect lateral variation in depositional water depth at beginning Pliocene time between the Dinaride foredeep and the central Adriatic and Apennine foredeep to the southwest. This variation may be real, or may be due to identification of different lower Pliocene horizons within the Apennine and Dinaride foredeeps, as the data in each basin were compiled from separate sources.

Depths to a middle Pliocene reflecting layer were recovered only in the western half of the Adriatic Sea (Figure 4a). The depth of this horizon increases to almost 4 kilometers in the internal part of the foredeep basin. Its age is inferred from its association with the first appearance of *Globorotalia crassaformis* in Piacenzian time (approximately 3 m.y. ago) [Iaccarino, 1985]. Faunal associations suggest depositional water depths were greater than 100 meters [open file well logs].

The youngest horizon studied here is a base Quaternary horizon dated on the basis of the first appearance of *Hyalina balthica* approximately 1.5 m.y. ago [Ruggieri et al.,

1984]. This layer shallows from a maximum depth of about 1 km in the central Adriatic toward the internal parts of both the Apennine and the Dinaride foredeep basins. Lower Quaternary marine sedimentary strata appear onshore near the Italian coastline and dip gently to the northeast. Lithologic and biostratigraphic data suggest the synclinal form of this horizon reflects in part its depositional geometry as older Quaternary sediments were deposited at greater depth in the central Adriatic sea than near the Italian coastline [Dondi et al., 1985].

Figures 4b–d and Table 1 show reconstructions of past geometries of the overlapping Apennine and Dinaride foredeep basins along profile B-B'. The base of the basin is represented by the base Tertiary horizon. Where we lack depositional water depth data, we have assumed that horizons were deposited at sea level, unless otherwise noted. For example, the depth to the base of the basins at the beginning of Quaternary time is computed simply by taking the difference in thickness between the Quaternary sediment fill and the total foredeep sediment thickness and then decompacting the pre–Pliocene sediments.

Figure 4b shows two interesting features. First, the shape of the Dinaride foredeep basin was similar to the present geometry by the beginning of Pliocene time, coincident with the end of the primary Dinaride convergent event. At this time only a uniform, thin layer of pre–Pliocene sediments had accumulated in the site of the present Apennine foredeep. Secondly, the angle of the basement dip of the internal part of the reconstructed foredeep basin at the beginning of Pliocene time is greater than that of the present basin.

Figure 4c illustrates that the downward deflection of the present Apennine foredeep basement commenced during early Pliocene time. The reconstruction at the beginning of Quaternary time (Figure 4d) shows that basement deflection increased through Pliocene time until the foredeep shape was similar to that at present. The shallowing of the present base Quaternary strata over the internal parts of the Apennine foredeep suggests, however, that uplift replaced subsidence of the basement over the internal parts of the foredeep during Quaternary time. The reconstruction shown in Figure 4d is based on the assumption of a uniform depositional water depth of lowermost Quaternary sediments and indicates that the basement and the internal part of the basin dipped more steeply at the time of cessation of Apennine thrusting in beginning Quaternary time than it does at present.

Profile C–C' (Apennine foredeep). Figure 5a shows depth data compiled for lowermost Pliocene and lowermost Quaternary horizons on Profile C-C' through the northern Adriatic Sea (see also Table 2). The age of these horizons and all horizons discussed below were determined by criteria identical to those described for data along profile B-B'. The faunal associations and sedimentary structures associated with these

horizons suggest only that they were deposited at water depths greater than 100 meters [open file well logs].

The base Pliocene horizon on Profiles C-C' and D-D' provides an effective marker of the base of the basin since pre-Pliocene sediments are very thin in this region. Assuming that both base Pliocene and base Quaternary depositional water depths were uniform but unknown, removal of the Quaternary sediments by backstripping (Figure 5b) shows that the southwestward dip of the foredeep may have been slightly steeper at beginning Quaternary time than at present, as in Profile B-B'.

Profile D–D' (Apennine foredeep). Present base Pliocene, middle Pliocene and base Quaternary depth data over the northern segment of the Adriatic foredeep exhibit features similar to those of the more southern Apennine foredeep segments (Figure 6a, Table 3). Lacking direct data on depositional water depths, we again assume that depositional water depths were uniform, but unknown, across the foredeep basin. Reconstructions based on these assumptions show that the deflection of the basement was less pronounced at middle Pliocene time than at present (Figure 6b) and that the overall slope of the base of the basin along D-D' is slightly steeper at present than it was at beginning Quaternary time (Figure 6c).

Profile E–E' (Apennine and southern Alp foredeeps). The present basement deflection beneath the north–thickening sediments adjacent to the Southern Alps is not preserved as in the Apennine and Dinaride basins because the Alpine basin sediment fill has been significantly disrupted by thrusting. We compiled data on the northern segment of profile E–E' from palinspastic reconstructions of basement geometries in the Southern Alp basin based on reconstructions of deformation since the onset of convergence in this region [Laubscher, 1985; Roeder] (Figure 7, Table 4). The basement geometry along the southern segment is equated with the present base Tertiary depths in the Apennine foredeep [Pieri and Groppi, 1981]. Water depth of sediment deposition at the beginning of Tertiary time is estimated to be about 1 km. The present northern Po basin and reconstructed Southern Alp basin are as thick as the most internal parts of the central Apennine and Dinaride foredeep basins (Figure 7). This compilation shows the steep opposing basement deflections are separated by a central high only 50 km wide.

FLEXURAL MODELING

The reconstructed basin geometries in Figures 4-7 record changes in deflection of the underlying lithosphere through time. Flexural modeling of the reconstructed basin geometries can therefore be used to examine the mechanical behavior of the lithosphere and

the magnitude of forces required to produce the reconstructed deflection. We treat the lithosphere as a two–dimensional thin elastic plate overlying an inviscid asthenosphere (Figure 8) and model the present lithospheric flexure by fitting for the deflection of a thin elastic plate simultaneously to both Bouguer gravity data and present foredeep basin depth data. A simultaneous least–squares fit to both types of data has a significant advantage in speed over forward modeling methods that require trial–and–error modeling of the gravity data or of both data sets. The method described here is an expansion of the techniques developed by Royden [1988] and Moretti and Royden [1988] for fitting the deflection of a thin elastic plate to foredeep basin depth data alone.

Following Royden's [1988] notation, the equation for the deflection of a thin elastic plate overlying an inviscid fluid under topographic, sediment and water loads can be written:

$$D\frac{d^4}{dx^4}[w(x)-w_{in}(x)] + g(\rho_m-\rho_i)[w(x)-w_{in}(x)] = g(\rho_i-\rho_w)w_{in}(x) + T(x) + g(\rho_s-\rho_i)s(x) \quad (1)$$

The definitions and values assumed for the variables in equation (1) are given in Table 5. The terms on the right hand side of (1) represent the loads overlying the plate and can be specified when the topography, sediment thicknesses, and the water depth prior to deflection are known. The general solution for the net plate deflection $[w(x) - w_{in}(x)]$ can be written

$$w(x) - w_{in}(x) = w_t(x) + [A\cos(x/\alpha) + B\sin(x/\alpha)]e^{-x/\alpha} + [C\cos(x/\alpha) + D\sin(x/\alpha)]e^{x/\alpha}. \quad (2)$$

$w_t(x)$ is the deflection due to the topographic, water, and basin sediment loads as specified on the right hand side of (1) or any solution to (1), and is computed numerically.

We assume that deflections of the Moho $\Delta w_{Moho}(x)$ are equal to the net elastic plate deflections $(w(x) - win(x))$ over the region $x_1 < x < x_2$. x_1 and x_2 are referred to here as the effective ends of the elastic plate, as they represent the locations beneath the thrust belts where lithospheric and hence Moho deflections diverge from a form that can be approximated by the deflection of a thin elastic plate. These effective plate end locations are set to values which give a subjectively determined best fit to the gravity data. For $x < x_1$ and $x > x_2$, Moho deflections are assumed to reflect local (Airy) isostatic compensation of topography.

The density anomalies associated with the Moho deflections within the deflecting lithosphere between the effective ends x_1 and x_2 can be approximated by density anomalies with zero vertical thickness lying at the mean Moho depth. The predicted gravity anomalies $\Delta g_{pred}(x)$ resulting from the deflection of the plate between x_1 and x_2 can then be written

$$\Delta g_{pred}(x,x_1,x_2) \approx \Delta g_t\,(x,x_1,x_2) + \Delta g_{in}(x,x_1,x_2) + A\Delta g_1(x,x_1,x_2) + B\Delta g_2(x,x_1,x_2) + C\Delta g_3(x,x_1,x_2) + D\Delta g_4(x,x_1,x_2). \tag{3}$$

Δg_t are the gravity anomalies resulting from the two–dimensional approximation to deflections of the Moho equal to $w_t(x)$. Δg_{in} approximates the gravity anomalies resulting from local isostatic compensation of the initial water depth $w_{in}(x)$ and the infilling of sediments over $w_{in}(x)$. Δg_1, Δg_2, Δg_3, and Δg_4 approximate the gravity anomalies resulting from Moho deflections of the form $cos(x/\alpha)e^{-x/\alpha}$, $sin(x/\alpha)e^{-x/\alpha}$, $cos(x/\alpha)e^{x/\alpha}$, and $sin(x/\alpha)e^{x/\alpha}$, respectively. We evaluate Δg_t, Δg_{in}, and Δg_1 through Δg_4 by summing over the effect of the two–dimensional density anomalies at the mean Moho depth evaluated numerically at 5 kilometer intervals between x_1 and x_2.

When the starting water depth $w_{in}(x)$ is known, the best–fitting elastic plate profile can be computed for specified values of the effective plate end locations x_1 and x_2 and the effective elastic plate thickness T_e. We then fit for the unknown coefficients A, B, C, and D with a weighted least–squares fitting procedure that minimizes the misfit between the elastic plate profile and the observed deflection and between the predicted and observed Bouguer gravity anomalies:

$$Min\Big[\sum_{i=1}^{n_d} \{s(x_i) - w_t(x_i) - w_{in}(x_i) - [A\cos x_i/\alpha + B\sin x_i/\alpha\,]e^{-x_i/\alpha} - [C\cos x_i/\alpha + D\sin x_i/\alpha\,]e^{x_i/\alpha}\}^2/s_i^* + \sum_{i=1}^{n_g} \{\Delta g_{obs}(x_i) - \Delta g_t(x_i) - \Delta g_{in}(x_i) - A\Delta g_1(x_i) - B\Delta g_2(x_i) - C\Delta g_3(x_i) - D\Delta g_4(x_i)\}^2 \cdot R\Big] \tag{4}$$

Here α is the flexural wavelength corresponding to the specified elastic plate thickness (see Table 5). $\Delta g_{obs}(x_i)$ are Bouguer gravity observations at locations x_i from which (1) the gravity anomalies due to known sediment thicknesses across the profile and (2) the gravity

anomalies from local (Airy) compensation of topography at $x < x_1$ and $x > x_2$ have been subtracted. x_i are the locations of the n_d discrete observations of depth to the base of the foredeep $s(x_i)$ and the n_g corrected Bouguer gravity observations $\Delta g_{obs}(x_i)$. s_i^* is a weighting factor for depth data such that $s_i^* = s(x_i)$ when $s(x_i) > 500$ m and $s_i^* = 500$ m when $s(x_i) \leq 500$ m. The variable R controls the weight placed on gravity data relative to depth data and compensates for the different absolute magnitudes of Bouguer gravity and depth data. In general we set R so that Bouguer gravity data is weighted approximately as strongly as depth data.

This fitting procedure of equation (4) is repeated, varying values of T_e, x_1, and x_2, until the combination of parameters is found that yields the best overall fit to the data. In cases where we assume plate deflections are one–sided, rather than two–sided, deflections $w(x)$ and the first derivative $dw(x)/dx$ are constrained to go to zero either at positive infinity by setting $C = D = 0$, or to go to zero at negative infinity by setting $A = B = 0$. Equation (4) is then used to fit for the remaining two nonzero coefficients.

When the initial depth $w_{in}(x)$ could not be determined from biostratigraphic or sedimentological data, we use an iterative procedure and assume that the starting water depth was a uniform value w_o, across the region of observations. The iterative path entails [1] setting an initial guess w_{o1}; [2] computing $w_t(x_i)$ corresponding to w_{o1}; [3] fitting the data with equation (4), replacing $w_{in}(x_i)$ and $\Delta g_{in}(x_i)$ with unknowns, w_o and $\Delta g_0(x)w_o$, respectively; [4] substituting the value for w_o obtained by the fitting in the step [3] into step [2] and repeating the loop [2]–[4] until the the value computed for w_o changes insignificantly from one iteration to the next. $\Delta g_0(x)$ is the numerically computed gravity anomaly resulting from sediment infill of unit thickness between x_1 and x_2. Finally, the best–fitting thin elastic plate deflection is computed from equation (2) using the values of A, B, C, D, and $w_{in}(x) = w_o$ derived through steps [1] through [4]. Generally this iterative scheme for finding the best–fitting depositional depth converges on a stable value of w_o only when both gravity and deflection data are used in the fit.

This gravity–data fitting procedure may not yield a good fit to the Bouguer data in settings where the two–dimensional approximation to the deflected plate density anomalies is poor. This occurs in regions where plate deflections are comparable to the crustal thickness. As a final step the quality of the gravity fit is evaluated by computing the 'three–dimensional' gravity anomalies expected from the best–fitting Moho deflections using the method of Talwani [1959]. We found the quality of the gravity fit for the present plate deflection along Profile B–B' to be adequate for the purposes of this study.

Reconstructed basin geometries are modeled in the same way as the present basin geometries, except that (1) gravity data are irrelevant and are not used in the fitting

procedure, and (2) the water depth $w_{in}(x)$ represents the difference between depositional water depth of the horizon at the base of the foredeep and the depositional water depth at the time of the reconstruction. When $w_{in}(x)$ is unknown, we assume that the difference in the two depositional water depths is a uniform but unknown value w_o. In practice we used the method of Royden [1988] and Moretti and Royden [1988] for determining best–fitting past plate deflections. Their method is equivalent to the method described above in equation (4) when fitting for deflection data alone, but it avoids the convergence problems of (4) when $w_{in}(x)$ is unknown and only deflection data are used in the fit.

In practice, when $w_{in}(x)$ is unknown it is difficult to distinguish a best–fitting T_e value from the deflection data alone. For example, Royden [1988] has shown that in many instances a strong plate with one value of w_o may produce as good a fit to the deflection data as a weak plate with a very different value of w_o. This ambiguity may be resolved for present basin geometries using gravity data, which are sensitive to plate deflections outside the limited regions over which deflection data are available as well as to the net deflections over the foredeep basin. For reconstructed basin geometries we limit the range of acceptable models by establishing limits on acceptable values of T_e and w_o. We set bounds on T_e by rejecting (1) models that fail to produce subjectively defined 'good' fits to the data, and (2) models that predict that the downgoing plate did not extend into the interior parts of the foredeep basin when there is evidence that a well–developed foredeep basin existed at that time. We limit w_o for reconstructed basin geometries simply by requiring that these marine sedimentary horizons were deposited below sea level.

The vertical shear forces $F(x)$ and bending moments $M(x)$ transmitted through a thin elastic plate of uniform thickness are functions of the flexural rigidity of the plate D (see Table 5) and of the plate deflection $w(x)$, where $F(x) = Dd^3w/dx^3$ and $M(x) = Dd^2w/dx^2$ (see Figure 9c for sign conventions). These parameters, computed for the best–fitting plate deflections, represent the vertical shear force and bending moment that must be applied to the plate at a point x if the plate were arbitrarily broken at x. Thus the value of $F(x)$ and $M(x)$ in the internal parts of the foredeep basins are of interest as they serve as a gauge of the magnitude of forces and stresses transmitted through the plate at greater depths. In practice, changes through time of the effective magnitude of transmitted forces and moments can be estimated by comparing the value of $F(x)$ at the location where $M(x)$ is zero, or vice versa, for plate profiles reconstructed at successive time intervals.

Two simplifying assumptions are made in our modeling: First, our formulation of the thin elastic plate equation neglects horizontal compressional stresses across the elastic plate. We expect such stresses to be small in the north–central Adriatic region, where compressional seismic and tectonic activity are absent. Furthermore, seismic activity along

the Italian peninsula generally suggests an extensional stress regime within and west of the Apennine mountains. Secondly, we do not try to reconstruct changes in the topographic load on the plate through time. By leaving the topographic load fixed in our models, the effect of changes in the topographic load through time are incorporated in changes in $F(x)$ and $M(x)$.

RESULTS

Profile B–B'

Present time. Figure 9 shows that the present deflection of Adriatic lithosphere, as recorded by present depth to the base of Tertiary rocks, can be adequately fit by two–sided deflection of a single elastic plate with uniform flexural rigidity. Each profile in Figure 9a corresponds to the initial water depth w_o and the effective plate end locations x_1 and x_2 that best fit the observed gravity and deflection data for the assumed value of the effective elastic plate thickness T_e. In each case we assume that w_o must be between -250 meters and sea level for $x > 290$ (as constrained by the paleobathymetric data) and that w_o decreases by one kilometer or more across the observed shelf break at $x = 290$ km.

The 2.5-km thick elastic plate model predicts an upwarping of the plate over the internal parts of the foredeep basins that is incompatible both with the gravity data (Figure 9a) and with the observation that the Apennine and Dinaride thrust fronts have migrated 100 kilometers or more over the Adriatic foreland during Cenozoic time. Plate deflections are therefore expected to extend downward beneath the thrust belts. Models for T_e of 5 km or more yield an acceptable fit to both deflection and gravity data. The quality of the fit for plate thicknesses greater than 20 kilometers is no worse than that of the 20-km model shown in Figure 9a. The value of T_e that yields the best fit to the combined deflection and gravity data is subjectively determined to be 10 kilometers.

Figure 9b illustrates for the $T_e = 10$ km model that values for the beginning Tertiary water depth w_o shallower than -1 km and deeper than -1.25 km for $x < 290$ km predict gravity anomalies that are more negative and more positive than those observed. This result holds true for the range of acceptable plate thicknesses ($T_e > 5$ km), where we find the data are best fit by models with w_o between -1.1 km and -1.5 km. The beginning Tertiary water depths associated with the best fitting T_e = 10-km plate model are -1.25 km for $x < 290$ km and -0.25 km for $x > 290$ km.

The effective plate end locations x_1 and x_2 were set in all cases to values which gave a subjectively determined best fit to the gravity data. x_1 falls between $x = 140$ and $x = 160$

km; x_2 is poorly constrained in the absence of Yugoslavian gravity data and is set to x = 330 km. The gravity models on Profile B–B' were constructed assuming the existence of a mass anomaly with total mass of 7 x 10^{11} kg/m distributed uniformly at depths of 100 to 150 km between x = -100 km and x = -25 km west of the Italian peninsula. This mass anomaly was included in our modeling because it successfully predicts the long–wavelength positive gravity anomaly observed over Italy and the Tyrrhenian Sea [Royden, 1988] (Figure 2b).

Figure 9c shows the vertical shear forces and bending moments associated with deflection of the best–fitting 10–km elastic plate beneath the internal parts of the foredeep basins and the regions where deflections are extrapolated beneath the thrust sheets. Bending moments associated with the more highly curved best–fitting deflections in the Dinaride foredeep basin are greater than those in the Apennine foredeep.

Beginning Pliocene time. We model the reconstructed deflection of the Dinaride foredeep basement between beginning Tertiary time and beginning Pliocene time with a one–sided elastic plate deflection model because deflections to the southwest over the Apennine foredeep were negligible throughout this period (Figure 10a). As discussed above, the flexural models assume that topography and bathymetry at beginning Pliocene time were identical to those at present.

Because the water depth in which lowermost Pliocene sediments were deposited is not known, we assume that the water depths at the beginning of Pliocene time were different from those at the beginning of Tertiary time by a uniform amount. This assumed uniform change in water depth is bounded by the constraint that these marine sediments must have been deposited below sea level. Figure 10a illustrates models corresponding to the value of beginning Pliocene water depth that satisfies the above constraint and yields the best possible fit to the reconstructed depth data for the three values of effective elastic plate thickness. The 20–km thick elastic plate model fails to fit the deflection data and water depth constraint, assuming that base Tertiary water depths were the best–fitting values of -250 meters for x > 290 km and -1250 meters for x < 290 km. Models with T_e greater than 20 kilometers yield comparable or worse fits to the data. The 2.5-km model is rejected as it predicts a shallowing of the downgoing plate near the Dinaride thrust belt which is physically implausible as hundreds of kilometers of shortening are recorded in the Dinaride thrust belt prior to Pliocene time. Models with effective elastic plate thickness between 5 and 15 kilometers produce subjectively defined acceptable fits to the data.

Figure 10b shows the best–fitting pairs of beginning Pliocene plate thickness and water depth, and the defined limits on acceptable values of T_e. The best–fitting beginning Pliocene water depths over the Dinaride foredeep range from –250 meters to sea level.

The transmitted forces and moments of the best–fitting models for both the present and reconstructed beginning Pliocene Dinaride basement deflections are illustrated in Figure 10c. If the Adriatic plate strength has remained constant through time with an effective elastic plate thickness of 10 kilometers, the forces transmitted through the downgoing plate in the Dinaride foredeep must have decreased since the beginning of Pliocene time.

Middle Pliocene time. Figure 11a illustrates the best–fitting two–sided deflection profiles based on the middle Pliocene Apennine foredeep basin reconstruction and on the beginning Pliocene reconstruction of the Dinaride foredeep basin. No data for the middle Pliocene were available in the Dinaride foredeep basin, but because the Dinaride basin geometry changed relatively little during Pliocene time, this substitution should have relatively little effect on our interpretations. Topographic loads are again assumed to be equivalent to the present loads. The middle Pliocene water depth is constrained to be uniform and negative (below sea level) for $x < 290$ km and to be uniform and negative, but not necessarily the same, for $x > 290$ km.

The 2.5–km thick plate model is rejected because it predicts unphysical shallowing over the internal parts of the foredeep basins. Five– and 10–km plate models produce acceptable fits to the data. The 20–km model, however, yields a slightly poorer fit in the deeper portions of the Dinaride basin, misfitting the depth of the most internal data point by more than one kilometer. The quality of the fit of models with T_e values greater than 20 kilometers is comparable to that of the 20–km model. We thus interpret 20 kilometers as a reasonable upper bound, but note that this bound is not as well defined as others discussed in this paper.

All models in Figure 11a indicate a middle Pliocene flexural high over the location of the present Apennine foredeep. The change in basement deflection in the Apennine foredeep basin between middle Pliocene and present time thus apparently records a northeastward migration of the flexural high subsequent to middle Pliocene time. Figures 11b shows the best–fitting pairs of values of middle Pliocene effective elastic plate thickness and water depths, assuming as above that base Tertiary water depths were -1250 meters for $x < 290$ km and -250 meters for $x > 290$ km. We subjectively define the lower and upper limits on acceptable values of T_e as 5 and 15 kilometers and on middle Pliocene water depths as 500 meters and sea level for $x < 290$ km and at sea level for $x > 290$ km. Figure 11c illustrates a comparison of the forces and moments transmitted through plate of the best–fitting 10–km models for middle Pliocene and present time. The change in sign of the modeled vertical shear force over the deeper parts of the Apennine foredeep basin reflects the transition of this region from a flexural high to an internal portion of the foredeep basin.

Beginning Quaternary time. Two–sided deflection models with plate thicknesses of 5 and 10 kilometers yield acceptable fits to the reconstructed beginning Quaternary basement depths. Under the restriction that the depositional depth of the beginning Quaternary horizon must be at or below sea level, a 20–km thick plate model fails to fit the deepest data point within the Dinaride foredeep. Models with larger values of T_e yield fits comparable to the 20–km model. Noting that our criteria for bounding T_e are based on a single data point, we nevertheless assume that 20 kilometers is a reasonable upper limit on the range of acceptable effective elastic plate thicknesses. Models with T_e values smaller than 5 kilometers are rejected because they predict upward deflections in the internal parts of the two foredeeps. The 5– to 20–km range of acceptable beginning Quaternary effective elastic plate thicknesses corresponds to beginning Quaternary water depths of -350 meters to sea level (Figure 12b).

Figure 12c shows that if the effective elastic plate thickness has remained constant between beginning Quaternary and present time, then the effective bending moment transmitted through the plate in the internal parts of the Apennine foredeep basin has decreased since beginning Quaternary time.

Profile C–C'.

Present time. The Bouguer gravity data and present plate deflection data (represented in Figure 13 by depths to the base Pliocene horizon) are best fit by a model with an effective elastic plate thickness of 20 to 40 kilometers and a starting base Pliocene water depth of approximately -800 to -1200 meters [Royden, 1988]. A one–sided flexural model was used in these calculations, as no information was available on the magnitude of the Dinaride foredeep basin across the northern Adriatic.

Beginning Quaternary time. Flexural modeling of the reconstructed basin geometry at the beginning of Quaternary time indicates that the steepness of the dip of the basement decreased between beginning Quaternary and present time (Figure 14a). Best–fitting models for effective elastic plate thicknesses of 5 km or less are rejected since they predict an unphysical shallowing near the Apennine mountains. Models with T_e of 40 kilometers or more predict an uplift of basement above sea level over the northeastern Adriatic which is incompatible with the observation of marine Pliocene–Quaternary deposits in this region. The range of acceptable effective elastic plate thicknesses that can describe the reconstructed beginning Quaternary depth data is thus limited to 10 to 40 kilometers. The beginning Quaternary depositional water depths that correspond to these best–fitting acceptable

models range from -600 meters to sea level (Figure 14b), assuming a starting base Pliocene water depth of -1000 meters.

Figure 14c shows that if the effective elastic plate thickness has not changed between beginning Quaternary and present time, then the Quaternary lithospheric flexure corresponds to a reduction in moments transmitted through the plate.

Profile D–D'.

Present time. One–sided flexural modeling of the present Apennine foredeep basin geometry along this profile through the Po Plain of Italy best fits the deflection data and Bouguer gravity anomalies with an effective elastic plate thickness of 15 to 25 kilometers and a starting base Pliocene water depth of approximately -500 to -1500 meters (Figure 15). Constraints on the starting water depth were not as good as on Profiles B-B' and C-C' because the gravity data are effected by the presence of a gravity signature associated with Alpine tectonics on the northern part of this profile (Figure 15). A 20-km plate thickness and -1000 meter starting water depth yielded the subjectively determined best overall fit to the data [Royden, 1988].

Middle Pliocene time. The reconstructed gently–dipping middle Pliocene foredeep basin shape can be successfully modeled with effective elastic plate thicknesses between 10 and 100 kilometers. Models with T_e of 5 kilometers or less are unacceptable as they predict unreasonable shallowing near the Apennine mountains. Models with T_e greater than 100 kilometers are rejected because they imply basement uplift in the northeastern Po Basin at middle Pliocene time of marine sediment deposition in this region. The acceptable best–fitting models imply Middle Pliocene water depths between -700 meters and sea level, assuming that base Pliocene deposition occurred at -1000 meter water depth (Figure 16b). Figure 16c indicates that the effective moments transmitted over the internal part of the Apennine foredeep basin along Profile D–D' have increased between middle Pliocene and present time.

Beginning Quaternary time. Along this profile it appears that the downward growth of the internal part of the Apennine foredeep basin continued during Quaternary time. Figure 17a shows best–fitting flexural models with beginning Quaternary water depths constrained to be below sea level. Effective elastic plate thicknesses of 5 kilometers or less are found unacceptable as they predict shallowing of the plate in the internal parts of the foredeep. As 100 km or more of shortening had occurred by beginning Quaternary time, we expect the downgoing plate to extend further southwestward beneath the Apennine thrust belt. Models with T_e of 50 kilometers or more predict basement uplift

over the northeastern Po Plain which appears incompatible with marine Quaternary sediment deposition in this region. Thus the range of beginning Quaternary effective elastic plate thickness that can satisfy all observations is defined as 10 to 40 kilometers, corresponding to beginning Quaternary water depths of -700 to 0 meters (Figure 17b). Figure 17c shows that changes in the modeled vertical shear force and bending moment along Profile D–D' may be quite small over Quaternary time if the effective plate thickness is constant through time.

Profile E–E'

Present time. Figure 18a shows the that the reconstructed present basement deflection data and Bouguer gravity anomalies along Profile E-E' can be fit by models assuming effective elastic plate thicknesses as great as 150 kilometers or more. Models with T_e between 5 and 150 kilometers produce fits to both the deflection and gravity data comparable to the fit of the 150-km model. The 2.5-km model yields a slightly poorer fit to the deflection data. Tighter constraints can be placed on the base Tertiary starting water depth, where water depths shallower than -1000 meters and deeper than -3000 meters predict slopes in the gravity data between x = 50 km and x = 100 km that differ significantly from the observed slope (Figure 18b). Models with starting water depths between -1500 and -500 meters gave subjectively determined best overall fits to the data.

For all models, we found the combination of the effective plate end locations x_1 and x_2 and the starting water depth that yield the best possible fit to the gravity data. The best–fitting value of the northern effective end x_2 is 145 kilometers in all cases. The best–fitting location of x_1 is 30 to 40 kilometers for a starting water depth of -2000 meters.

Figure 18c shows the results of fitting the gravity data and only the depth data over the Apennine foredeep basin, neglecting the palinspastically restored depths over the north–dipping basin. We find that, even without the northernmost depth data, the best–fitting plate deflection is tightly flexed, with a flexural high well south of the gravity high near x = 170 km. Comparable results are achieved for models with plate thicknesses from 5 to 150 kilometers or more. The quality of the fit to the gravity data is equivalent for models using only the southern depth data and models fitting all depth data.

All models on Profile E–E' misfit observed Bouguer gravity within 50 kilometers of the Italian coast. The more positive Bouguer anomalies near the coast coincide with the edge of a large regional Bouguer gravity high over the Tyrrhenian Sea and may be explained by anomalously dense material, perhaps a deep slab, at depth between 75 and 150 kilometers west of Italy [Royden, 1988].

UNCERTAINTIES

In this section we address whether uncertainties in the assumptions in our flexural modeling can modify the results of the preceding section. Figures 19a and 19b show that the effect of uncertainties in sediment and lithospheric density structure can modify our estimates of starting water depths by several hundred meters. Variations of +/– 5 kilometers in the assumed pre–deflection Moho depth of 35 kilometers yield uncertainties in the starting water depths of comparable magnitude.

Uncertainties in estimates of the starting water depths are of principal concern in this study because they produce an uncertainty in the upper bounds inferred for effective elastic plate thicknesses at past times. The starting water depth of the horizon at the base of the foredeep basin is used in combination with the constraint that marine horizons must have been deposited below sea level to limit the possible change in depositional water depth between the times of deposition of the base horizon and of a younger horizon. In practice, this restriction on the change in water depths has no effect on models with small elastic plate thicknesses, but modifies the fit of models with large effective elastic plate thicknesses to the reconstructed depth data.

The results discussed for Profile B-B' are not affected by such uncertainties in water depths because the bounds on effective elastic plate thicknesses are defined on the basis of data in the Dinaride foredeep where the starting water depth is well (and conservatively) constrained to be shallower than -250 meters. Figures 19c and 19d show that the best fit of large elastic plate thickness models on Profiles C-C' and D-D' does not change significantly from the results discussed above when very conservative limits on the beginning Pliocene starting water depths are imposed. Most importantly, in these cases the dependence of the best–fitting flexural profiles on the starting water depth is small enough that our criteria for approximately bounding the effective elastic plate thickness is not affected by the starting water depth uncertainties.

One of the uncertainties in models for Profiles C-C' and D-D' is a lack of knowledge of the thickness of pre–Pliocene sediments, which are less than a few hundred meters over the Apennine foredeep [Bally et al., 1986] but could be thicker to the northeast. However, the similarity between our results in the Apennine foredeep basin for Profile B-B' based on total Tertiary sediment thicknesses and the results of Royden [1988], who ignored pre–Pliocene sediment thicknesses, suggests that the results for Profile C-C' and D-D' will not be significantly altered by consideration of pre–Pliocene thicknesses.

Uncertainties in the magnitude of past topographic and water loads have negligible impact on modeled lithospheric deflections within the foredeep basin unless topographic loads were present over the central foredeep regions. This is unlikely as the thrust fronts have migrated through time toward the external parts of the foredeep basins. Deflections beneath topographic loads and the corresponding transmitted forces and moments are, however, significantly affected by changes in elevations. The changes in the modeled forces thus incorporate changes in the topographic load, and the uncertainty in our modeling lies in how much of the modeled forces to attribute to past topographic loads as opposed to other convergence zone processes.

The magnitude of the transmitted forces and moments in the thin elastic plate models (Figures 9c through 17c) are proportional to the flexural rigidity of the plate and hence vary strongly with effective elastic plate thickness. Thus the nature of changes in transmitted forces and moments through time described for the modeling above are valid only under the assumption that the effective elastic plate thickness remains constant through time. Uncertainties in transmitted forces and moments resulting from uncertainties in sediment compaction effects and starting water depths are much smaller than those associated with changes in effective elastic plate thickness, and do not effect the qualitative conclusions drawn above on the temporal variations in forces and moments.

DISCUSSION

The modeling described above suggests several interesting features of the deflection of the lithosphere beneath the Adriatic foredeep basins, namely that (1) the Apennine–Dinaride and Apennine–Southern Alps foredeep basin pairs can be described in terms of the two–sided deflection of an elastic plate; (2) there is no significant weakening of the Adriatic lithosphere between the times of the Eocene Dinaride and Pliocene Apennine convergent events, so that the evolution of both the Dinaride and Apennine foredeep basins can be explained by deflection of an elastic plate with uniform and constant thickness constant over 50 m.y.; and (3) subsequent to the cessation of the Pliocene Apennine thrusting events the downgoing Adriatic lithosphere has 'unflexed' on Profiles B–B' and C–C' as uplift replaced subsidence over the internal part of the foredeep basin during Quaternary time.

Temporal and spatial variations in T_e

Table 6 summarizes the best–fitting present effective elastic plate thicknesses and the bounds on past thicknesses and displays an important result of this study, namely that for

each of the profiles the bounds on acceptable values of T_e at past times bracket the present best–fitting value of T_e. The data are thus compatible with a constant effective elastic plate thickness or flexural rigidity for the lithosphere along each profile both during the periods of the basin formation and subsequent to the cessation of convergent surface deformation. In particular the effective elastic plate thickness of the pre–Pliocene plate deflection beneath the Dinaride foredeep (5 km < T_e < 15 km) is comparable to the best–fitting elastic plate thickness for the present Adriatic lithosphere along Profile B–B' (T_e = 10 km), suggesting that changes in the mechanical properties of the central Adriatic lithosphere were relatively small both during the Eocene Dinaride and Pliocene Apennine events as well as between the times of the Eocene and Pliocene events.

The best–fitting effective elastic plate thicknesses derived in this study, particularly along Profile B–B' (5 km < T_e < 30 km), are quite small in comparison with values found in other continental settings, which may be up to and greater than 100 kilometers [e.g. *Karner and Watts*, 1983; *Lyon–Caen and Molnar*, 1983]. In this context it is interesting to note that the Adriatic lithosphere appeared weak (low T_e) during the pre–Pliocene Dinaride deflection prior to the period of rapid extension in the Tyrrhenian Sea and convergence in the Apennine thrust belt in late Miocene–Pliocene time. Thus this weakness is not a product of regional warming related to the late Miocene–Pliocene back–arc–type extensional processes active in Italy and the Tyrrhenian Sea.

Success of the uniform thin elastic plate model in describing the depth and gravity data in the Adriatic region may be due in part to the high curvatures of the basement flexure (10^{-5} to 10^{-6} m^{-1}). The following argument suggests that the assumption that mechanical behavior of the lithosphere approximates that of a uniformly thick elastic plate may be quite good for lithosphere with high curvature such as in the Adriatic–Po region. The thin elastic plate model assumes that the bending moment $M(x)$ and curvature of the plate $C(x)$ are linearly related at any point x by the flexural rigidity $D(x) = M(x)/C(x)$. $D(x)$ is in turn proportional to T_e^3 (see Table 5). For the true lithospheric rheology, the bending moment, the sum through a cross section of the lithosphere of the moments of the fiber stresses associated with bending of the lithosphere, will be a more complicated function of the curvature. Thus a thin elastic plate model with uniform flexural rigidity (constant T_e) is a good approximation when changes in the true ratio $M(x)/C(x)$ are small as curvatures vary along the profile.

For rheologies commonly assumed for oceanic and continental lithosphere, the magnitude of changes in the ratio $M(x)/C(x)$ as a function of curvature

$$\frac{dM/dC}{dC} = \frac{1}{C}\left(-\frac{dM}{dC} + \frac{M}{C}\right)$$

may be small where curvatures are large. Figures 20a and b illustrate that both parts of the term in parentheses, $dM(x)/dC(x)$ and $M(x)/C(x)$, are smaller at high curvatures. For the typical yield stress envelopes shown in these figures, a given increase in the curvature of lithosphere that is already highly curved results in a smaller increase in bending stresses within the lithosphere than for lithosphere with lower initial curvature. Thus incremental changes in the bending moment $dM(x)/dC(x)$ grow increasingly smaller with increasing plate curvature. Similarly the ratio of the moment to curvature $M(x)/C(x)$ decreases at high curvatures for these rheologies. Figure 20c shows for a simplified rheological model that as the size of $dM(x)/dC(x)$ and $M(x)/C(x)$ decrease with increasing curvature, $(dM(x)/dC(x))/dC(x)$, which is their difference reduced by a factor of $1/C$, is also reduced. The true lithospheric behavior may thus more closely approximate the uniform thin elastic plate assumption that $M(x)/C(x)$ is a constant value when lithospheric curvatures are high.

Figure 20c is derived following the technique of McNutt [1984]. The bending moment induced when a given amount of curvature is imposed on lithosphere with rheology as shown in the inset is equated with the bending moment induced in a thin elastic plate with the same curvature. The thickness of the elastic plate that yields the same bending moment as then plotted as a function of the curvature. This figure illustrates that variations in the effective elastic plate thickness T_e (corresponding to the flexural rigidity $D(x) = M(x)/C(x)$) as a function of curvature are smaller at higher curvatures. More realistic continental yield stress envelopes in which a zone of weakness lies near the neutral plane may reduce even further the effect of variations in curvature of highly flexed plates on the corresponding effective elastic plate thickness.

We note that the estimate by Royden [1988] of a 15 to 30–km mechanical plate thickness (the depth at which deviatoric stresses maintained in the lithosphere become negligibly small) for the Adriatic lithosphere in the Apennine foredeep system was based on incorrect computations of plate curvature that underestimate curvature by a factor of ten. For the simple yield stress envelope assumed in Figure 20c, the correctly computed curvatures of Profiles B-B', C-C', and D-D' and best–fitting elastic plate thicknesses correspond to a mechanical plate thickness of about 75 kilometers. The relationship between a mechanical plate thickness and an effective elastic plate thickness, however, is highly dependent on the rheology assumed and is highly uncertain in continental lithosphere. The meaning of the mechanical plate thickness furthermore becomes obscured

for complicated rheologies such as that depicted in Figure 20b, where zones of weakness are not restricted to the base of the lithosphere.

Loads and forces

The vertical shear forces and bending moments transmitted through the deflected plate in the internal parts of the foredeep basins (as plotted in Figures 9 through 17) represent the combined effect of unmodeled surface loads and stresses off the ends of the plate. The modeled forces and moments were generally smaller at middle Pliocene time than at present and greater at beginning Quaternary time than at present. These changes in the forces and moments reflect changes in topographic loads and in additional forces that act on the downgoing plate. These additional forces may include the load of a negatively buoyant deep slab extending beneath the convergent zone or stresses associated with motions in the asthenosphere.

The weight of the present Apennine and Dinaride mountains on the downgoing lithosphere are insufficient to explain the formation of such steep and deep foredeep basins. Although the total mass of the topographic loads ($\sim 2 \times 10^{12}$ N/m) is comparable in magnitude to the vertical shear forces maintained by the present plate at the internal edge of the basin, the broad mountain topography renders this load ineffective in inducing a moment on the plate. Thus the present topographic load cannot produce the sharp deflections and curvatures observed in the downgoing plate.

Past mountain elevations may have been considerably larger than the present elevations since thrusting has abated while erosional processes accompanied in western Italy by significant onshore extension remained active in Quaternary time. Thus topographic loads alone may be sufficient to explain certain basement deflections which have relatively small curvatures, such as the reconstructed middle Pliocene Apennine deflections. Figure 21a shows that the middle Pliocene basin shape along Profile B–B' could be produced by a 1–km high topographic load near the present Italian coastline over a plate with an effectively 'free' end (with negligible forces and moments transmitted through the plate). The curvature of the beginning Quaternary Apennine profiles, on the other hand, is apparently too large to be induced by past topographic loads. Figure 21b shows that a beginning Quaternary topographic load could supply the vertical force required to produce the plate deflection but only a minor component of the required bending moment.

Changes in the plate deflections through time may be better explained by a combination of changes in topographic load and changes in processes acting at greater depth. In the following paragraphs we turn to the question of whether the downgoing

lithosphere continues to descend as a 'deep slab' beneath either the Apennine or Dinaride thrust belts. Verification of the presence or absence of a deep slab in these convergence zones would allow us not only to estimate the contribution of the load of a deep slab on the deflection of the lithosphere observed beneath the foredeep basins, but also to interpret our modeling as representative of either a well developed oceanic–type subduction zone or a region where convergence has been accommodated principally by crustal or lithospheric shortening.

Data relevant to the question of the extent of subduction are unfortunately unavailable for the Dinaride foredeep and ambiguous on the northern and central Apennine convergence zone. These data are nevertheless summarized here because of their importance to this study.

Evidence pointing towards significant subduction beneath these thrust belts includes palinspastic restorations that show up to 100–200 km or more of shortening in both the Apennine and Dinaride thrust belts [Bally et al., 1986]. In these convergent zones it is difficult to account for the observed shortening without lithospheric subduction. The low elevations of peninsular Italy and the Dinaride mountains argue that these regions have relatively small crustal roots that could not have not accommodated significant amounts of crustal shortening by local thickening. For example, assuming to crustal material is lost to the mantle, the amount of crustal shortening Δl in a convergence zone that could be contained in a crustal root that isostatically balances the mountain range is approximately $\Delta l = (v_t \rho_t)/(\Delta\rho\, h_c)$, where v_t is the volume of the topography per unit distance along strike, ρ_t is the density of the topography, $\Delta\rho$ is the crust–mantle density contrast and h_c is the thickness of the shortening crust. Crustal shortening thus squeezed into a Apennine or Dinaride crustal root is limited to Δl =15 km or less, for v_t = 70–100 km^2, h_c = 35 km, ρ_t = 2600 kg/m^3 and $\Delta\rho$ = 600 kg/m^3.

Further evidence supporting the presence of a subducting slab beneath the Apennine foredeep includes the anomalously high Bouguer gravity signal over the Tyrrhenian Sea. This gravity high could reflect a partially dynamically supported slab at depths of 100–150 km [Royden, 1988], for which the positive contribution of cold (dense) subducting mantle lithosphere outweighs the negative contribution to the gravity signal of attached continental crust.

Evidence against a deep slab beneath northern and central Italy includes the lack of a Benioff zone and arc–type volcanism along the Italian peninsula. The seismic Benioff zone in the Calabrian arc dips northwest, while a deep slap associated with the Apennine foredeep should dip southwest [Gasparini et al., 1982; Ritsema, 1979]. The Calabrian Benioff zone does not extend northward past 41°N. A preliminary residual sphere

analysis of large ISC earthquakes of magnitude also shows no indication of anomalously high seismic velocities beneath central Italy and the Tyrrhenian Sea, although this analysis may not be sensitive to shorter slabs in such a complex environment. Seismic tomography studies of Spakman [1986, 1988] are also in conflict with the notion of a continuous cold slab descending more than 150 km from the Apennine foredeep. Spakman [1988] shows a band of positive P–wave velocity anomalies extending to depths of 150 kilometers beneath the Po Plain and the eastern coast of north–central Italy which implies that cold material is limited to depths above 150 km and does not extend beneath the Tyrrhenian Sea. The tomography data should be interpreted with caution, however, as the errors associated with this method may be significant and the nature of travel–time anomalies associated with subduction of continental lithosphere is not well understood.

In contrast with the Apennine and Dinaride foredeep basins, it is unlikely that underthrusting extended far beyond the reconstructed basin area in the north–dipping basin fronting the Southern Alps (Figure 13). The gravity data on Profile E-E' are best fit by an effective plate end just north of the deepest reconstructed depth point in the Southern Alp basin.

Unflexing

Flexural models of deflection on Profiles B-B' and C-C' predict that uplift of the basin has occurred in the internal part of the Apennine foredeep since beginning Quaternary time. This 'unflexing' of the basement coincides with the cessation of thrusting in the Apennine thrust belt and marks a departure from the increase in basin depths during Pliocene time. The magnitude of this post–thrusting unflexing inferred from reconstructions in the central Apennine foredeep segments depends critically on the base Quaternary depth data and on our assumption of a uniform depositional depth for Apennine base Quaternary horizon.

Figure 22 illustrates that the inferred unflexing could not be explained away through uncertainties in the base Quaternary depth data alone. Relatively large random uncertainties of +/-500 meters in the reconstructed beginning Quaternary foredeep depth data are required to produce a range of best-fitting beginning Quaternary profiles that are not necessarily more 'highly flexed' than present best-fitting profile.

Stratigraphic constraints on the beginning Quaternary depositional water depth on Profiles B–B' and C-C' suggest, however, that the estimates of the magnitude of the Apennine unflexing presented here are probably upper bounds on true unflexing. The lithology and faunal associations in older Pleistocene sediments in the western Adriatic

suggest that sediment deposition took place at greater depths in the central Adriatic sea than near the Italian coastline [Dondi et al., 1985]. Thus it appears likely that some fraction of the present variation in depth between nearshore and offshore beginning Quaternary deposits is due to a lateral variation in depositional depth rather than subsequent unflexing.

A three–dimensional view of the Pliocene–Quaternary Apennine foredeep geometry between Profiles B-B' and C-C' indicates, however, that a significant component of the geometry of the Quaternary fill reflects lithospheric motions rather than local control on sediment deposition. If Quaternary sediments were deposited into a preexisting void, we would expect the shape of Quaternary isopachs to parallel sediment sources, in this case the Apennine thrust front. Early Quaternary sediments were carried predominantly outward from the Italian coast rather than along the axis of the Adriatic Sea [Dondi et al., 1980]. On the other hand, if lithospheric motions are responsible for the present synclinal shape of base Quaternary deposits, we expect that Quaternary isopachs should follow the trends of the segmentation of the Apennine foredeep basin. This segmentation, which is observed in stepwise offsets of base Pliocene isopachs and Bouguer gravity contours, appears to be controlled by tears in the downgoing lithosphere [Royden et al., 1987]. Figure 23 shows that the Quaternary isopachs indeed exhibit an offset across a segment boundary instead of paralleling the more arcuate Apennine thrust front. The lateral offset in the Quaternary isopachs coincides with a 100 kilometer lateral offset in Pliocene isopachs, strongly suggesting that the shape of this horizon reflects to a considerable degree motions of the underlying segmented lithosphere.

Independent support of the existence of some unflexing comes also from onshore geological observations in eastern Italy. Early Quaternary rocks outcrop near the eastern coast of Italy along Profile B–B' quite near the location predicted by uplift associated with unflexing in our simple flexural model (see Figure 4d) [Crescenti et al., 1980]. Pleistocene rocks on the Italian coast are commonly found dipping gently to the northeast, as would also be expected from the unflexing model. This observation alone is not convincing, however, as it could be argued, that the Quaternary dips and uplifts were produced by the Quaternary Apennine thrusting rather than vertical motions of the underlying basement.

The base Pliocene horizon within the Dinaride foredeep on Profile B-B' has a geometry comparable to that of the base Quaternary in the Apennine foredeep. No equivalent external constraints on the existence of unflexing are available in the Dinaride foredeep, however. We interpret the Dinaride data as suggestive, but certainly not conclusive, evidence that unflexing subsequent to the cessation of thrusting may be a process not unique to the Apennine foredeep.

The apparent Quaternary Apennine unflexing cannot be explained by simple migration of the plate away from the thrust belt (slab roll–back) [Dewey, 1980] as found in the Himalaya, where younger sediments onlap older sediments on the external edge of the foredeep basin [Lyon–Caen and Molnar, 1985]. Viscoelastic relaxation of the plate subject to a steady force at depth [Beaumont, 1978; Lambeck and Nakiboglu, 1981] also fails to predict uplift of the internal parts of the foredeep basin.

Here we examine whether other processes such as erosion of the topographic load, reduction in the load of a deep slab, dissipation of preexisting regional compressive stress, failure or weakening of the downgoing plate, and asthenospheric drag on the plate could explain the post–tectonic unflexing modeled along Profiles B–B' and C–C'. Figure 24 shows a series of models in which forces on the plate external to the foredeep basin are assumed to be constant throughout Quaternary time. Unless otherwise specified we assume a uniform, constant elastic plate thickness of 10 kilometers for Profile B-B' and 20 kilometers for Profile C-C' A force F_t and the moment M_t are fixed on the end of the downgoing plate at location x_1. We use the plate end location that best fits the gravity data [Royden, 1988]. Computations were done with a finite–difference solution of the thin elastic plate equation that allows F_t and M_t and a horizontal stress P across the plate to be specified as boundary conditions [Sheffels and McNutt, 1986].

Figure 24a shows that the more pronounced plate flexure at beginning Quaternary time could be produced by a hypothetical 2–km high topographic load in eastern Italy along B–B'. An equivalent load on the stronger C–C' basin segment cannot reproduce the reconstructed beginning Quaternary basin shape (Figure 24b). We conclude that erosion of eastern Italian topography at a 1 mm/yr rate would be sufficient to explain much of the apparent unflexing along Profile B–B', but not along Profile C-C'.

A simple calculation suggests that the reduction in effective moment associated with unflexing on profiles B-B' and C-C' (Figures 12c, 14c) could be produced by conductive warming of a deep slab if convergence ceases in Quaternary time. The change in moment ΔM on the foredeep basin lithosphere associated with deep slab warming is approximated by $\Delta M = L/2 \cdot \Delta\rho g L(\kappa\Delta t)^{1/2}$ where L is length of the slab, $L/2$ is the moment arm of the deep slab, and the latter term is the change in the mass of the slab as it warms on contact with the surrounding mantle. $\Delta\rho$ is the change in slab density associated with the thermal expansion and $(\kappa\Delta t)^{1/2}$ is the length scale of conductive warming into the interior of the slab, where κ is the thermal diffusivity and Δt is the time scale of warming. A change in moment ΔM of 0.25 to 1 x 10^{17} N (per unit length along strike) as estimated on Profiles B-B' and C-C' could be produced by warming of a slab 50 to 200 kilometers long over 2 million years, assuming that $\Delta\rho = \rho_o \alpha \Delta T$, where ρ_o is the mantle density, α is the

coefficient of thermal expansion, and ΔT is the average temperature contrast between downgoing slab and surrounding mantle, and setting ρ_o = 3300 kg/m^3, α = 3 x 10^{-5} °C^{-1}, ΔT = 500 °C, κ = 10^{-6} m^2/s, and Δt = 2 m.y. This mechanism requires the rate of change in slab mass exceeds the response of any viscous forces partially supporting the slab.

A dissipation of preexisting compressive stress across the Apennine foredeep during Quaternary time could also produce the unflexing along B–B' (Figure 24c). Such a process fails, however, to predict the reconstructed beginning Quaternary curvature of the foredeep basement along Profile C–C' for any magnitude of uniform compressive stress (Figure 24d). Furthermore, the existence of compressive stress in the Adriatic lithosphere appears unlikely at beginning Quaternary time as western Italy and the Tyrrhenian region underwent considerable extension at this time. If recent changes in lithospheric deflection were dominated by a reduction in compressive stress, we might expect that the Apennine thrust belt and foredeep basin systems paralleled each other more closely in the past. The existence of the basin segmentation at the beginning of Quaternary time as discussed above coupled with restorations that show an arcuate shape of the beginning Quaternary thrust front [Scandone and Patacca, unpublished manuscript, 1987] refute this notion.

Brittle failure in the downgoing plate in the region of highest curvature, which generally falls at the internal edge of the foredeep, predicts a downwarping rather than uplift of the plate near the basin edge along both Profiles B-B' and C-C' (Figures 24e and f). Weakening of the downgoing plate at greater depths could explain a reduction in the transmitted forces and moments, however. At these depths weakening may be equivalent to a decoupling of the shallower portion of the plate from deeper portions. A decoupling of the pull of a negatively buoyant slab from the shallower downgoing plate could thus potentially explain the subsequent foredeep uplift. Analogous failure is observed in seismic evidence of normal faulting in a variety of subduction zones at the location where the dip of the downgoing slab steepens [Spence, 1987].

Finally, the coincidence in time of unflexing in the Apennine foredeep basin and diminished thrusting in the overriding plate may reflect a fundamental change in mantle processes active in the convergence zone. These phenomena may be recorded in other foredeep basins as well, such as the Alps [Lyon–Caen and Molnar, 1989] the southeast Carpathian foredeep basin [Paraschiv, 1979] and the Alberta basin [Beaumont, 1981].

CONCLUSIONS

Reconstructions and flexural modeling of the evolution in the shape of the Apennine, Dinaride and Southern Alpine foredeep basins yield the following conclusions:

1. The data are compatible with a constant flexural behavior of the Adriatic lithosphere throughout the evolution of the individual Apennine foredeep basin segments and the Dinaride foredeep basin. The flexural rigidity of the Adriatic lithosphere (10^{22} – 10^{23} Nm) (effective elastic plate thickness of 10 to 20 kilometers) was comparable during Eocene and Pliocene convergence events.

2. A component of the shallowing of the younger horizons in the internal parts of the central Apennine foredeep basin segments is probably due to 'unflexing' of the downgoing lithosphere coincident with the cessation of thrusting in the Apennine thrust belt. Apennine foredeep base Quaternary isopachs show an offset in map view coincident with the segmentation observed in the total foredeep sequence. These data support the hypothesis that the geometry of the sediment package is controlled primarily by the response of the downgoing lithosphere to loads applied outside the basin rather than local sedimentation processes related to proximity to the Apennine thrust belt. This post-tectonic stage of basin evolution is a marked departure from previous unidirectional basin growth.

3. Modeling suggests that changes in topographic load, changes in regional stresses, or lithospheric weakening in regions of highest plate curvature alone may not be sufficient in some cases to explain the Quaternary unflexing. The unflexing can be explained by a combination of these processes with changes in forces applied to the plate outside of the basin at depth. Candidates for processes acting outside the basin are thermal weakening of the downgoing plate, reduction in the load of a negatively buoyant slab by heating, and stresses associated with asthenospheric motions. Better data and an improvement of our current understanding of the rheology of continental lithosphere are required to improve our resolution of such deeper convergence zone processes.

REFERENCES

Bally, A.W., L. Burbi, C. Cooper, and R. Ghelardoni, Balanced sections and seismic reflection profiles across the central Apennines, *Mem. Soc. Geol. It., 35*, 257–310, 1986.

Beaumont, C., The evolution of sedimentary basins on a viscoelastic lithosphere: Theory and examples, *Geophys. J. R. astr.. Soc., 55*, 471–497, 1978.

Beaumont, C., Foreland basins, *Geophys. J. R. astr. Soc., 65*, 291–329, 1981.

Cermak, V., Crustal thickness in Europe (contour map), Geol. Inst. Czech. Acad. Sci., Prague, 1978.

Civetta, L., G. Orsi and P. Scandone, Eastwards migration of the Tuscan anatectic magmatism due to anticlockwise rotation of the Apennines, *Nature, 276*, 604–606, 1978.

Crescenti, U., C. D'Amato, A. Balduzzi, and M. Tonna, Il Plio–Pleistocene del sottosuolo Abruzzese–Marchigiano tra ascoli Piceno e Pescara, *Geologica Rom., 19*, 63–84, 1980.

Dewey, J.F., Episodicity, sequence, and style at convergent plate boundaries, in *The Continental Crust and Its Mineral Deposits*, edited by D.W. Strangway, p. 553–573, Geol. Assoc. of Canada Special Paper 20, 1980.

Dondi, L., A. Rizzini and P. Rossi, Recent geological evolution of the Adriatic Sea, in *Geological Evolution of the Mediterranean Basin*, edited by D.J. Stanley and F.C. Wezel, pp. 195–214, Springer–Verlag, New York, 1985.

Finetti, I., S. Gellemo and G. de Visintini, Preliminary investigation of the earth's crust in the south Adriatic Sea, *Boll. Geofis. Teor. Appl., 8*, 21–39, 1966.

Giese, P. and C. Morelli, Crustal structure in Italy, in *Structural Model of Italy*, edited by L. Ogniben, M. Parotto and A. Praturion, no. 90, pp. 453–490, Consiglio Nazionale Delle Ricerche, Rome, 1975.

Gasparini, C. G. Iannaccone, P. Scandone, and R. Scarpa, Seismotectonics of the Calabrian Arc, *Tectonophysics, 84*, 267–286, 1985.

Goetze, C. and B. Evans, Stress and temperature in the bending lithosphere as constrained by experimental rock mechanics, *Geophys. J. R. astr. Soc., 59*, 463–478, 1979.

Hanks, T.C., The Kuril trench–Hokkaido rise system: Large shallow earthquakes and simple models of deformation, *Geophys. J. R. astr. Soc.*, *23*, 173–189, 1971.

Karner, G.D. and A.B. Watts, Gravity anomalies and flexure of the lithosphere at mountain ranges, *J. Geophys. Res.*, *88*, 10449–10477, 1983.

Kastens, K. Mascle, J. et al., ODP Leg 107 in the Tyrrhenian Sea: Insights into passive margin and back–arc basin evolution, *Geol. Soc. Am. Bull.*, *100*, 1140–1156, 1988.

Klingele, Gravity map of Switzerland (contour map), Commission Suisse de Geophysique, Wabern, 1976.

Lambeck, K. and S.M. Nakiboglu, Seamount loading and stress in the ocean lithosphere 2. Viscoelastic and elastic–viscoelastic models, *J. Geophys. Res.*, *86*, 6961–6984, 1981.

Laubscher, H.P., Large–scale, thin–skinned thrusting in the southern Alps: Kinematic models, *Geol. Soc. Am. Bull.*, *96*, 710–718, 1985.

Lyon–Caen, H. and P. Molnar, Constraints on the structure of the Himalaya from an analysis of gravity anomalies and a flexural model of the lithosphere, *J. Geophys. Res.*, *88*, 8171–8191, 1983.

Lyon–Caen, H. and P. Molnar, Gravity anomalies, flexure of the Indian plate, and the structure, support and evolution of the Himalaya and Ganga basin, *Tectonics*, *4*, 513–538, 1985.

Lyon–Caen, H. and P. Molnar, Constraints on the deep structure and dynamic processes beneath the Alps and adjacent regions from an analysis of gravity anomalies, *Geophys. J. Int.*, in press, 1989.

Malinverno, A. and W.B.F. Ryan, Extension of the Tyrrhenian Sea and shortening in the Apennines as a result of arc migration driven by sinking lithosphere, *Tectonics*, *5*, 227–245, 1986.

McAdoo, D.C., J.G. Caldwell and D.L. Turcotte, On the elastic–perfectly plastic bending of the lithosphere under generalized loading with application to the Kuril Trench, *Geophys. J. R. astr. Soc.*, *54*, 11–26, 1978.

McNutt, M.K., Lithospheric flexure and thermal anomalies, *J. Geophys. Res.*, *89*, 11180–11194, 1984.

Morelli, C. et al., Regional geophysical study of the Adriatic Sea., *Boll. Geofis. Teor. Appl.*, *11*, 3–56, 1969.

Moretti, I., and L. Royden, Deflection, gravity anomalies and tectonics of doubly subducted continental lithosphere: Adriatic and Ionian Seas, *Tectonics*, *7*, 875–893, 1988.

Nunn, J.A., M. Czerniak, and R.H. Pilger, Jr., Constraints on the structure of Brooks Range and Colville Basin, northern Alaska, from flexure and gravity analysis, *Tectonics*, *6*, 603–618, 1987.

Ogniben, L., M. Parotto, and A. Praturion, ed., *Structural Model of Italy,* no. 90, 502 pp., Consiglio Nazionale Delle Ricerche, Rome, 1975.

Ori, G. G., M. Roveri, and F. Vannoni, Plio–Pleistocene sedimentation in the Apenninic–Adriatic foredeep (Central Adriatic Sea, Italy), *Spec. Publs Int. Ass. Sediment.*, *8*, 183–198, 1986.

Paraschiv, D., Oil and gas in Romania: Institutul de Geologie si Geofizica, Studii Tehnice si Economice, Series A, Bucharest, 382 p., 1979.

Parsons, B. and P. Molnar, The origin of outer topographic rises associated with trenches, *Geophys. J. R. astr. Soc.*, *45*, 707–712, 1976.

Pieri, M. and G. Groppi, Subsurface geological structure of the Po plain, Italy, *Final Geodynamic Project Publ. 414*, Italy, 1981.

Ritsema, A.R., Active or passive subduction at the Calabrian Arc, *Geologie en Mijnbouw*, 58, 127–134, 1979.

Royden, L., Flexural behavior of the continental lithosphere in Italy: Constraints imposed by gravity and deflection data, *J. Geophys. Res.*, *93*, 7747–7766, 1988.

Royden L., and G.D. Karner, Flexure of lithosphere beneath Apennine and Carpathian foredeep basins: Evidence for an insufficient topographic load, *Am. Ass. Pet. Geol. Bull.*, *68*, 704–712, 1984.

Royden, L., E. Patacca and P. Scandone, Segmentation and configuration of subducted lithosphere in Italy: An important control on thrust belt and foredeep basin evolution, *Geology*, *15*, 714–717, 1987.

Ruggieri, G., D. Rio, and R. Sprovieri, Remarks on the chronostratigraphic classification of lower Pleistocene, *Boll. Soc. Geol. Ital.*, *103*, 251–259, 1984.

Scandone, P., Origin of the Tyrrhenian Sea and Calabrian Arc, *Boll. Soc. Geol. Ital.*, *98*, 27–34, 1979.

Sclater, J.G., and P.A.F. Christie, Continental stretching: An explanation of the post–mid–Cretaceous subsidence of the central North Sea basin, *J. Geophys. Res.*, *85*, 3711–3739, 1980.

Sheffels, B. and M. McNutt, Role of subsurface loads and regional compensation in the isostatic balance of the Transverse Ranges, California: evidence for intracontinental subduction, *J. Geophys. Res.*, *91*, 6419–6431, 1986.

Spakman, W., Subduction beneath Eurasia in connection with the Mesozoic Tethys, *Geologie en Mijnbouw*, *65*, 145–153, 1986.

Spakman, W., The upper mantle structure in the central European–Mediterranean region, in press, EST Central Segment, ESF special publication, 1988.

Spence, W., Slab pull and the seismotectonics of subducting lithosphere, *Rev. Geophys. Space Phys.*, *25*, 55–69, 1987.

Talwani, M., J.L. Worzel and M. Landisman, Rapid gravity computations for two–dimensional bodies with application to the Mendocino submarine fracture zone, *J. Geophys. Res.*, *64*, 49–59, 1959.

Watts, A.B. and M. Talwani, Gravity anomalies seaward of deep–sea trenches and their tectonic implications, *Geophys. J. R. astron. Soc.*, *36*, 57–90, 1974.

FIGURE CAPTIONS

Figure 1. Generalized map of the Apennine (AP), Dinaride (DI), and Southern Alp (SA) thrust belts. Barbed lines indicate thrust faults; ticked lines show Pliocene–Quaternary normal faulting; dashed line marks coastline. T's mark endpoints of profiles B–B' through E–E'. Modified after Royden [1988].

Figure 2. (a) Topography and bathymetry of the Adriatic region. Thick lines show the location of profiles B–B' through E–E'. Interval between solid contours is 1000 meters. Dashed line marks 500 meter contour. (b) Bouguer gravity anomaly map of the Adriatic region. Contour interval = 40 mgal.

Figure 3. Schematic of backstripping technique used to reconstruct past basin geometries. (a) Thick line indicates a layer of age t_2 that coincides with the base of the basin. Thinner line marks depth to a younger horizon of age t_1. (b) The basin geometry at past time t_1 can be reconstructed by restoring the layer of age t_1 to its starting depth. The base layer (age t_2 is shifted up by an equal amount and decompacted. (c) Thick line indicates the base layer restored to its starting depth at time t_2. The net basement deflection between times t_2 and t_1 and between time t_2 and present can be found by taking the differences between the depths of the base layer at these times.

Figure 4. (a) Depth data on Profile B–B'. Location shown on Figures 1 and 2. AP and DI labels mark the Apennine and Dinaride foredeep basins. Open symbols indicate depths to layers within the basin fill. Solid triangle indicates onshore outcrop of marine base Quaternary rocks. Data and sources are listed in Table 1. Uppermost line shows, from southwest to northeast, topography of eastern Italy, bathymetry of Adriatic Sea, topography of western Yugoslavia. Large inverted triangles mark the Italian and Yugoslavian coastlines. Distances are given from the west coast of Italy. (b) Reconstructed depths to the base of the Dinaride foredeep basin at beginning Pliocene time (~ 5 m.y. ago), assuming base Pliocene sediments were deposited at 1 kilometer depth over the Apennine foredeep region and at sea level over the Dinaride foredeep. See text for discussion of parameters used in computing effects of sediment compaction. Reconstructed depths corresponding to actual basin fill compaction properties should lie somewhere between the X's and open diamonds. (c) Reconstructed depths to the base of the Apennine and Dinaride foredeep basins at middle Pliocene time (~ 3 m.y. ago), assuming middle Pliocene sediments were

deposited at sea level. Reconstruction assumes that no deflections occurred in the Dinaride foredeep between beginning Pliocene and middle Pliocene time and that base Tertiary depths increase linearly between the central Adriatic and Dinaride foredeep. Symbols as described for Figure 4b. (d) Reconstructed depths to the base of the Apennine and Dinaride foredeep basins at beginning Quaternary time, assuming beginning Quaternary sediments were deposited at sea level. Symbols as described for Figure 4b.

Figure 5. (a) Depth data on Profile C–C'. Location shown on Figures 1 and 2; data and sources are listed in Table 2. X's mark depth to base Quaternary sediments extrapolated from 90 kilometers to the southeast. X's were not used in basin reconstructions. The base of Pliocene sediments coincides with the base of the Apennine foredeep. (b) Reconstructed depths to the base of the Apennine foredeep basin at beginning Quaternary time, assuming beginning Quaternary sediments were deposited at sea level. Symbols as described for Figure 4b.

Figure 6. (a) Depth data on Profile D–D' across the Po plain of Italy. Location shown on Figures 1 and 2; data and sources are listed in Table 3. The base of Pliocene sediments coincides with the base of the Apennine foredeep. (b) Reconstructed depths to the base of the Apennine foredeep basin at middle Pliocene time, assuming middle Pliocene sediments were deposited at 400 meters depth. Symbols as described for Figure 4b. (c) Reconstructed depths to the base of the Apennine foredeep basin at beginning Quaternary time, assuming beginning Quaternary sediments were deposited at 200 meters depth. Symbols as described for Figure 4b.

Figure 7. Depths to base Tertiary deposits that coincided with the base of the foredeep basins on profile E–E' through the western Po Plain of Italy. Location shown on Figures 1 and 2. Data at distances $x > 100$ kilometers are based on palinspastic restorations of Cenozoic deposits. See Table 4 for data and sources.

Figure 8. Schematic of the thin elastic plate model for deflection of lithosphere beneath (a) a single foredeep basin or (b) a pair of opposing foredeep basins. The base of the foredeep is deflected from an initial depth w_0. F and M indicate forces and moments transmitted through the ends of the plate that produce plate deflection $w(x)$ that best fits deflection data. Gravity anomalies are negative over regions where lighter crust is depressed downward into denser mantle (areas with vertical shading) and are more

positive over regions of upward deflection (stippled areas). The two flexural highs (stippled areas) shown in (b) may merge into a single flexural high when the separation of the foredeep basins is smaller.

Figure 9. (a) Top. Observed Bouguer gravity anomalies and gravity anomalies predicted by flexural models of present lithospheric deflections along profile B–B'. Crosses show observed Bouguer gravity anomalies (see text for sources). Short dashed line shows gravity anomalies predicted from local (Airy) compensation of topography. Solid and longer dashed lines show gravity anomalies predicted by best–fitting thin elastic plate deflections shown in lower plots. The bars at the top of the figure show the assumed lateral extent of Moho deflections that parallel the elastic plate deflections. Table 5 lists the densities assumed for foredeep basin sediments, crust, and mantle. All gravity models assume the existence of a mass anomaly of magnitude 7 x 10^{11} kg/m distributed uniformly between 100 and 150 km depth between x=–100 km and x=–25 km. Bottom. Crosses mark present depths to base Tertiary (the base of the basins). Solid and dashed lines indicate best–fitting models for elastic plate deflections with effective plate thickness T_e between 2.5 and 20 kilometers. Beginning Tertiary starting water depths w_o corresponding to each model are listed first for $x < 290$ km and then in parentheses for $x > 290$ km. (b) Effect of variation in starting water depth on gravity. Notation and as for (a). (c) Vertical shear force $F(x)$ and bending moment $M(x)$ transmitted through the deflected plate of the best–fitting 10–km thick elastic plate model. Counter–clockwise bending moments are positive; vertical shear forces are plotted as positive when they act to increase the downward curvature of the plate in the foredeep basins. $F(x) = Dd^3w/dx^3$ for x < 250 km; $F(x) = -Dd^3w/dx^3$ for x > 250 km.

Figure 10. (a) Reconstructed basin depths at beginning Pliocene time and best–fitting thin elastic plate models on profile B–B'. Crosses mark reconstructed depths; solid line indicates best–fitting plate deflection assuming no sediment compaction. Open diamonds show reconstructed depths assuming shale compaction parameters; long–dashed line indicates corresponding best–fitting plate deflection. Short dashed line shows the best–fitting present 10–km thick plate deflection. See text for discussion of acceptable models. (b) Best–fitting pairs of values of the beginning Pliocene water depth and the effective elastic plate thickness T_e. X's mark values associated with models assuming no sediment compaction; open diamonds mark values from models assuming shale compaction parameters. The best–fitting T_e value for the present plate

deflection is indicated. Vertical dashed lines mark the upper and lower limits on values of T_e that yield acceptable fits to the data. (c) Vertical force F and bending moment M transmitted through the best–fitting beginning Pliocene and present 10–km thick deflected plates. Sign convention as in Figure 9c. Solid circles show the magnitude of M at the location where F is zero for each model.

Figure 11. (a) Reconstructed basin depths at middle Pliocene time and best–fitting thin elastic plate models on profile B–B', assuming no deflections occurred in the Dinaride foredeep between beginning and middle Pliocene time. Symbols as described in Figure 10a. See text for discussion of acceptable models. (b) Best–fitting pairs of values of the middle Pliocene water depth and the effective elastic plate thickness T_e and limits on acceptable values of T_e. Symbols as described in Figure 10b. For each value of T_e, the more negative set of water depth values are those over the Apennine foredeep, while the less negative set are those over the Dinaride foredeep. See text for discussion of restrictions on water depths. (c) The vertical force F and bending moment M transmitted through the deflected plate for best–fitting 10–km thick elastic plate models for middle Pliocene and present deflections. Sign convention as in Figure 9.

Figure 12. (a) Reconstructed basin depths at beginning Quaternary time and best–fitting thin elastic plate models on profile B–B'. Symbols as described in Figure 10a. See text for discussion of acceptable models. (b) Best–fitting pairs of values of the beginning Quaternary water depth and the effective elastic plate thickness T_e, and limits on acceptable values of T_e. Symbols as described in Figure 10b. For each value of T_e the more negative set of water depth values are those over the Apennine foredeep while the less negative set are those over the Dinaride foredeep. See text for discussion of restrictions on water depths. (c) The vertical force F and bending moment M transmitted through the deflected plate for best–fitting 10–km thick elastic plate models for middle Pliocene and present deflections. Sign convention as in Figure 9. Solid circles indicate the value of M where the force F is zero.

Figure 13. Present depths to base Pliocene (base of foredeep basin), observed Bouguer gravity anomalies, and deflections and Bouguer gravity anomalies predicted by thin elastic plate models along Profile C–C', modified from Royden [1988]. Bouguer gravity anomalies are sensitive to the base Pliocene starting water depth w_o. See Royden [1988] for a full description of the sensitivity of the combined data to the effective elastic plate thickness T_e.

Figure 14. (a) Reconstructed basin depths at beginning Quaternary time and best–fitting thin elastic plate models on profile C–C'. Symbols as described in Figure 10a. See text for discussion of acceptable models. (b) Best–fitting pairs of values of beginning Quaternary water depth and the effective elastic plate thickness T_e, and limits on acceptable values of T_e. Symbols as described in Figure 10b. (c) The vertical force F and bending moment M transmitted through the deflected plate for best–fitting 20–km thick beginning Quaternary and present elastic plate models. Sign convention as in Figure 9. Solid circles indicate the value of M where the force F is zero.

Figure 15. Present depths to base Pliocene (base of foredeep basin), observed Bouguer gravity anomalies, and deflections and Bouguer gravity anomalies predicted by thin elastic plate models along Profile D–D', modified from Royden [1988]. See Royden [1988] for a full description of the sensitivity of the combined data to the effective elastic plate thickness T_e.

Figure 16. (a) Reconstructed basin depths at middle Pliocene time and best–fitting thin elastic plate models on profile D–D'. Symbols as described in Figure 10a. See text for discussion of acceptable models. (b) Best–fitting pairs of values of middle Pliocene water depth and the effective elastic plate thickness T_e, and limits on acceptable values of T_e. Symbols as described in Figure 10b. (c) The vertical force F and bending moment M transmitted through the deflected plate for best–fitting 20–km thick middle Pliocene and present elastic plate models. Sign convention as in Figure 9. Solid circles indicate the value of M where the force F is zero.

Figure 17. (a) Reconstructed basin depths at beginning Quaternary time and best–fitting thin elastic plate models on profile D–D'. Symbols as described in Figure 10a. See text for discussion of acceptable models. (b) Best–fitting pairs of values of beginning Quaternary water depth and the effective elastic plate thickness T_e, and limits on acceptable values of T_e. Symbols as described in Figure 10b. (c) The vertical force F and bending moment M transmitted through the deflected plate for best–fitting 20–km thick beginning Quaternary and present elastic plate models. Sign convention as in Figure 9. Solid circles indicate the value of M where the force F_t is zero.

Figure 18. (a) Top. Observed Bouguer gravity anomalies and gravity anomalies predicted by flexural models of present deflections along profile E–E'. Crosses show observed

Bouguer gravity anomalies (see text for sources). Short dashed line shows gravity anomalies predicted from local (Airy) compensation of topography. Solid and long dashed lines show gravity predicted by flexural models with T_e = 2.5 and 150 km. The bars below the gravity data shows the assumed lateral extent of Moho deflections that parallel the elastic plate deflections. Table 5 lists the densities assumed for foredeep basin sediments, crust, and mantle. Bottom. X's show present and palinspastically restored depths to base Tertiary (the base of the basins). Solid and dashed lines show best–fitting thin elastic plate models. (b) Top. Observed Bouguer gravity anomalies and gravity anomalies predicted by best–fitting flexural models as for (a), for varying values of base Tertiary starting water depth w_o. Bottom. Symbols as for (a). The models predict indistinguishable deflection profiles. (c) Observed Bouguer gravity anomalies, deflection data, and gravity anomalies and plate deflections predicted by best–fitting flexural models as for 18a. Model (a) corresponds to fit to data at x < 100 km only. Model (b) corresponds to fit to all deflection data. T_e = 20 km for both models.

Figure 19. (a) Effect of assumption of foredeep sediment densities on best–fitting starting depths. Top. Observed Bouguer gravity anomalies (crosses) and gravity anomalies predicted by models of present deflections along profile B–B' (solid and dashed lines). T_e = 10 km for all models. Models (1), (2), and (3) assume foredeep sediment densities are 2500 kg/m^3, 2200-2500 kg/m^3, and 2300 kg/m^3, and yield best–fitting values of w_o of -1.0 (0.0) km, -1.25 (-0.25) km, and -1.5 (-0.5) km, respectively. Values for w_o given in parentheses are those over the Dinaride foredeep basin. Densities assumed in model (2) are equal to those assumed in the modeling above and are listed in Table 5. Bottom. Present foredeep basin depth data (X's) and best–fitting thin elastic plate deflections (solid and dashed lines) of models (1), (2), and (3). (b) Effect of assumption of the density contrast at the crust–mantle boundary on best–fitting starting depths. Top. Observed and predicted Bouguer gravity anomalies. Models (4), (5), and (6) assume crust–mantle density contrasts of 800 kg/m^3, 600 kg/m^3, and 400 kg/m^3, and yield best–fitting values of w_o of -1.5 (-0.5) km, -1.25 (-0.25) km, and -1.10 (-0.10) km, respectively. Bottom. Present foredeep basin depth data (X's) and best–fitting thin elastic plate deflections (solid and dashed lines) of models (4), (5), and (6). (c) Effect of the assumption of beginning Pliocene starting water depth w_o on best–fitting T_e = 40 km models on Profile C-C' for reconstructed depths at beginning Quaternary time. w_o = -1000 meters is Royden's [1988] best–fitting value. w_o = -1500 meters is a conservative lower bound derived by subtracting

an uncertainty of 300 meters from Royden's lower bound of w_o = -1200 meters. (d) Effect of the assumption of beginning Pliocene starting water depth w_o on best–fitting T_e = 50 km models on Profile D-D' for reconstructed depths at beginning Quaternary time. w_o = -1000 meters is Royden's [1988] best–fitting value. w_o = -1800 meters is a conservative lower bound derived by subtracting an uncertainty of 300 meters from Royden's lower bound of w_o = -1500 meters.

Figure 20. Schematic yield stress envelope. Thick lines maximum deviatoric stresses that can be maintained in the lithosphere assuming brittle and ductile rheologies. Thin lines indicate stresses induced by bending of the lithosphere. Single hatched area shows stresses maintained in lithosphere with low curvature (a) and high curvature (b). Double hatched area shows increase in bending stresses associated with an increase in curvature. The magnitude of the increase in curvature is the same in both (a) and (b). The increase in curvature produces a greater increase in bending stresses in the lithosphere with lower total curvature. (c) Thick lines show equivalent elastic plate thickness T_e as a function of curvature, derived from equating bending moment sustained in elastic plate with that sustained assuming stress envelope shown in inset. Crosses mark maximum curvatures observed in Apennine foredeep basin and best–fitting T_e values for Profiles B-B', C-C', and D-D'. Dashed lines mark range of acceptable T_e values. There is no upper limit on acceptable T_e values for Profile B–B'.

Figure 21. Effect of topographic loads. (a) Top. Dashed line shows best–fitting plate deflection if topographic elevations over eastern Italy were one kilometer greater at middle Pliocene time than at present. Thick line shows best–fitting deflection assuming middle Pliocene topography equaled present topography. Deflection profiles overlap at distances x > 275 km. X's mark reconstructed middle Pliocene depths. Bottom. Thick lines and thin dashed lines show forces and moments transmitted through plate at middle Pliocene time assuming present and present+1 km topography, respectively. The middle Pliocene basin shape can be explained by the deflection of a plate with a 'free' end (F and M at end set to zero) beneath present+1 km topography. (b) As for (a), for beginning Quaternary time. Best–fitting plate deflections for models with present topography and present+2 km topography are indistinguishable. Even with excess topographic load at beginning Quaternary time plate deflections cannot be produced without significant transmitted bending moment M_t.

Figure 22. Effect of random uncertainties in beginning Quaternary depth data on inferred Quaternary unflexing. (a) Profile B–B'. Top. Dashed lines show the envelope that enclose 90% of values of beginning Quaternary plate deflections fit to basin reconstructions based on Gaussian errors (σ = 500 meters) added to base Quaternary depth data. Solid line shows present best–fitting plate deflection. Bottom. Thick lines show best–fitting present transmitted forces and moments. Thin lines show envelopes that enclose 90% of values derived from adding Gaussian errors to base Quaternary depth data. (b) as for (a) on Profile C–C'. These envelopes of profiles were computed using a Monte Carlo method. We add an error $\Delta d_i(x_i)$to each depth or reconstructed depth value $d_i(x_i)$ and compute the corresponding best–fitting flexural profile. This sequence is repeated 1000 times to form a Gaussian distribution of the errors $\Delta d_i(x_i)$. The envelopes that enclose 90% of the values of plate deflection and transmitted forces and moments at each position x are plotted.

Figure 23. Contours of depth to base Pliocene (dashed lines) and base Quaternary (solid lines) in the Apennine foredeep basin segments crossed by profiles C–C' and B–B'. An approximately 100–km right lateral offset occurs in both base Pliocene and base Quaternary contours in the central part of the figure. Barbed lines mark the outer edge of the Apennine thrust front.

Figure 24. Mechanisms for unflexing. Forces and moments transmitted through elastic plate at distance x = 160 on Profile B-B' and x = 150 on Profile C-C' and effective elastic plate thicknesses are assumed equal at beginning Quaternary and present time. Crosses mark reconstructed beginning Quaternary depth data. Solid lines indicate best–fitting present plate deflections. (a) Dashed line shows best–fitting beginning Quaternary deflection assuming 2 kilometer additional elevations in eastern Italy on Profile B-B'. (b) Similarly on Profile C-C'. Long dashed and short dashed lines correspond to topographic loads indicated at beginning Quaternary time and fail to fit deflection data. (c) Dashed line shows best–fitting beginning Quaternary deflection along profile B-B' assuming 10^8 Pa horizontal stress across plate. (d) Similarly on Profile C-C' with 10^8 Pa and 4 x 10^8 Pa stress across plate. (e) Solid line shows best–fitting beginning Quaternary deflection on Profile B-B'. Dashed line shows deflection that occurs if plate weakens (T_e is reduced) over region of highest curvature in internal part of foredeep. Short dashes show region of weakening. Crosses mark bounds of weakened region. Weakening of the plate does not cause shallowing near Italian coast. (f) Similarly on profile C-C'.

TABLE 1.

DEFLECTION DATA FOR PROFILE B–B'

x (km)[a]	Base Tertiary (km)[b]	x (km)[a]	Base Pliocene (km)[b]	x (km)[a]	Middle Pliocene (km)[b]	x (km)[a]	Base Quaternary (km)[b]
195	5.9	195	5.5	195	3.7	195	0.50
197	5.9	197	5.5	215	1.6	205	0.75
200	5.4	200	5.0	226	2.1	216	1.00
204	4.9	204	4.5	241	1.0	228	1.00
208	4.4	208	4.0	268	1.2	262	0.75
211	3.5	216	2.5	275	1.4	282	0.75
215	3.0	223	3.0			300	0.50
223	2.7	225	2.4			310	0.50
227	2.5	228	2.0			324	0.50
307	2.3	232	2.0				
309	2.6	237	1.5				
311	2.9	239	1.5				
313	3.1	240	1.3				
315	3.3	243	1.0				
317	3.4	248	1.0				
319	3.6	250	1.0				
321	4.1	256	1.0				
323	5.2	266	1.3				
325	6.0	280	1.5				
327	6.3	295	0.95				
		297	0.80				
		299	0.75				
		301	0.80				
		303	0.85				
		305	0.75				
		307	0.75				
		309	0.80				
		311	0.70				
		313	0.75				
		315	0.65				
		317	0.65				
		319	0.60				
		321	0.55				
		323	0.50				
		325	0.50				
		327	0.50				
		329	0.45				
		331	0.45				
		333	0.45				

[a] Measured from x=0 on the west coast of Italy.

[b] Data from Patacca and Scandone (unpublished map, 1987), scale 1:500,000; Scandone et al. [1987]; open file well reports and open file seismic lines

TABLE 2.

DEFLECTION DATA FOR PROFILE C–C'

x (km)[a]	Base Pliocene (km)[b]	x (km)[a]	Base Quaternary (km)[b]
232	4.5	220	1.90
237	4.0	225	1.90
244	3.5	230	1.75
250	3.0	235	1.75
261	2.5	240	1.80
268	2.0	245	1.80
280	1.5	250	1.70
		255	1.60
		260	1.50
		265	1.40
		248	1.50 [c]
		262	1.50 [c]
		273	1.25 [c]
		282	1.00 [c]
		295	0.75 [c]
		310	0.50 [c]

[a] Measured from x=0 on the west coast of Italy.

[b] Data from Patacca and Scandone (unpublished map, 1987), scale 1:500,000; Scandone et al. [1987]; open file well reports and open file seismic lines

[c] Data extrapolated from 90 km to the southeast.

TABLE 3.

DEFLECTION DATA FOR PROFILE D–D'

x (km)[a]	Base Pliocene (km)[b]	x (km)[a]	Middle Pliocene (km)[b]	x (km)[a]	Base Quaternary (km)[b]
135	5.0	138	2.8	133	1.6
138	4.5	144	2.6	136	1.5
145	4.0	148	2.4	142	1.4
149	3.5	150	2.2	153	1.2
155	3.0	152	2.0	158	1.0
160	2.5	154	1.8	163	0.9
168	2.0	157	1.6	167	0.8
177	1.5	160	1.4	170	0.7
183	1.0	166	1.2	177	0.6
192	0.5	168	1.0		
227	0.5	173	0.8		
260	0.5	175	0.7		

[a] Measured from x=0 on the west coast of Italy.

[b] Data from Pieri and Groppi [1981]; open file well reports and open file seismic lines.

TABLE 4.

DEFLECTION DATA FOR PROFILE E–E'

x (km)[a]	Base Tertiary (km)
80	8.50[b]
82	7.25[b]
84	6.00[b]
88	5.75[b]
93	5.50[b]
117	5.50[c]
120	6.20[c]
122	6.70[c]
125	6.90[c]
128	7.20[c]
131	7.20[c]
133	7.50[c]
136	8.20[c]
139	8.80[c]
142	9.20[c]

[a] Measured from x=0 on the west coast of Italy.

[b] Data from Pieri and Groppi [1981]

[c] Palinspastically restored depths to base Tertiary from Laubscher, 1985; Roeder ?? open file well reports and open file seismic lines.

TABLE 5.

SYMBOL	DEFINITION	VALUE
D	flexural rigidity	$ET_e^3/12(1-\nu^2)$
T_e	effective elastic plate thickness	
α	flexural wavelength	$[D/4(\rho_m-\rho_i)g]^{1/4}$
E	Young's modulus	$8.1 \cdot 10^{10}$ Pa
ν	Poisson's ratio	0.25
ρ_i	density of infilling material over plate	2600 kg/m^3
ρ_m	mantle density	3200 kg/m^3
ρ_s	sediment density	
	assumed to have water density above seafloor	1000 kg/m^3
	at depths 0–1 km beneath seafloor	2200 kg/m^3
	1–2 km	2300 kg/m^3
	2–3 km	2400 kg/m^3
	> 3 km	2500 kg/m^3
ρ_t	density of topography	2600 kg/m^3
$s(x)$	observed depth to base of sediments	
$T(x)$	topographic load	$\rho_t \cdot g \cdot$elevation
h	initial crustal thickness	35 km
g	gravitational acceleration	9.8 m/s^2
$w(x)$	final depth of effective elastic plate	
$w_{in}(x)$	initial depth of effective elastic plate	
w_o	initial plate depth if assumed uniform	
x	lateral position	
x_1, x_2	effective elastic plate ends	

TABLE 6.

BEST–FITTING ELASTIC PLATE THICKNESS (KM)

TIME	PROFILE B–B'	C–C'	D–D'	E–E'
present[a]	>5 (10)	20–40[b] (20)[b]	15–30[b] (20)[b]	>2.5
beg. Quaternary	5–20	10–30	10–40	
middle Pliocene	5–20		10–80	
beg. Pliocene	5–15			

[a] Numbers in parentheses are subjectively determined best fit to gravity and deflection data.
[b] From Royden [1988].

TABLE 7.

BEST–FITTING DEPOSITIONAL WATER DEPTH (METERS)[a]

TIME	PROFILE B–B' x<290 km[b]	B–B' x>290 km	C–C'	D–D'	E–E'
beg. Quaternary	350–0[c]	0[d]	500–0[e]	700–0[e]	
middle Pliocene	500–0[c]	0[d]		700–0[e]	
beg. Pliocene		250–0[d]	1200–800[f] (1000)[f]	1500–500[f] (1000)[f]	
beg. Tertiary	1500–1250 (1250)	250–0 (250)			2500–1500

[a] Numbers in parentheses are subjectively determined best fit to gravity and deflection data. Depths are positive below sea level.

[b] x = distance along profile from west coast of Italy.

[c] Assumes beginning Tertiary water depth = 1250 meters for $x < 290$ km.

[d] Assumes beginning Tertiary water depth = 250 meters for $x > 290$ km.

[e] Assumes beginning Pliocene water depth = 1000 meters.

[f] From Royden [1988].

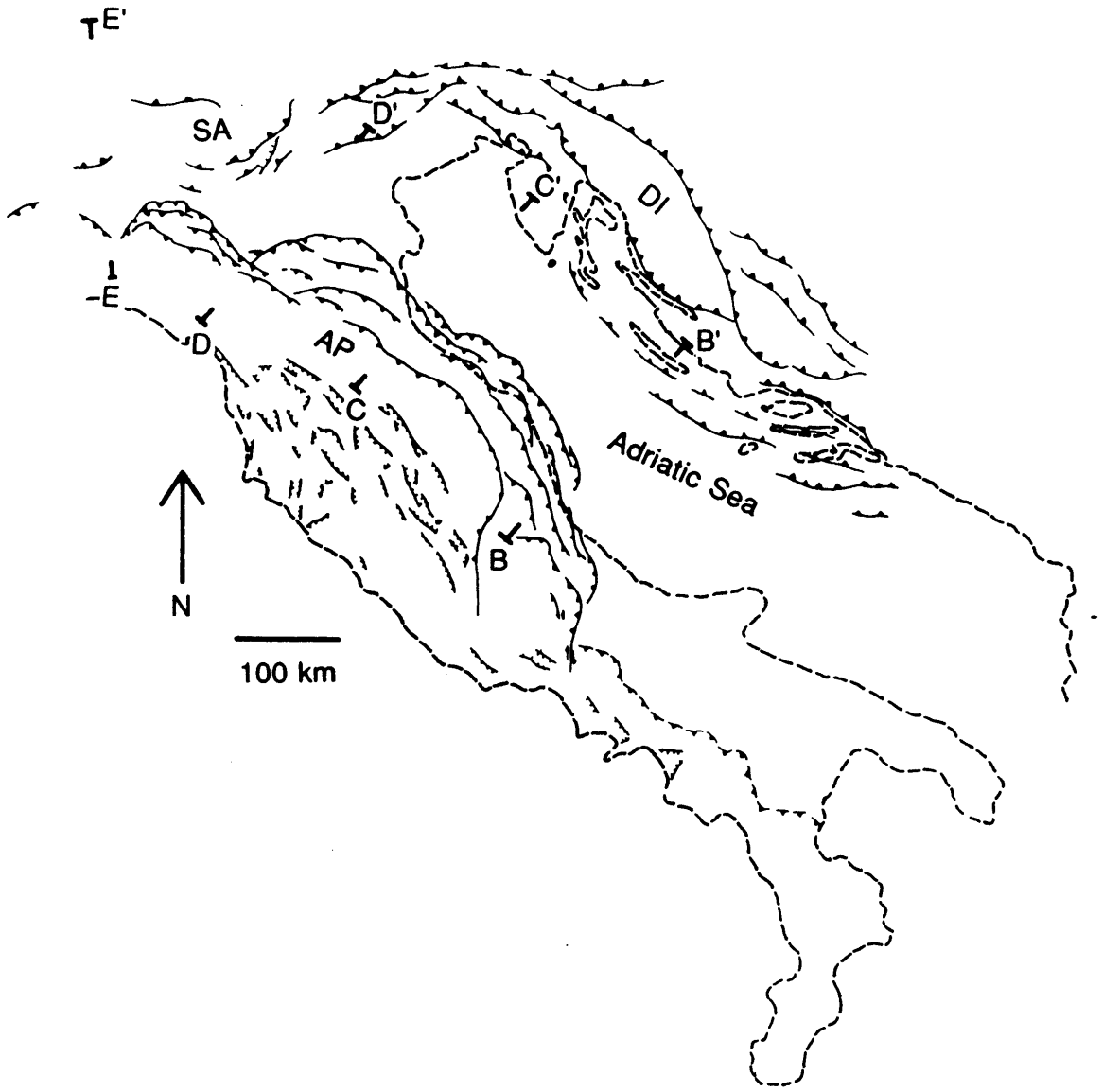

Figure 1

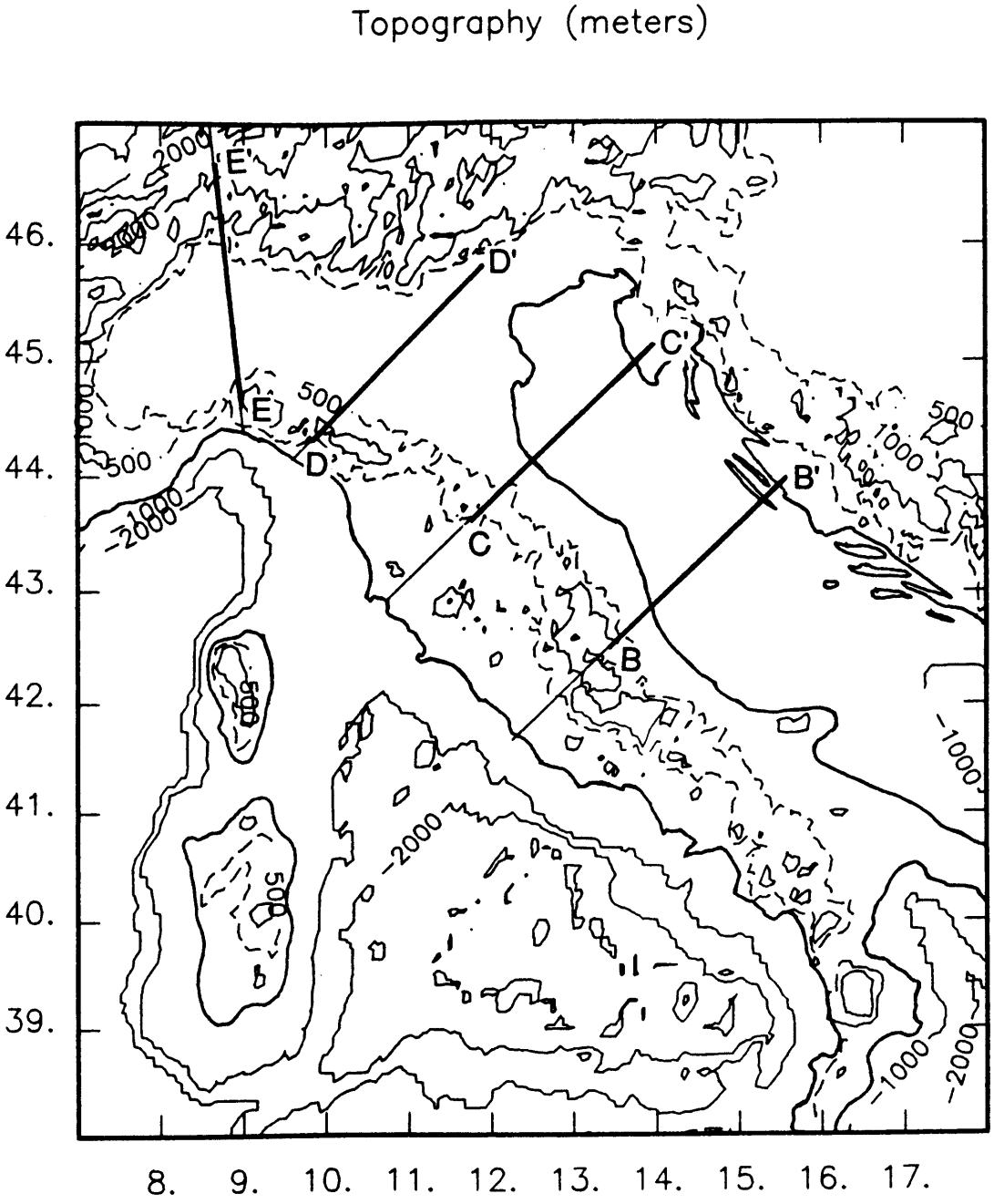
Topography (meters)
E'
D'
C'
B'
E
D
C
B
2000
500
1000
-2000
-1000
46.
45.
44.
43.
42.
41.
40.
39.
8.
9.
10.
11.
12.
13.
14.
15.
16.
17.

Figure 2(a)

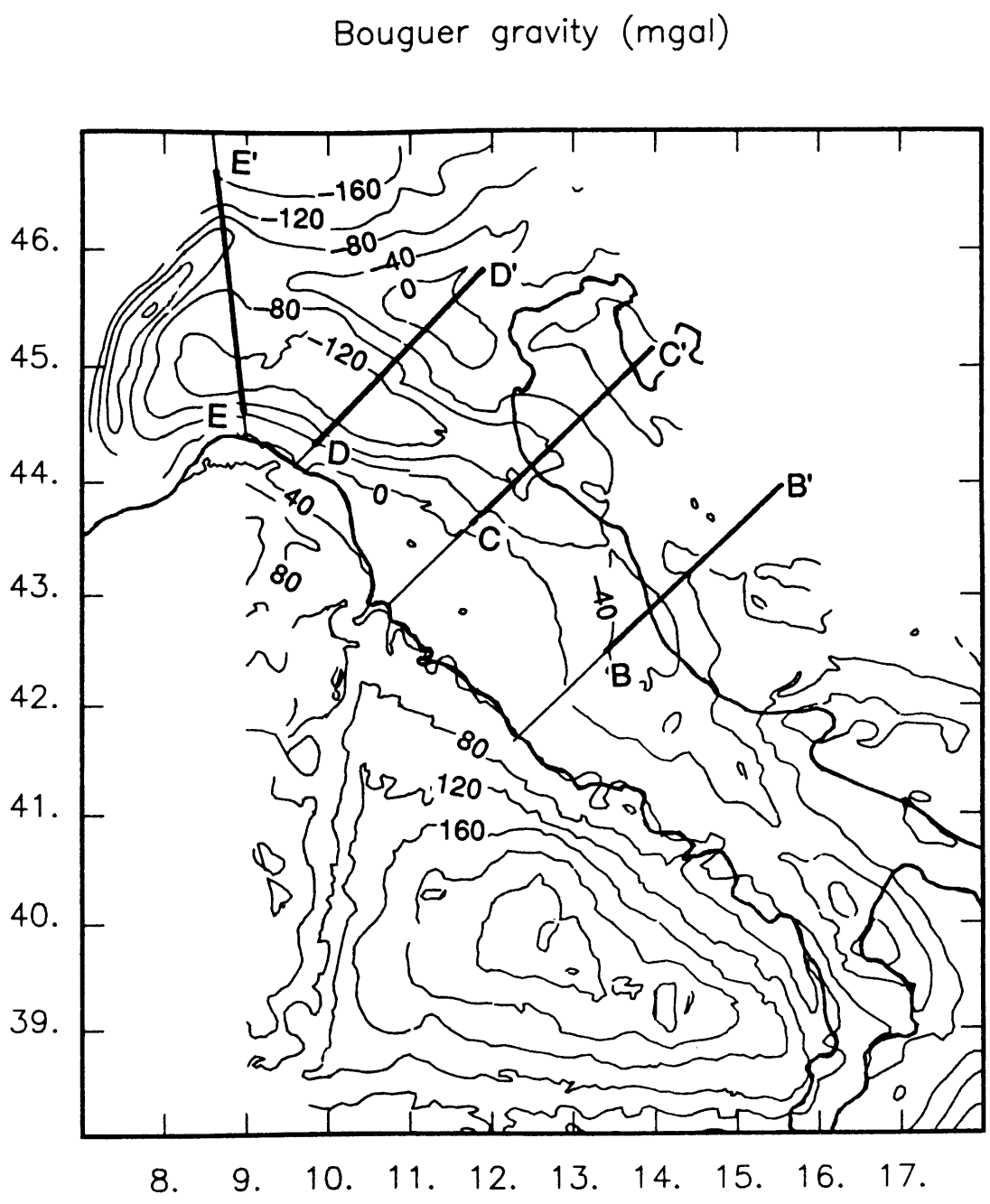
Bouguer gravity (mgal)
E'
-160
-120
-80
-40
0
D'
-80
-120
C'
E
D
0
-40
B'
C
-80
-40
B
-80
-120
-160
46.
45.
44.
43.
42.
41.
40.
39.
8.
9.
10.
11.
12.
13.
14.
15.
16.
17.

Figure 2(b)

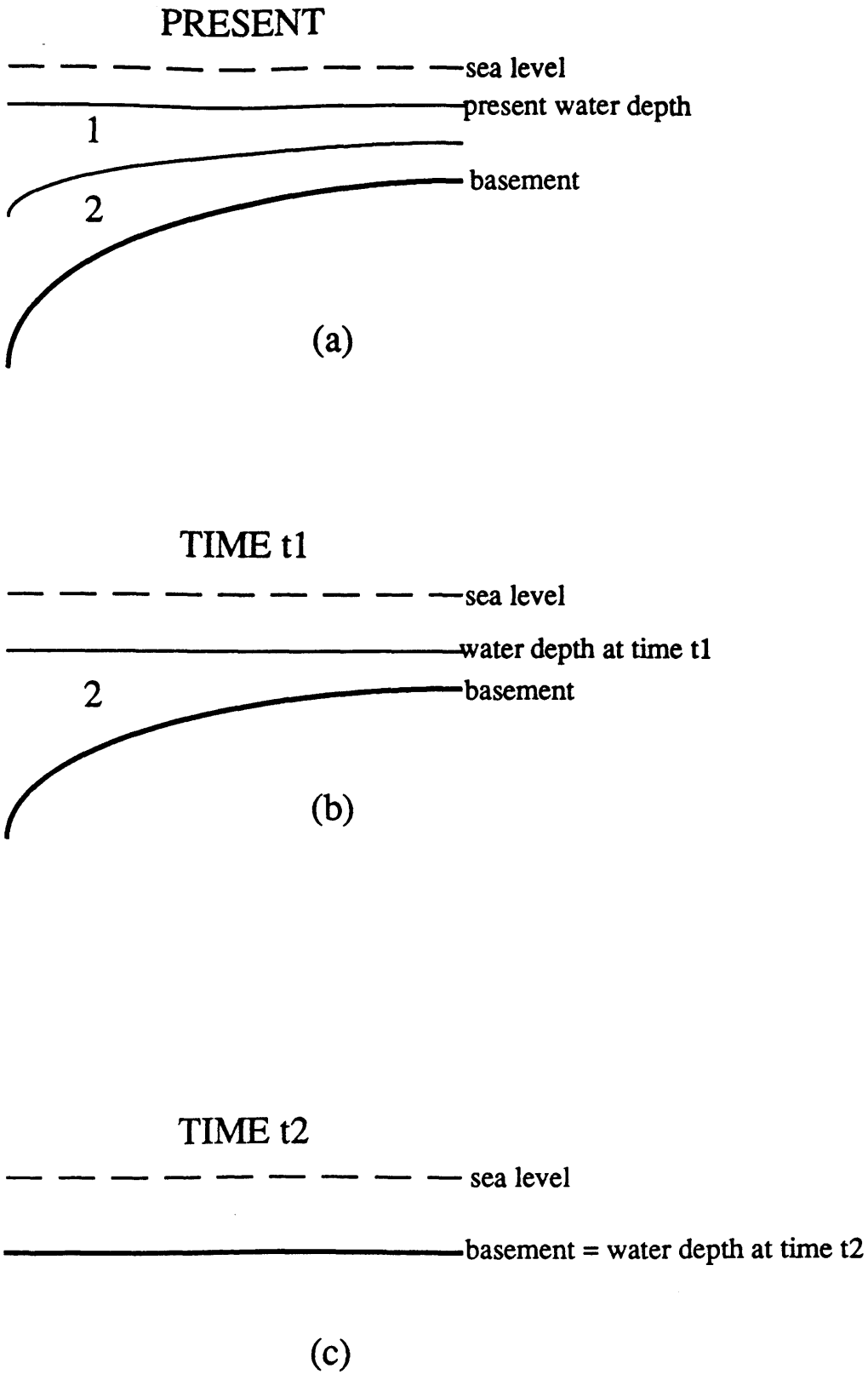
PRESENT
sea level
present water depth
1
basement
2
(a)
TIME t1
sea level
water depth at time t1
2
basement
(b)
TIME t2
sea level
basement = water depth at time t2
(c)

Figure 3

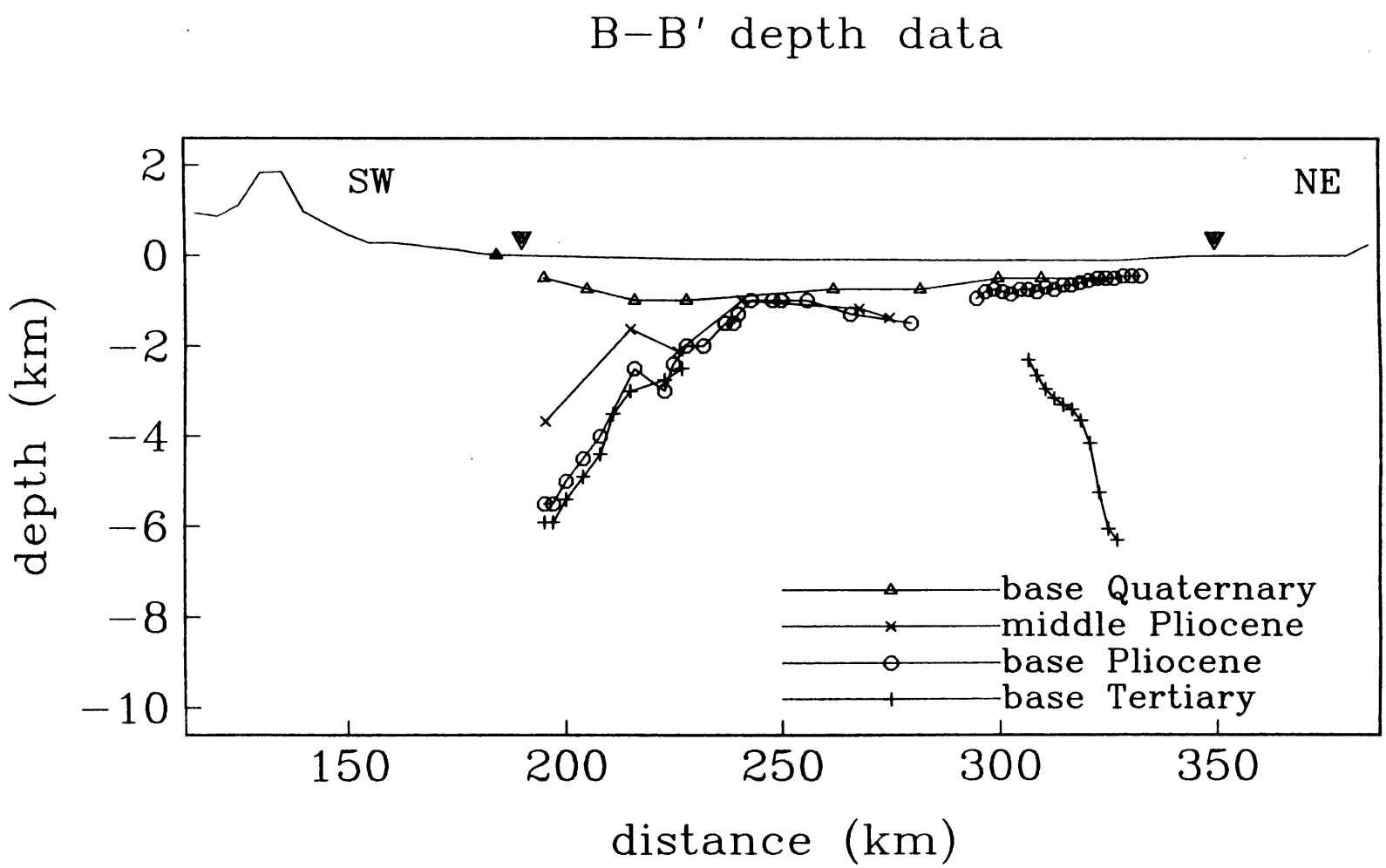
B–B′ depth data
SW
NE
depth (km)
2
0
−2
−4
−6
−8
−10
150
200
250
300
350
distance (km)
base Quaternary
middle Pliocene
base Pliocene
base Tertiary

Figure 4(a)

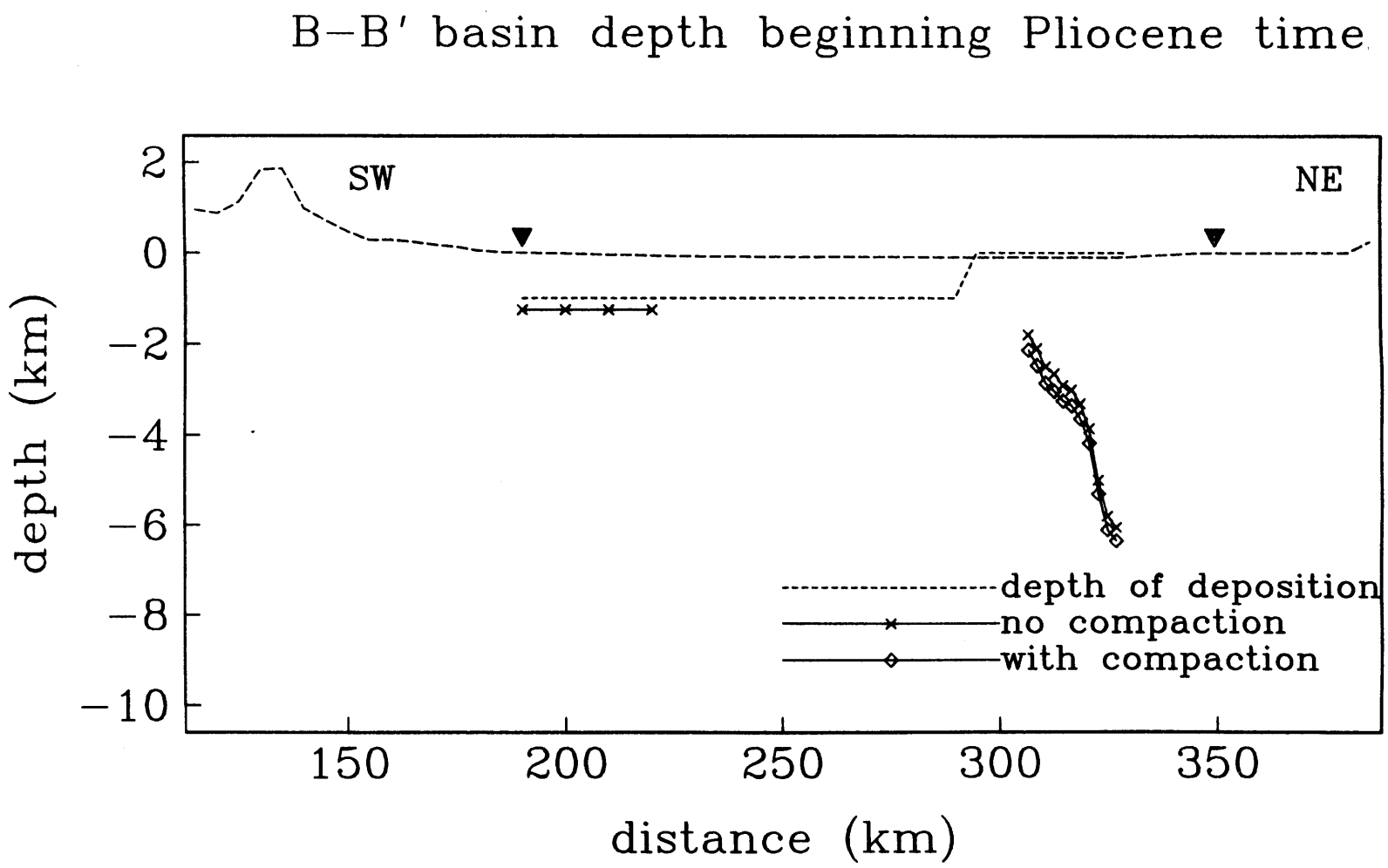
B–B′ basin depth beginning Pliocene time
SW
NE
depth (km)
2
0
−2
−4
−6
−8
−10
150
200
250
300
350
distance (km)
depth of deposition
no compaction
with compaction

Figure 4(b)

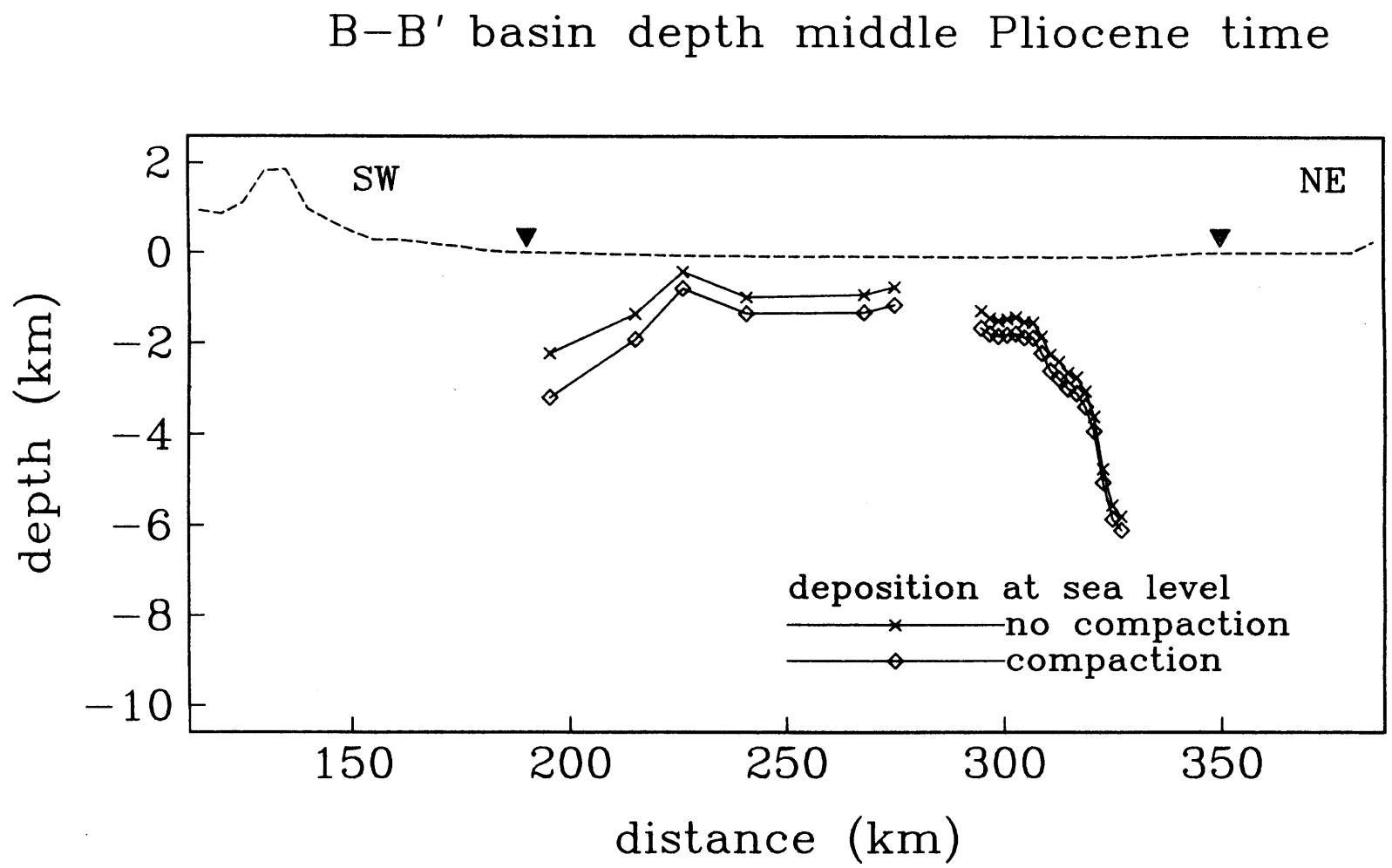
B–B′ basin depth middle Pliocene time
SW
NE
depth (km)
2
0
−2
−4
−6
−8
−10
150
200
250
300
350
distance (km)
deposition at sea level
no compaction
compaction

Figure 4(c)

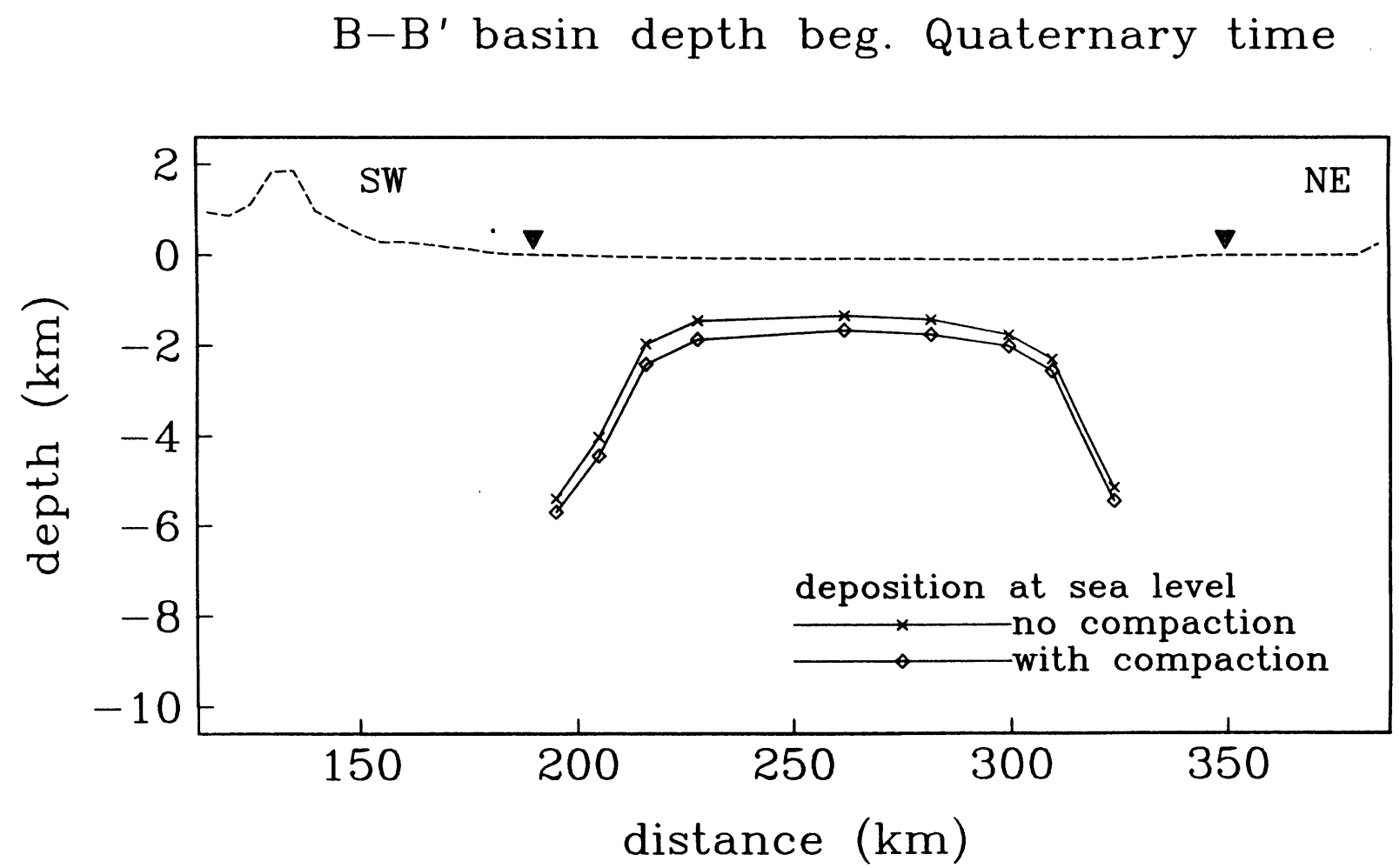
B–B′ basin depth beg. Quaternary time
SW
NE
depth (km)
2
0
−2
−4
−6
−8
−10
150
200
250
300
350
distance (km)
deposition at sea level
no compaction
with compaction

Figure 4(d)

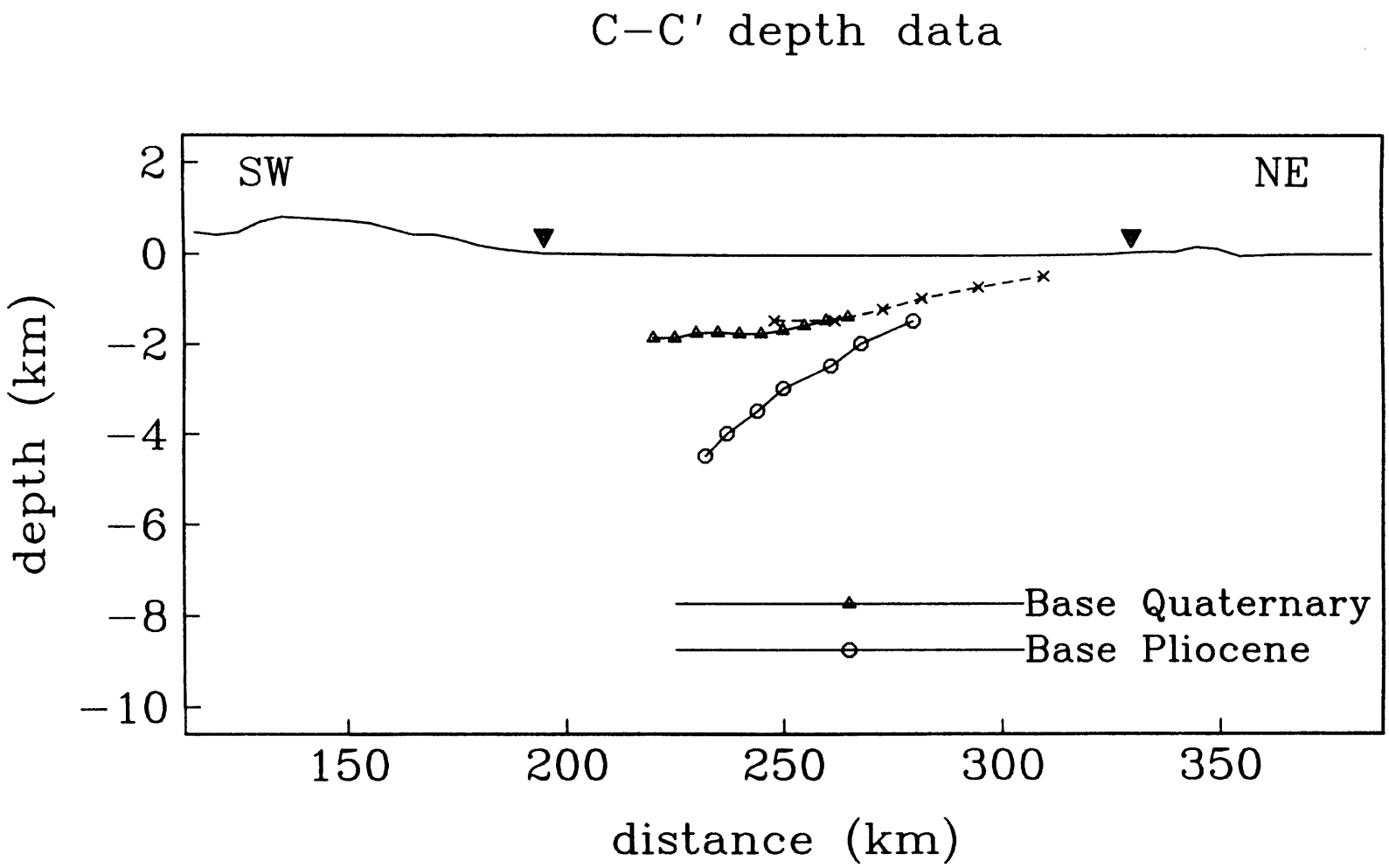
C–C′ depth data
SW
NE
2
0
−2
−4
−6
−8
−10
depth (km)
150
200
250
300
350
distance (km)
Base Quaternary
Base Pliocene

Figure 5(a)

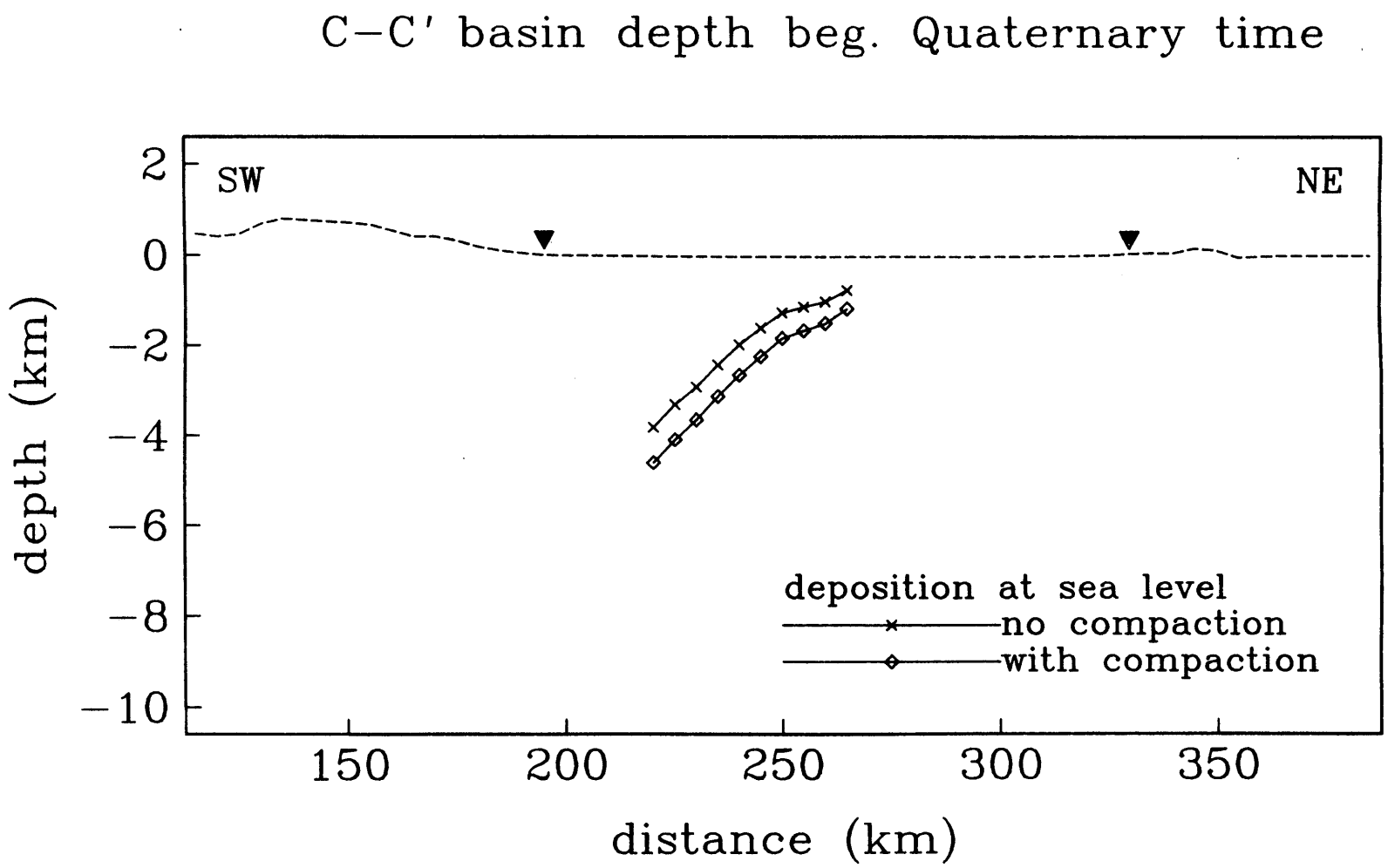
C–C′ basin depth beg. Quaternary time
SW
NE
2
0
−2
−4
−6
−8
−10
depth (km)
150
200
250
300
350
distance (km)
deposition at sea level
no compaction
with compaction

Figure 5(b)

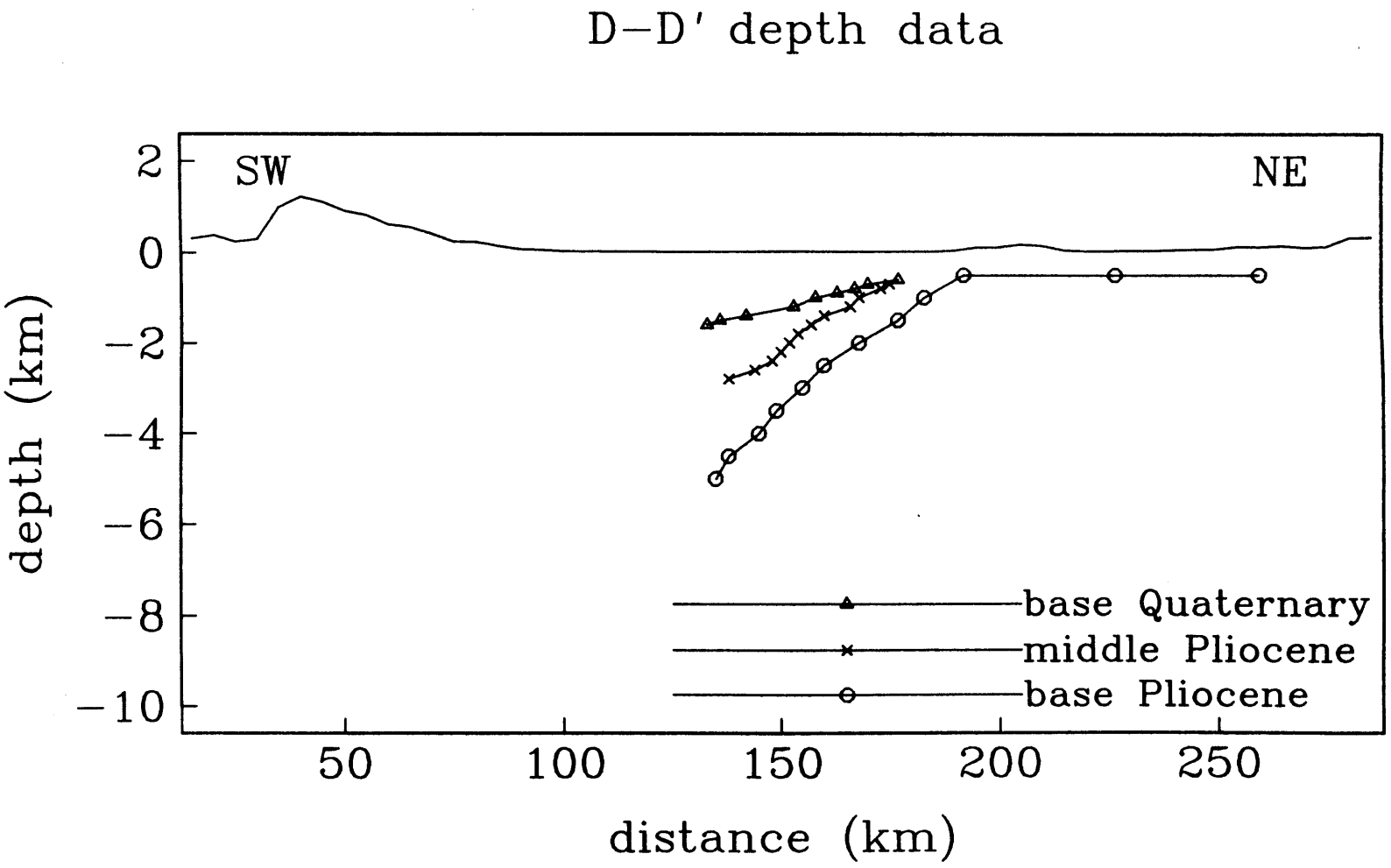
D–D′ depth data
SW
NE
2
0
−2
−4
−6
−8
−10
depth (km)
50
100
150
200
250
distance (km)
base Quaternary
middle Pliocene
base Pliocene

Figure 6(a)

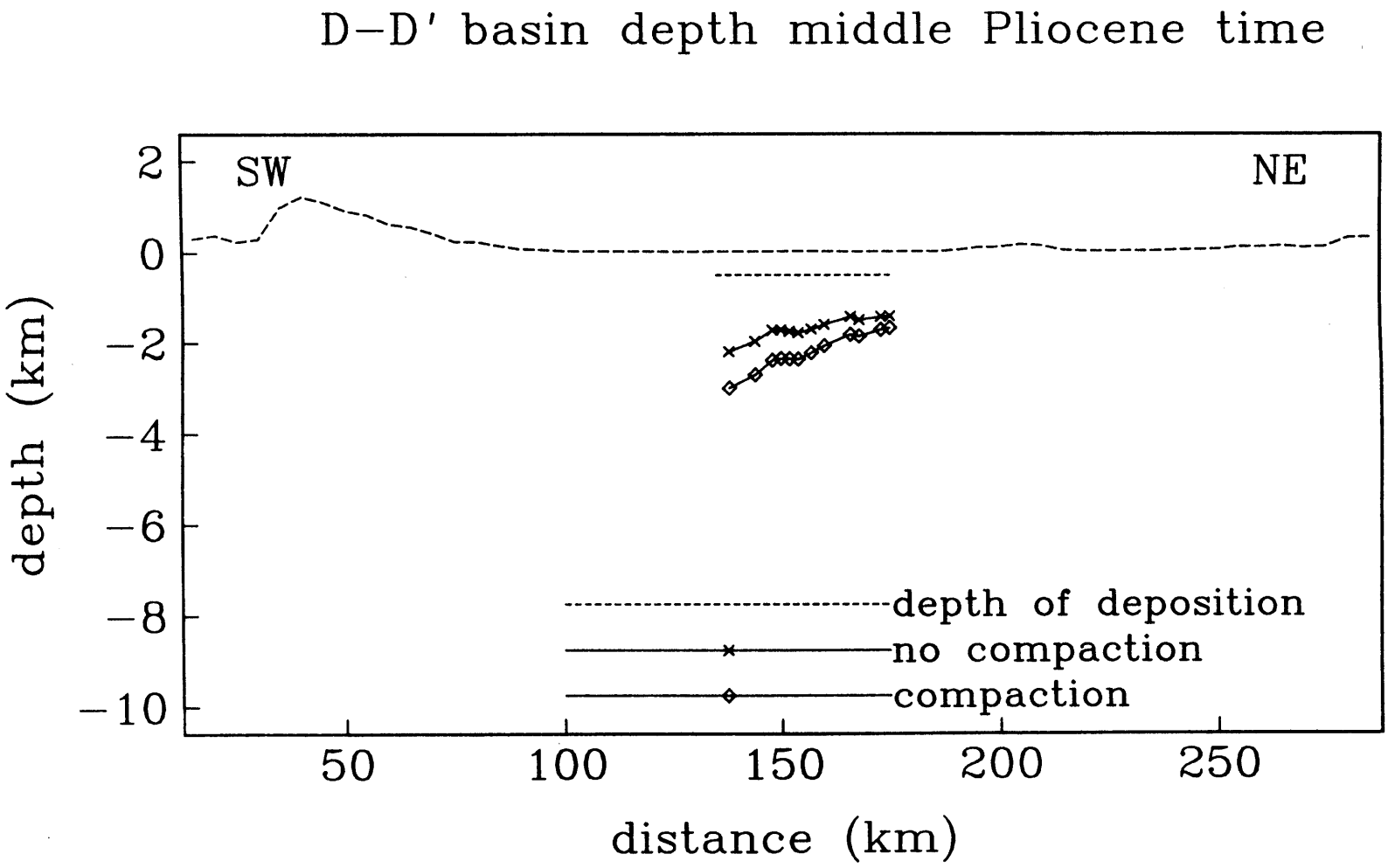
D–D′ basin depth middle Pliocene time
SW
NE
depth (km)
2
0
−2
−4
−6
−8
−10
50
100
150
200
250
distance (km)
depth of deposition
no compaction
compaction

Figure 6(b)

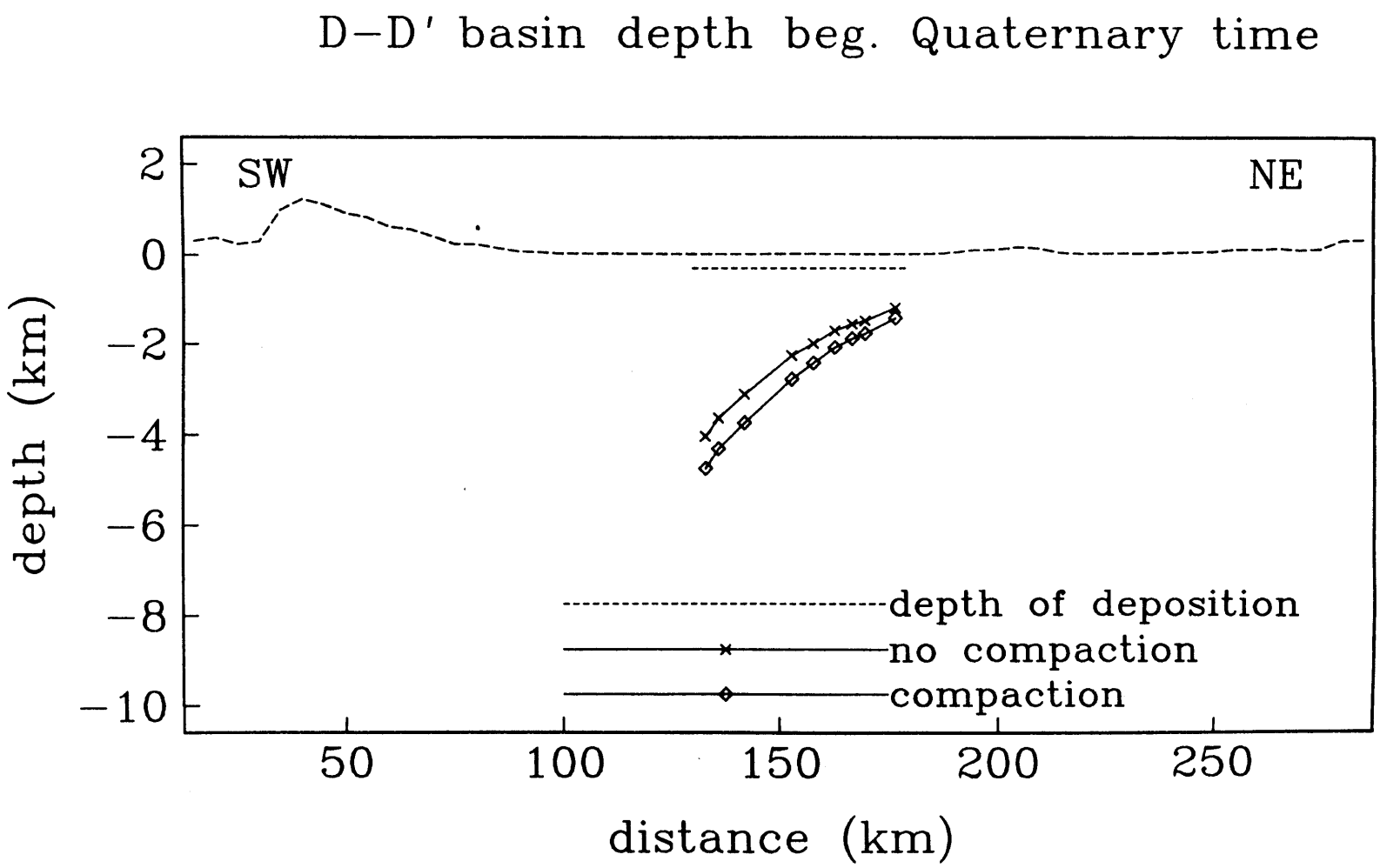
D–D′ basin depth beg. Quaternary time
SW
NE
depth (km)
2
0
−2
−4
−6
−8
−10
50
100
150
200
250
distance (km)
depth of deposition
no compaction
compaction

Figure 6(c)

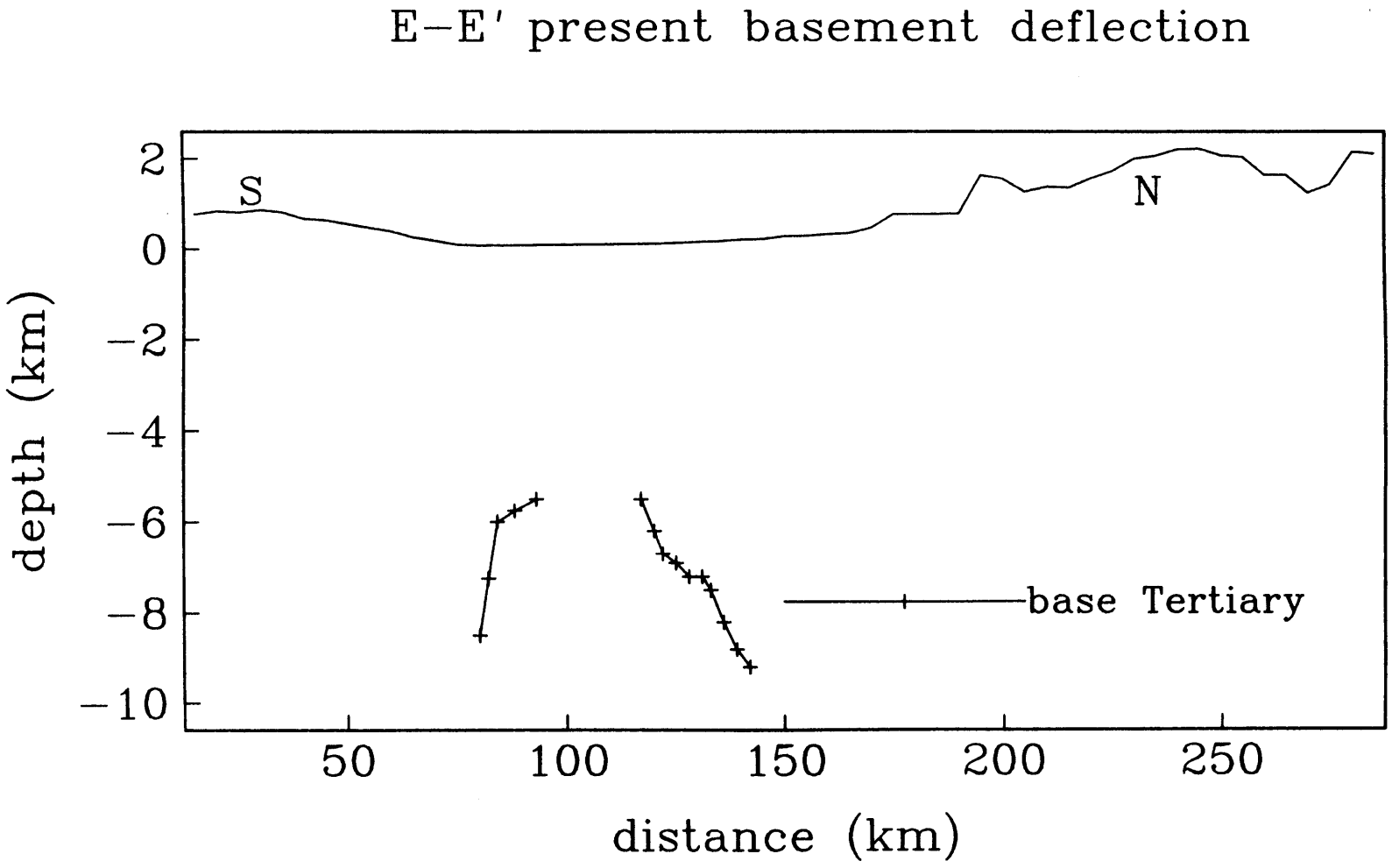
E–E′ present basement deflection
S
N
2
0
−2
−4
−6
−8
−10
depth (km)
50
100
150
200
250
distance (km)
base Tertiary

Figure 7

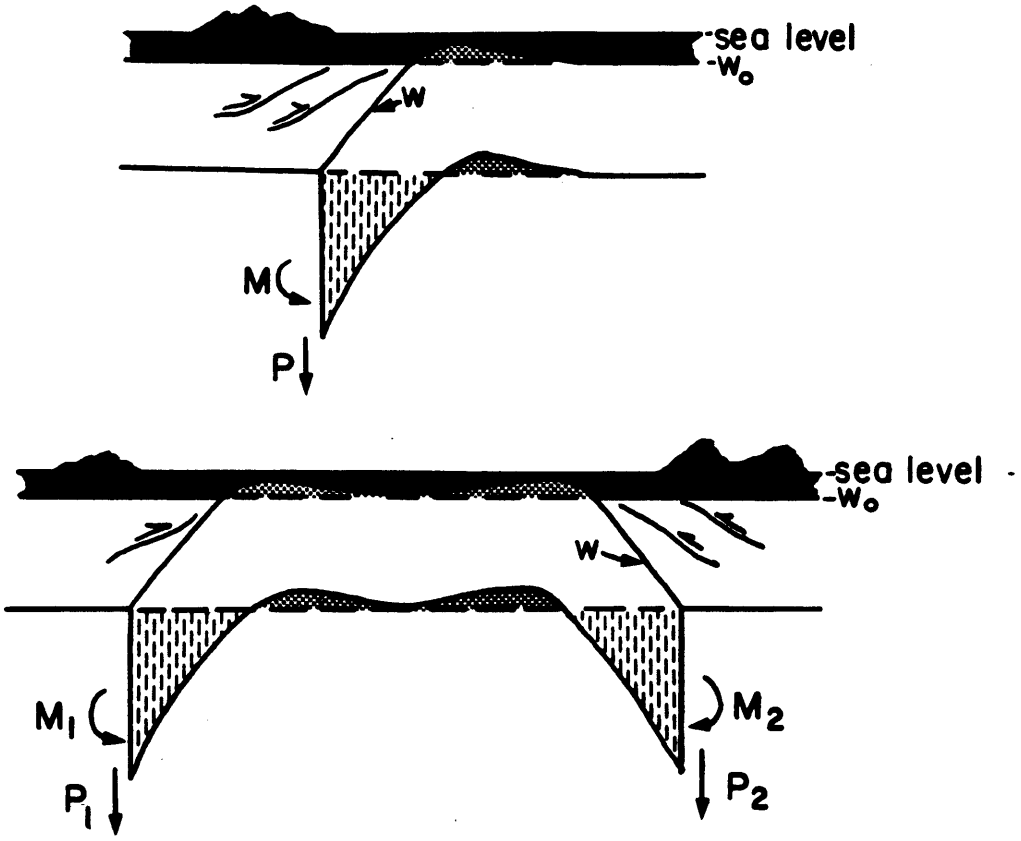

Figure 8

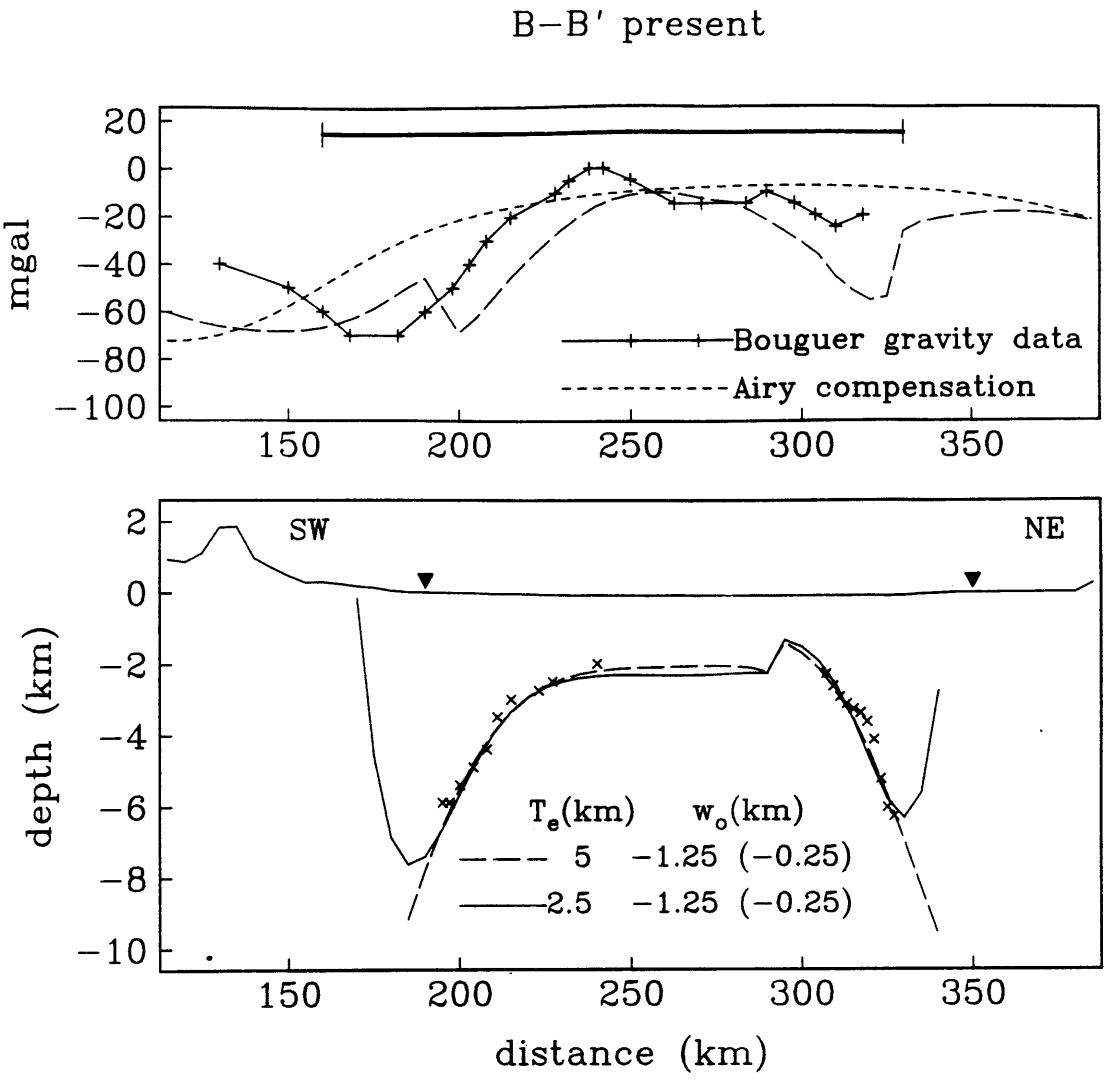
B–B′ present
mgal
20
0
−20
−40
−60
−80
−100
150
200
250
300
350
Bouguer gravity data
Airy compensation
depth (km)
SW
NE
2
0
−2
−4
−6
−8
−10
T_e(km) w_o(km)
5 −1.25 (−0.25)
2.5 −1.25 (−0.25)
distance (km)

Figure 9(a)

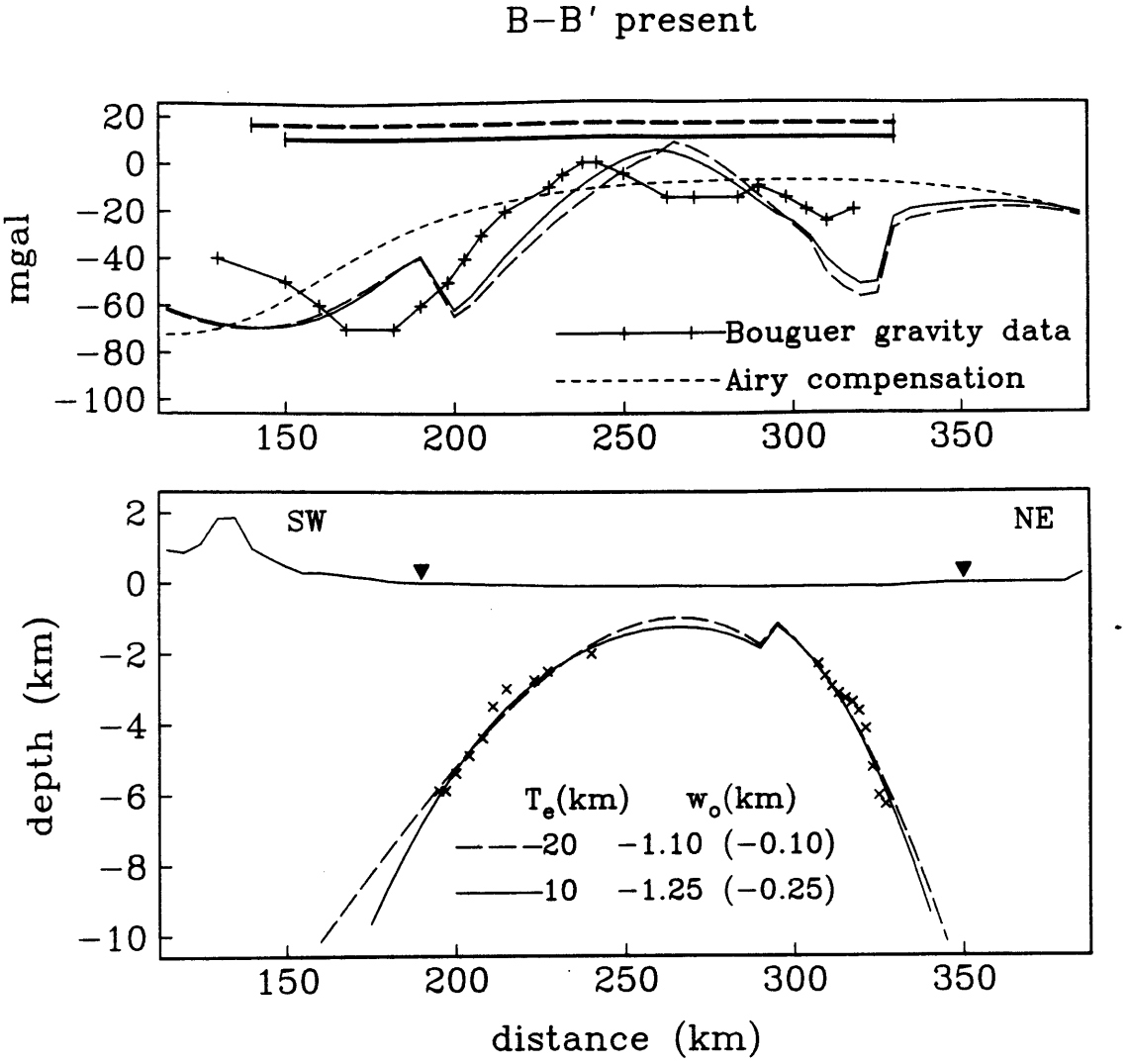

Figure 9(a)
(con't,)

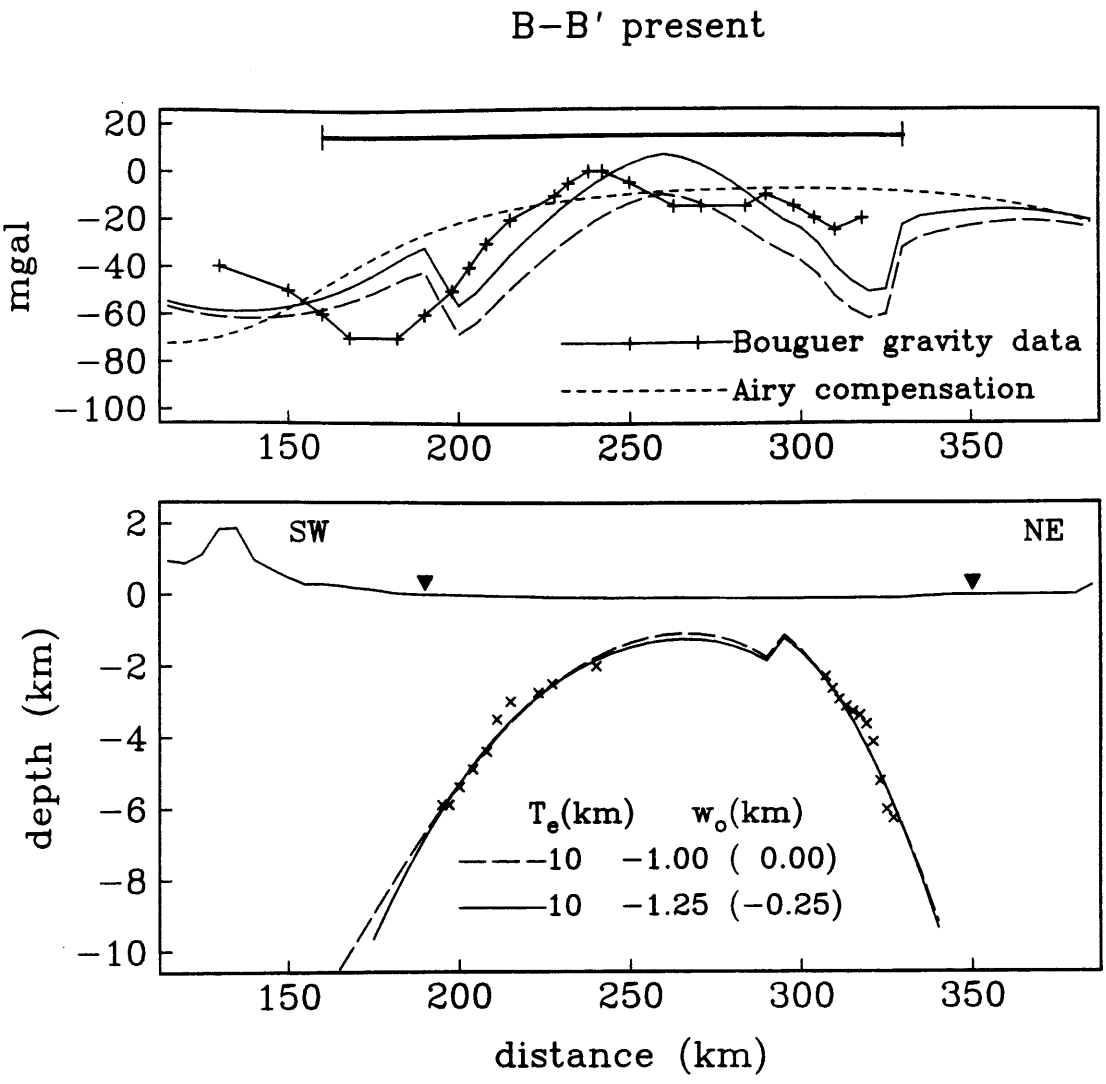
B–B′ present
mgal
20
0
−20
−40
−60
−80
−100
150
200
250
300
350
Bouguer gravity data
Airy compensation
SW
NE
depth (km)
2
0
−2
−4
−6
−8
−10
T_e(km) w_o(km)
10 −1.00 (0.00)
10 −1.25 (−0.25)
distance (km)

Figure 9(b)

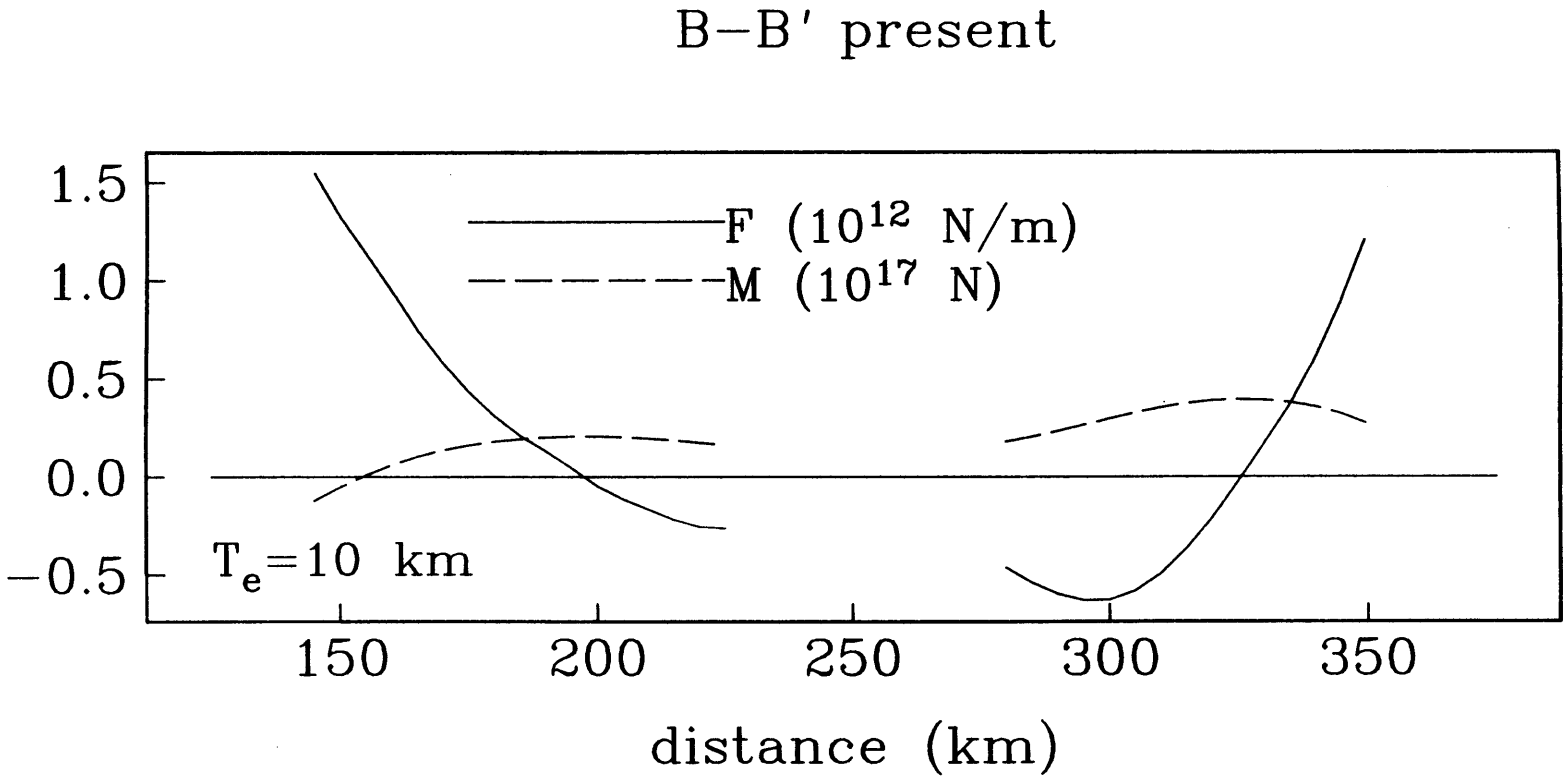
B–B′ present
1.5
1.0
0.5
0.0
−0.5
F (10^12 N/m)
M (10^17 N)
T_e=10 km
150
200
250
300
350
distance (km)

Figure 9(c)

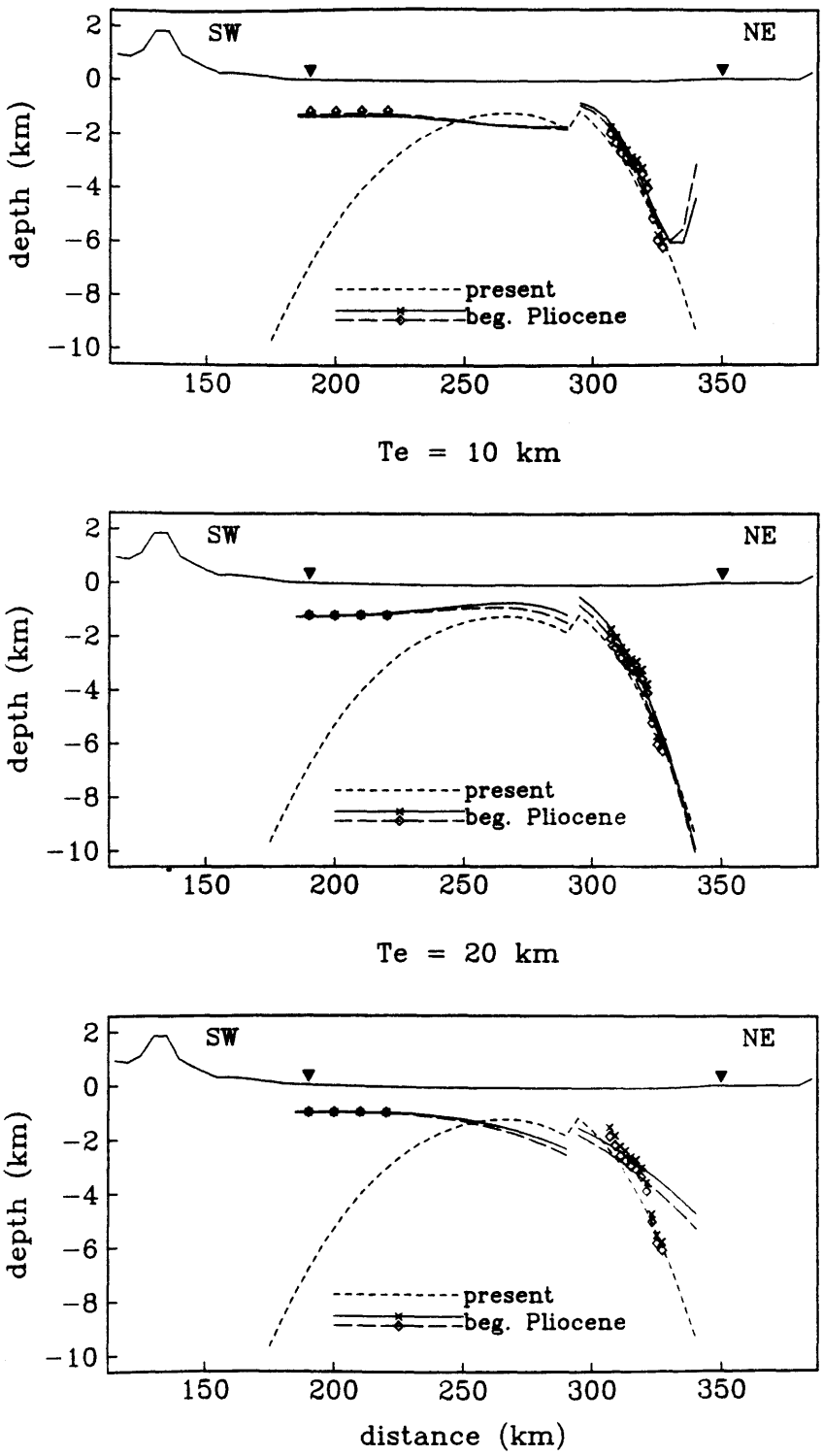
B–B'
Te = 2.5 km
SW
NE
depth (km)
present
beg. Pliocene
Te = 10 km
SW
NE
depth (km)
present
beg. Pliocene
Te = 20 km
SW
NE
depth (km)
present
beg. Pliocene
distance (km)

Figure 10(a)

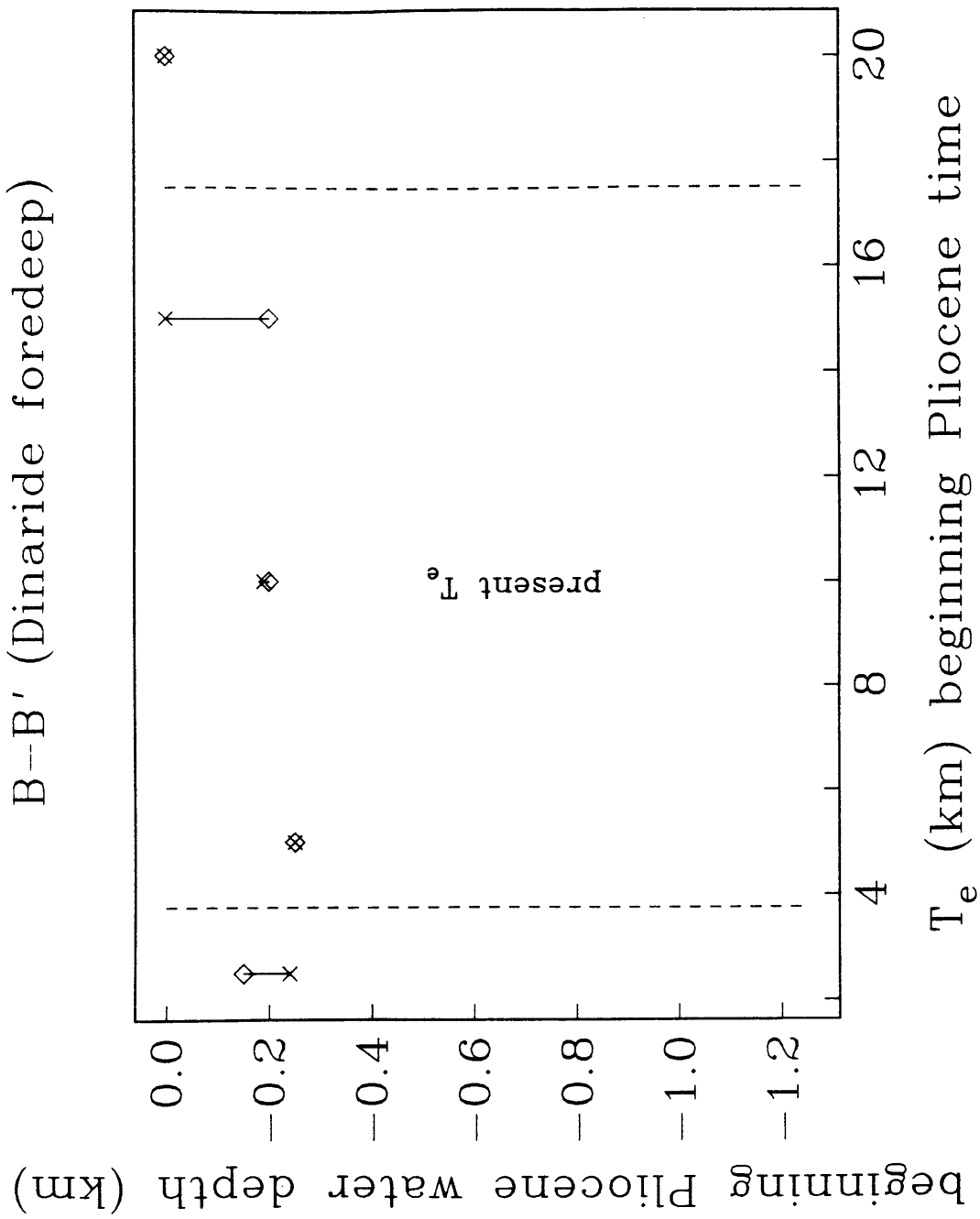
B--B' (Dinaride foredeep)
present T_e
beginning Pliocene water depth (km)
0.0
−0.2
−0.4
−0.6
−0.8
−1.0
−1.2
4
8
12
16
20
T_e (km) beginning Pliocene time

Figure 10(b)

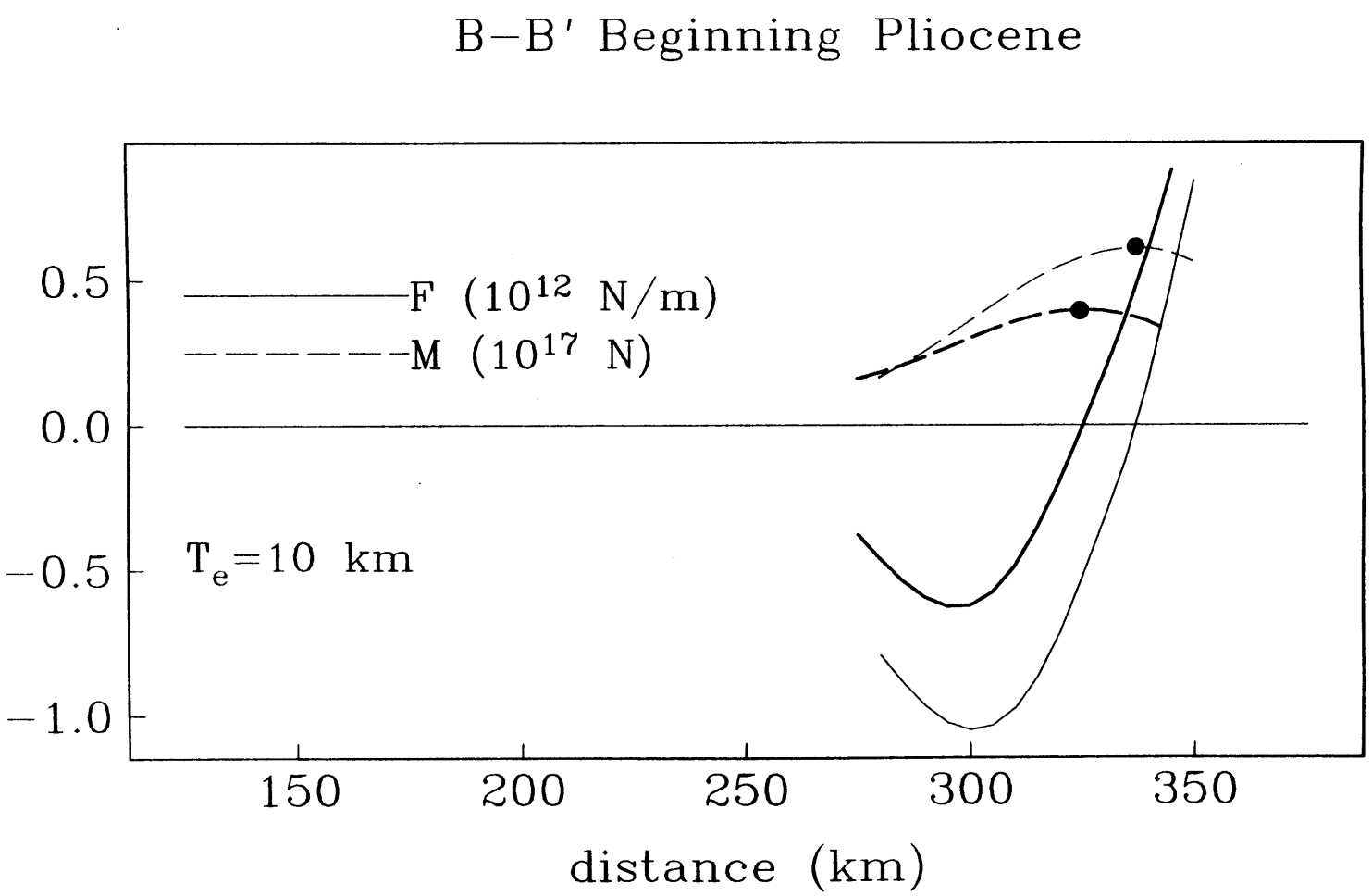
B–B′ Beginning Pliocene
0.5
0.0
−0.5
−1.0
F (10^12 N/m)
M (10^17 N)
T_e=10 km
150
200
250
300
350
distance (km)

Figure 10(c)

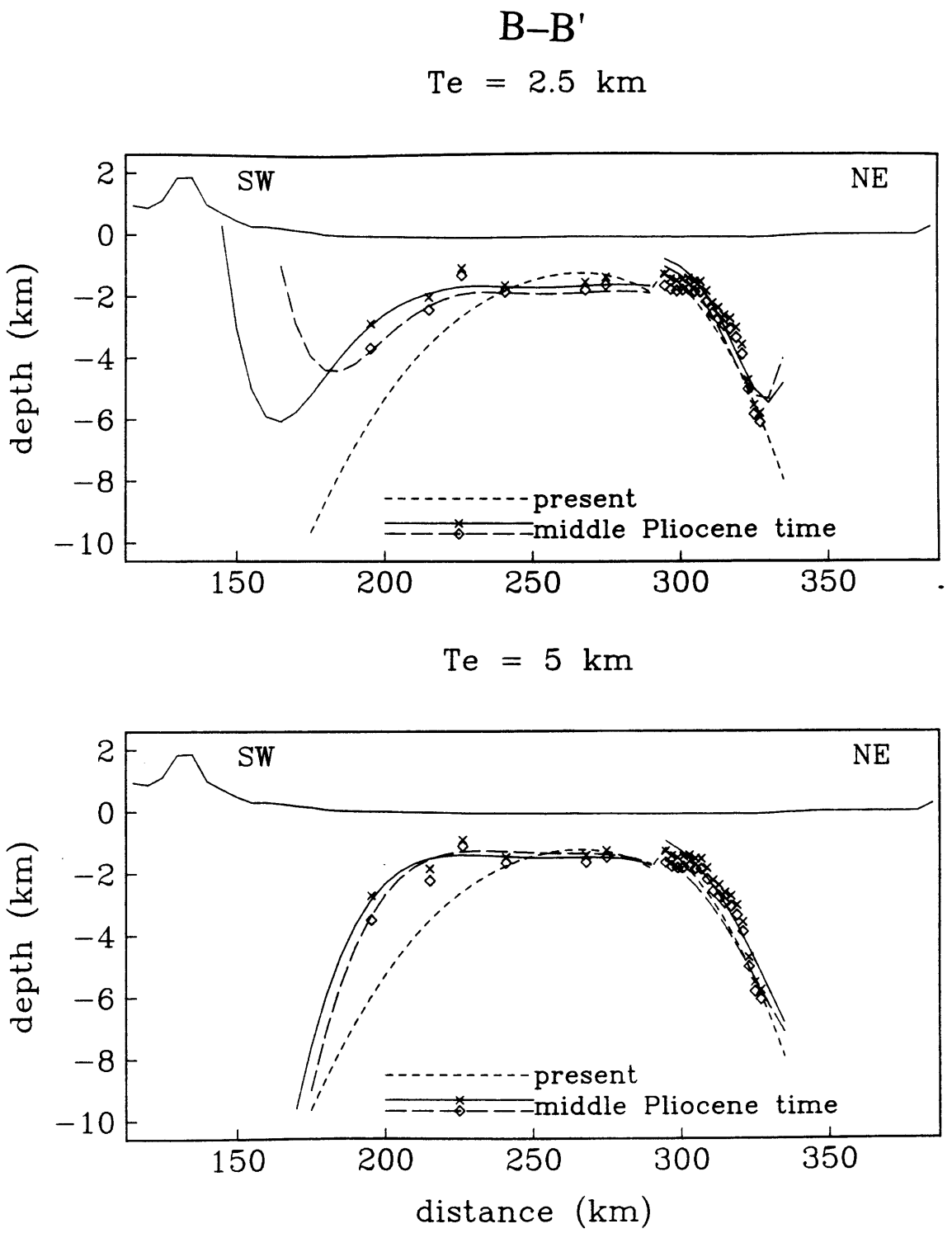
B–B'
Te = 2.5 km
SW
NE
depth (km)
2
0
−2
−4
−6
−8
−10
150
200
250
300
350
present
middle Pliocene time
Te = 5 km
SW
NE
depth (km)
2
0
−2
−4
−6
−8
−10
150
200
250
300
350
distance (km)
present
middle Pliocene time

Figure 11(a)

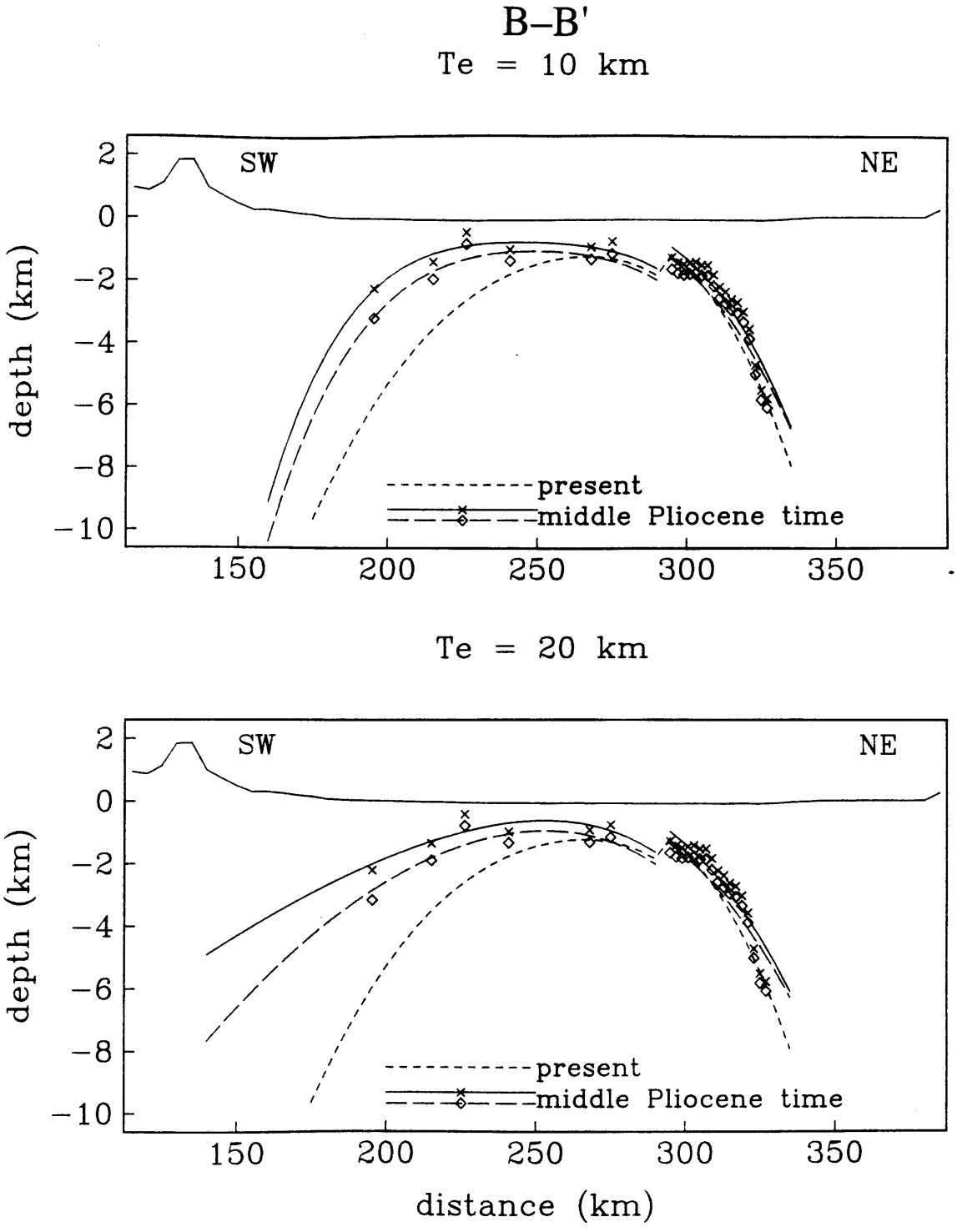

Figure 11(a)
(con't.)

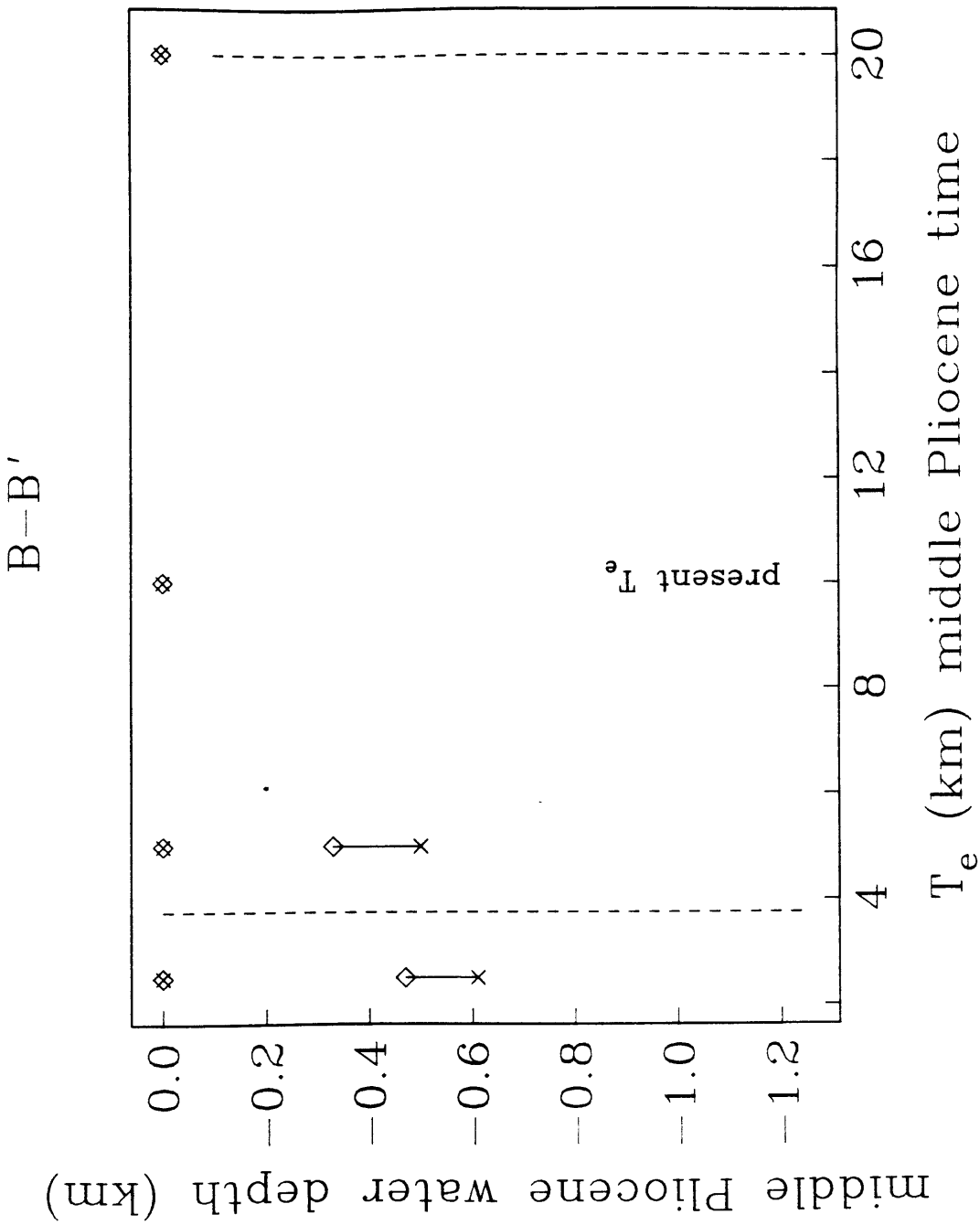
B—B′
present T_e
0.0
0.2
0.4
0.6
0.8
1.0
1.2
middle Pliocene water depth (km)
4
8
12
16
20
T_e (km) middle Pliocene time

Figure 11(b)

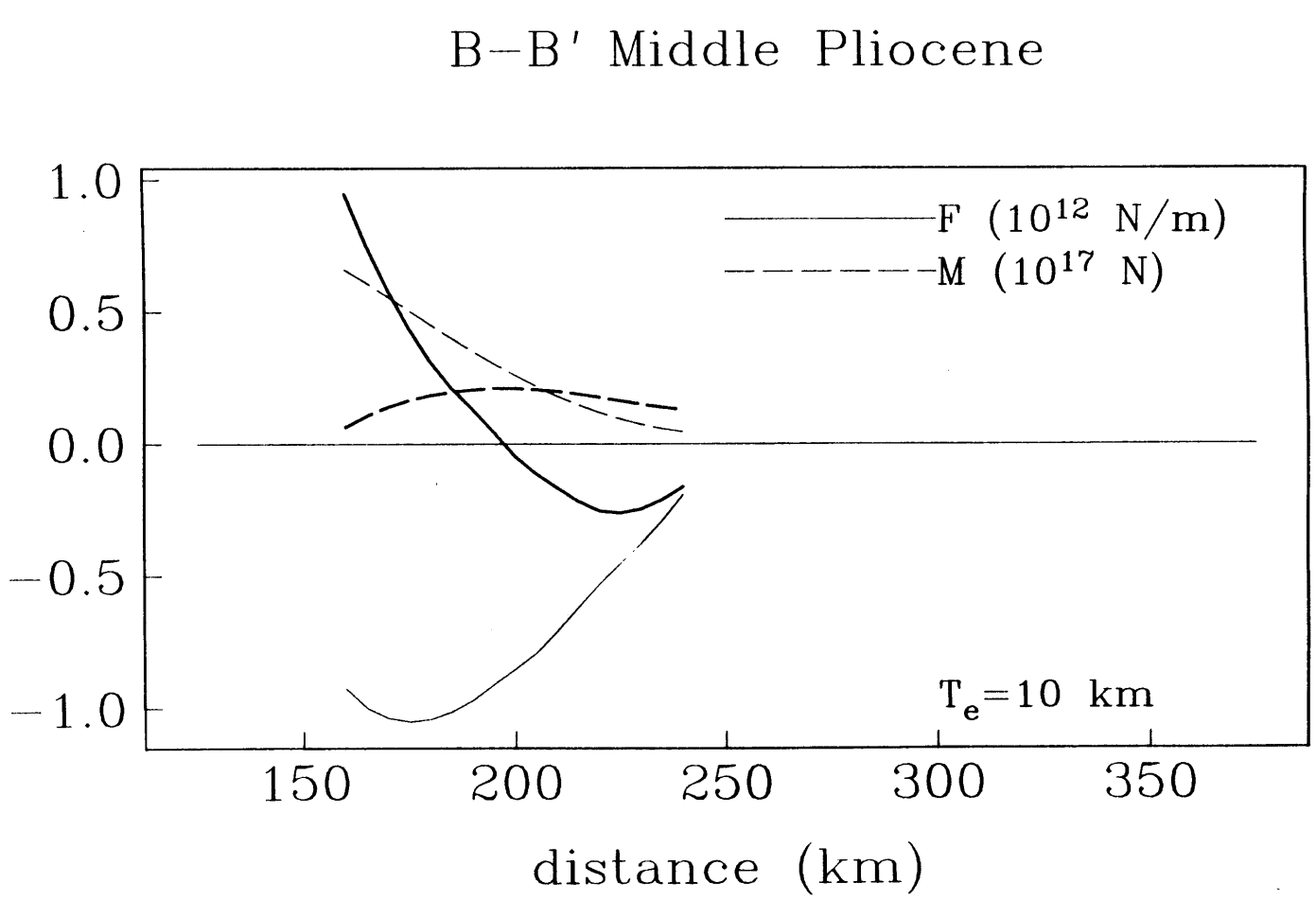
B–B′ Middle Pliocene
1.0
0.5
0.0
−0.5
−1.0
F (10^12 N/m)
M (10^17 N)
T_e=10 km
150
200
250
300
350
distance (km)

Figure 11(c)

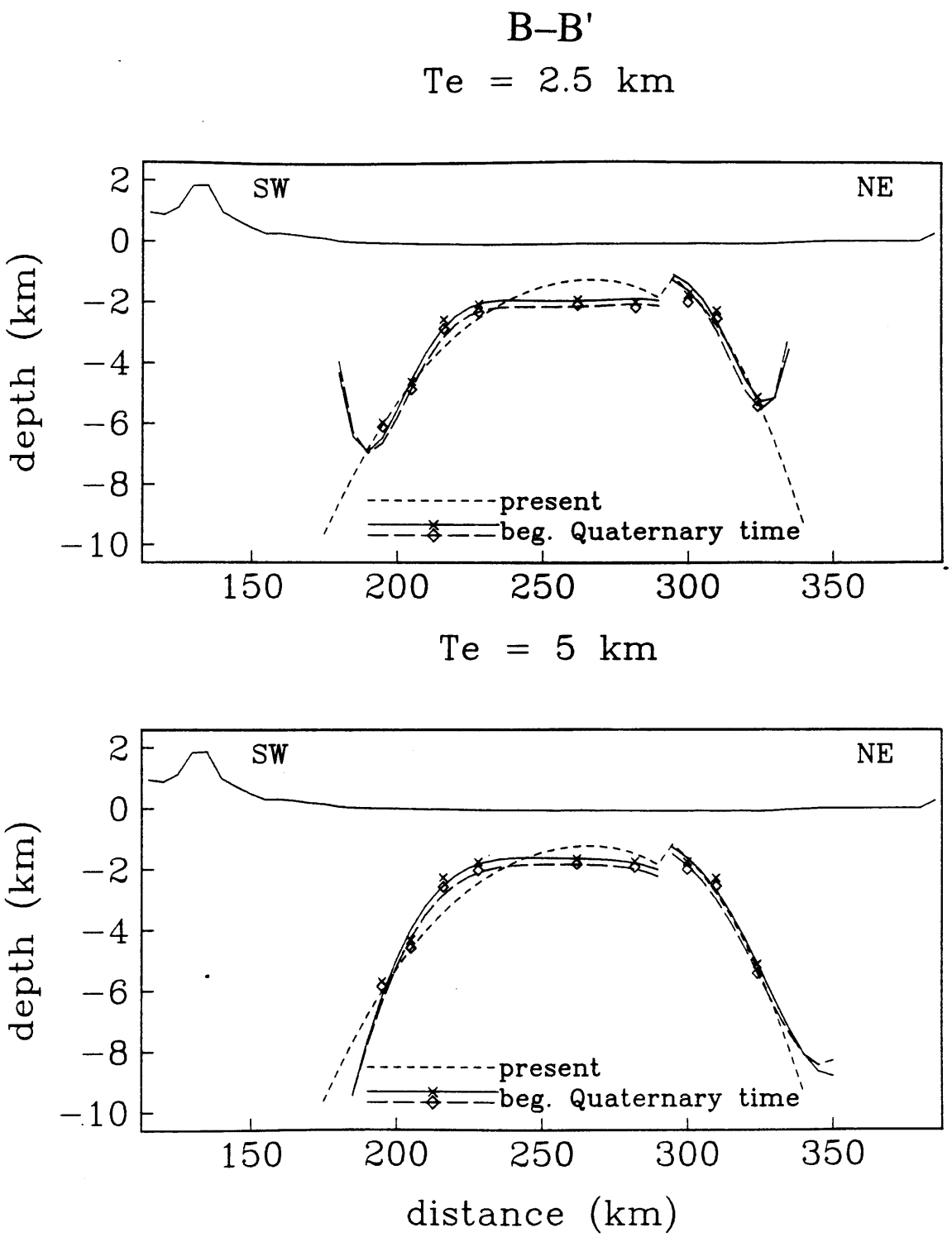
B–B'
Te = 2.5 km
SW
NE
depth (km)
2
0
−2
−4
−6
−8
−10
150
200
250
300
350
present
beg. Quaternary time
Te = 5 km
SW
NE
depth (km)
2
0
−2
−4
−6
−8
−10
150
200
250
300
350
present
beg. Quaternary time
distance (km)

Figure 12(a)

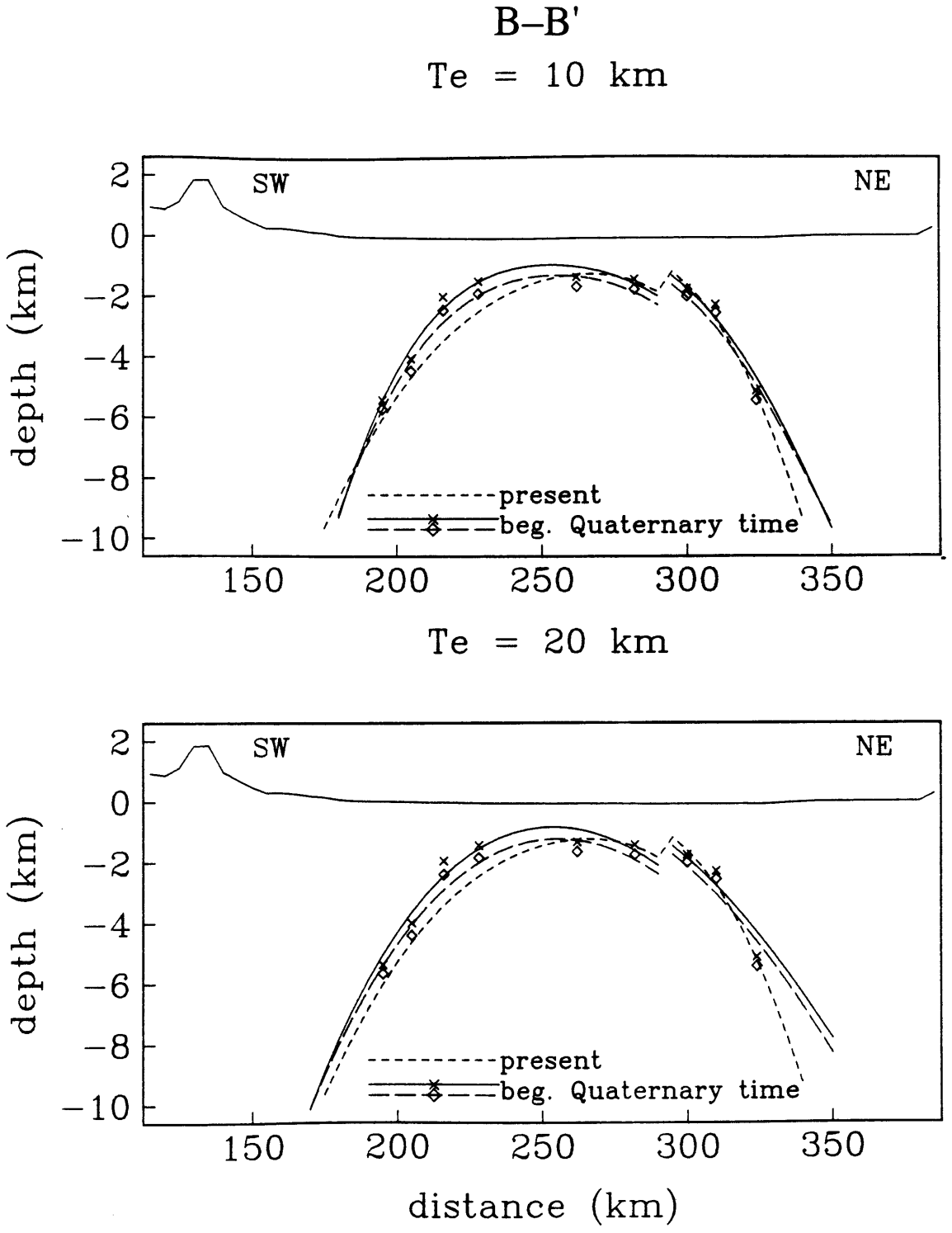

Figure 12(a)
(con't,)

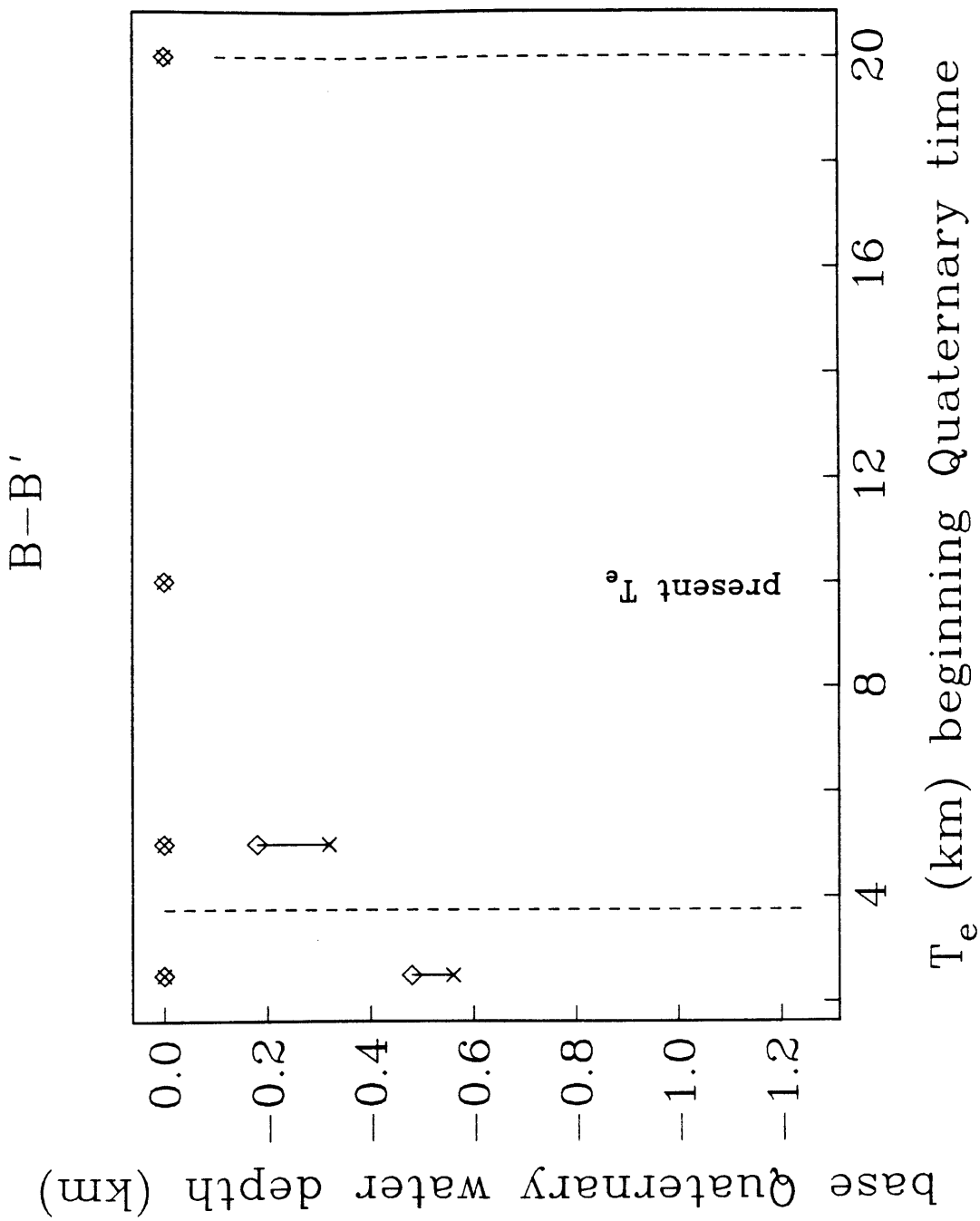
B–B′
base Quaternary water depth (km)
0.0
−0.2
−0.4
−0.6
−0.8
−1.0
−1.2
present T_e
4
8
12
16
20
T_e (km) beginning Quaternary time

Figure 12(b)

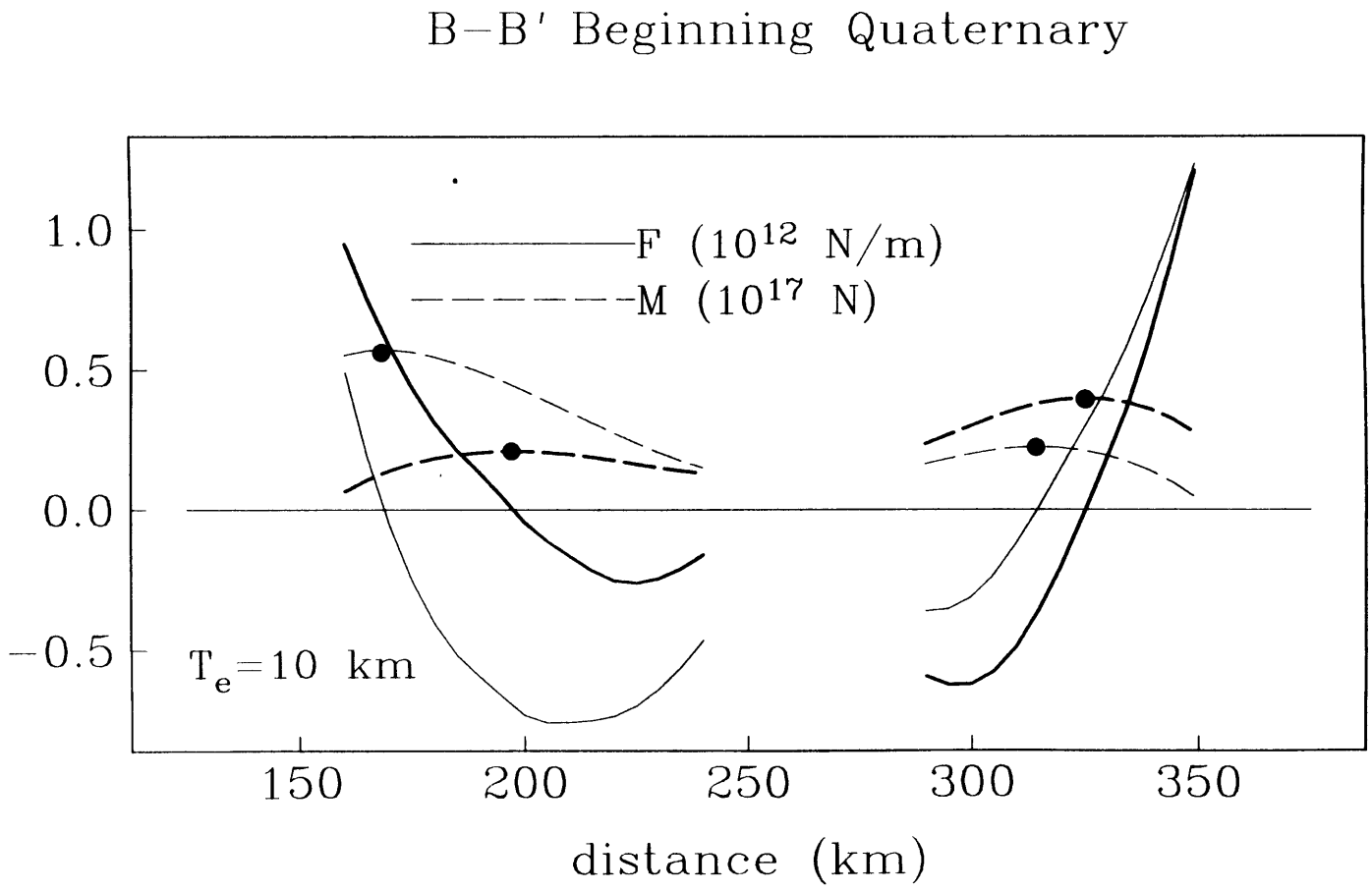
B–B′ Beginning Quaternary
1.0
0.5
0.0
−0.5
F (10^12 N/m)
M (10^17 N)
T_e=10 km
150
200
250
300
350
distance (km)

Figure 12(c)

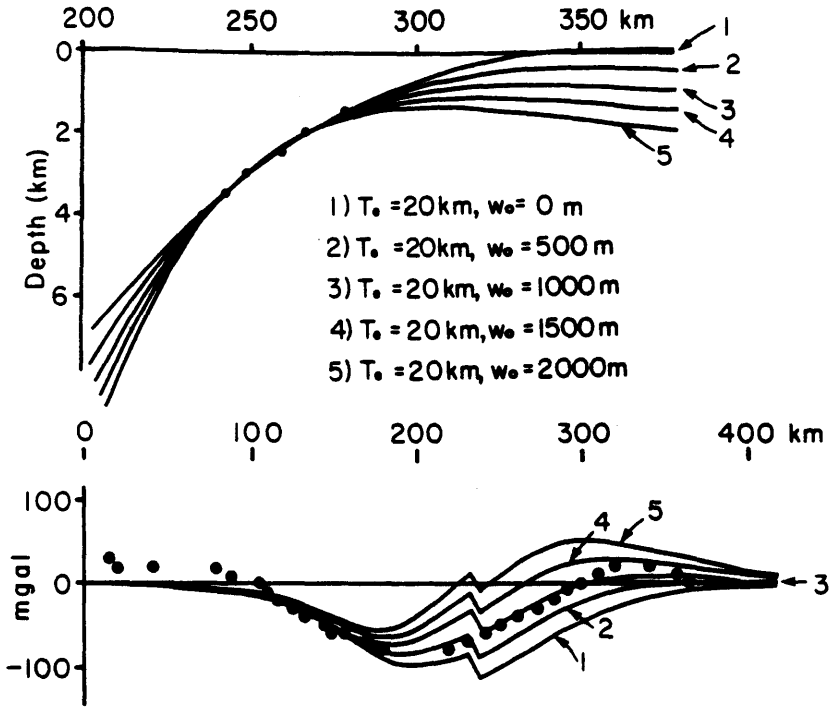

PROFILE CC'

Figure 13

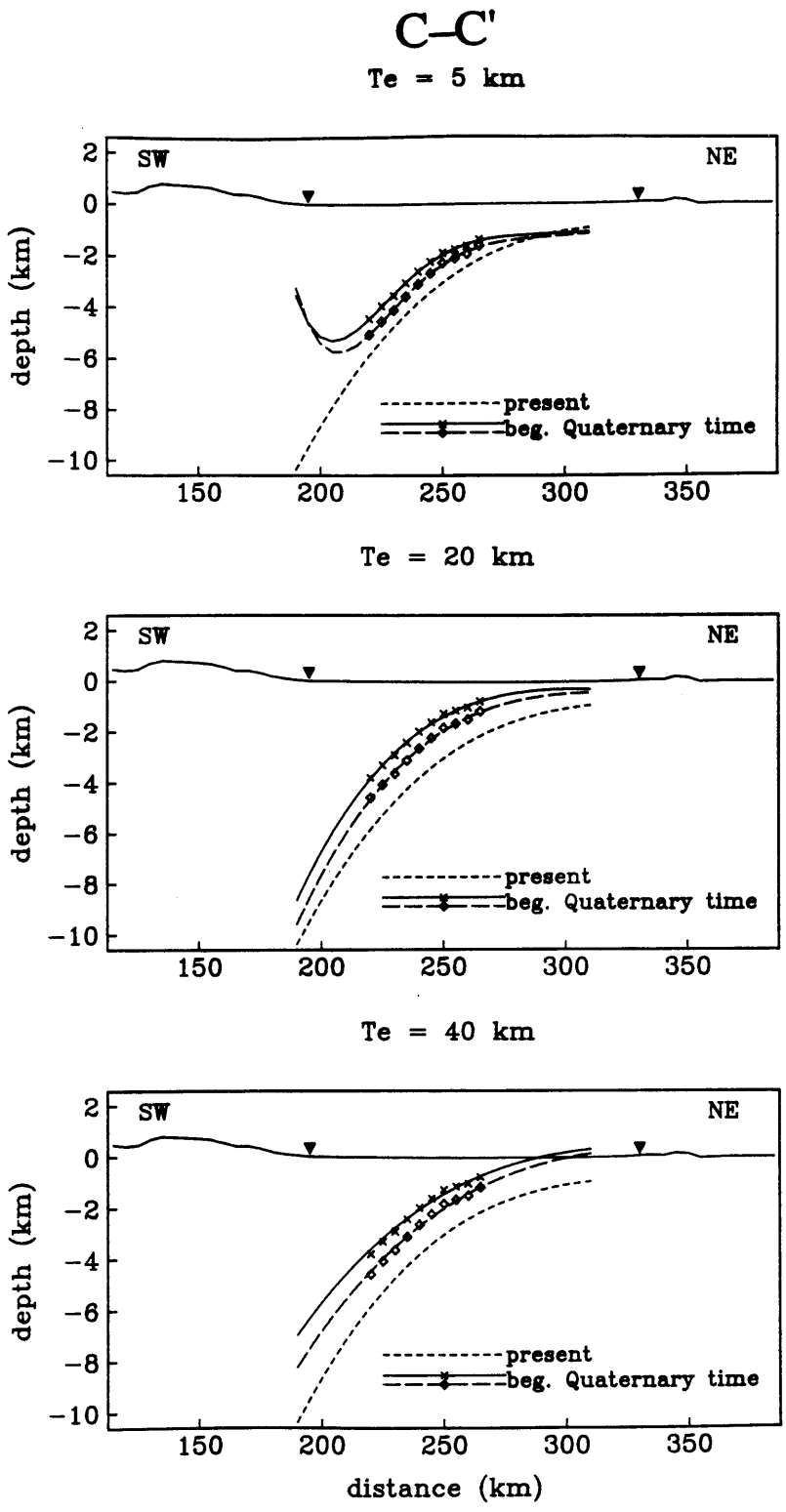
C–C'
Te = 5 km
SW
NE
depth (km)
2
0
−2
−4
−6
−8
−10
150
200
250
300
350
present
beg. Quaternary time
Te = 20 km
SW
NE
depth (km)
present
beg. Quaternary time
Te = 40 km
SW
NE
depth (km)
present
beg. Quaternary time
distance (km)

Figure 14(a)

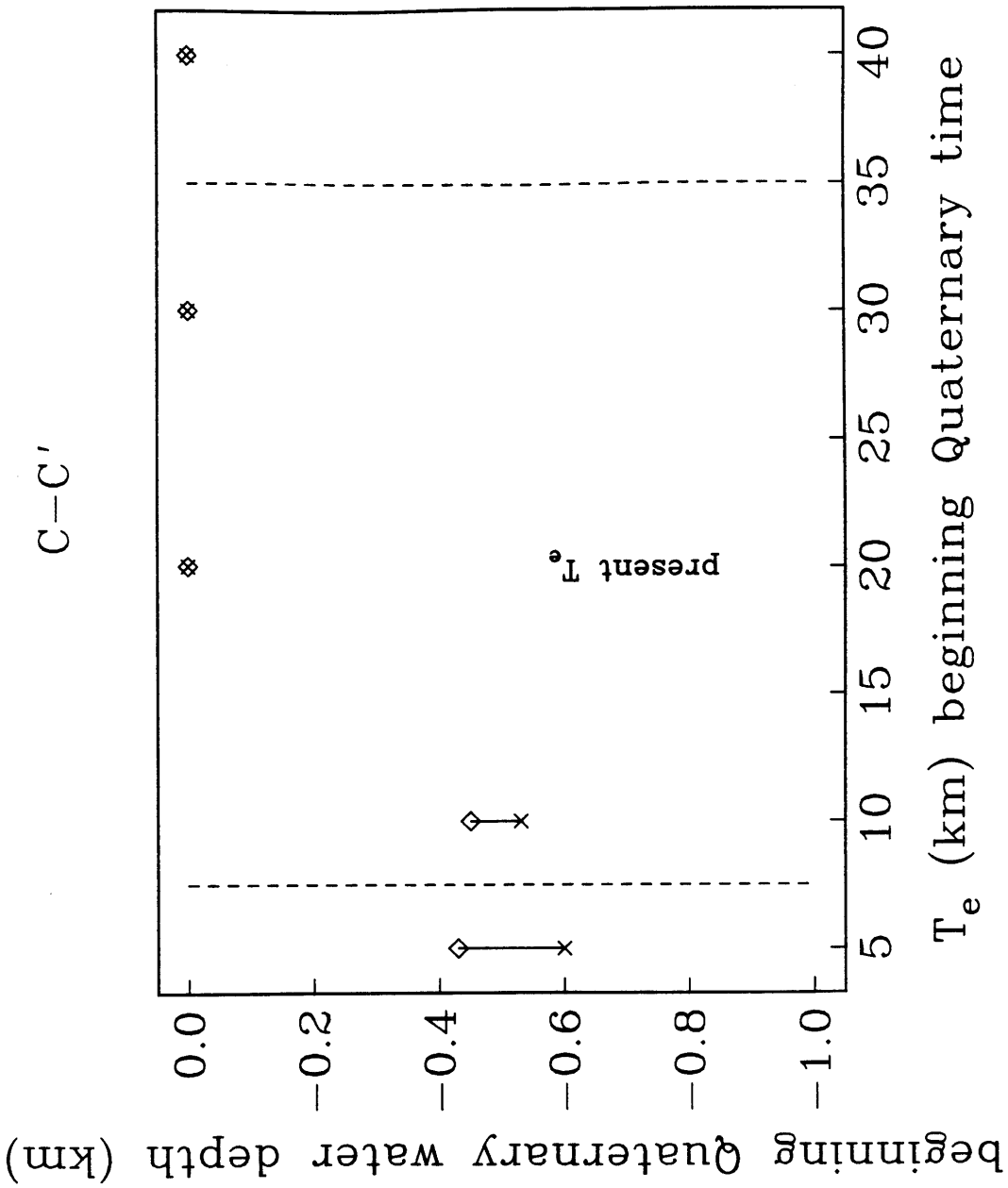
C–C'
present T_e
beginning Quaternary water depth (km)
0.0
–0.2
–0.4
–0.6
–0.8
–1.0
5
10
15
20
25
30
35
40
T_e (km) beginning Quaternary time

Figure 14(b)

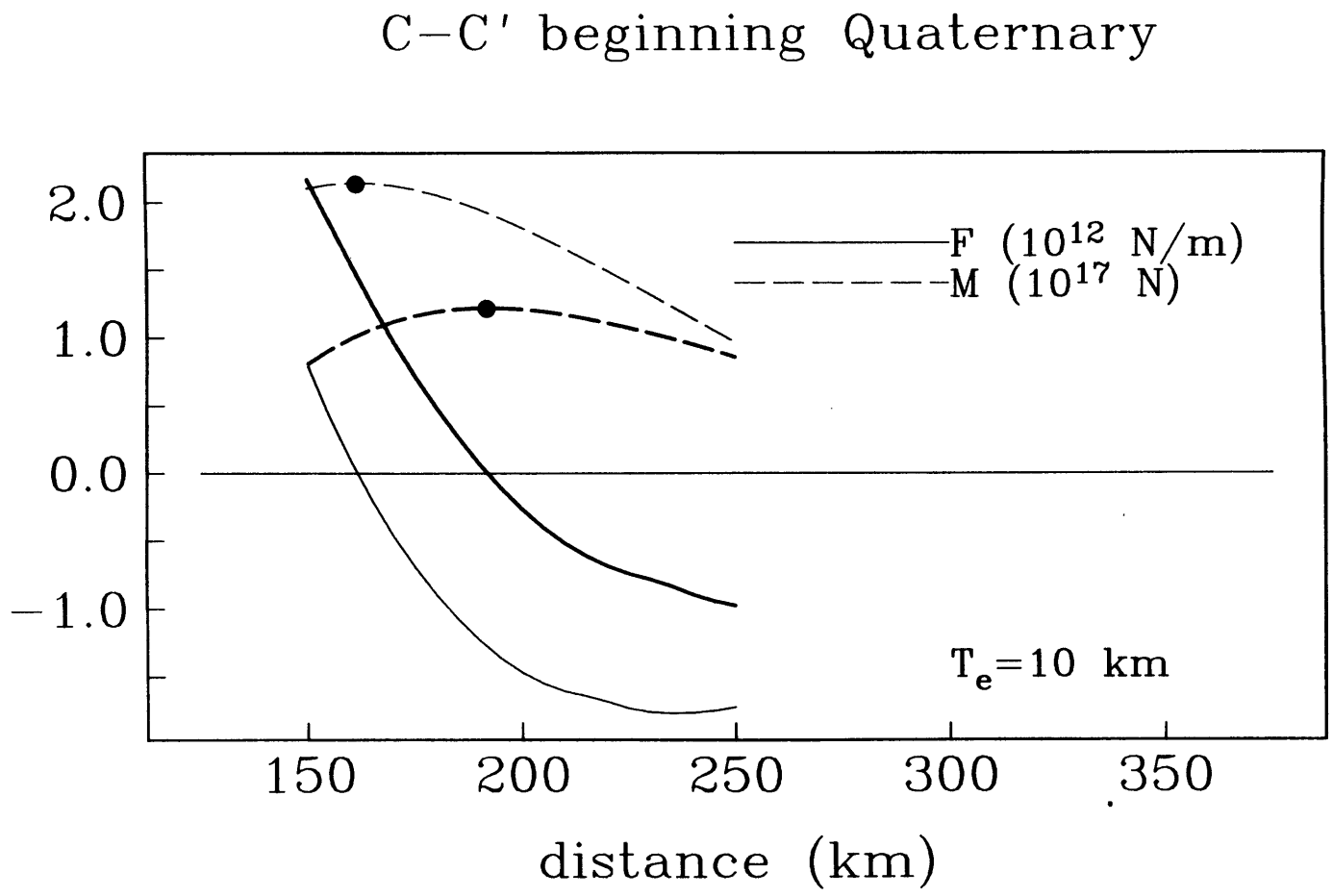
C–C′ beginning Quaternary
2.0
1.0
0.0
−1.0
F (10^12 N/m)
M (10^17 N)
T_e=10 km
150
200
250
300
350
distance (km)

Figure 14(c)

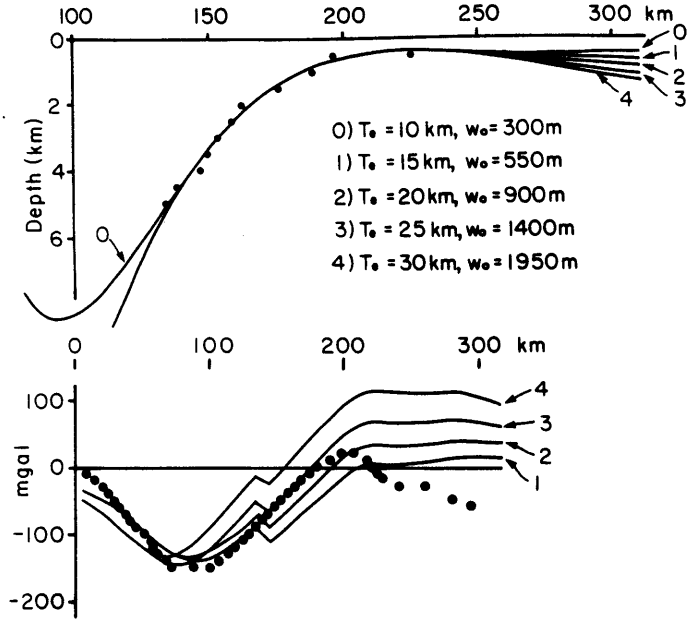
100
150
200
250
300 km
0
2
4
6
Depth (km)
0
0) Te = 10 km, we = 300m
1) Te = 15 km, we = 550m
2) Te = 20 km, we = 900m
3) Te = 25 km, we = 1400m
4) Te = 30 km, we = 1950m
0
100
200
300 km
100
0
-100
-200
mgal
4
3
2
1

Figure 15

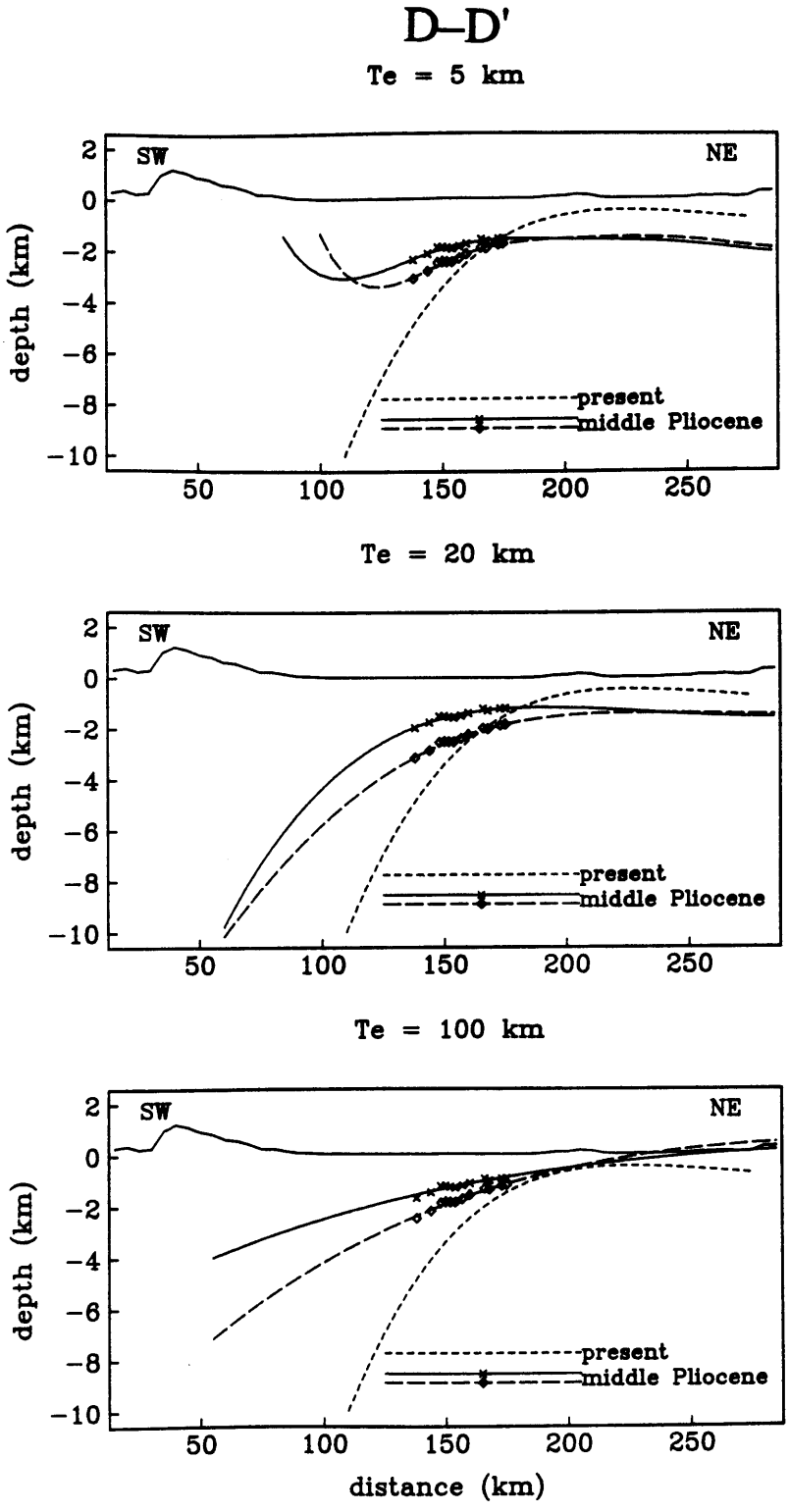
D–D'
Te = 5 km
SW
NE
depth (km)
2
0
−2
−4
−6
−8
−10
50
100
150
200
250
present
middle Pliocene
Te = 20 km
SW
NE
depth (km)
present
middle Pliocene
Te = 100 km
SW
NE
depth (km)
present
middle Pliocene
distance (km)

Figure 16(a)

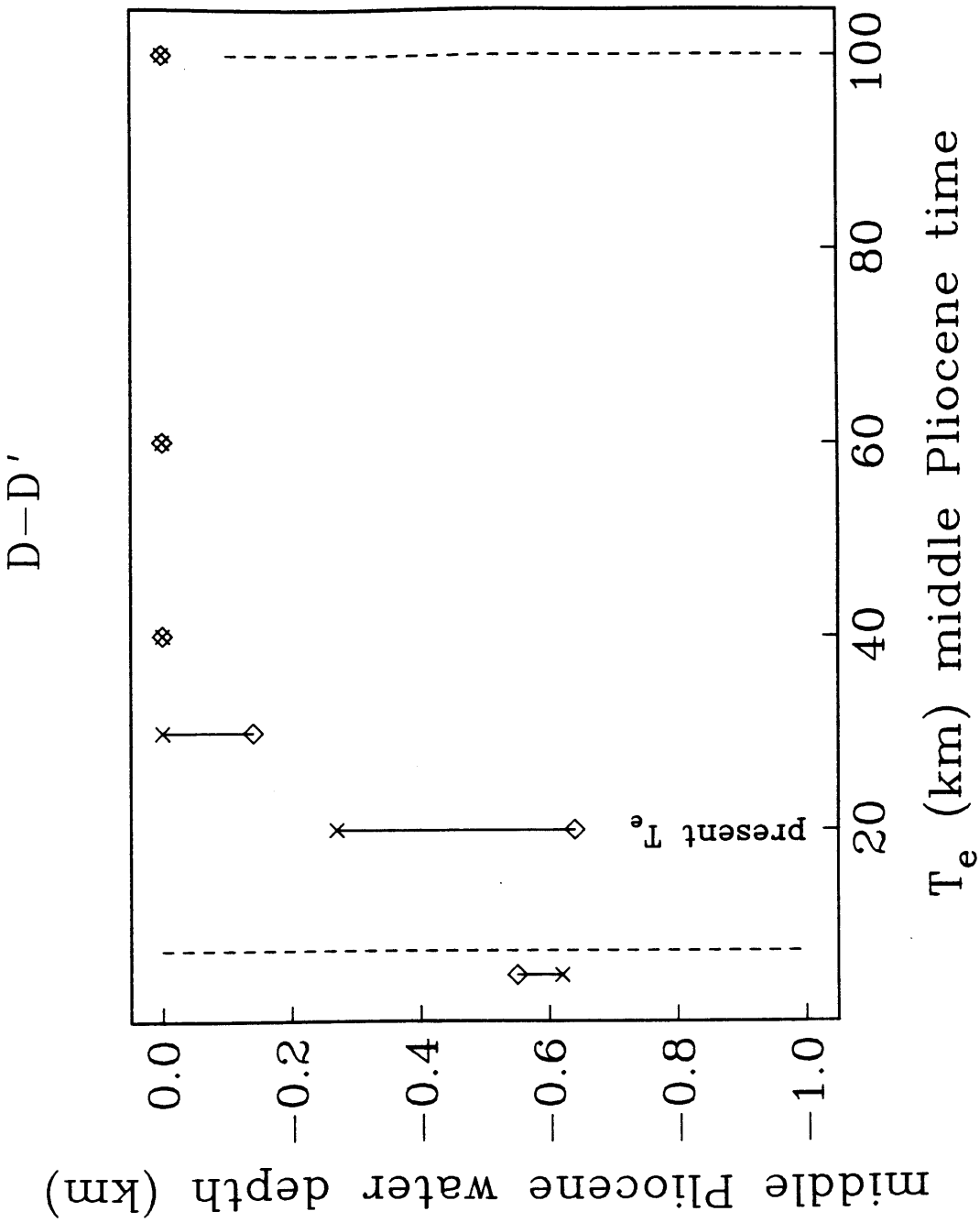
D–D′
middle Pliocene water depth (km)
0.0
0.2
0.4
0.6
0.8
1.0
20
40
60
80
100
T_e (km) middle Pliocene time
present T_e

Figure 16(b)

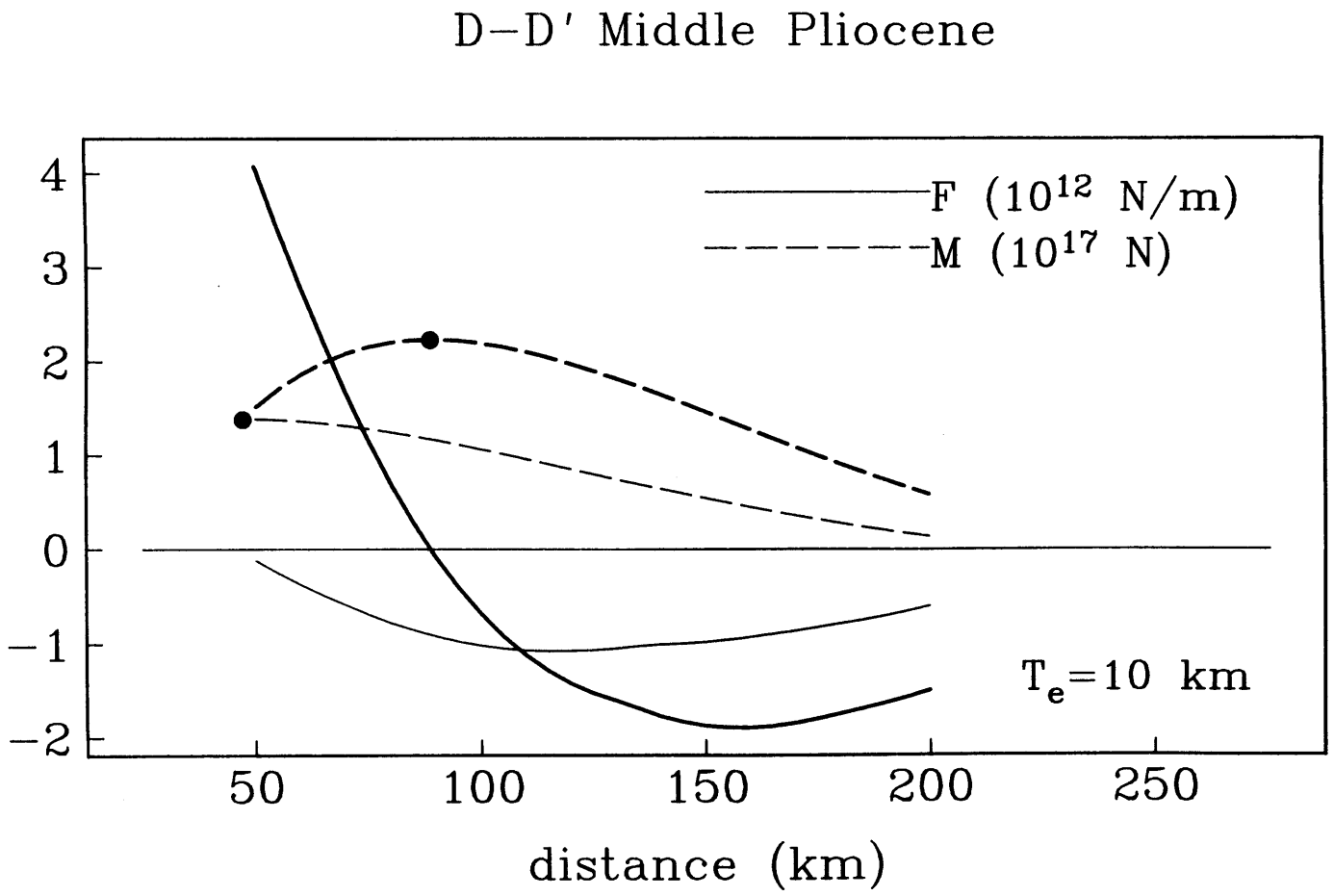
D–D′ Middle Pliocene
F (10^{12} N/m)
M (10^{17} N)
T_e=10 km
4
3
2
1
0
−1
−2
50
100
150
200
250
distance (km)

Figure 16(c)

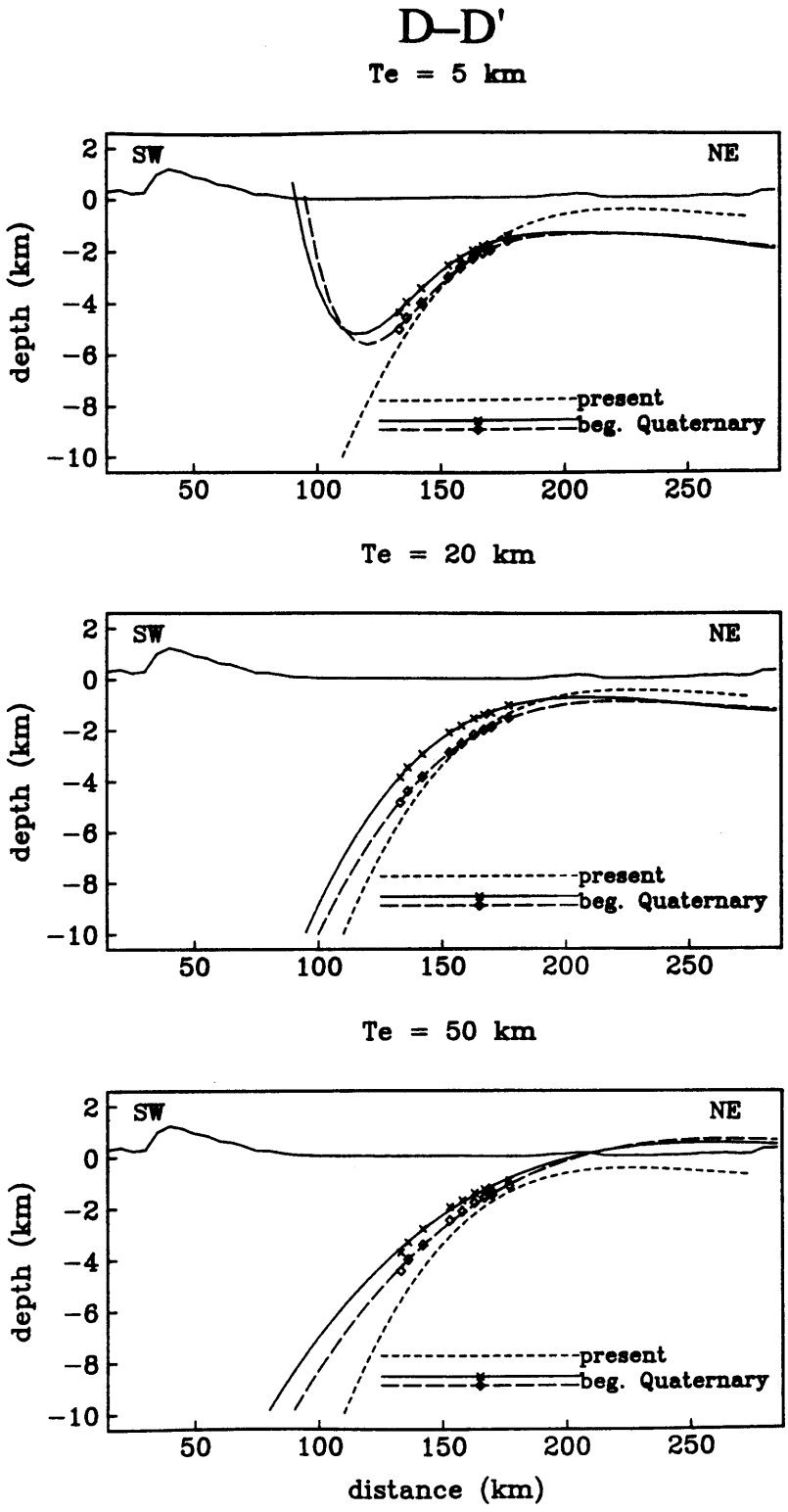
D–D'
Te = 5 km
SW
NE
depth (km)
2
0
−2
−4
−6
−8
−10
50
100
150
200
250
present
beg. Quaternary
Te = 20 km
SW
NE
depth (km)
present
beg. Quaternary
Te = 50 km
SW
NE
depth (km)
present
beg. Quaternary
distance (km)

Figure 17(a)

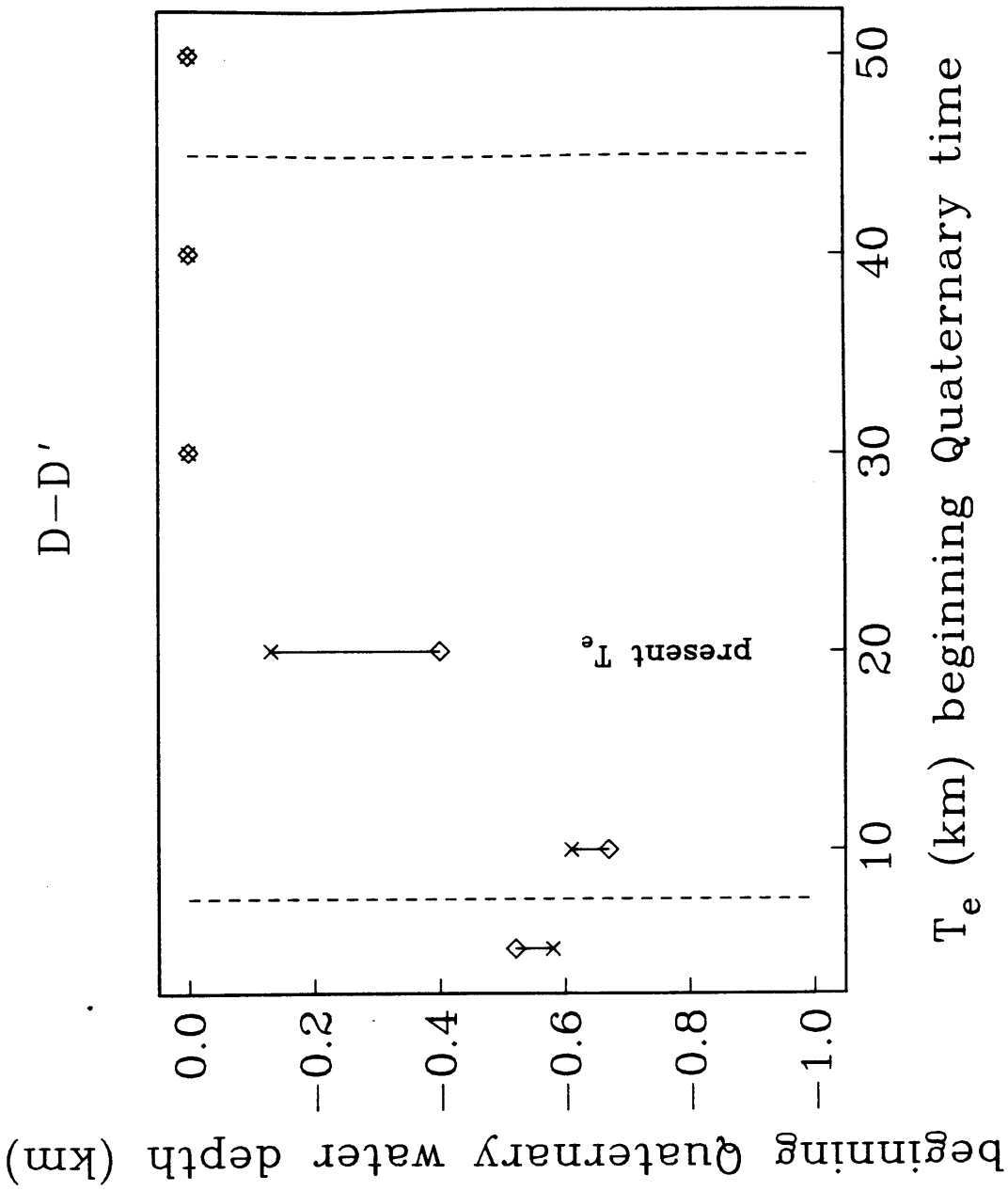
D–D′
present T_e
0.0
–0.2
–0.4
–0.6
–0.8
–1.0
beginning Quaternary water depth (km)
10
20
30
40
50
T_e (km) beginning Quaternary time

Figure 17(b)

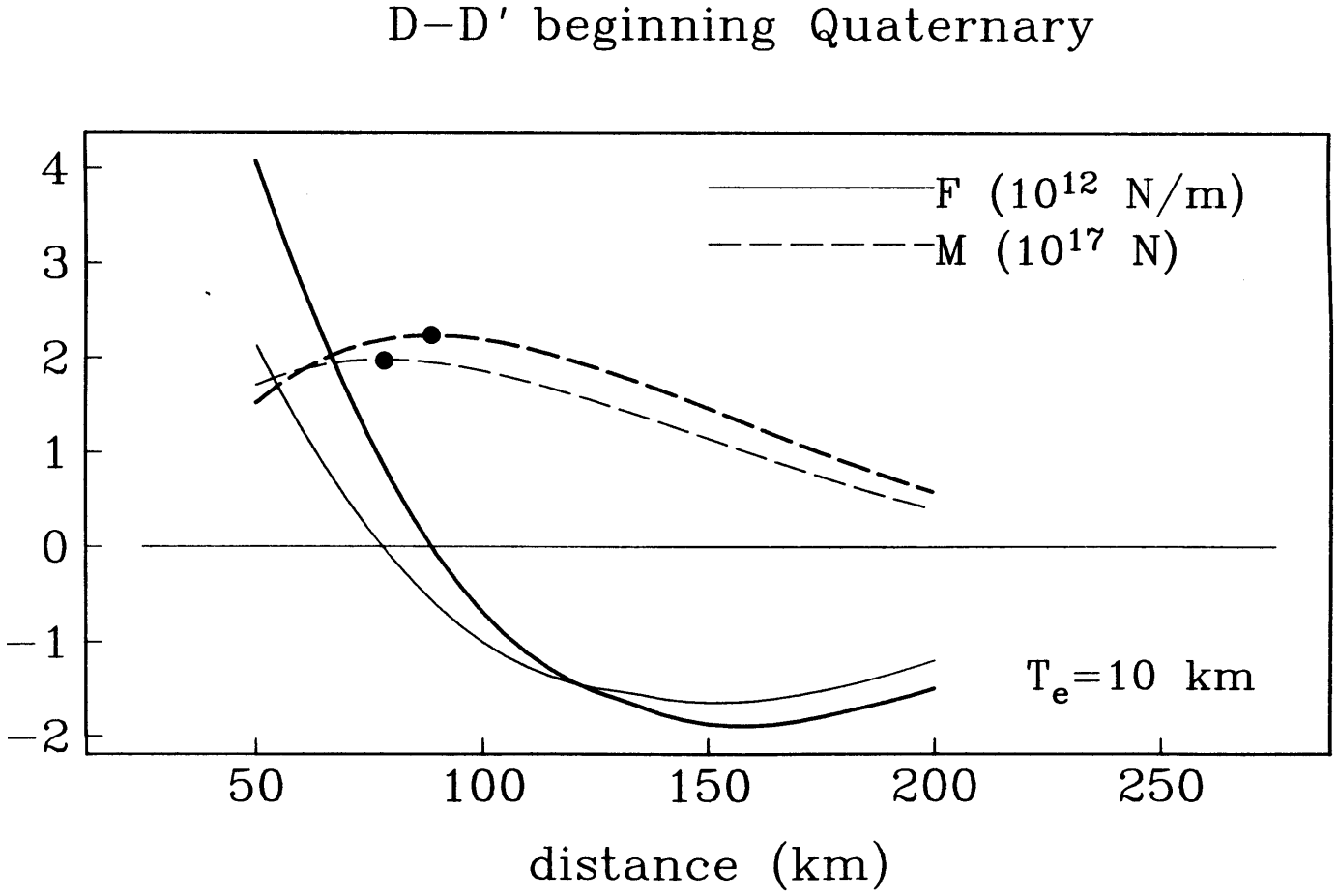
D–D′ beginning Quaternary
F (10^12 N/m)
M (10^17 N)
T_e=10 km
4
3
2
1
0
−1
−2
50
100
150
200
250
distance (km)

Figure 17(c)

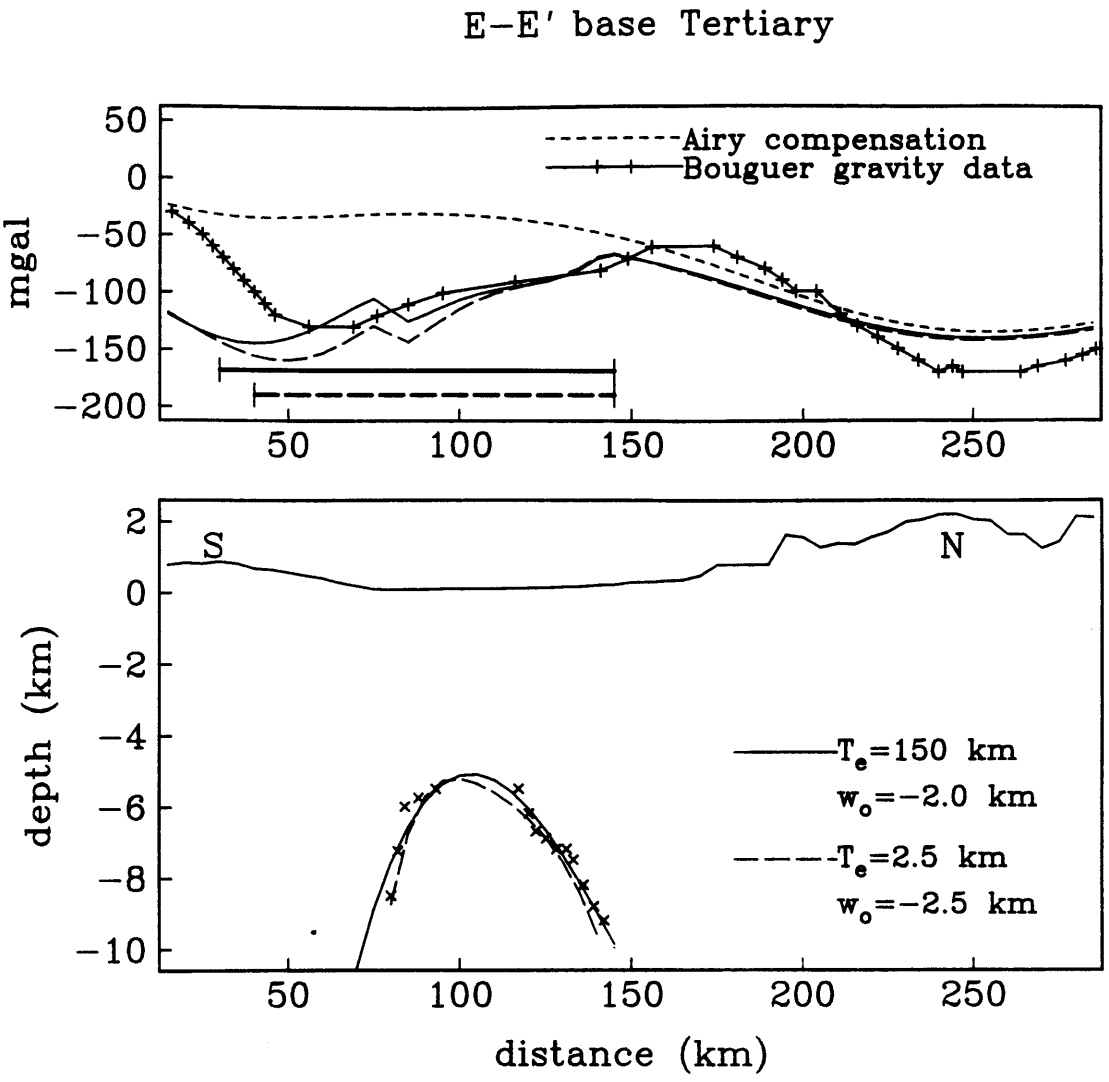
E–E′ base Tertiary
Airy compensation
Bouguer gravity data
mgal
50
0
−50
−100
−150
−200
50
100
150
200
250
S
N
depth (km)
2
0
−2
−4
−6
−8
−10
T_e=150 km
w_o=−2.0 km
T_e=2.5 km
w_o=−2.5 km
distance (km)

Figure 18(a)

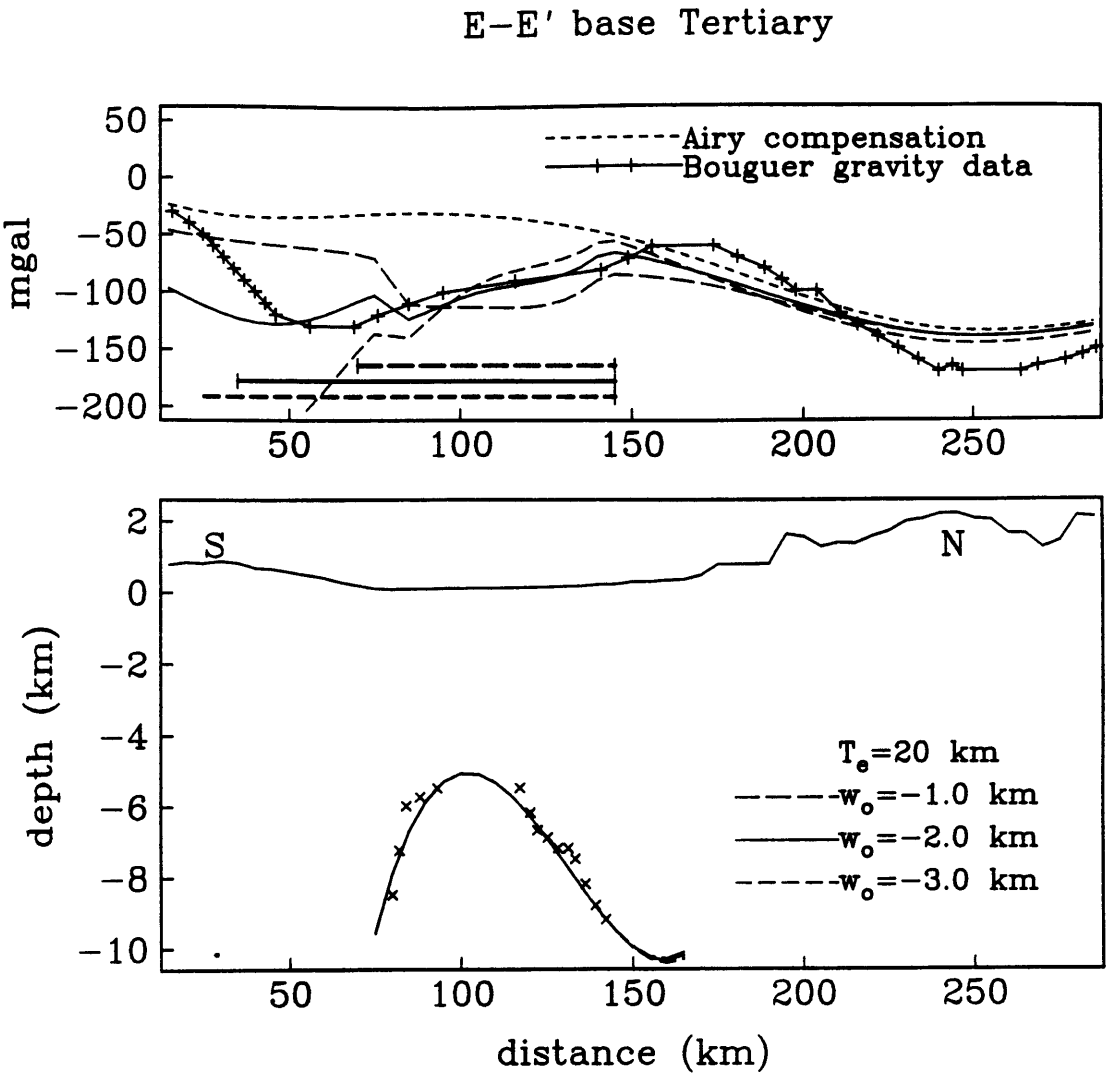
E–E' base Tertiary
Airy compensation
Bouguer gravity data
mgal
50
0
−50
−100
−150
−200
50
100
150
200
250
S
N
depth (km)
2
0
−2
−4
−6
−8
−10
T_e=20 km
w_o=−1.0 km
w_o=−2.0 km
w_o=−3.0 km
distance (km)

Figure 18(b)

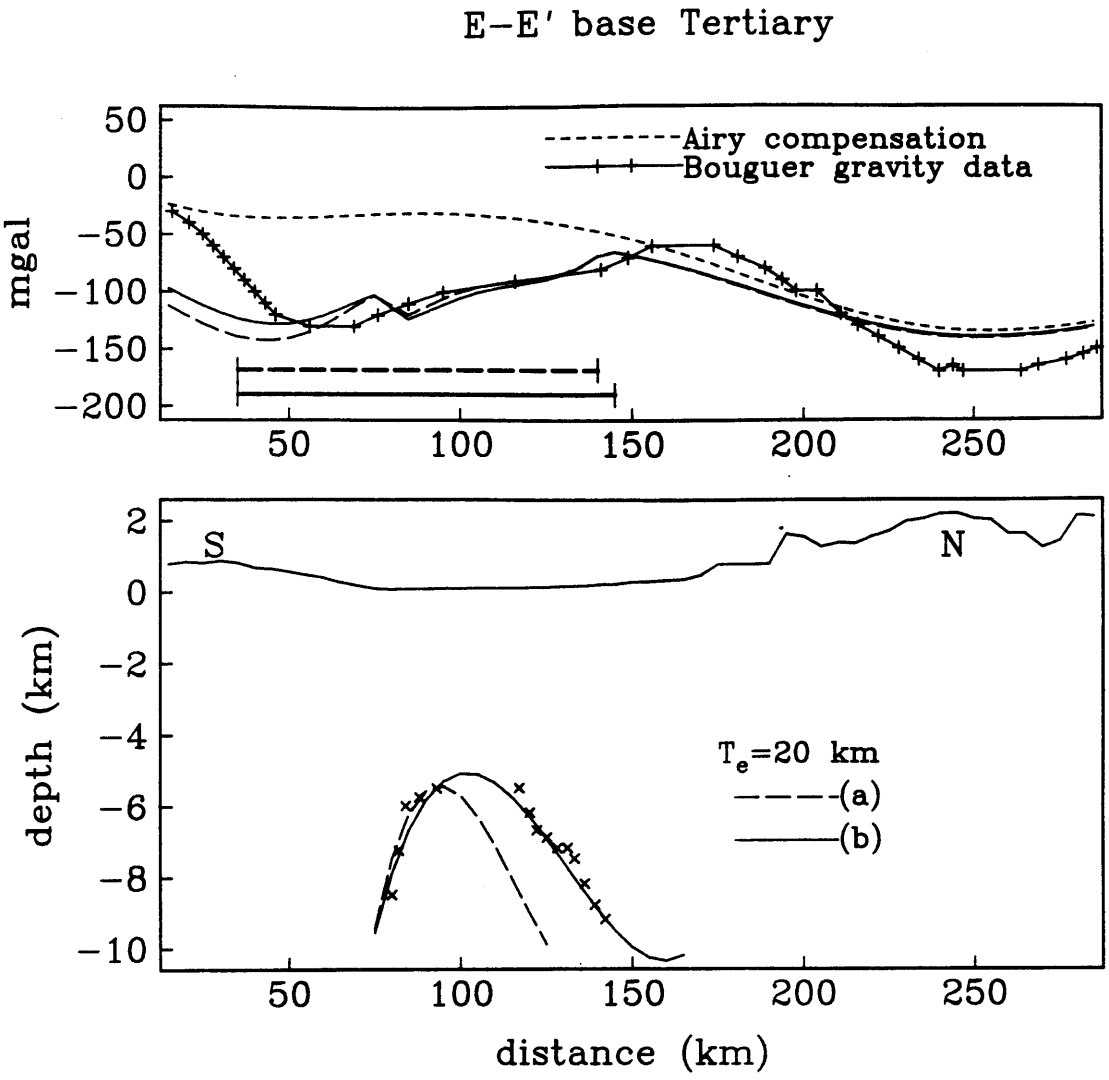
E–E′ base Tertiary
Airy compensation
Bouguer gravity data
mgal
50
0
−50
−100
−150
−200
50
100
150
200
250
S
N
depth (km)
2
0
−2
−4
−6
−8
−10
T_e=20 km
(a)
(b)
distance (km)

Figure 18(c)

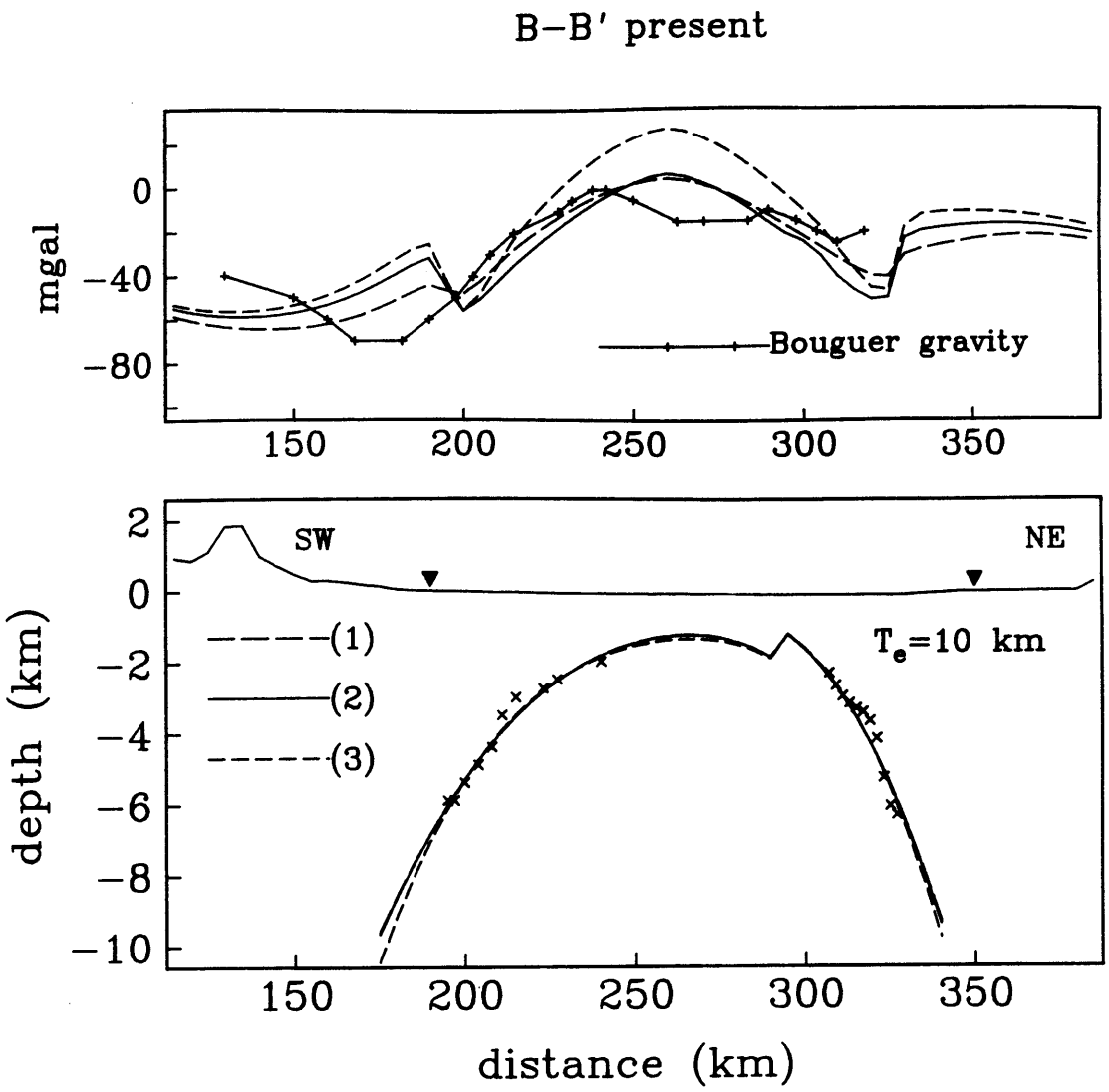
B–B′ present
mgal
0
−40
−80
Bouguer gravity
150
200
250
300
350
SW
NE
2
0
−2
−4
−6
−8
−10
(1)
(2)
(3)
T_e=10 km
depth (km)
distance (km)

Figure 19(a)

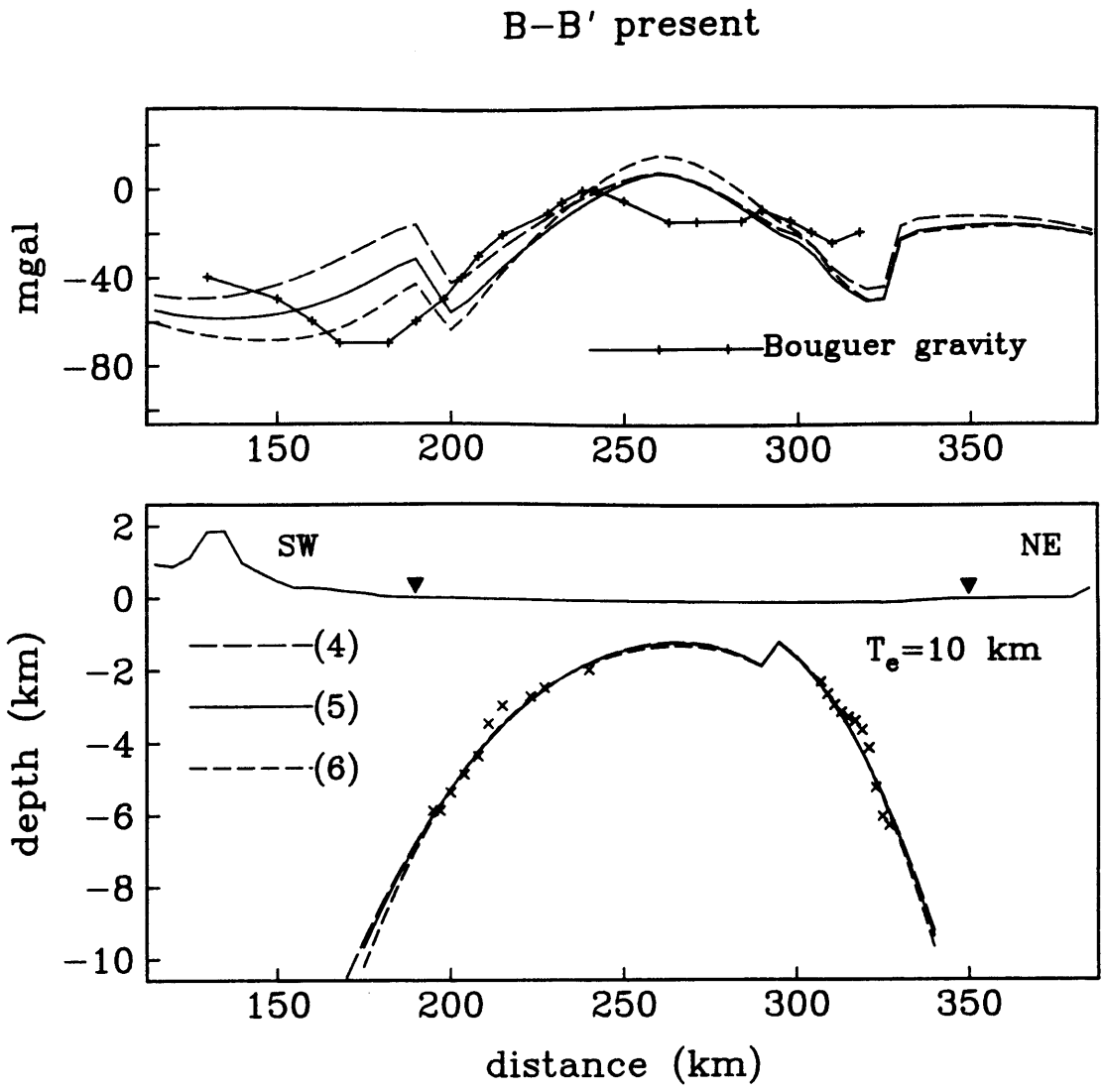
B–B′ present
mgal
0
−40
−80
Bouguer gravity
150
200
250
300
350
SW
NE
2
0
−2
−4
−6
−8
−10
depth (km)
(4)
(5)
(6)
T_e=10 km
distance (km)

Figure 19(b)

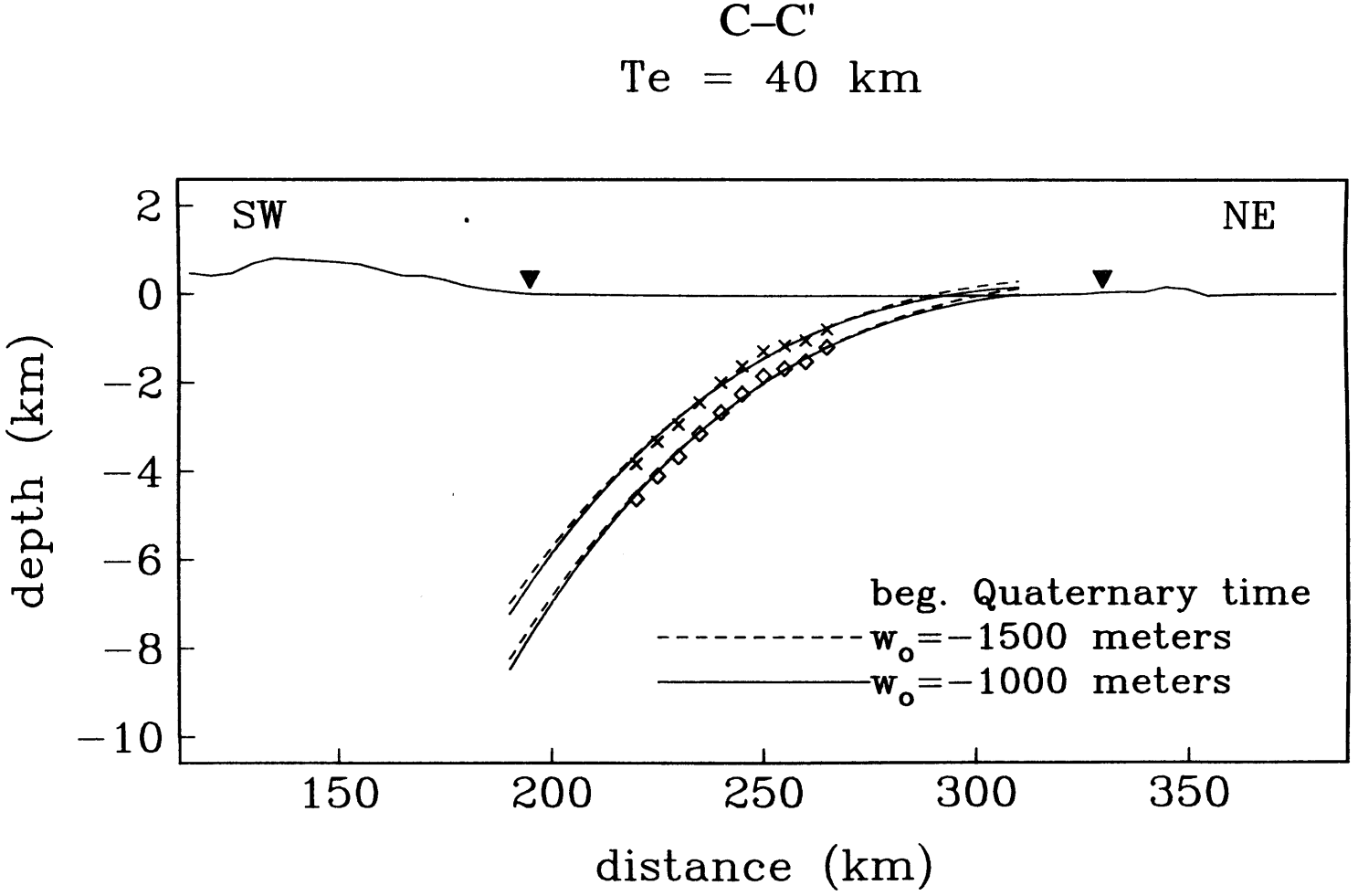
C–C'
Te = 40 km
SW
NE
2
0
−2
−4
−6
−8
−10
depth (km)
150
200
250
300
350
distance (km)
beg. Quaternary time
w_o=−1500 meters
w_o=−1000 meters

Figure 19(c)

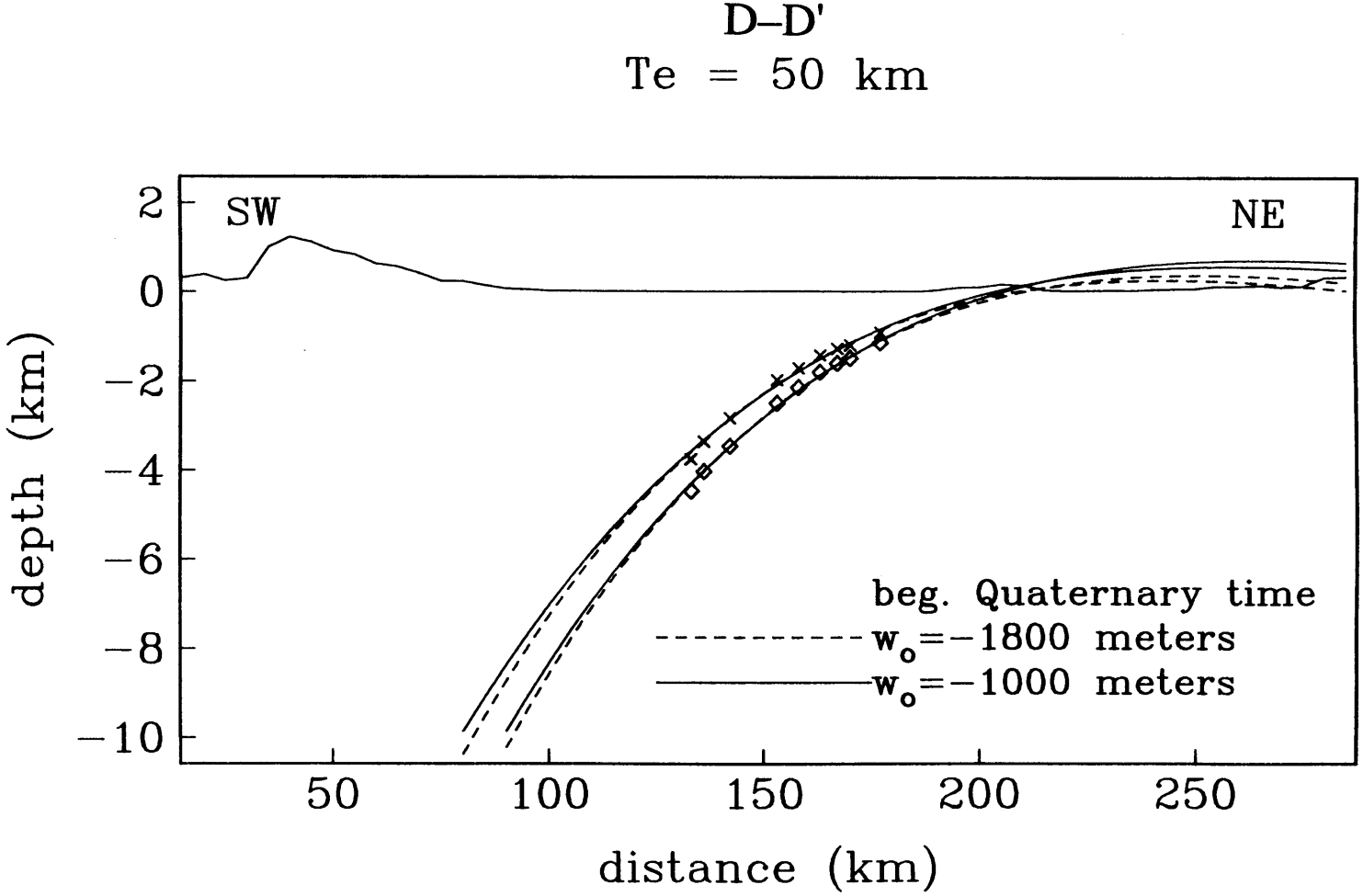
D–D'
Te = 50 km
SW
NE
depth (km)
2
0
−2
−4
−6
−8
−10
50
100
150
200
250
distance (km)
beg. Quaternary time
w_o=−1800 meters
w_o=−1000 meters

Figure 19(d)

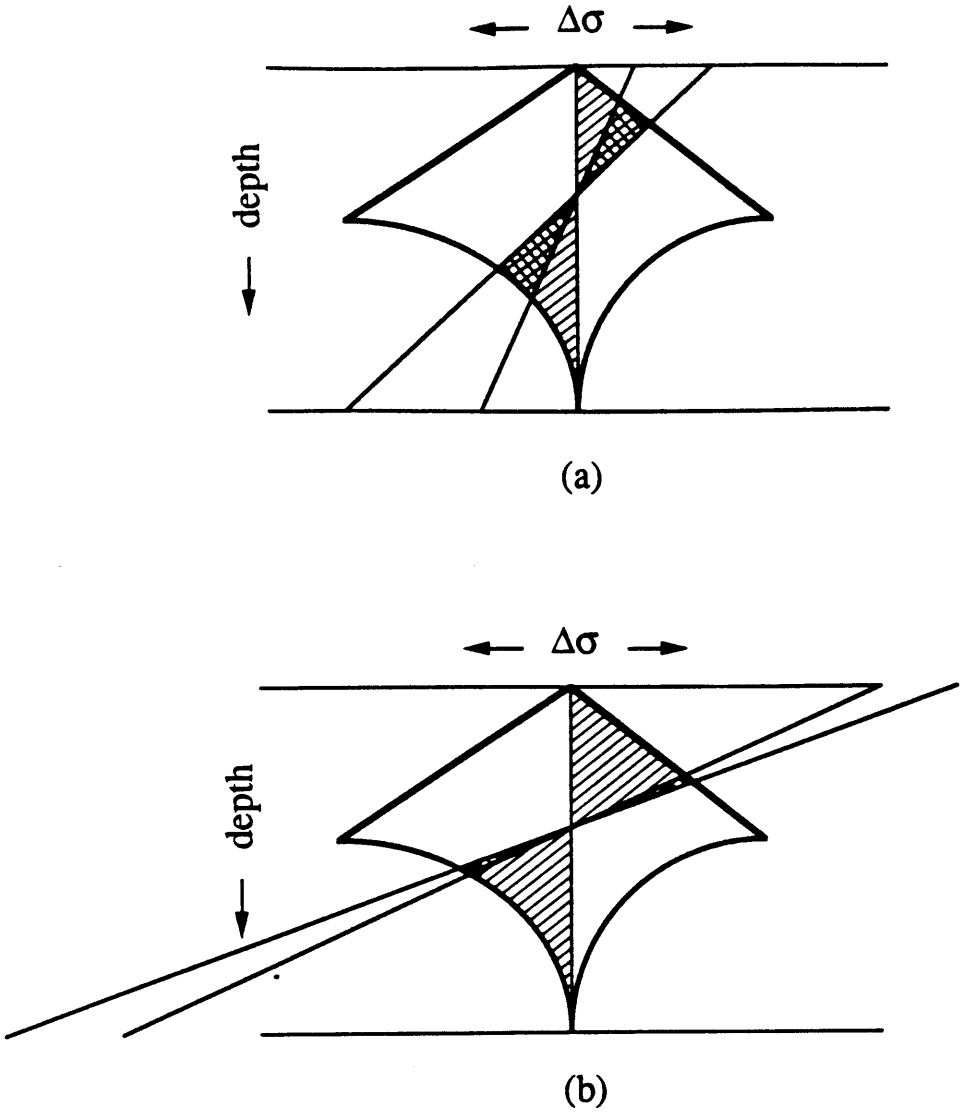

Figure 20(a,b)

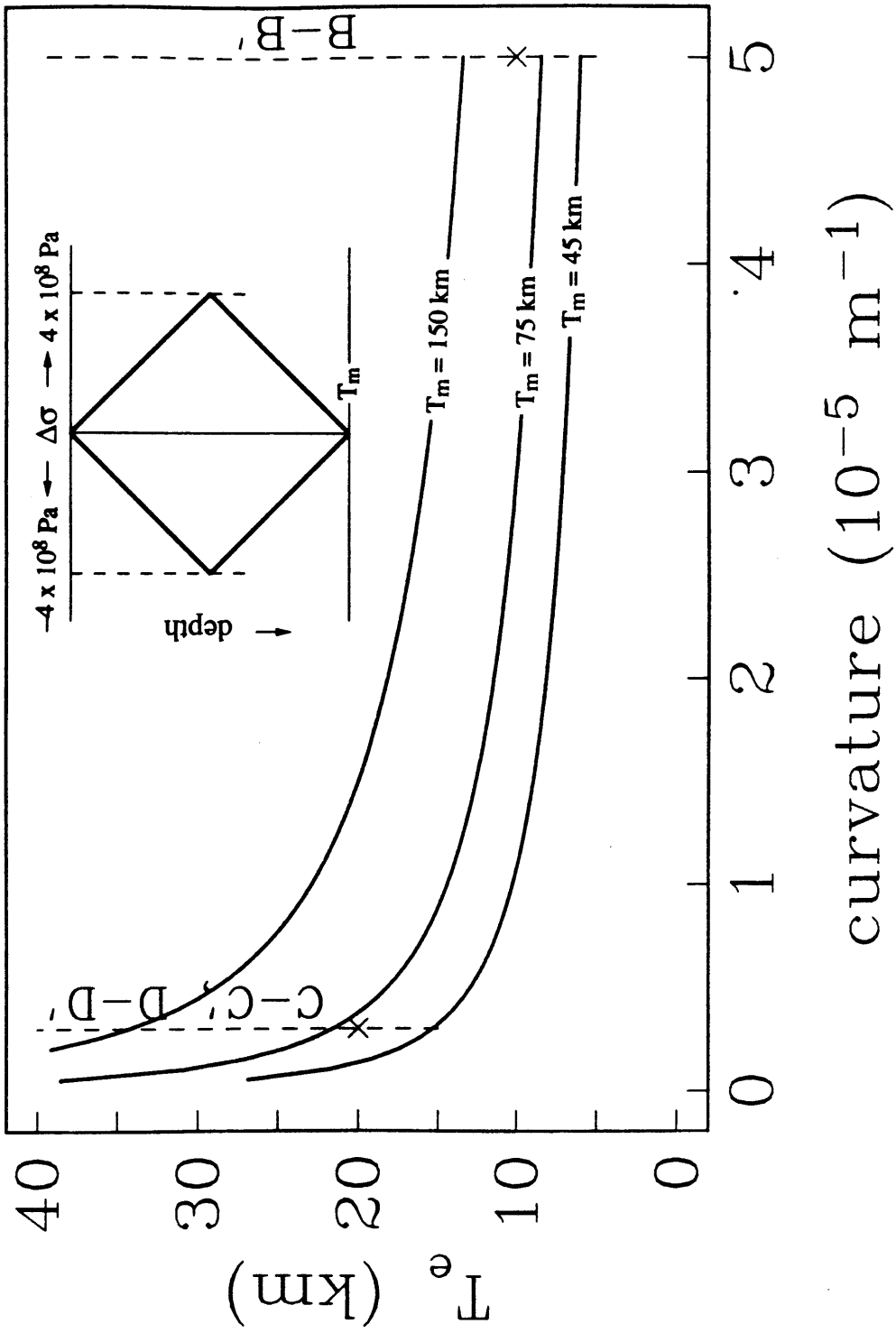
B–B'
C–C', D–D'
T_m = 150 km
T_m = 75 km
T_m = 45 km
-4×10^8 Pa ← Δσ → 4×10^8 Pa
T_m
depth
T_e (km)
curvature (10^{-5} m^{-1})
0
10
20
30
40
0
1
2
3
4
5

Figure 20(c)

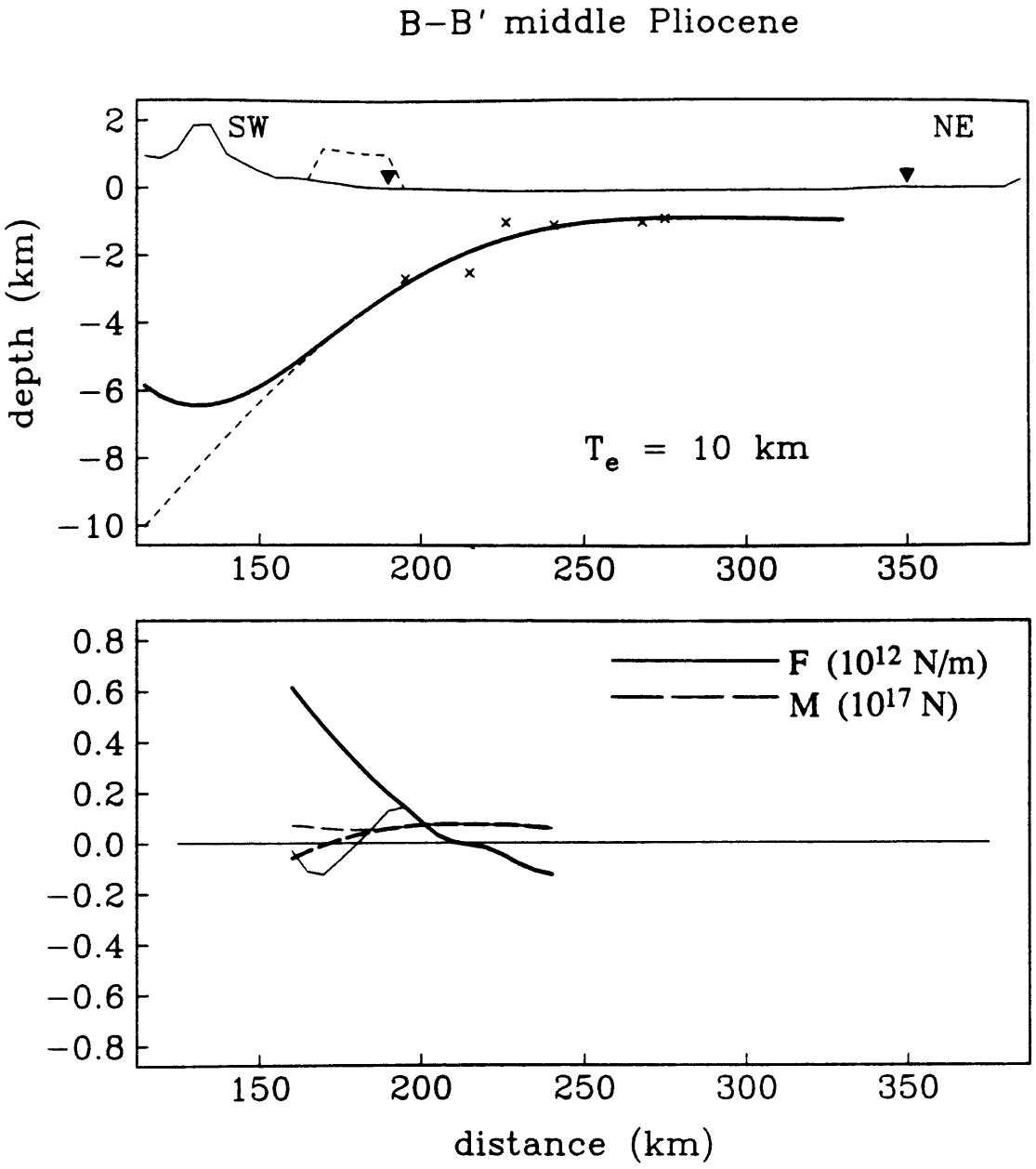
B–B′ middle Pliocene
SW
NE
depth (km)
2
0
−2
−4
−6
−8
−10
T_e = 10 km
150
200
250
300
350
0.8
0.6
0.4
0.2
0.0
−0.2
−0.4
−0.6
−0.8
F (10^{12} N/m)
M (10^{17} N)
distance (km)

Figure 21(a)

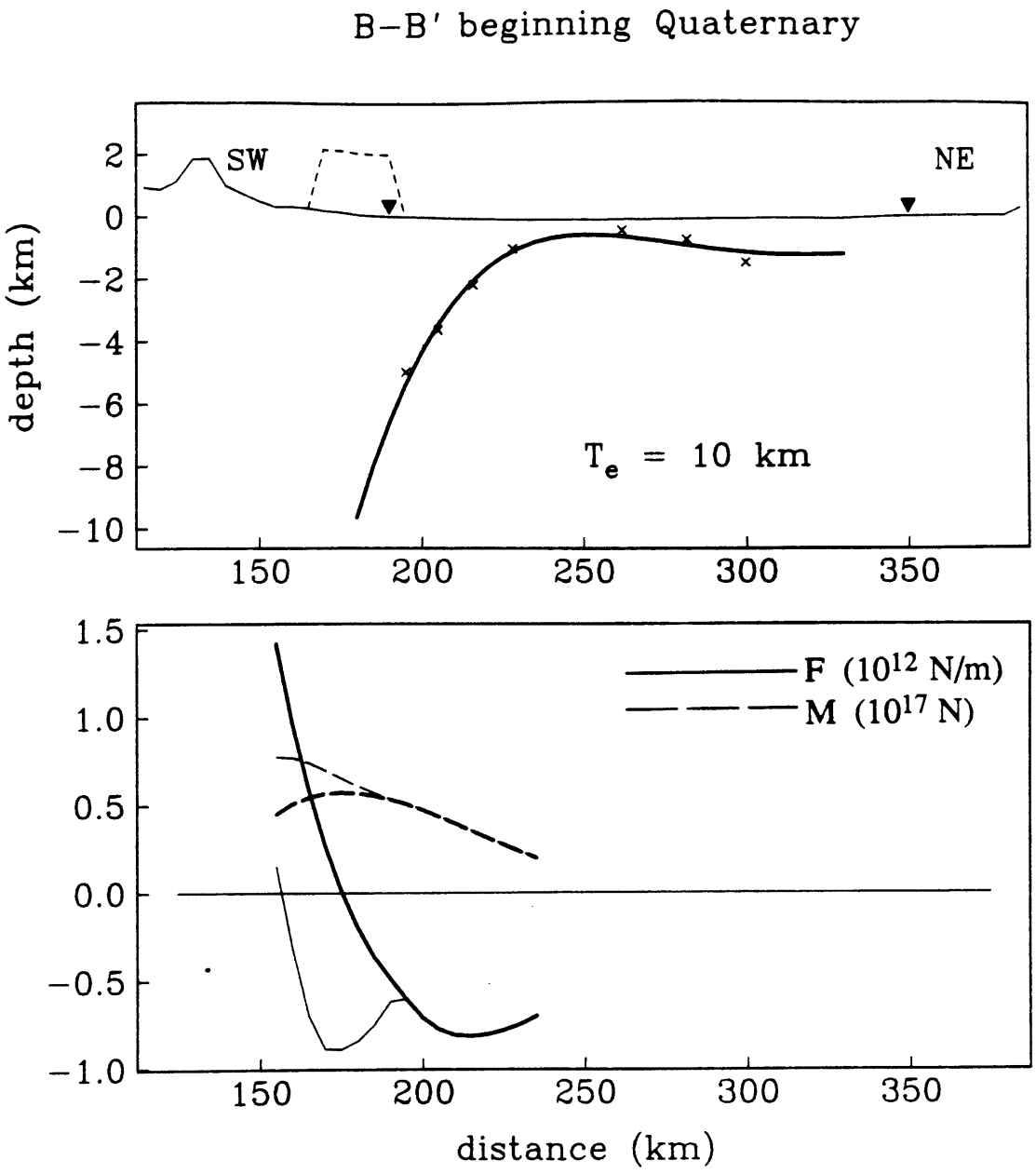
B–B′ beginning Quaternary
SW
NE
depth (km)
2
0
−2
−4
−6
−8
−10
T_e = 10 km
150
200
250
300
350
1.5
1.0
0.5
0.0
−0.5
−1.0
F (10^{12} N/m)
M (10^{17} N)
distance (km)

Figure 21(b)

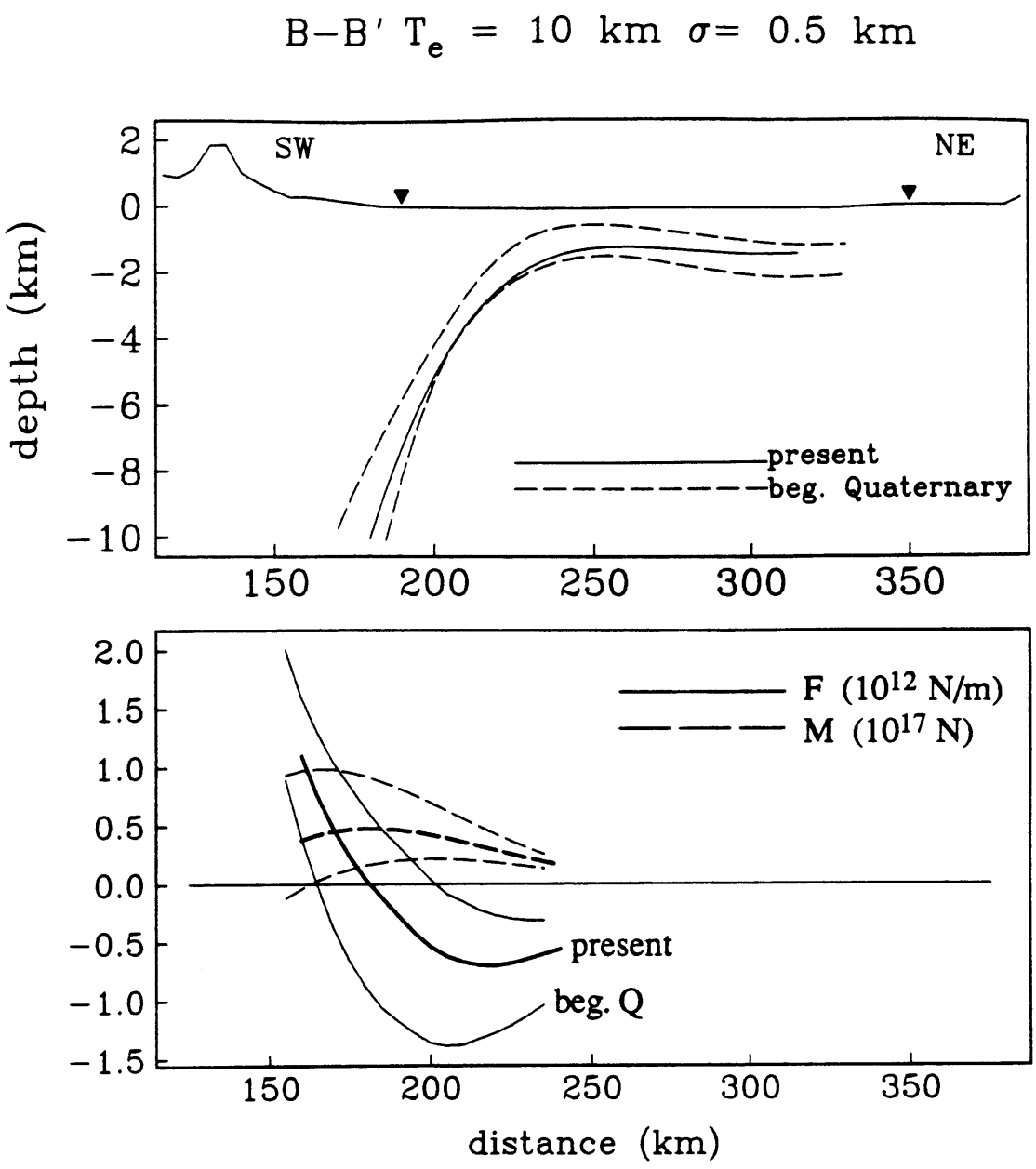
B–B′ T_e = 10 km σ= 0.5 km
SW
NE
depth (km)
2
0
−2
−4
−6
−8
−10
150
200
250
300
350
present
beg. Quaternary
2.0
1.5
1.0
0.5
0.0
−0.5
−1.0
−1.5
F (10^{12} N/m)
M (10^{17} N)
present
beg. Q
distance (km)

Figure 22(a)

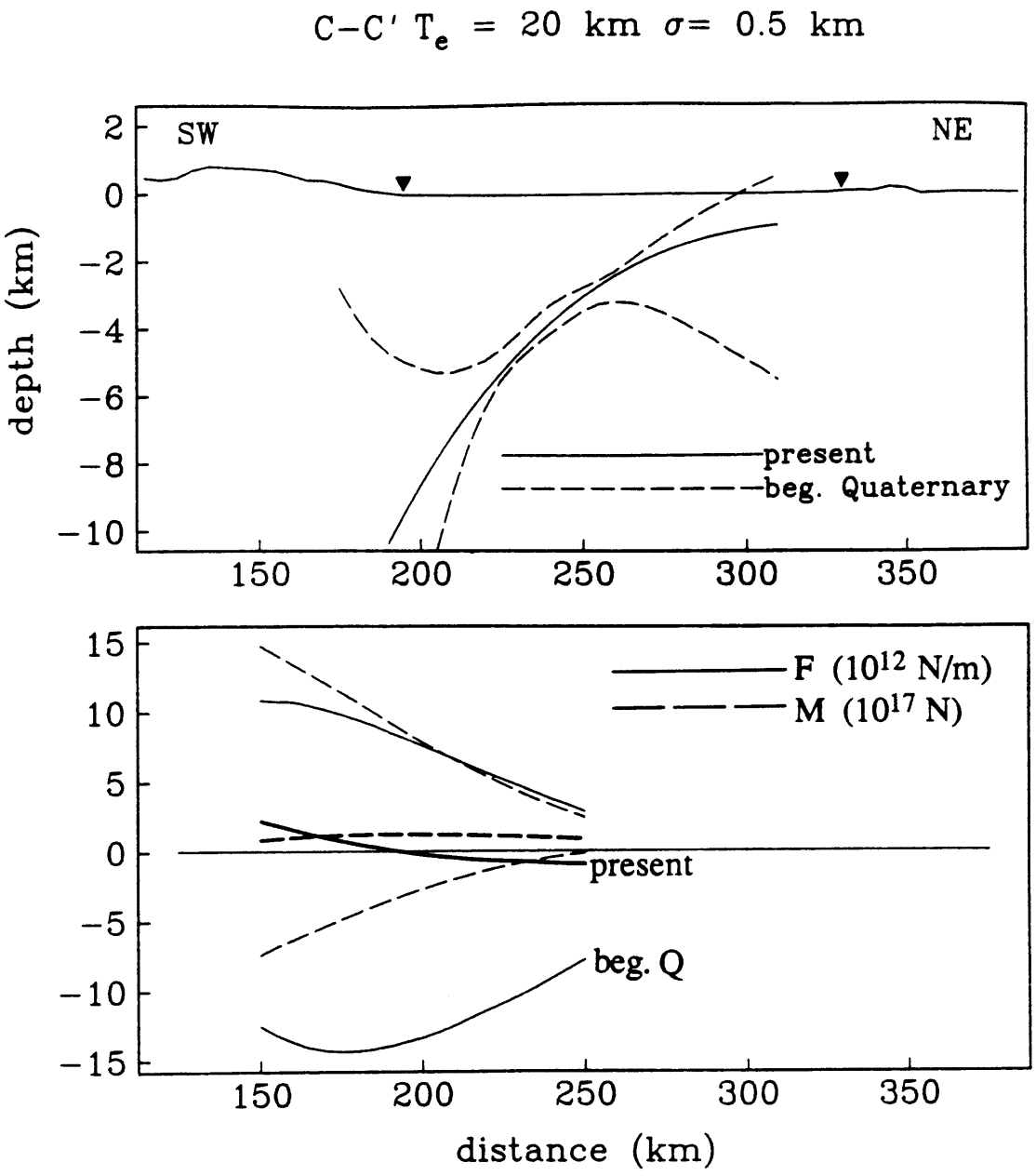
C–C′ T_e = 20 km σ= 0.5 km
SW
NE
depth (km)
2
0
−2
−4
−6
−8
−10
150
200
250
300
350
present
beg. Quaternary
15
10
5
0
−5
−10
−15
F (10^{12} N/m)
M (10^{17} N)
present
beg. Q
distance (km)

Figure 22(b)

Figure 23

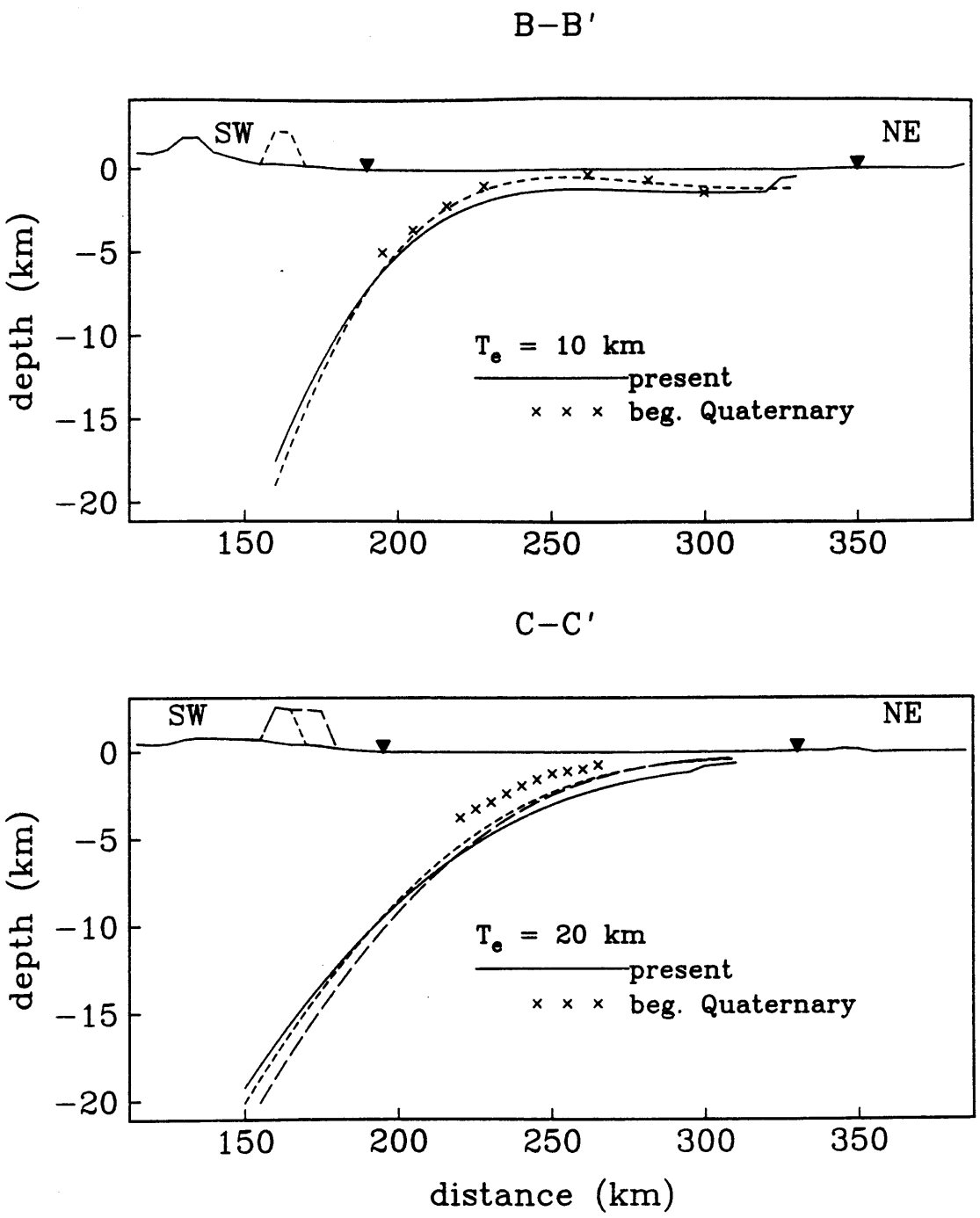
B–B′
SW
NE
0
−5
−10
−15
−20
depth (km)
T_e = 10 km
present
beg. Quaternary
150
200
250
300
350
C–C′
SW
NE
0
−5
−10
−15
−20
depth (km)
T_e = 20 km
present
beg. Quaternary
150
200
250
300
350
distance (km)

Figure 24(a,b)

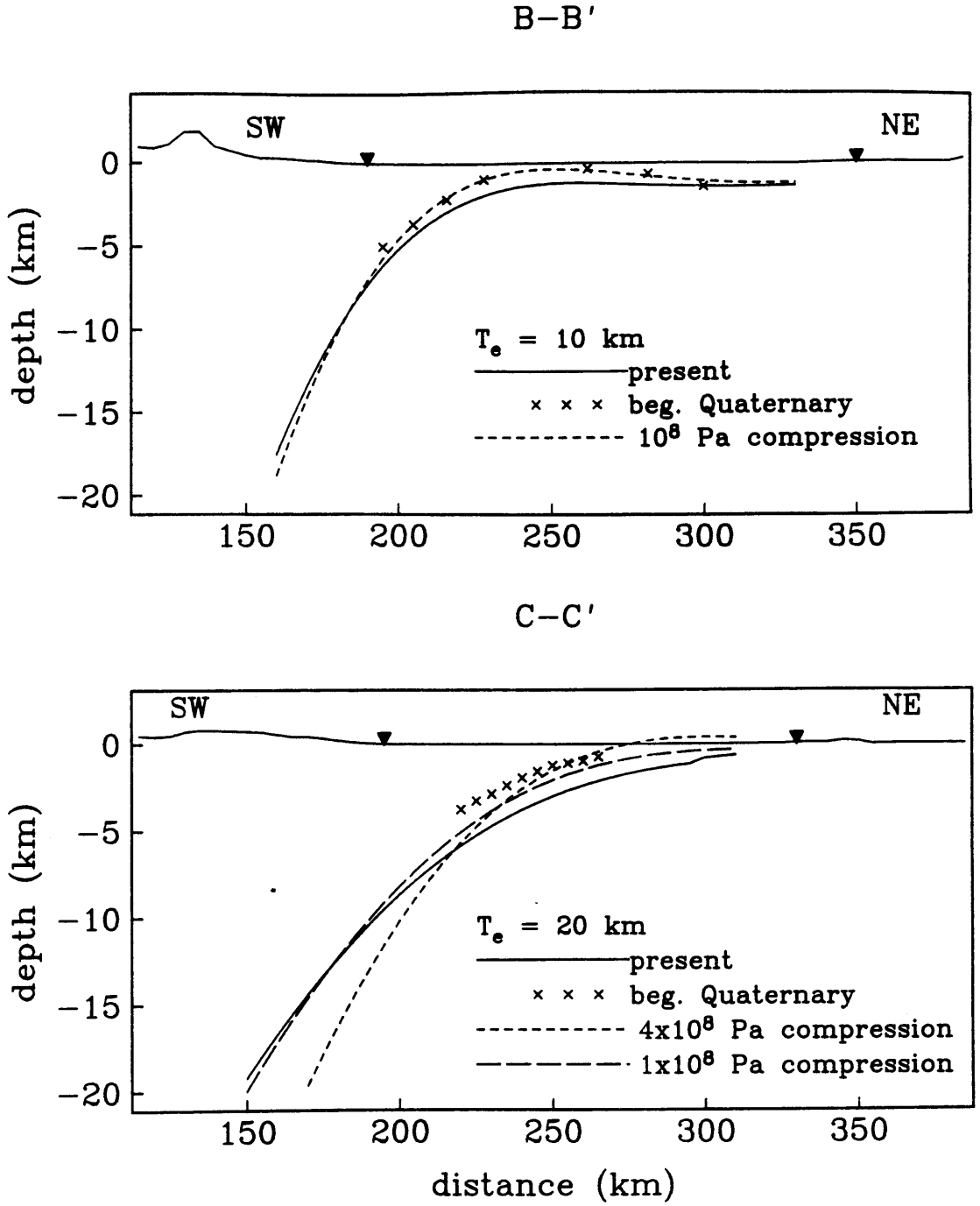
B–B′
SW
NE
0
−5
−10
−15
−20
depth (km)
150
200
250
300
350
T_e = 10 km
present
beg. Quaternary
10^8 Pa compression
C–C′
SW
NE
0
−5
−10
−15
−20
depth (km)
150
200
250
300
350
distance (km)
T_e = 20 km
present
beg. Quaternary
$4x10^8$ Pa compression
$1x10^8$ Pa compression

Figure 24(c,d)

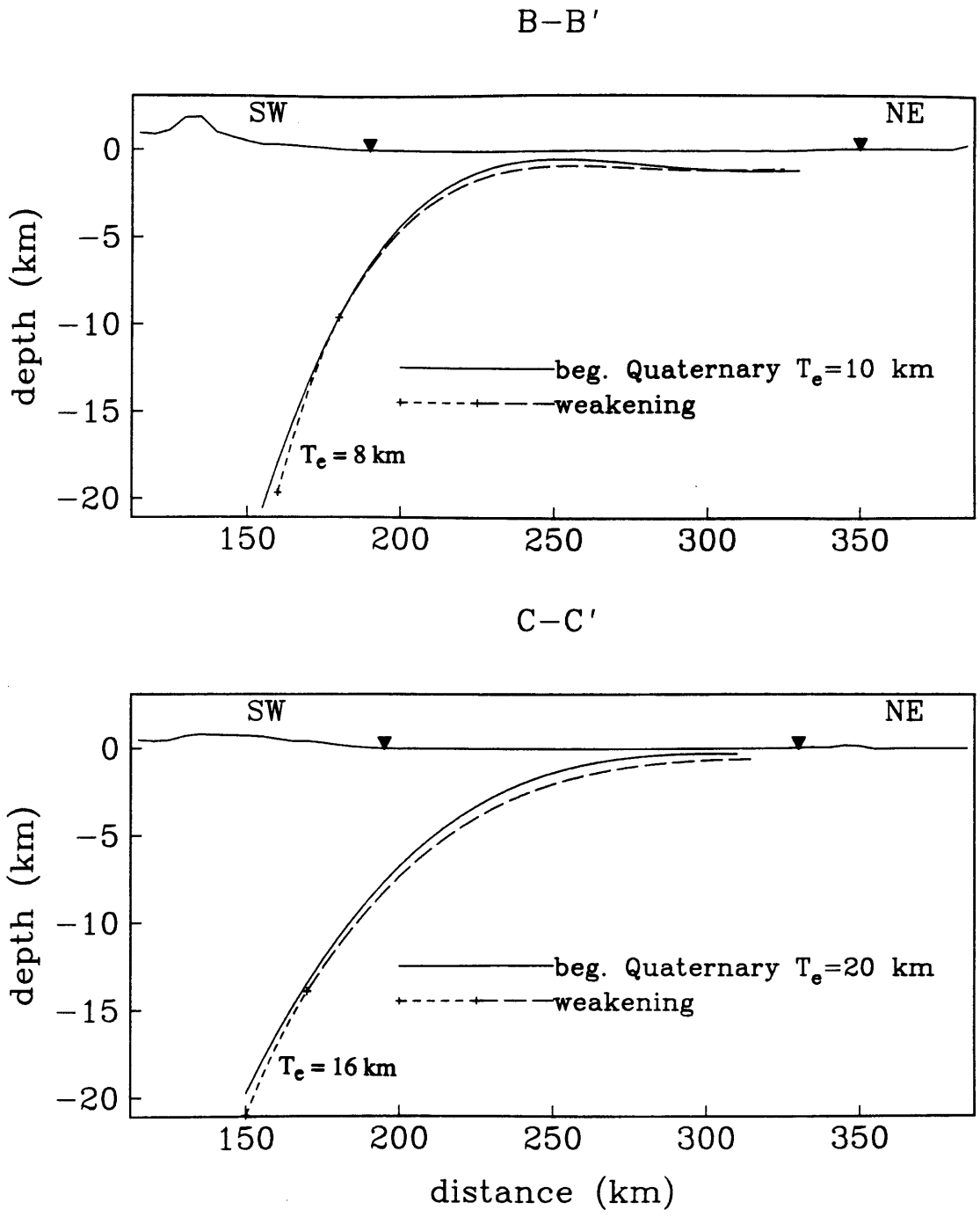
B–B′
SW
NE
0
−5
−10
−15
−20
depth (km)
beg. Quaternary T_e=10 km
weakening
T_e = 8 km
150
200
250
300
350
C–C′
SW
NE
0
−5
−10
−15
−20
depth (km)
beg. Quaternary T_e=20 km
weakening
T_e = 16 km
150
200
250
300
350
distance (km)

Figure 24(e,f)

CHAPTER 3
LITHOSPHERIC EXTENSION NEAR LAKE MEAD, NEVADA: A MODEL FOR DUCTILE FLOW IN THE LOWER CRUST

INTRODUCTION

Numerous authors have noted that parts of the Basin and Range in the western United States that have undergone considerable crustal extension or denudation lie at comparable or only slightly lower elevations than nearby unextended areas [for example *Mayer* [1986]; *Thompson and McCarthy* [1986]; *McKenzie* [1988]; *Block and Royden* [1989]). This observation is puzzling because a local (Airy) isostatic compensation model predicts that highly extended areas with thinned crust should be considerably lower topographically than unextended regions. Lithospheric warming associated with extension of the entire lithosphere (as in the pure shear model of *McKenzie* [1978]) will only partially offset the effect of crustal thinning on surface elevations. Similarly, differences in observed Bouguer gravity anomalies between extended and unextended regions are smaller than those predicted from simple models for crustal thinning.

Several hypotheses have been proposed to explain the relatively small differences in topography and gravity anomalies between adjacent regions that have undergone very different amounts of extension or upper crustal denudation. These include (1) a greater initial crustal thickness in areas subsequently extended; (2) a difference in mantle properties beneath thinned and unextended crust; (3) transport of material along low angle normal faults; (4) crustal underplating processes that add material to the base of the crust in thinned areas; and (5) ductile flow of lower crustal material from regions of thicker upper crust toward regions of thinner upper crust that reduces lateral variations in net crustal thickness.

We test these hypotheses in the area around Lake Mead, Nevada, which is a transition zone between highly extended Basin and Range crust and the unextended Colorado Plateau. This area was chosen because it exhibits an offset in topography (1000 meters) between the Basin and Range and Colorado Plateau provinces that is smaller than the value predicted by pure shear models considering extension estimates of a factor of 2 [*Wernicke et al.*, 1988]. Data are also available to evaluate the potential of several of the mechanisms described above to explain the topography and gravity observations. In particular, constraints exist on the crustal thickness prior to the onset of Basin and Range extension and on the geometry of normal faulting in the region. Finally, we focus on the conditions under which ductile flow of lower crustal material can explain the gravity and topography data in the Lake Mead area as well as observations of uniform crustal thickness across metamorphic core complexes and other regions of variable amounts of extension.

TECTONIC SETTING

The breakaway zone separating the Basin and Range and Colorado Plateau provinces in the western United States at the latitude of Lake Mead trends roughly north–south. The Basin and Range province to the west is characterized by elevations of 500 to 1500 meters, anomalously high heat flow values, and a crustal thickness of about 30 km [*Allmendinger et al.*, 1987]. The Colorado Plateau to the east lies at elevations approximately 1000 meters above the adjacent Basin and Range and consists of flat–lying or gently dipping strata overlying crust estimated to be approximately 40 km [*Thompson and Zoback*, 1979] or 50 km thick [*Hauser and Lundy*, 1989]. Colorado Plateau surface heat flow values are roughly half those of the Basin and Range [*Lachenbruch and Sass*, 1978].

The abrupt transition between the Basin and Range and Colorado Plateau provinces near Lake Mead is delineated by a 5 to 10 km–wide sedimentary basin that separates east–dipping normal–faulted blocks of the Basin and Range from the flat–lying strata at the western margin of the Colorado Plateau (Figures 1,2). The Gold Butte block, which lies between Lake Mead and the transition zone, may record 10 to 20 kilometers of unroofing, where we define the magnitude of unroofing as the amount of upward vertical motion undergone by rocks now at the surface (Figure 2) [J. Fryxell, personal communication, 1989; *Wernicke and Axen*, 1988]. Along the breakaway zone, the detachment surface dips westward away from the Colorado Plateau beneath the tilted blocks of the eastern margin of the faulted region.

Based on reconstructions of the relative positions of structural units, extension across the entire Basin and Range at this latitude is estimated by *Wernicke et al.* [1988] to be 190 to 300 km (an extension factor β of 2 to 6) with net orientation about N73°W. These authors similarly estimate extension across the eastern part of the Basin and Range (between the Colorado Plateau and the Spring Mountains) to be between 60 and 125 km (β = 1.7 to 7) with an orientation roughly N 70° E. Extension in the Lake Mead region has occurred principally in the last 15 m.y. [*Wernicke et al.*, 1988].

Pre–extensional tectonic boundaries lie near, but do not coincide exactly with, the present breakaway zone. A latest Precambrian–Paleozoic hinge line for the Paleozoic continental margin trends NE–SW near Las Vegas, some 50–60 km west of the breakaway zone. East–vergent thin–skinned Cretaceous thrusts overlap this hinge zone and extend farther eastward, terminating near Lake Mead [*Burchfiel et al.*, 1974]. The frontal thrust overlies the craton rather than continental margin basement and lies generally west of the breakaway zone. Structural differentiation of regional ash–flow tuffs suggests that the elevation difference between the Basin and Range and the Colorado Plateau may have

predated Basin and Range extension by several million years in southwestern Utah [*Rowley et al.*, 1978]. There are, however, no direct observations of differences in pre–extensional elevation between the two provinces at the latitude of Lake Mead.

Variations in crustal thickness across the Lake Mead area prior to extension were probably small, as the Mesozoic hinge line and the thin–skinned Cretaceous thrust front lie to the west of the breakaway zone. The stable foreland region east of the thrust front which includes the Lake Mead transition zone was not affected by earlier thrust belt activity.

Together the unroofing of Gold Butte block and the extension estimates of *Wernicke et al.* [1988] suggest a minimum of 10 kilometers of crustal thinning associated with extension in the area west of the Lake Mead transition zone. This 10 kilometer value is a conservative minimum, corresponding to an extension factor of only 1.33 if pre–extension crustal thicknesses were 40 kilometers. The Gold Butte block unroofing further suggests the onset of at least 10 kilometers of crustal thinning occurs quite abruptly, within 50 kilometers of the transition zone.

TOPOGRAPHY, GRAVITY, SEISMIC, AND HEAT FLOW OBSERVATIONS

Seven hundred meter elevations in the Lake Mead region increase eastward across a transition zone less than 50 kilometers wide to approximately 1500 meters on the Colorado Plateau (Figures 3,5). Elevations on the Colorado Plateau increase gently to the east to approximately 2000 meters over the central Plateau. Bouguer gravity anomalies of approximately –120 mgal over the Basin and Range grow increasingly negative eastward to approximately –190 mgal over the Colorado Plateau (Figures 4,5). The transition in gravity values occurs over approximately 200 kilometers.

Figure 6a shows that the topography and Bouguer gravity together are compatible with a local (Airy) compensation model in which variations in elevation are compensated locally by deflections of the Moho (Airy mechanism). The gravity data are also compatible with a lithospheric flexural rigidity up to 10^{22} Nm (effective elastic plate thickness up to about 15 km) (Figure 6a). In these models the lower elevations over the Basin and Range are compensated by an approximately 5 kilometer decrease in crustal thickness, assuming a crustal density of 2700 kg/m^3 and mantle density of 3300 kg/m^3. The topography and gravity data are thus compatible with variations in crustal thickness in the Lake Mead area that are smaller than the difference between the 30–km crustal thickness recorded in COCORP profiling across the central Basin and Range [*Allmendinger et al.*, 1987] and the 40 or 50–km thickness of the Colorado Plateau interpreted from refraction and reflection data [*Thompson and Zoback*, 1979; *Hauser and Lundy*, 1989].

No direct seismic observations of crustal structure are available for the Lake Mead transition zone. Data across the Basin and Range–Colorado Plateau transition at other locations, however, show a variety of features. A 3 kilometer Moho offset is observed across the transition in west–central Arizona [*Hauser et al.*, 1987]. The COCORP transect across the transition zone at 40°N [*Allmendinger et al.*, 1987] shows a region without strong reflectors in the transition zone separating strong reflectors at 30 km in the Basin and Range from strong reflectors at both 30 km and 45 km depth beneath the Colorado Plateau.

A recent estimate of *Pn* velocities of 8.1 km/s in the mantle beneath the Colorado Plateau [*Beghoul and Barazangi*, 1989] suggests these velocities are significantly higher than the 7.8 km/s values found in the Basin and Range. The length scale of the transition in velocities is undetermined.

Data compiled by *Lachenbruch and Sass* [1978] indicate heat flow in the Basin and Range (60 to 100 mW/m^2) is considerably greater than that observed in the Colorado Plateau (30 to 60 mW/m^2). Heat flow data across the transition zone are sparse. Assuming an exponential distribution of radioactive heat production with depth, *Lachenbruch and Sass* [1978] derive crustal geotherms of 25 to 30°C/km in the Basin and Range and approximately 15°C/km for stable lithosphere such as the Colorado Plateau, and temperatures of 700 to 1000°C near the base of the crust at 30 to 40 km depth beneath the Basin and Range. Their modeling suggests temperature differences at subcrustal depths between the Basin and Range and unextended lithosphere like the Colorado Plateau may be 200 to 500°C. The difference in heat flow between the two provinces, however, may instead reflect the time lag associated with conduction of Cenozoic changes in the thermal regime to the surface of the Colorado Plateau [*Thompson and Zoback*, 1979]. The elevation of the Colorado Plateau and the presence of Cenozoic volcanism over both the Basin and Range and the Colorado Plateau near Lake Mead suggest that deep crustal and subcrustal temperatures may be unusually high in both provinces.

MODELS FOR LITHOSPHERIC EXTENSION

A local (Airy) compensation mechanism predicts a decrease in elevation over thinned crust that is almost twice the value observed between the extended Basin and Range and the unextended Colorado Plateau near Lake Mead, for the lower bound estimate of 10 kilometers of Basin and Range crustal thinning. The elevation change Δe can be written $\Delta e = -\Delta h(\rho_m - \rho_c)/\rho_m$, where Δh is the crustal thinning, and ρ_m and ρ_c are mantle and crustal densities, respectively. For Δh = 10 km, ρ_m = 3300 kg/m3, and ρ_c = 2700 kg/m3, we find the Airy model predicts Δe = 1800 meters, as compared with the observed 1000

meter topographic step observed across the transition zone. The simple uniform lithospheric extension model of *McKenzie* [1978] can predict the difference in topography between unextended and extended regions for the the lower bound 10 kilometer estimate of crustal thinning. This model assumes that the temperature at the base of the lithospheric plate remains constant as the mantle and crust extend and thin. The change in elevation Δe in lithosphere extending uniformly by a factor β can be written

$$\Delta e = -h_c \frac{(\rho_m - \rho_c)}{\rho_m}\left(1 - \frac{1}{\beta}\right) + \frac{\rho_m \alpha T_m l}{2\rho_c}\left(1 - \frac{1}{\beta}\right) \quad (1)$$

[*McKenzie*, 1978] where h_c is the pre–extensional crustal thickness, ρ_m and ρ_c are as defined above, α is the coefficient of thermal expansion, T_m is the temperature at the base of the mantle, and l is the pre–extensional thickness of the lithosphere. For a lower bound estimate of the extension corresponding to an extension factor of $\beta = 1.33$ (10 km of thinning of crust initially 40 km thick), setting $\rho_m = 3300$ kg/m^3, $\rho_c = 2700$ kg/m^3, $\alpha = 3 \times 10^{-5}$ °C^{-1}, $T_m = 1350$°C, and $l = 125$ kilometers, Equation 1 predicts that $\Delta e = -1$ kilometer. This model also yields a fit to the gravity data which is not as good as that of the Airy model, but does roughly predict the change in gravity anomalies across the transition zone (Figure 6b).

The uniform extension model fails, however, to predict the both the topography and gravity data for the extension estimates corresponding to the β values of 1.7 or more preferred by *Wernicke et al.* [1988]. For an extension factor $\beta = 2$, corresponding to 20 km of thinning of crust initially 40 km thick, and other lithospheric parameters equal to the values in the preceding example, this model predicts a decrease in elevation over the eastern Basin and Range of approximately 2 kilometers, or twice that observed. Gravity anomalies associated with extension by a factor of two also misfit the observed values (Figure 6b).

To explain elevations across Lake Mead transition zone, the uniform extension model also requires that the transition in mantle temperatures that result from lithospheric thinning coincides exactly with, and occurs as abruptly as, the transition in crustal thickness. This may be unreasonable over the 50–km wide Lake Mead transition zone, where some geologic evidence points to elevated temperatures beneath the unextended Colorado Plateau as well as beneath the Basin and Range (see discussion above).

Several different mechanisms have been proposed to explain the extension estimates and the topography and gravity data by predicting a difference between whole crustal thinning and the crustal thinning estimated from surface extension. These include (1) initial

thickening of extended areas, (2) crustal thinning in the footwall of large scale low–angle normal faults, (3) crustal underplating, and (4) ductile flow in the lower crust. These processes will thin the crust in the unextended region or thicken the crust in the extending region prior to, during, or subsequent to the extension process.

The first mechanism, that presently extended regions correspond to areas of unusually large crustal thickness prior to the onset of extension, has been proposed by several authors (for example *Mayer*, 1986; *Holt et al.*, 1986; *Sonder et al.* 1987; *Dewey*, 1988). Subsequent extension may return the crust in these regions to an 'average' crustal thickness. This process appears unlikely in the Lake Mead area, where evidence discussed above points to a uniform pre–extensional crustal thickness across the transition zone.

The second mechanism invokes large scale low–angle normal faulting, which will tend to smooth out an abrupt transition in crustal thickness between extended and unextended regions by thinning the apparently unextended footwall crust, if the detachment faults dip beneath the unextended area [*Wernicke*, 1985]. This process may be active along part of the eastern boundary of the Basin and Range province, where breakaway faults dip to the east, but is not viable at the latitude of Lake Mead, where the breakaway fault dips westward away from the Colorado Plateau.

The third mechanism, crustal underplating, predicts that addition of mantle–derived material at the base of the crust can occur as a result of melt generation associated with mantle upwellings to crustal depths (for example *Furlong and Fountain*, 1986). Several authors have suggested this process may be a viable mechanism for crustal replenishment in the Basin and Range [*Furlong and Fountain*, 1986; *Okaya and Thompson*, 1986; *Thompson and McCarthy*, 1986; *Gans*, 1987]. The underplating model is somewhat ad hoc explanation for apparent discrepancy between crustal extension and crustal thinning, however, as it does not predict that the mantle upwellings producing underplating should coincide precisely with regions of crustal extension.

The underplating mechanism may also not be capable of adding an amount of crustal material sufficient to explain the observations near Lake Mead. Unless we invoke an exceptionally large and abrupt discontinuity in mantle densities across the transition zone (as discussed above), the underplating mechanism must add on the order of 5 to 10 kilometers of material to the base of the extended crust to explain the discrepancy between the zero to 5 km transition in crustal thickness of the simple Airy compensation model that best fits the gravity data, and the minimum of 10 km of crustal thinning west of the transition zone. To add 5 to 10 kilometers to the base of the crust at 30 to 40 km depth, however, requires an extremely warm plume capable of efficient segregation of melts generated at depths to 100 km or more [*Furlong and Fountain*, 1986].

The fourth mechanism, redistribution of ductile lower crustal material driven by lateral pressure gradients due to variations in the thickness of the overlying upper crust, will also tend to smooth out variations in total crustal thickness. Ductile crustal flow has previously been proposed to explain the relative uniformity of topography over regions of variable extension [*Gans*, 1987; *McKenzie*, 1988] and the lack of subsidence over denuded core complexes [*Block and Royden*, 1989]. *McCarthy and Thompson* [1988] interpret the large number of lower crustal reflectors in extensional provinces in the western United States as possible evidence for ductile strain (or intrusive layering) in the lower crust. Influx of crustal material beneath uplifted regions is also assumed in the isostatic response of the crust in *Buck* 's [1988] model for the generation of low angle normal faults in metamorphic core complexes and in the model of *Wernicke and Axen* [1988] for the uplift of footwalls of normal faults. In the following sections we examine the conditions under which such ductile flow in the crust could add 5 to 10 kilometers to the thickness of extended crust observed at Lake Mead.

DUCTILE FLOW MODELS

Rheological Justification

Justification for modeling the effects of ductile flow at lower crustal depths comes from laboratory experiments (e.g. *Goetze and Evans*, 1979; *Brace and Kohlstedt*, 1980; *Kirby*, 1983) and geological and seismic observations (for example *Smith and Bruhn*, 1984; *Gans*, 1987; *McCarthy and Thompson*, 1988) which suggest that crustal materials may deform ductilely under the pressure and temperature conditions found in the lower crust. Both laboratory and field observations suggests that the lower crust may be a weak layer bounded above and below by stronger layers. Figure 7a illustrates the maximum deviatoric stresses predicted for a continental lithosphere with a temperature gradient 10–20°C/km in the upper crust and approximately 10°C/km in the lower crust and mantle, for a strain rate of 10^{-15} s^{-1}. The weak region at lower crustal depths where maximum deviatoric stresses are small is presumably bounded above by a transition from brittle to ductile behavior and from below by a compositional transition at the Moho. Both the nature and depth of these transitions, however, are highly dependent on the geotherm, strain rates and compositions assumed and are in general poorly known. *Carter and Tsenn* [1987] have shown that the depth of a brittle–ductile transition may occur over virtually any depth greater than 10 km, depending on the composition, temperature, and strain rates

within the crust. Under certain conditions more than one weak ductile layer may exist as well (Figure 7b, *Smith and Bruhn*, 1984).

In the following sections we discuss three models for lower crustal ductile flow that give progressively better approximations to the lithospheric rheology assumed for and the conditions observed at the Lake Mead transition zone: (1) an analytical approximation to two–dimensional linear viscous flow in a channel; (2) finite element modeling of linear viscous flow under geometric conditions more closely approximation those at Lake Mead; and (3) modeling of flow governed by power law creep mechanisms.

Channel flow approximation

Figure 8a illustrates the highly simplified two–dimensional model of lithospheric structure we use to examine the conditions under which ductile flow of lower crustal material can significantly thicken the lower crust beneath regions of extended upper crust. Ductile flow is assumed to occur within a channel with distinct boundaries. The upper crust overlying the ductile channel is assumed to have no flexural rigidity and acts as a passive load on the ductile layer. In this paper we use the term upper crust to describe all material above the ductile channel. We prescribe thinning of the upper crust as a boundary condition on the underlying ductile flow. In the first series of models the lower boundary of the ductile channel is assumed to be rigid and flat, ignoring deflections associated with deformation in deeper layers. We also assume initially that there is no difference in density between material forming the upper crust and the material in the ductile channel, and that the ductile layer behaves as a linear (Newtonian) viscous fluid.

In this model lateral variations in the mass of upper crustal material induce lateral variations in pressure in the underlying fluid layer. Flow in response to these pressure gradients carries material away from regions of high pressure corresponding to areas with large upper crustal thicknesses toward regions of lower pressure where upper crust is thinner. Pressure gradients are reduced as flow in the fluid layer increases the mass of ductile material, hence increasing the pressure in regions of initially lower pressure.

An approximate upper bound on the viscosity required for flow in a channel to redistribute lower crustal material such that lateral variations in total crustal thickness go to zero or to some fraction of the variations in upper crustal thickness can be derived as follows. We can approximate such flow with an analytical solution for two–dimensional linear viscous flow in a channel. The flow rate q of a fluid with Newtonian viscosity μ through a channel with thickness D under a lateral pressure gradient dp/dx can be written

$$q = \frac{D^3}{12\mu}\frac{dp}{dx} \tag{2}$$

where x is the horizontal coordinate (see for example *Turcotte and Schubert*, 1982). This approximation assumes that lateral variations in the thickness of the ductile layer are gentle, such that $dD(x)/dx$ is small compared to D.

Horizontal pressure gradients in the ductile channel are produced by differences in the weight of the overlying crust. We assume that the initial pressure gradient can be approximated by the difference between pressures associated with unextended upper crust and with upper crust thinned by an amount Δh and can be expressed as

$$\frac{dp}{dx} \approx \frac{\rho_c g \Delta h}{L/2} \tag{3}$$

where ρ_c is the density of the crust and g is the gravitational acceleration. L is the horizontal length scale, or distance required for flow between unextended and thinned regions. Assuming that upper and lower crustal densities are equal, flow is 'complete' in the sense that all lateral variations in total crustal thickness are eliminated when a volume of lower crustal material equivalent to one half the volume of upper crustal material removed during thinning has moved a distance L from the unextended to the thinned region. If we require that this volume of crustal material must flow during the time interval Δt, we find a corresponding fluid flow rate q of

$$q \approx \frac{\Delta h L}{4\Delta t} \tag{4}$$

Equating the flow rates of Equation (4) and Equation (2) and assuming that the pressure gradients over the time Δt may be represented by an average pressure that is equal to half the initial pressure in Equation (3), we solve for the viscosity μ required for 'complete' flow:

$$\mu \approx \frac{D^3 \rho_c g \Delta t}{3L^2} \tag{5}$$

The viscosity required for ductile flow to be effective at reducing lateral variations in total crustal thickness thus depends most strongly on the channel thickness D and the length scale L. Low viscosities are required to maintain flow of material in narrow channels and

across longer distances. The viscosity is independent of the magnitude of the crustal thinning Δh when variations in the channel thickness as flow occurs are small compared to D.

Setting values appropriate for the minimum crustal thinning west of the Lake Mead transition zone: $\rho_c = 2600$ kg/m^3, $g = 10$ m/s^2, $\Delta t = 10$ m.y., we find that ductile channel flow keeps pace with upper crustal thinning over the length scale of the eastern Basin and Range and western Colorado Plateau ($L \approx 700$ km) for viscosities less than 2×10^{20} Pa·s and 1×10^{19} Pa·s for channels with thicknesses of 25 and 10 km, respectively. For ductile flow of narrower lateral extent (for example $L = 150$ km), viscosities less than 4×10^{22} Pa·s and 2×10^{21} Pa·s for 25 and 10 km thick channels, respectively, are required. Viscosities twice as large correspond to flow that reduces the lateral variations in crustal thickness by a factor of two over the same time period (for example producing 5 kilometers of net crustal thinning in a region that has undergone 10 kilometers of upper crustal thinning). These viscosities are fairly conservative upper bounds since we have neglected the effects of thinning of the channel as lower crust material flows away from unextended regions or as flow beneath the channel modifies its shape.

Finite element models of linear viscous flow

Finite element modeling was used to examine the pattern of flow and the viscosities of linear viscous flow that could produce 5 to 10 kilometers of thickening in a ductile channel under conditions more closely approximating those in the Lake Mead area. A description of the method used is contained in the Appendix. Figure 8b illustrates the boundary conditions imposed on the finite element grid in order to simulate the effect of upper crustal thinning on ductile lower crustal and mantle layers. Thinning of the upper crust is imposed over the left side of the grid (the 'Basin and Range') and is described by a vertical stress $\sigma_y = \rho_c g \Delta h$ specified on the left side of the upper boundary. A progressive increase in upper crustal thinning through time is modeled with an increase in the imposed upward stress through time. Horizontal velocities are set to zero on the upper and lower boundary of the unextended region. The boundary conditions on the sides of the grid are stress free in the vertical direction, with zero horizontal velocity on the right (unextended) side, and a specified horizontal velocity on the left (extending) side.

The first models discussed below (Figures 11 through 16) assume a single lower crustal channel with a lower boundary with zero vertical velocity, such that the boundary is fixed, as in Figure 8b. Horizontal velocities on the lower boundary are set to zero beneath the right side and are specified on the extending left side. These simple one–layer models

thus neglect the effects of an underlying mantle fluid layer and are equivalent to a rigid (infinite flexural rigidity) mantle.

Figure 9a illustrates an example of the initial grid used in the single–layer models, in this case for a channel 25 kilometers thick. For thinner channels the vertical dimension of the elements was simply scaled down, such that the ductile layer was modeled in each case with the same number of elements. Computation of the deformation of the viscous layer through time is described in the Appendix. An example of the state of the finite element grid for the 25–km thick channel after 10 m.y. of flow in response to 10 km of upper crustal thinning over the left side of the grid is shown in Figure 9b.

In a set of models (Figures 10 through 12) we assume that horizontal velocities on the upper and lower boundaries of the extending region (left side of grid) are zero. This assumption represents a simple shear type of extension or unroofing of the upper crust in which the ductile channel is not actively extending as the upper crust thins. Boundary conditions approximating the Lake Mead setting are then imposed. We assume 10 kilometers of crustal thinning has occurred over the last 10 m.y over one half a 700–km wide region. For ease of computation, stress boundary conditions corresponding to upper crustal thinning in one–kilometer increments every one million years were imposed. The width of a transition zone where stresses vary linearly from 'unextended' to 'thinning' values was set to 20 kilometers.

An example of the pattern of lateral flow between the regions of unextended and thinned upper crust in such a ductile channel is illustrated in Figure 10, where we have assumed a fluid viscosity of 10^{20} Pa·s in a channel 25 km thick. Flow is still concentrated near the transition zone after 2 million years (2 kilometers) of thinning, but, by 8 million years (and 8 kilometers of thinning), horizontal flow is well developed throughout the channel.

In modeling the observations in the Lake Mead area we are interested in finding the range of conditions under which ductile flow will produce a variation in crustal thickness between the Basin and Range and the Colorado Plateau that is 5 kilometers or less, given 10 kilometers of upper crustal thinning in the Basin and Range over the last 10 m.y. Crustal thickness variations between zero and 5 kilometers may be compatible with the topography and gravity data if lateral variations in elevations are compensated by lateral density variations within the crust. This is discussed further below. Figure 11 illustrates the changes in the thickness of the ductile channel and the associated change in total crustal thickness for the flow conditions shown in Figure 10, and for flow of viscosity 10^{19} Pa·s under identical boundary conditions. After 10 m.y., 10 kilometers of upper crustal thinning, and underlying channel flow, the discrepancy in total crustal thickness between

the unextended and thinned regions is approximately 5 kilometers for 10^{20} Pa·s flow and virtually zero for 10^{19} Pa·s flow. Thus both models are defined as successful in that they satisfy the above criteria for total crustal thickness variations across the Lake Mead transition zone.

We note here that the apparent ~100 meter jaggedness in the elevation in the upper boundary of the ductile channel (and hence in the upper crustal surface) does not correspond to a real physical process but is an artifact of the finite element technique, grid spacing, and boundary conditions used in this study. This jaggedness serves as an indication of the resolution of this model for displacements near the transition zone. See the Appendix for further discussion.

Finite element modeling under the boundary conditions above indicates that 'acceptable' fluid viscosities, those that reduce crustal thickness variations across the transition zone to 5 kilometers or less, are highly dependent on the channel thickness assumed. The relationship between the upper limit on acceptable viscosity and the channel thickness are shown in Figure 12. The upper limiting viscosities range from somewhat more than 10^{19} Pa·s for flow in a 25–km thick channel to less than 10^{17} Pa·s for a 5–km thick channel.

Figure 12 indicates that the analytical approximation to the viscosity that yields zero variations in total crustal thickness (dashed line) is in reasonably good agreement with the results of the finite element modeling. Thus the flow features neglected in the analytical approximation, such as flow near the transition zone, pinching of the channel as flow is driven from the unextended region, and imposed side boundary conditions, are shown to be second order effects compared to the value of the initial channel thickness.

If we assume that the ductile channel itself is actively extending, we modify the models above such that the horizontal velocities on the upper and lower boundaries of the channel in the extending region (left side of the grid) impose displacements away from the unextended region. Figure 13 shows velocities in a 25–km thick channel 5 m.y. after the onset of extension and upper crustal thinning. The imposed horizontal velocities on the grid boundaries correspond to extension in the left half of the ductile channel by a factor of two over 10 m.y. The horizontal velocities imposed on the upper and lower boundaries of the extending region enhance the lateral flow in this region relative to the models with zero horizontal velocity boundary conditions. The amount of thinning of the extending part of the ductile channel (left side) ,which is equivalent to the volume of material 'lost' from the model through displacement across the left boundary, however, is greater than the amount of rethickening due to an increase in volume influx from the unextended region (right side). Thus we find that lower viscosities are required for acceptable models if we assume that

material in the ductile channel is actively extending as well as responding to upper crustal thinning. For example, the upper bound on acceptable viscosities for the Lake Mead geometry is reduced from 10^{20} Pa·s for the simple crustal thinning model to 10^{19} Pa·s for the extending ductile channel model when a 25–km channel thickness is used.

In the following paragraphs we relax the assumption that the lower boundary of the ductile channel is fixed, and consider the effect of motions of the lower boundary and material beneath the ductile channel. We assume in these models that the lower boundary of the ductile channel coincides with the crust–mantle boundary (as in Figure 7) and thus use the terms 'lower boundary' and 'Moho' interchangeably. The lower boundary will move whenever flow rates within the mantle in response to upper crustal thinning exceed those in the ductile crustal layer. These models maintain Airy isostasy when mantle flow rates are fast compared to the time steps of the models. The observation that the Lake Mead gravity data are compatible with a simple Airy compensation mechanism suggests a two–layer model in which mantle flow rates are fast is a much better approximation to flow behavior in the Lake Mead region.

Finite element models assuming a linear viscous mantle underlying the viscous crustal channel were run using the grid and boundary conditions illustrated in Figure 14. In each case we assumed a mantle viscosity of 10^{21} Pa·s. The Moho is deflected upward beneath the extended areas as flow occurs in the mantle. The upward deflection of the Moho introduces a kink into the crustal channel at the transition zone and reduces the lateral pressure gradients in the lower crustal channel. These processes are addressed in more detail in the discussion below. The finite element models show the net effect of the Moho deflections is to reduce the upper limits on acceptable viscosities for the crustal channel by approximately 30% from the values of the fixed lower boundary models for a 25–km thick crustal channel and 50% for a 10–km thick channel. In the 5–km thick channel model, the kink induced in the channel at the transition zone after 2–3 km of upper crustal thinning is sufficient to produce a constriction of the channel that drastically inhibits flow. Numerical instabilities prevented quantification of the reduction in flow rates as the channel is constricted.

In summary, the most conservative upper bounds on viscosities required for linear viscous flow to produce total crustal thickness variations of 5 kilometers or less under conditions approximating those observed at Lake Mead (a length scale of 700 kilometers; crustal thinning of 10 kilometers over 10 m.y.) range from 10^{18} Pa·s to 10^{20} Pa·s for channels 5 to 25 kilometers thick (Figure 12). Consideration of the effects of extension in the ductile channel and flow in the mantle may reduce these upper bounds by as much as an order of magnitude.

Modeling of power law flow

Experimental evidence indicates that lower crustal material flows according to a power law, rather than linear viscous rheology [*Goetze and Evans*, 1979] and that strain rates ε in the ductile regime can be described by the relation

$$\dot{\varepsilon} = A(\sigma_1 - \sigma_3)^n e^{-Q/(RT)} \tag{6}$$

where $(\sigma_1 - \sigma_3)$ is the deviatoric stress, R is the universal gas constant, T is the temperature in Kelvin and A,n, and Q are experimentally determined constants. An effective viscosity can be defined for power law flow which allows us to use the previous results for Newtonian viscous flow to estimate the conditions under which power law flow rates can produce significant redistribution of crustal material. The effective viscosity μ_{eff} of the power law stress–strain rate can be written in terms of the strain rate

$$\mu_{eff} = \frac{\dot{\varepsilon}^{(1/n)-1} e^{Q/(nRT)}}{2A^{1/n}} \tag{7}$$

or in terms of the deviatoric stress

$$\mu_{eff} = \frac{(\sigma_1 - \sigma_3)^{(1-n)} e^{Q/(RT)}}{2A} \tag{8}$$

where the parameters are defined for Equation 6 above. Table 1 shows the temperatures needed for flow of several crustal rocks at viscosities between 10^{18} Pa·s to 10^{21} Pa·s, requiring strains of 0.5 over 10 m.y., or a strain rate of 10^{-15} s^{-1}, assuming experimentally determined coefficients Q, A, and n. Olivine is shown for comparison with mantle materials. Table 2 shows the temperatures computed using Equation 8, equating the deviatoric stress with yield stresses of 1 MPa to 10 MPa expected in the lower crust (see Figure 7). Table 2 demonstrates that the effective viscosities of 10^{19} Pa·s to 10^{20} Pa·s necessary to thicken the lower crust under the Lake Mead conditions, for ductile channel thicknesses of 15 to 25 kilometers, may be attained at lower crustal temperatures of 700 to 1000°C (or less for wet quartzite). Higher temperatures are required for sufficient flow rates through channels with thickness of 5 to 10 kilometers.

Finite element modeling of power law flow confirms that elevated lower crustal temperatures (700–1000°C) are necessary for acceptable flow rates within channels 25–km thick or less in the Lake Mead region, for the quartz diorite and quartzite rheologies. Under

the boundary conditions assumed in this study the pattern of flow for power law rheologies may be quite similar to that of linear viscous flow. Figure 15 illustrates the flow pattern and resulting topography for a quartzite rheology (see Table 1). This flow is comparable to that of linear viscous flow with viscosity of 10^{20} Pa·s under identical boundary conditions, as shown in Figures 10 and 11. The similarity between the power law and linear viscous flow results from the fact that spatial variations in the effective viscosities within the ductile layer in the power law flow model are relatively small under the conditions modeled here. For the flow illustrated in Figure 15, we assume upper crustal thinning occurs in discrete instantaneous increments of 1 kilometer ever 1 million years. We find that variations between the effective viscosities computed at each element within the finite element grid are a maximum immediately after each 1 kilometer increment of upper crustal thinning, but decrease as ductile flow occurs during the 1 million year intervals between increases in upper crustal thinning. In this case the spatial variations in effective viscosities are generally less than a factor of two 0.5 million years after each instantaneous increment of thinning, except for elements on the side boundaries of the grid. These results suggest that the flow rates computed for linear viscous flow are a good approximation to the flow rates expected for lower crustal deformation by power law mechanisms.

DISCUSSION

Approximations in the modeling

By assuming a rigid lower boundary (or Moho) in the first set of models above we overestimated the lateral pressure gradients in the ductile channel, and neglected a kink that may be introduced into the channel at the transition zone as the Moho is deflected upward beneath the region of upper crustal thinning. Both observations are illustrated in Figure 16, assuming that mantle flow and Moho deflections completely compensate variations in crustal thickness. We expect the pressure gradients in an inviscid mantle model (Figure 16) to be smaller by a factor of $(\rho_m - \rho_c)/\rho_m$ than the gradients in the fixed lower boundary model. For ρ_m = 3300 kg/m^3 and ρ_c = 2700 kg/m^3 gradients should differ by a factor of 5. However, we find as described in the finite element modeling above that the thickening of the lower crust beneath the thinned areas in the two–layer crust–mantle model is only 30% slower for a 25–km thick crustal channel, and only 50% slower for 10–km thick channel. This apparently enhanced flow rate in the two–layer model stems from the fact that lateral flow occurs on the crust–mantle boundary in these models (Figure 17). Flow in the crustal channel in the two–layer model may be better approximated by flow in a channel

with a zero shear stress on the lower boundary, rather than with zero velocity along the lower boundary as assumed in the analytical approximation for channel flow discussed above. Flow rates in a channel of fixed thickness under equal pressure gradients are 4 times greater with zero shear stress than with zero velocity along the lower boundary. Considering both the difference in pressure gradients and the difference in flow along the lower boundary we expect flow rates in the two–layer models to be roughly 20% lower than in comparable one–layer models, which is comparable to the value we observe. The fixed lower boundary model thus appears to overestimate only moderately the maximum viscosities for models with channel thickness greater than 10 km.

An offset in the channel at the transition zone is important in models where the size of the offset in the channel is comparable to the total thickness of the channel, and flow is pinched off at the transition zone. Assuming Moho deflections compensate upper crustal thinning, and neglecting crustal flow, the offset in the channel equals the mantle uplift Δm which in turn equals the crustal thinning Δh times the ratio of crustal and mantle densities (ρ_c/ρ_m). The offset in the channel thus becomes important in choking off flow when the ductile layer thickness is comparable in size to the thinning in the upper crust. Thus the upper bounds on acceptable viscosities derived from the fixed lower boundary models are probably too large for models with channel thickness of 5 or 10 kilometers. Any flexural rigidity in the upper mantle or in the upper crust, however, will diminish the abruptness of an offset at the transition zone and the associated restriction of flow.

In the modeling above we assume that crustal thinning occurred in 1 kilometer intervals every 1 m.y. over the last 10 m.y. Crustal thinning in the Lake Mead area is in reality only loosely constrained to have occurred within the last 10 to 15 m.y [*Wernicke et al.*, 1988], may have been episodic (for example *Taylor et al.*, 1989). Equation 5 suggests we may have underestimated the upper bounds on acceptable viscosities for flow in the Lake Mead area by a factor of 2/3 if upper crustal thinning occurred in 15 m.y., rather than in 10 m.y.

In our models of Lake Mead we assume that material flows over roughly 700 kilometers, thickening the lower crust over several hundred kilometers in the eastern Basin and Range. The viscosities of acceptable flow models are roughly inversely proportional to the square of the length scale assumed, however, as can be seen in Equation 5. A discussion of the effect of the length scale is deferred to the section below on flow beneath narrower regions of extension such as metamorphic core complexes.

The above models assume that the transition zone between the extended and unextended areas (the region over which crustal thinning decreases from its maximum value to zero) is 20 kilometers wide. Finite element modeling of broader or narrower

transition zones indicate that variations in the width of this zone have no significant impact on the derived upper bounds on acceptable viscosities.

The two–dimensional finite element models neglect ductile flow parallel to the transition zone. In the Lake Mead area, it is possible that variations in upper crustal thinning within the Basin and Range may drive lower crustal flow towards the highly extended Lake Mead area. If the high heat flow values in the Basin and Range are interpreted to reflect elevated crustal temperatures, then flow within the Basin and Range may be facilitated by effective viscosities lower than in the adjacent Colorado Plateau. Consideration of three–dimensional flow, which may enhance effective flow rates into an extended region and hence raise the upper bounds on acceptable viscosities, is beyond the scope of this paper.

Temperatures associated with lower crustal flow

The experimentally derived flow parameters summarized in Tables 1 and 2 for crustal materials suggest that temperatures on the order of 700 to 1000°C are required to sustain the effective viscosities necessary for lower crustal flow over the 700 kilometer length scale assumed near Lake Mead. These values, although highly dependent on the rheology assumed, are higher than the lower crustal/upper mantle temperatures of 500 to 800°C estimated by *Lachenbruch and Sass* [1979] on the basis of heat flow data over the Basin and Range. Slight elevations in crustal temperatures, however, may be quite effective in increasing ductile flow rates as they simultaneously reduce the effective viscosity and increase the thickness of the effective ductile channel by increasing the depth range over which yield stresses in the crust are small. We interpret these combined results as suggestive that ductile flow over the length scale assumed here is most likely to occur in thicker effective channels (on the order of 15 to 25 kilometers) where sufficient flow rates can be maintained at higher effective viscosities.

Topography across the transition zone

Acceptable ductile flow models with 25–kilometer channel thicknesses show a smooth variation in total crustal thickness across across the transition zone (see Figure 11). We expect comparably smooth variations in elevations across the transition zone if these crustal thickness variations are compensated at the Moho. Thus these models do not predict the abrupt change in topography observed at the Lake Mead transition zone, where elevations

decrease about 1000 meters from the Colorado Plateau to the Basin and Range over a distance less than 70 kilometers.

Models for flow in channel 10 kilometers thick will predict more abrupt changes in topography at the transition zone (Figure 18). Two additional alternative explanations for the observed short–wavelength change in elevation are considered here.

A difference in density between lower crustal rocks involved in ductile flow and the thinned upper crustal rocks could produce a change in elevation across the transition zone that is as abrupt as the change in crustal thinning. This is illustrated most simply by considering the case where flow of lower crustal material has gone 'to completion' in the sense that lateral pressure gradients within the ductile layer are zero. In this case, if ductile channel and upper crustal densities are equal, then the volume and mass of material added to the lower crust in the extended region exactly equal the volume and mass of upper crustal material removed during thinning and the crustal thickness is uniform. (We assume the ductile channel itself is not actively extending, as in the upper plot of Figure 11.) If, however, the ductile material has a higher density, then the volume added to the ductile layer is smaller than the amount removed by thinning. Elevations over the region of upper crustal thinning will then be lower since the net crustal thickness is smaller. The width of the transition in crustal thickness and in elevations will be the same as the width of the transition between the regions of unextended and thinned upper crust.

We can compute the density contrast between the ductile channel rocks and upper crustal rocks necessary to produce differences in elevation where lower crustal flow is still active, assuming that variations in the weight of crustal columns are compensated at the Moho. For example, a 1 kilometer difference in elevation Δe between the Basin and Range and Colorado Plateau requires a density contrast $\Delta\rho$ such that:

$$\Delta\rho = \frac{\rho_m(\Delta e - \Delta h + \Delta r) + \rho_c(\Delta h - \Delta r)}{\Delta r} \tag{9}$$

where Δh is the upper crustal thinning, Δr is the ductile channel thickening, and ρ_m and ρ_c are mantle and upper crustal densities, respectively. For 10 kilometers of upper crustal thinning and 5 kilometers of thickening in the ductile channel in the extended region, we set Δh = 10 km, Δr = 5 km, ρ_m = 3300 kg/m^3, and ρ_c = 2700 kg/m^3 and find $\Delta\rho$ = 60 kg/m^3. Such a density contrast is within the range of densities of crustal materials.

The abrupt change in elevation at the transition zone could also be a structural offset that is maintained by crust with nonzero flexural rigidity. We can model such a topographic step, assuming compensation of the step by flexure over an inviscid crustal

layer, without any infilling of the flexural relief (Figure 18). For flexural rigidities on the order of 10^{21} to 10^{22} N·m (corresponding to effective elastic plate thicknesses T_e of 5 to 12 km) and a step of approximately 1000 meters, this model predicts a trough approximately 100 meters deep and about 100–150 km wide on both sides of transition zone. Such a trough is not apparent in the topography data across the Lake Mead transition, although the topography is locally quite rough. Therefore, if the topographic step is flexurally maintained, either flexural rigidities on the order of 10^{23} N·m (T_e = 25 km) are required, in which case the flanking troughs are reasonably small, or the topography between the troughs and the transition zone has been eroded from an initially greater step. A flexural rigidity of 10^{23} N·m is greater, however, than values obtained by forward modeling of the gravity data above and coherence studies [*Bechtel and Forsyth*, 1987]. This suggests that 100 meters or more of material has been eroded from the Grand Wash Cliffs, if the topographic step is principally flexurally maintained.

Implications of the Ductile Flow Model for Older Transition Zones

The ductile flow models predict (1) that lateral variations in total crustal thickness are smaller than expected from estimates of extension or unroofing, and (2), that any variations in crustal thickness and in topography at transition zones should decrease with age after the cessation of extension, unless flow is inhibited by decreasing temperatures. The predictions are examined at two older breakaway faults on the eastern margin of the region of Cenozoic extension in the western United States (Figure 19). Figures 20 and 21 show topography and gravity data and gravity modeling across Eocene age (40–55 m.y.ago) breakaway zones in southern British Columbia and in northern Idaho.

Gravity modeling suggests the first prediction holds true along both profiles. Palinspastic reconstructions on profile 1–1' in southern British Columbia by *Parrish et al.* [1988] suggest that the crust was 50–60 km thick prior to the onset of extension. These authors estimate subsequent extension to be approximately 30%, about half of which occurred between 50 and 60 m.y. ago. Such extension of the entire crust predicts thinning on the order of 15 kilometers over the extending region. The topography data require that a 15–km discontinuity in crustal thickness must be compensated by the presence of low density material in the mantle. The gravity data are incompatible, however, with compensation of crustal thinning by mantle density contrasts of 100 kg/m^3 or less (Figure 20b). A simple Airy compensation model with crustal thickness variations on the order of 5 kilometers or less yields a much better fit to the gravity data. We note, however, that we cannot rule out several other possible explanations for these observations, including (1)

pre–extensional overthickening of crust west of the breakaway fault, since the eastern limit of the late Cretaceous to Tertiary thrust faulting lies 150 km eastward of the breakaway fault [e.g. *Miller et al.*, 1989], and (2) thinning of the region east of the surface outcrop of the detachment fault, since the detachment fault dips to the east.

Similar modeling on Profile 2–2' across northern Idaho suggests crustal thickness variations are smaller than 5–18 kilometers of uplift estimated by [*Hyndman et al.*, 1988] for a metamorphic zone bounding the breakaway zone in the Bitterroot batholith. Figure 21b shows that an intermediate estimate of crustal thinning of 12 km west of the breakaway fault cannot satisfy both gravity and topography data with reasonable lateral variations in mantle densities. As was the case in the Lake Mead area and in Profile 1–1' in southern British Columbia, the gravity data are best fit assuming total crustal thickness variations less than geological estimates of crustal thinning in the extended area. Again, alternative mechanisms for explaining the apparent uniformity in crustal thickness may be viable, as the eastern limit of Cordilleran thrust belt lies some 200 km east of northern Idaho breakaway fault and the breakaway fault dips east.

The second prediction of the ductile flow model, that any variations in crustal thickness should diminish with time after extension, is not born out in the topography profiles across these Eocene breakaway zones. While the change in elevation across the southern British Columbia breakaway zone is smaller than at the more recently active Lake Mead zone, the change in elevation along the northern Idaho profile is comparable to that at Lake Mead. The amount of crustal thinning in northern Idaho was probably not greater than at Lake Mead. Thus it appears that ductile flow subsequent to periods of extension may in some cases be inhibited, perhaps by an increase in viscosities associated with regional cooling. Elevations in this region may also have been modified more recently by Miocene extension. Better constraints on the crustal density and temperature structure, pre–extensional crustal thicknesses, and the amounts of crustal thinning are needed to resolve the causes of changes in topography across breakaway zones.

Implications for Metamorphic Core Complexes

Block and Royden [1989] have shown that the development of metamorphic core complexes, where rocks uplifted from mid–crustal levels are exposed, must be accompanied by infilling from below of material with densities comparable to upper crustal densities, unless the crust in the region of uplift was substantially thicker prior to uplift. Their argument is based on seismic and gravity evidence that the Moho is presently flat beneath these regions [*Allmendinger et al.*, 1987; *Hauser et al.*, 1987] .

We can examine the viscosities required for lower crustal infilling beneath the uplifted metamorphic core complexes by modifying the length scale in our models to a value of 150 kilometers, approximating the width of metamorphic core complexes. Figure 22 shows that the analytical channel flow approximation of Equation 5, assuming a horizontal length scale of 150 km and a 10 million year time scale for flow. We find that viscosities of 10^{19} to 10^{21} Pa·s satisfy the analytical approximation for 'complete' ductile channel thickening beneath thinned upper crust. The inverse squared dependence of the upper bound viscosity on the length scale increases these values more than an order of magnitude from the viscosities calculated for 700 kilometers of flow at Lake Mead.

Finite element modeling of flow over shorter length scales yields similar results. We model symmetric flow from two sides of a metamorphic core complex by modeling the 'right half' of the flow and specifying the horizontal velocity to be zero over the center of the metamorphic core complex which is represented by the left boundary of the grid (shorter grid is shown in Figure 9a). The length of the unextended region (on the right side of the half–model) is set to 100 kilometers. The transition zone is assumed to be 20 kilometers wide, and crustal thinning is again assumed to occur at a rate of 1 km/m.y. (1 mm/yr) for 10 million years. Figure 22 illustrates the results of models for various viscosities and channel thicknesses, indicating whether the thickening of the ductile channel beneath the thinned region was more or less than 5 kilometers, or a 'complete' 10 kilometers.

The higher acceptable viscosities for flow on the length scale of metamorphic core complexes correspond to temperatures in the ductile channel on the order of 500 to 700°C for the materials listed in Tables 1 and 2. Such temperatures are compatible with heat flow data over the Basin and Range [*Lachenbruch and Sass*, 1979], suggesting that flow beneath metamorphic core complexes as envisioned by *Block and Royden* [1989] is physically reasonable under the temperature and stress conditions associated with metamorphic core complex development.

CONCLUSIONS

Ductile flow in the lower crust driven by lateral pressure gradients associated with lateral variations in upper crustal thinning appears to be a viable mechanism for reconciling gravity and topography data and estimates of extension near Lake Mead, Nevada, but may require elevated temperatures (on the order 700–1000°C) in the lower crust. Other proposed models, such as overthickening of subsequently extended areas and thinning of the footwall over low–angle normal faults, are incompatible with the geologic observations

in the Lake Mead area. The ductile flow mechanism has an advantage over crustal underplating models or models assuming lateral variations in mantle densities in that lower crustal flow is driven by lateral variations in upper crustal thickness. The amount of ductile channel thickening thus correlates spatially with the amount of upper crustal thinning, even when variations in upper crustal thinning are abrupt, as is the case near Lake Mead.

Analytical approximations and finite element modeling of flow in a lower crustal channel show that the effective viscosities required for significant redistribution of lower crustal material are highly dependent on the thickness of the ductile channel and the length scale of the flow. Upper bounds on effective viscosities range from 10^{18} to 10^{20} Pa·s for ductile channels 10 to 25 kilometers thick, respectively, for flow that yields 5 kilometers or more of ductile channel thickening beneath 10 kilometers of upper crustal thinning over the last 10 m.y. in the eastern Basin and Range near Lake Mead. Power law creep parameters derived for crustal material such as quartzite and quartz diorite imply that these effective viscosities correspond to temperatures (700–1000°C) somewhat greater than those estimated from heat flow data.

Simple lower crustal ductile flow models fail to predict the abruptness of the change in topography at the Lake Mead transition zone as well as the amplitude of the change in topography across older (Eocene) breakaway zones in northern Idaho and British Columbia. The amplitude and wavelength of the topographic step between extended and unextended regions may reflect flexurally maintained structures and variations in intracrustal density structure as well as varying amounts of upper crustal thinning and lower crustal ductile flow.

Infilling of lower crustal material beneath metamorphic core complexes can occur at temperatures lower than those required for the flow modeled at Lake Mead. Ductile lower crustal flow driven by the pressure gradients associated with the unroofing of metamorphic core complexes is thus a plausible mechanism for explaining the flat Moho observed beneath the uplifted regions.

The good fit of the Airy compensation mechanism to the gravity data in the Lake Mead suggests that compensation of topography occurs near Moho depths, and thus that some lateral pressure gradients persist in the lower crust. Compensation in the mantle implies that mantle flow rates exceed ductile crustal flow rates. The strong dependence of flow rate on channel thickness indicates, however, that mantle flow rates may be greater than crustal rates even where effective mantle viscosities are greater than crustal viscosities. Thus the results here are compatible with asthenospheric viscosities of 10^{21} Pa·s as derived from post–glacial rebound studies [e.g. *Peltier*, 1986], if mantle flow occurs over a depth range of 50 to 100 or more kilometers.

Seismic experiments in the Lake Mead transition zone and other parts of the Basin and Range which have undergone highly variable amounts of extension could improve our resolution of deep crustal structure in these regions and our estimates of the conditions under which lower crustal ductile flow is significant.

APPENDIX

The finite element technique

Finite element computations were done with a modified version of the program FEM2D of *Reddy* [1984]. As a detailed description of the method is available in *Reddy* [1984], we focus here on adaptations of the program for the modeling described above. The momentum equation for two–dimensional Newtonian viscous flow is solved using nine–node quadrilateral elements with quadratic basis functions. Incompressibility is enforced at four Gaussian points within each element using a penalty function technique. A penalty parameter $\gamma = 10^8\mu$, where μ is the viscosity, is used to separate the precision used to solve for shear strain components from that used to impose incompressibility. This method is equivalent to treating the fluid as a slightly compressible material with bulk modulus very large compared to shear modulus.

The pressure is evaluated at the Gaussian points where incompressibility is enforced. Body forces are computed at each node from element densities and interpolated over the elements using the element shape functions. Stress and velocity boundary conditions are imposed on the grid boundaries as discussed in the text (Figures 8 and 14).

We compute displacements by integrating velocities through time. Time steps were generally set so that the maximum displacement within a given interval did not exceed 250 meters. To alleviate problems associated with large displacements near the transition zone, we set a new mesh at the end of each time step. The nodes of the new mesh retain the horizontal coordinates of the nodes of the initial mesh (see Figure 9). The vertical displacements of nodes marking key horizons such as the upper and lower surfaces and a crust–mantle boundary are retained at the end of each time step. The new mesh is formed by linearly interpolating the y–values of the displaced nodes of the key horizons onto the new mesh. Y–coordinates of nodes between the key horizons are then set so that the vertical spacing of the new nodes within each column in a given layer is even. The finite element mesh at each time step thus does not record the cumulative deformation history of the original elements, but does record the change in the thickness of each layer as flow occurs within each time step.

We modified the above technique to model a power law stress–strain relation of the form of equation 6 above. The computation of stress and pressure from the viscosity and the derivatives of the velocities at the Gauss points within each element at each time step was replaced by the following sequence of calculations:

(1) Set the viscosity to some initial guess (generally we used 10^{19} Pa·s at all nodes) and compute a stiffness matrix and velocities and stresses at each node as done for Newtonian viscous flow.
(2) Compute the deviatoric stress ($\sigma_1-\sigma_3$) at each node, where ($\sigma_1-\sigma_3$) is computed from the second invariant of the deviatoric stress tensor τ_{kl} such that $(\sigma_1-\sigma_3) = (\tau_{kl}\tau_{kl})^{1/2}$.
(3) Compute the effective viscosity at each node from the deviatoric stress based on the power law constitutive relation, where

$$\mu_{eff} = \frac{(\sigma_1 - \sigma_3)^{(1-n)} e^{Q/(RT)}}{2A}.$$

The coefficients n,Q, and A related to the material composition (see Equation 6 in text for definitions) are assumed to be uniform throughout the ductile layer. The temperature T is specified at each element. For the simple models discussed in this paper, T is assumed to be uniform throughout the ductile layer and constant through time.
(4) Update the viscosity at each element. To generate a stable solution the new trial viscosity is set to the average of the viscosity computed in the previous iteration and the new viscosity computed in step (3).
(5) Set a new stiffness matrix based on the new viscosities at each element and find the velocities and stresses associated with the new stiffness matrix.
(6) Compare the velocities with those computed in the last iteration; if the difference is greater than a specified criteria for convergence go to step (2), otherwise go to step (7)
(7)) Once convergence is reached compute displacements and update grid.

We defined a convergence criterion limiting the maximum change in a velocity on the grid in both x and y directions to less than 1% of the maximum x and y velocities, respectively, at the given iteration. Generally between 5 and 30 iterations were required for convergence.

The approximately 100 meter undulations in y values between adjacent nodes observed in the modeling above are representative of the resolution of the finite element technique. The jaggedness in the finite element solutions is characteristic of undersampling of flow near abrupt boundaries like the transition zone modeled here. Tests of the program against analytical solutions show that deformations with wavelengths greater than the spacing between two nodes are accurate representations of ductile flow and that the jaggedness increases with increasing coarseness in the mesh and sharpness in the transition zone. We chose a mesh sufficiently coarse that the computer programs ran reasonably fast, but fine

enough that the spatial resolution (corresponding to the jaggedness) was good to approximately 100 meters.

Comparison of the Viscous Model With Lithospheric Necking Models

Fletcher and Hallet [1983] and *Zuber et al.* [1986] show that necking instabilities with wavelengths comparable to the spacing of ranges within the Basin and Range will grow in extending stratified lithosphere with a surface layer that deforms plastically and deeper layers that deform by power law creep. The lithospheric necking models, however, assume that perturbations in horizontal strain rate are small compared to the overall strain rate. The models presented here allow large lateral variations in strain rate in response to large lateral variations in the strain rate of the upper crust which are imposed as a boundary condition on deeper flow.

Comparison of the Viscous Model With Viscoelastic Models

The time scale for the ductile flow presented here (thousands to millions of years) is much longer than the time scale of tens or hundreds of years found for the viscoelastic response of the lithosphere to faulting and earthquake rupture (*Stein et al.*, 1988). The viscoelastic model is appropriate for describing strains in a medium where stresses are imposed rapidly and do not exceed the elastic yield stress of the material. The viscoelastic strain rate $d\varepsilon/dt$ is a sum of an elastic strain rate associated with the rate of change in stress $d\sigma/dt$ and a viscous strain rate proportional to the stress σ such that

$$\frac{d\varepsilon}{dt} = \frac{\sigma}{2\mu} + \frac{1}{E}\frac{d\sigma}{dt}$$

where μ and E are the material viscosity and bulk modulus, respectively. When stresses are induced rapidly, the second term in this equation is larger than the first term. The viscous flow model, which does not contain the second term, is thus appropriate for considering strains corresponding to gradually increasing stresses or for modeling net strains in settings where the viscous strain is much greater than the elastic strain. The latter condition is valid for large scale lower crustal flow, where elastic strains should be quite small compared with the total strains. For example, for stresses σ of 10^8 Pa associated with 10 km of upper crustal thinning, corresponding elastic strains $\varepsilon = \sigma/E$ are only 1.5 x 10^{-3}, assuming $E = 7 \times 10^{10}$ Pa, while the total strains over 10 m.y. are on the order of

0.5. The viscous model applied here thus fails to properly represent strain rates during periods of rapid stress redistributions, but does estimate the rate of viscous strain which constitutes the bulk of the total strain.

TABLE 1. Flow Law Constants and Temperatures (°C) for flow at 10^{-15} s^{-1} strain rate[a]

Material	Flow law constants			Temperatures corresponding to viscosity (Pa·s)		
	$\log_{10}A$[b]	n	Q[c]	10^{19}	10^{20}	10^{21}
quartzite	1.9	2.9	149	2100	990	590
quartzite (wet)	3.0	2.6	134	940	560	360
quartz diorite	4.3	2.4	219	1150	820	620
Westerly granite	1.6	3.4	139	11400	1530	700
olivine	4.8	3.5	533	8030	3790	2420

[a]See text for derivation.
[b]A in units of $GPa^{-n}s^{-1}$
[c]Q in units of kJ mol^{-1}

TABLE 2. Temperatures (°C) for flow at 1–10 MPa deviatoric stress[a]

Material[b]	Temperatures corresponding to viscosity (Pa·s) 10^{18}	10^{19}	10^{20}	10^{21}
quartzite	780–1140	650–920	550–760	470–640
quartzite (wet)	500–660	450–550	350–460	300–390
quartz diorite	790–940	700–830	620–730	560–650
Westerly granite	910–1690	750–1270	620–1000	210–810
olivine	2790–3950	2480–3390	2240–2960	2030–2630

[a]See text for derivation.
[b]See Table 1 for flow law constants.

REFERENCES

Allmendinger, R.W., T.A. Hauge, E.C. Hauser, C.J. Potter, S. L. Klemperer, K.D. Nelson, P. Knuepfer and J. Oliver, Overview of the COCORP 40°N transect, western United States: The fabric of an orogenic belt, *Geol. Soc. Am. Bull.*, *98*, 308–319, 1987.

Bechtel, T.D. and D.W. Forsyth, Isostatic compensation in the Basin and Range, U.S.A., *EOS*, *68*, p. 1450, 1987.

Beghoul, N. and M. Barazangi, Mapping high *Pn* velocity beneath the Colorado Plateau constrains uplift models, *J. Geophys. Res.*, *94*, 7083–7104, 1989.

Block, L. and L. Royden, Core complex geometries and regional scale flow in the lower crust, submitted to *Tectonics*, 1989.

Brace, W.F. and D.L. Kohlstedt, Limits on lithospheric stress imposed by laboratory experiments, *J. Geophys. Res.*, *85*, 6248–6252, 1980.

Buck, W.R., Flexural rotation of normal faults, *Tectonics*, *7*, 959–973, 1988.

Burchfiel, B.C., R.J. Fleck, D.T. Secor, R.R. Vincelette and G.A. Davis, Geology of the Spring Mountains, Nevada, *Geol. Soc. Am. Bull.*, *85*, 1013–1022, 1974.

Carter, N.L. and M.C. Tsenn, Flow properties of continental lithosphere, *Tectonophysics*, *136*, 27–63, 1987.

Dewey, J.F., Extensional collapse of orogens, *Tectonics*, *7*, 1123–1140, 1988.

Eaton, G.P., R.R. Wahl, H.J. Prostka, D.R. Mabey, and M.D. Kleinkopf, Regional gravity and tectonic patterns: Their relation to late Cenozoic epeirogeny and lateral spreading in the western Cordillera, in *Cenozoic Tectonics and Regional Geophysics of the Western Cordillera*, edited by R.B. Smith and G.P. Eaton, pp. 51–92, Geological Society of America Memoir 152, 1978.

Fletcher, R.C. and B. Hallet, Unstable extension of the lithosphere: A mechanical model for Basin–and–Range structure, *J. Geophys. Res.*, *88*, 1983.

Furlong, K.P., Continental crustal underplating: Thermal considerations and seismic–petrologic consequences, *J. Geophys. Res.*, *91*, 8285–8294, 1986.

Gans, P.B., An open–system, two–layer crustal stretching model for the eastern Great Basin, *Tectonics*, *6*, 1–12, 1987.

Goetze, C. and B. Evans, Stress and temperature in the bending lithosphere as constrained by experimental rock mechanics, *Geophys. J. R. astr. Soc.*, *59*, 463–478, 1979.

Hauser, E.C. and J. Lundy, COCORP deep reflections: Moho at 50 km (16 s) beneath the Colorado Plateau, *J. Geophys. Res.*, *94*, 7071–7081, 1989.

Hauser, E.C., J. Gephart, T. Latham, J. Oliver, S. Kaufman, L. Brown and I. Luccitta, COCORP Arizona transect: Strong crustal reflections and offset Moho beneath the transition zone, *Geology*, *15*, 1103–1106, 1987.

Holt, W.E., C.G. Chase and T.C. Wallace, Crustal structure from three–dimensional gravity modeling of a metamorphic core complex: A model for uplift, Santa Catalina–Rincon mountains, Arizona, *Geology*, *14*, 927–930, 1986.

Hyndman, D.W., D. Alt and J.W. Sears, Post–Archean metamorphic and tectonic evolution of western Montana and northern Idaho, in *Metamorphism and Crustal Evolution of the Western United States*, W.G. Ernst, editor, pp. 332–361, Rubey Volume 7, Prentice–Hall, 1988.

Kirby, S.H., Rheology of the lithosphere, *Rev. Geophys. Space Phys.*, *21*, 1458–1487, 1983.

Lachenbruch, A.H. and J.H. Sass, Models of an extending lithosphere and heat flow in the Basin and Range province, in *Cenozoic Tectonics and Regional Geophysics of the Western Cordillera*, edited by R.B. Smith and G.P. Eaton, pp. 209–250, Geological Society of America Memoir 152, 1978.

Mayer, L., Topographic constraints on models of lithospheric stretching of the Basin and Range province, western United States, in *Extensional Tectonics of the Southwestern United States: A Perspective on Processes and Kinematics*, edited by L Mayer, pp. 1–14, Geological Society of America Special Paper 208, 1986.

McCarthy, J. and G.A. Thompson, Seismic imaging of extended crust with emphasis on the western United States, *Geol. Soc. Am. Bull.*, *100*, 1361–1374, 1988.

McKenzie, D., Some remarks on the development of sedimentary basins, *Earth Planet. Sci. Lett.*, *40*, 25–32, 1978.

McKenzie, D., Gravity currents in the lower crust, *Geol. Soc. Newsletter*, *17*, p.12, 1988.

Miller, D.M., T.H. Nilsen and W.L. Bilodeau, Late Cretaceous to early Eocene geology of the U.S. Cordillera: Eastward migration of igneous and tectonic activity, in *The Cordilleran Orogen: Conterminous U.S.*, Burchfiel, B.C., P. Lipman, and M. Zoback, editors, DNAG, Geol. Soc. America, in press.

Okaya,, D.A. and G.A. Thompson, Involvement of deep crust in extension of Basin and Range province, in *Extensional Tectonics of the Southwestern United States: A Perspective on Processes and Kinematics*, edited by L Mayer, pp. 15–21, Geological Society of America Special Paper 208, 1986.

Parrish, R.R., S.D. Carr and D.L. Parkinson, Eocene extensional tectonics and geochronology of the southern Omineca Belt, British Columbia and Washington, *Tectonics, 7*, 181–212, 1988.

Peltier, W.R., Deglaciation–induced vertical motion of the North American continent and transient lower mantle rheology, *J. Geophys. Res., 91*, 9099–9213, 1986.

Reddy, J.N., *An Introduction to the Finite Element Method*, 495 pp., McGraw–Hill, New York, 1984.

Rowley, P.D., J.J. Anderson, P.L. Williams, R.J. Fleck, Age of structural differentiation between the Colorado Plateaus and Basin and Range provinces in southwestern Utah, *Geology, 6*, 51–55, 1978.

Smith, R.B. and R.L. Bruhn, Intraplate extensional tectonics of the eastern Basin–Range: Inferences on structural style from seismic reflection data, regional tectonics, and thermal–mechanical models of brittle–ductile deformation, *J. Geophys. Res., 89*, 5733–5762, 1984.

Sonder, L.J., P.C. England, B.P. Wernicke and R.L. Christiansen, A physical model for Cenozoic extension of western North America, in *Continental Extensional Tectonics,* edited by M.P. Coward, J.F. Dewey and P.L. Hancock, pp. 187–201, Geological Society Special Publication No. 28, 1987.

Spencer, J.E., Role of tectonic denudation in warping and uplift of low–angle normal faults, *Geology, 12*, 95–98, 1984.

Stein, R.S., King, G.C.P., and Rundle, J.B., The growth of geological structures by repeated earthquakes. 2. Field examples of continental dip–slip faults, in *J. Geophys. Res.*, 93, 13319–13331, 1988.

Taylor, W.J., J.M. Bartley, D.R. Lux and G.J. Axen, Timing of Tertiary extension in the Railroad Valley–Pioche transect, Nevada: Constraints from $^{40}Ar/^{39}Ar$ ages of volcanic rocks, *J. Geophys. Res., 94*, 7757–7774, 1989.

Thompson, G.A. and J. McCarthy, Geophysical evidence for igneous inflation of the crust in highly extended terranes, *EOS, 67*, p.1184, 1986.

Turcotte, D.L. and G. Schubert, *Geodynamics*, 450 pp., John Wiley, New York, 1982.

Wernicke, B., Uniform–sense normal simple shear of the continental lithosphere, *Can. J. Earth. Sci., 22*, 108–125, 1985.

Wernicke, B., G.J. Axen and J.K. Snow, Basin and Range extensional tectonics at the latitude of Las Vegas, Nevada, *Geol. Soc. Am. Bull., 100*, 1738–1757, 1988.

Wernicke, B. and G.J. Axen, On the role of isostasy in the evolution of normal fault systems, *Geology*, *16*, 848–851, 1988.

Zuber, M.T., E.M. Parmentier and R.C. Fletcher, Extension of continental lithosphere: A model for two scales of Basin and Range deformation, *J. Geophys. Res.*, *91*, 4826–4838, 1986.

FIGURE CAPTIONS

Figure 1. Location map showing ranges in eastern Basin and Range at latitude of Lake Mead. N–S line marked A shows location of western end of profiles in Figure 5. T's shown near 36°N and 114°W indicate ends of profile in Figure 2. Modified from *Wernicke et al.* [1988].

Figure 2. Schematic cross–section perpendicular to strike of transition zone at the latitude of Lake Mead showing inferred uplift of Gold Butte block. Location of profile shown in Figure 1. Modified from *Wernicke and Axen* [1988].

Figure 3. Topographic map of Lake Mead area and western Colorado Plateau. Thick lines mark state boundaries and the shore of Lake Mead. Thin straight lines show the location of topography profiles in Figure 5. Data taken from the NOAA TGP–0030 30' topography data set.

Figure 4. Bouguer gravity anomalies in Lake Mead area and western Colorado Plateau. Thick lines mark state boundaries and the shore of Lake Mead. Thin straight lines show the location of topography profiles in Figure 5.

Figure 5. Bouguer gravity anomalies and topography perpendicular to the strike of the Basin and Range–Colorado Plateau transition. Profile locations shown in Figures 3 and 4. Arrows mark the location and amount of extension across the eastern Basin and Range estimated by *Wernicke et al.* [1988].

Figure 6. Bouguer gravity anomalies near the transition zone predicted by simple models. Bouguer gravity and topography data used in modeling are averaged from the five profiles of Figure 5. Crosses mark observed averaged Bouguer gravity anomalies. Short vertical line between upper and lower plots marks location of transition zone. (a). Solid line shows local (Airy) compensation of topography by deflections of the Moho. Dashed line shows compensation at Moho assuming a flexural rigidity of 10^{22} Nm. (b). Bouguer gravity anomalies and Moho depths corresponding to uniform stretching of the lithosphere west of the transition zone according to the model of *McKenzie* [1978]. Solid lines indicate values associated with extension by a factor β of 1.33, resulting in 10 kilometers of crustal thinning of crust initially 40 kilometers thick. Dashed lines show values predicted from extension by a factor of 2 with 20

kilometers of crustal thinning. Bouguer gravity anomalies are calculated assuming the lithosphere in the extended region has thinned uniformly, maintaining a linear temperature gradient between the surface and a temperature of 1350°C at the base of the lithospheric plate. The unextended thickness of the lithospheric plate is set to 125 kilometers. Deflections of the Moho maintain local (Airy) isostasy. To best fit the observed gravity data –200 mgal were added to the gravity predicted by the model for β = 1.33 (solid lines) and –250 added to the gravity predicted by the $\beta = 2$ (dashed lines).

Figure 7. Maximum deviatoric stress that can be maintained in continental lithosphere, assuming an olivine rheology for the mantle and a strain rate of 10^{-15} s^{-1}. Regions of linearly increasing yield stress with depth deform according to Byerlee's Law for brittle deformation. Ductile deformation occurs in the regions where yield stress decreases exponentially with depth. (a) Quartz diorite crustal rheology. (b) Wet granite rheology in the upper crust introduces a second layer of ductile deformation and substantially weakens the crust relative to model (a).

Figure 8. (a) Schematic representation of ductile flow in response to upper crustal thinning. (b) Boundary conditions on finite element models for a ductile channel with a fixed lower boundary.

Figure 9. Finite element mesh used for modeling flow in ductile channel with fixed lower boundary. Thick vertical lines show side boundaries of grid used to model flow over a 150 kilometer length scale. Lines connect nodes of 9–node elements. (a) Mesh for 25–km thick channel model prior to deformation. (b) Sample of mesh after 10 m.y. of flow at viscosity 10^{20} Pa·s in response to 1 km/m.y. upper crustal thinning.

Figure 10. Velocity vectors for flow in a 700–km long channel initially 25 km thick with viscosity 10^{20} Pa·s at times 0, 2 m.y. and 8 m.y. assuming upper crustal thinning over the left side of the mesh at a rate of 1 km/m.y.

Figure 11. Variations in total crustal thickness and ductile channel thickness for flow in a channel initially 25 km thick with a fixed lower boundary, assuming upper crustal thinning over the left side of the mesh at a rate of 1 km/m.y. beneath an upper crust with zero flexural rigidity thinning at a rate of 1 km/m.y.

Figure 12. Compilation of finite element and analytical modeling results for linear viscous flow. Diamonds mark parameters of runs that predicted 5 kilometers or more of ductile channel thickening beneath the Basin and Range after 10 m.y. of upper crustal thinning at a rate of 1 km/m.y. Crosses mark runs that predicted less than 5 kilometers of ductile channel thickening. Squares mark runs in which total crustal thicknesses are uniform across the transition zone after 10 m.y. Dashed line shows the viscosities corresponding to 'complete' flow (uniform total crustal thickness) computed with Equation 5.

Figure 13. Velocity vectors for flow in which the boundaries of the ductile channel are extending by a factor of 2 over the left side of the grid. Upper crustal thinning is assumed to be 1 km/m.y. Upper plot shows flow at zero time associated with 1 kilometer of instantaneous upper crustal thinning. Lower plot shows flow 5 m.y. after the onset of extension.

Figure 14. (a) Boundary conditions applied to two–layer finite element model. (b) Finite element mesh used in two–layer modeling, prior to flow and after 10 m.y. of flow with crustal channel viscosity of 10^{19} Pa·s and mantle viscosity of 10^{21} Pa·s . Lines connect nodes of 9–node elements. The example shown here is for a ductile crustal channel 25 kilometers thick. The mantle thickness was assumed in all cases to be 200 kilometers.

Figure 15. (a) Velocity vectors for flow in a 25–km thick channel assuming a quartzite rheology with flow parameters as listed in Table 1 at times 0, 1.8 m.y. and 5.5 m.y. Boundary conditions are identical to those assumed in Figure 10. (b) Variations in total crustal thickness and ductile channel thickness under conditions identical to those assumed in 10 and 11.

Figure 16. Schematic illustration of difference in pressure gradients between rigid lower boundary and two–layer models. Overburden pressure as a function of depth is plotted for the unextended (u) and thinned region (t). Average pressure gradients at a given depth correspond to the horizontal distance between the two lines. See text for discussion.

Figure 17. Velocity vectors for flow in a two–layer model at time t = 0, assuming upper crustal thinning over the left side of the mesh at a rate of 1 km/m.y. Shallower, closely

spaced vectors mark velocities in a 25–km thick crustal channel with viscosity 10^{20} Pa·s and density of 2600 kg/m^3. Deeper, more widely spaced vectors show flow in the underlying 200–km thick mantle channel with viscosity also 10^{20} Pa·s and density of 3300 kg/m^3. The vectors fifth from the top show velocities at the crust–mantle boundary. A significant component of horizontal velocity at the crust–mantle boundary near the transition zone is found even at time t = 0.

Figure 18. Models for the topographic step across the transition zone. Dashed lines show the approximate shape of a flexurally maintained discontinuity in the topography superimposed on the smooth topographic step predicted from linear viscous flow at 10^{20} Pa·s for 10 m.y. The shape of the step is a function of the flexural rigidity. Thick solid line shows the original 10^{20} Pa·s ductile flow profile. Thin solid line shows the topography after 10 m.y. for flow at 10^{19} Pa·s in a 10–km thick channel. 100 meter 'jaggedness' in elevation produced by the finite element models has been removed.

Figure 19. Location map showing Profiles 1–1' and 2–2', boundary of Mesozoic thrusting, and Cenozoic normal faulting and related features. T's mark the endpoints of profiles 1–1' and 2–2'. Thick barbed line marks location of eastern boundary of Mesozoic thrusting. Thinner lines indicate Cenozoic normal faults.

Figure 20. (a) Bouguer gravity anomalies and topography along profiles roughly perpendicular to N–S Eocene normal faults on the eastern boundary of an extended region in southern British Columbia. Location shown in Figure 19. (b) Gravity models along Profile 1–1'. Crosses show observed Bouguer gravity anomalies averaged from the five profiles shown in (a). Solid line shows simple Airy compensation model. Dashed line assumes 15 kilometers of crustal thinning is supported by a uniform –50 kg/m^3 density anomaly extending to 205 kilometers depth in the mantle beneath the thinned crust. Crustal and unextended mantle densities are assumed to be 2700 kg/m^3 and 3300 kg/m^3, respectively. Local variations in topography are supported by deflections of the Moho superimposed on the abrupt crustal thinning.

Figure 21. (a) Bouguer gravity anomalies and topography along profiles roughly perpendicular to N–S Eocene normal faults near the Bitterroot batholith of northern Idaho. Location shown in Figure 19. (b) Gravity models along Profile 2–2'. Crosses show observed Bouguer gravity anomalies averaged from the five profiles shown in

(a). Solid line shows simple Airy compensation model. Dashed line assumes 12 kilometers of crustal thinning is supported by a uniform –50 kg/m^3 density anomaly extending to 172 kilometers depth in the mantle beneath the thinned crust. Crustal and unextended mantle densities are assumed to be 2700 kg/m^3 and 3300 kg/m^3, respectively. Local variations in topography are supported by deflections of the Moho superimposed on the abrupt crustal thinning.

Figure 22. Compilation of finite element and analytical modeling results for linear viscous flow assuming a channel length of 150 kilometers. Symbols as described for Figure 12. Finite element grid used is shown in Figure 9.

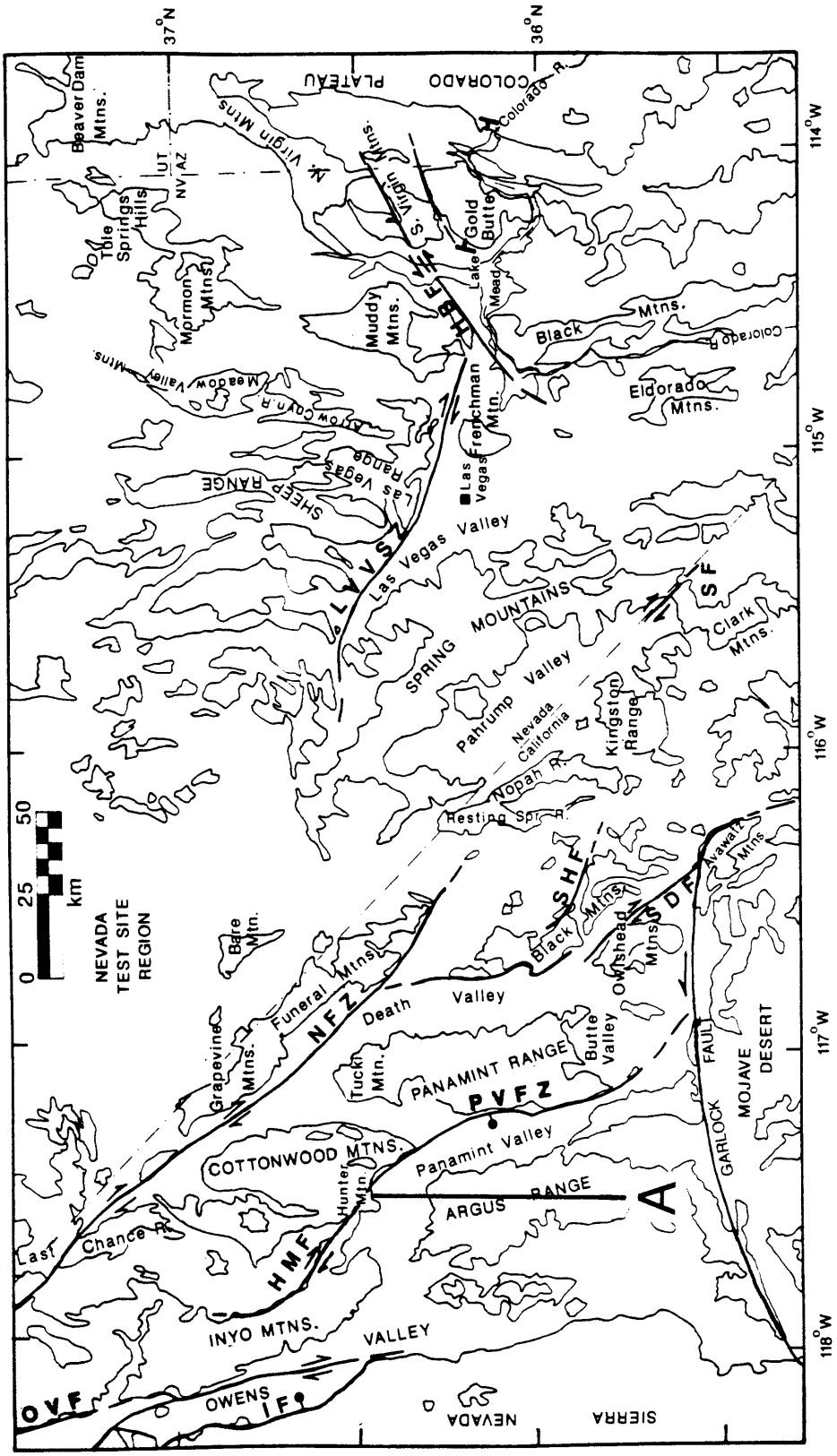
37°N
36°N
114°W
115°W
116°W
117°W
118°W
COLORADO PLATEAU
Colorado R.
Beaver Dam Mtns.
Virgin Mtns
Virgin Mtns
S. Virgin
Gold Butte
Lake Mead
Tole Springs Hills
UT
NV AZ
Mormon Mtns.
Muddy Mtns.
MVFZ
Black Mtns.
Colorado R.
Meadow Valley Mtns.
Meadow Valley Wash
Arrow Canyon Range
Las Vegas Range
SHEEP RANGE
Frenchman Mtn.
Eldorado Mtns.
Las Vegas
LVVSZ
Las Vegas Valley
SPRING MOUNTAINS
SF
Clark Mtns.
Pahrump Valley
Nevada
California
Kingston Range
Nopah R.
Resting Spr. R.
SHF
Avawatz Mtns
SDF
Owlshead Mtns
Black Mtns
Bare Mtn.
NEVADA TEST SITE REGION
0
25
50
km
Funeral Mtns.
NFZ
Death Valley
Grapevine Mtns.
Tucki Mtn.
PANAMINT RANGE
Butte Valley
PVFZ
FAULT
GARLOCK
MOJAVE DESERT
COTTONWOOD MTNS.
Panamint Valley
Hunter Mtn.
ARGUS RANGE
A
A'
Last Chance R.
HMF
INYO MTNS.
VALLEY
OVF
OWENS
IF
NEVADA
SIERRA

Figure 1

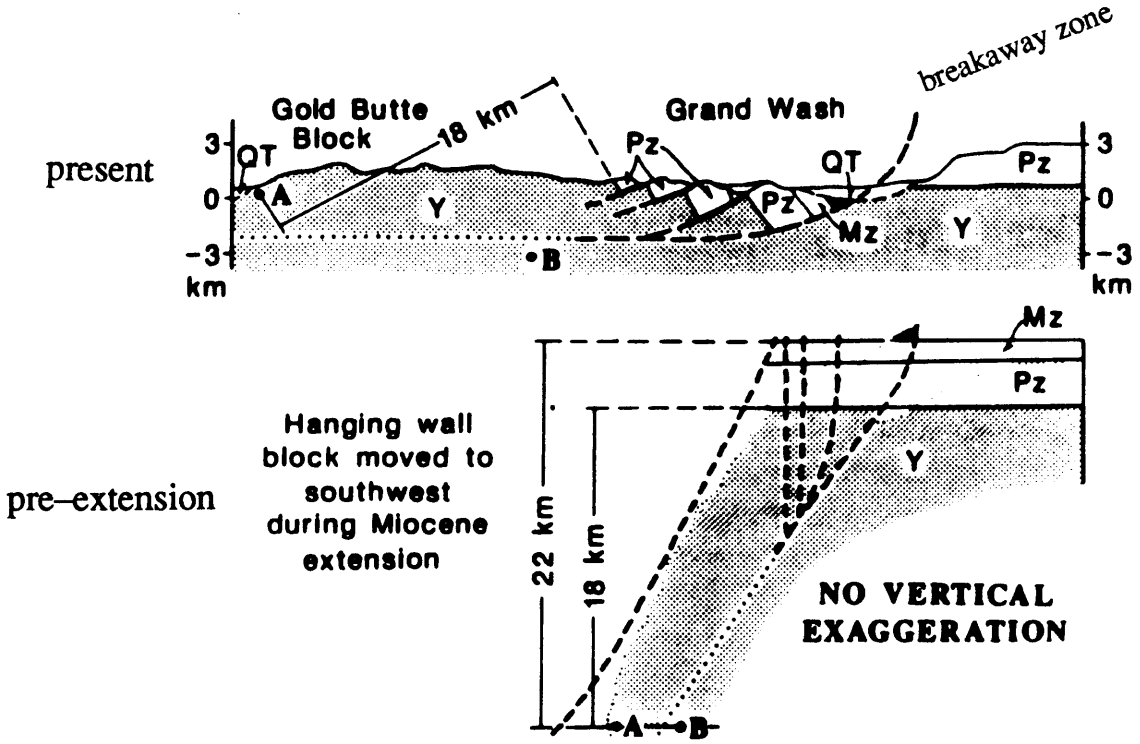
present
Gold Butte Block
18 km
Grand Wash
breakaway zone
QT
Pz
Mz
Y
A
B
3
0
-3
km
pre–extension
Hanging wall block moved to southwest during Miocene extension
22 km
18 km
NO VERTICAL EXAGGERATION

Figure 2

Topography (meters)

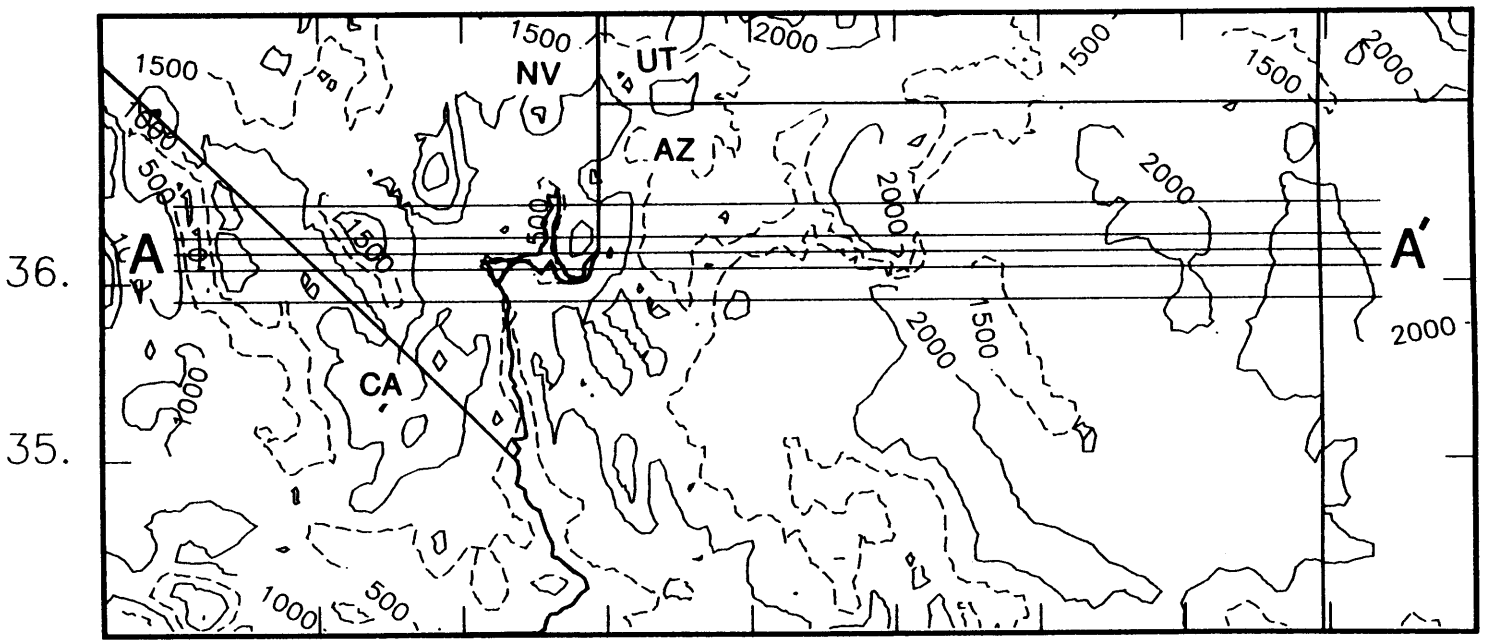

Figure 3

Bouguer Gravity (mgal)

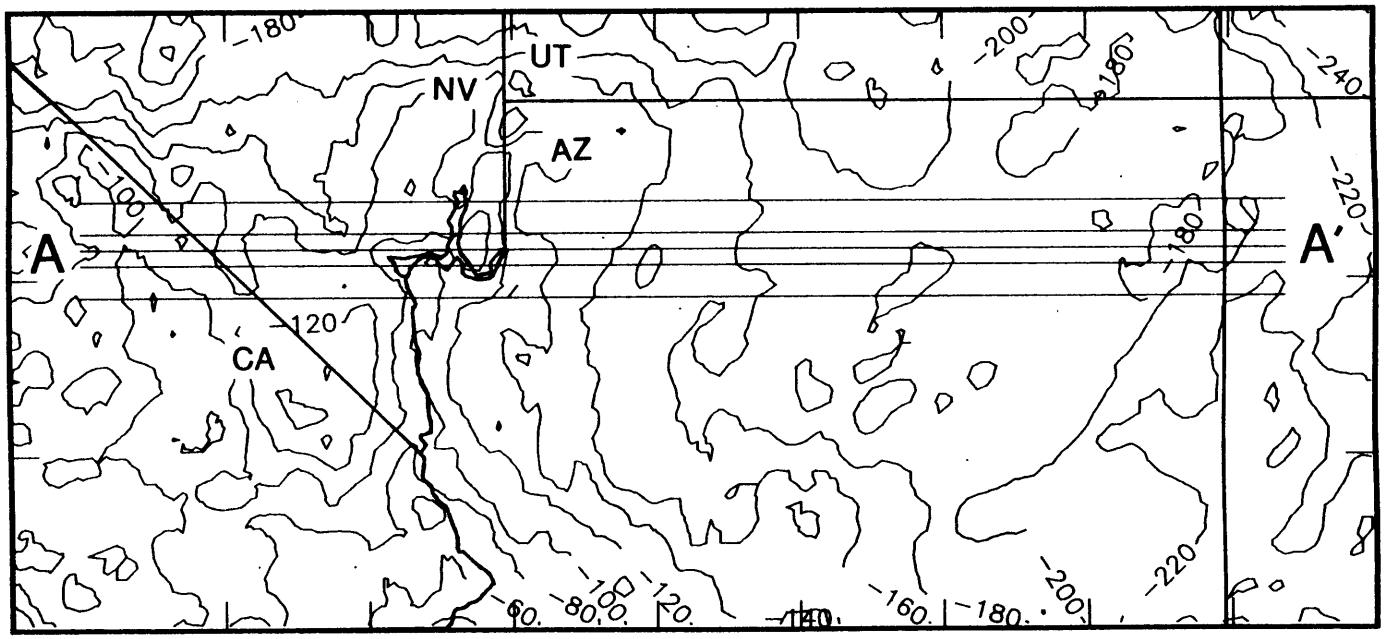

Figure 4

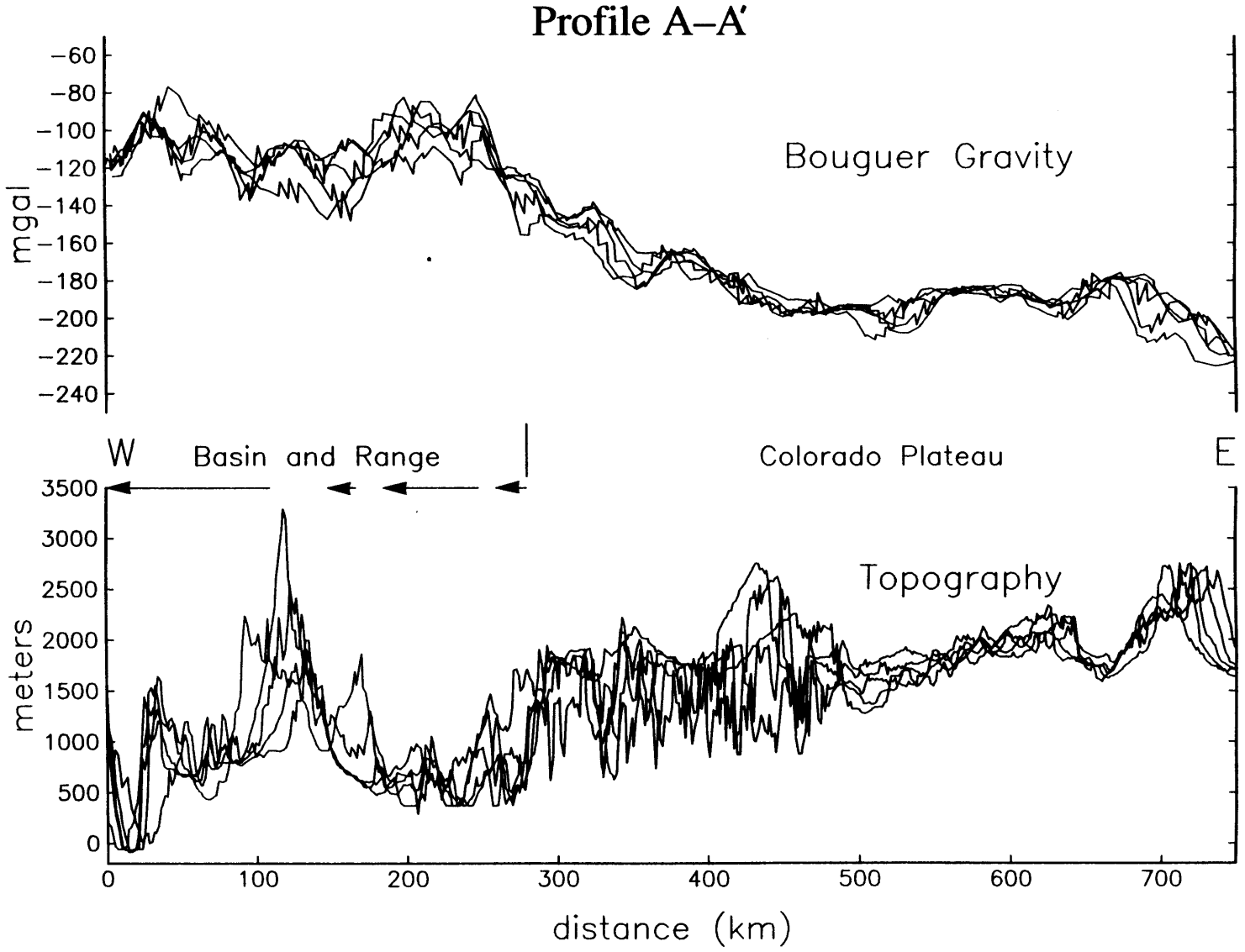
Profile A–A′
Bouguer Gravity
mgal
−60
−80
−100
−120
−140
−160
−180
−200
−220
−240
W
Basin and Range
Colorado Plateau
E
Topography
meters
3500
3000
2500
2000
1500
1000
500
0
0
100
200
300
400
500
600
700
distance (km)

Figure 5

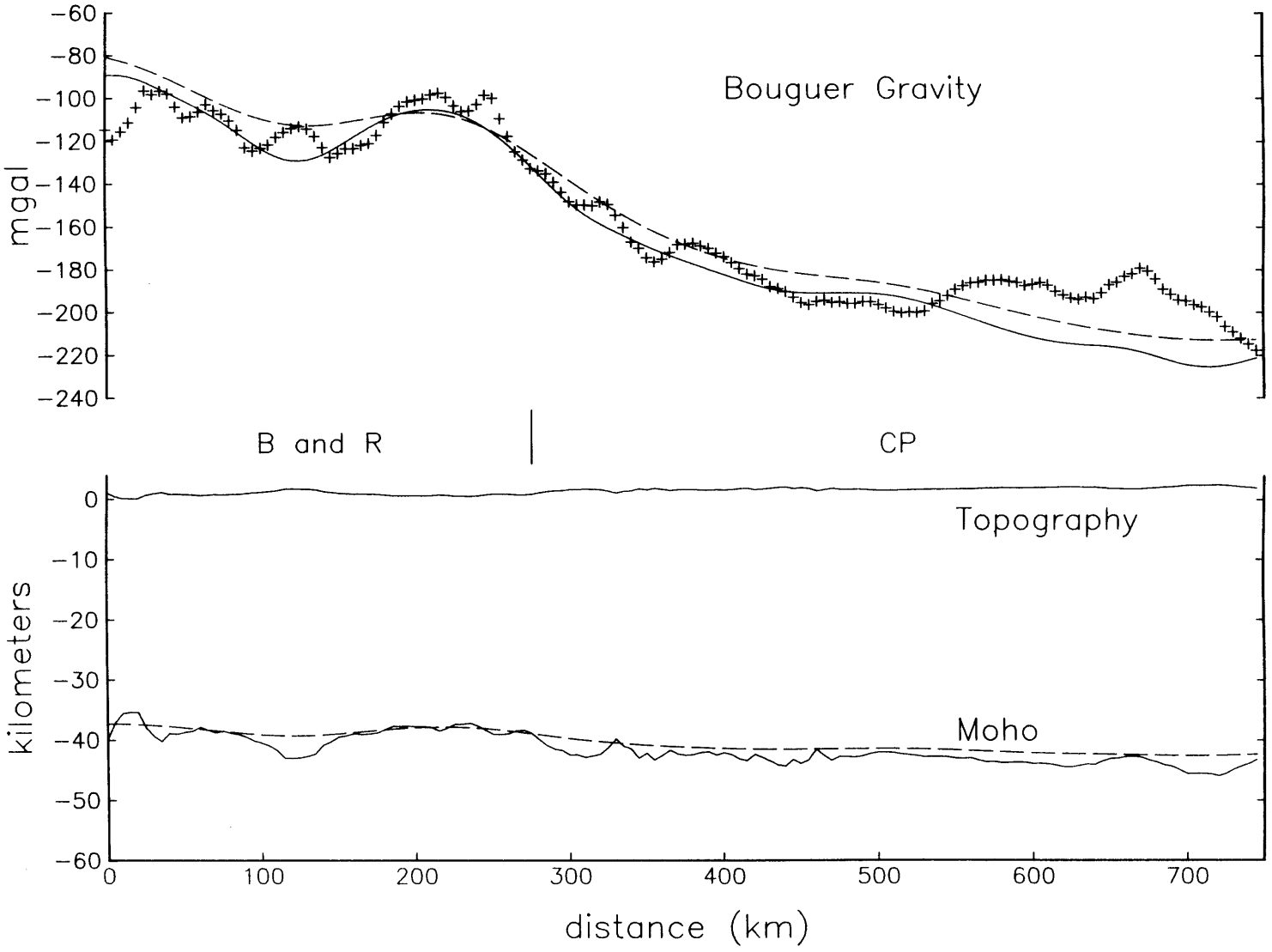
Bouguer Gravity
mgal
-60
-80
-100
-120
-140
-160
-180
-200
-220
-240
B and R
CP
Topography
Moho
kilometers
0
-10
-20
-30
-40
-50
-60
0
100
200
300
400
500
600
700
distance (km)

Figure 6(a)

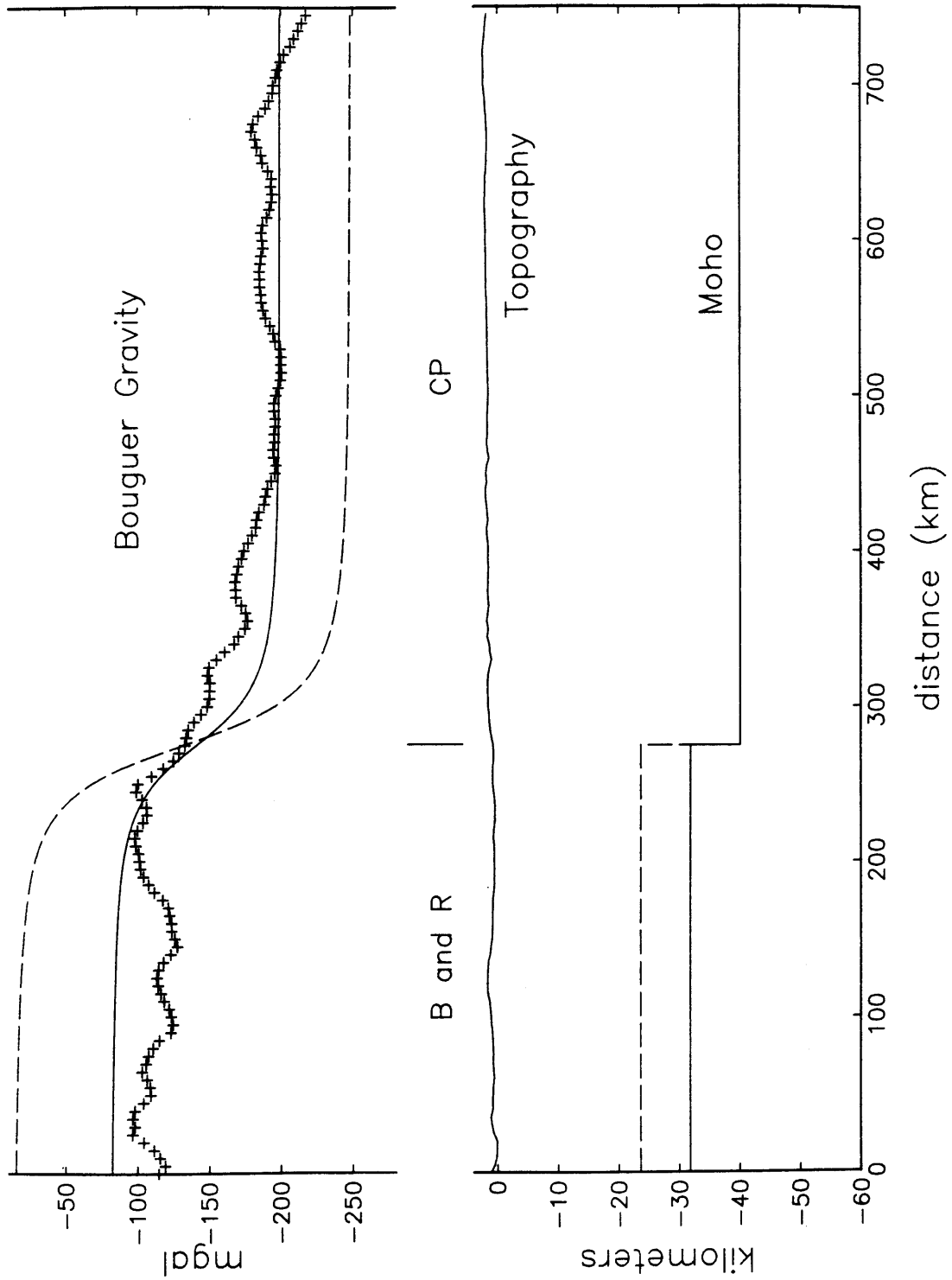
Bouguer Gravity
mgal
−50
−100
−150
−200
−250
CP
B and R
Topography
Moho
kilometers
0
−10
−20
−30
−40
−50
−60
0
100
200
300
400
500
600
700
distance (km)

Figure 6(b)

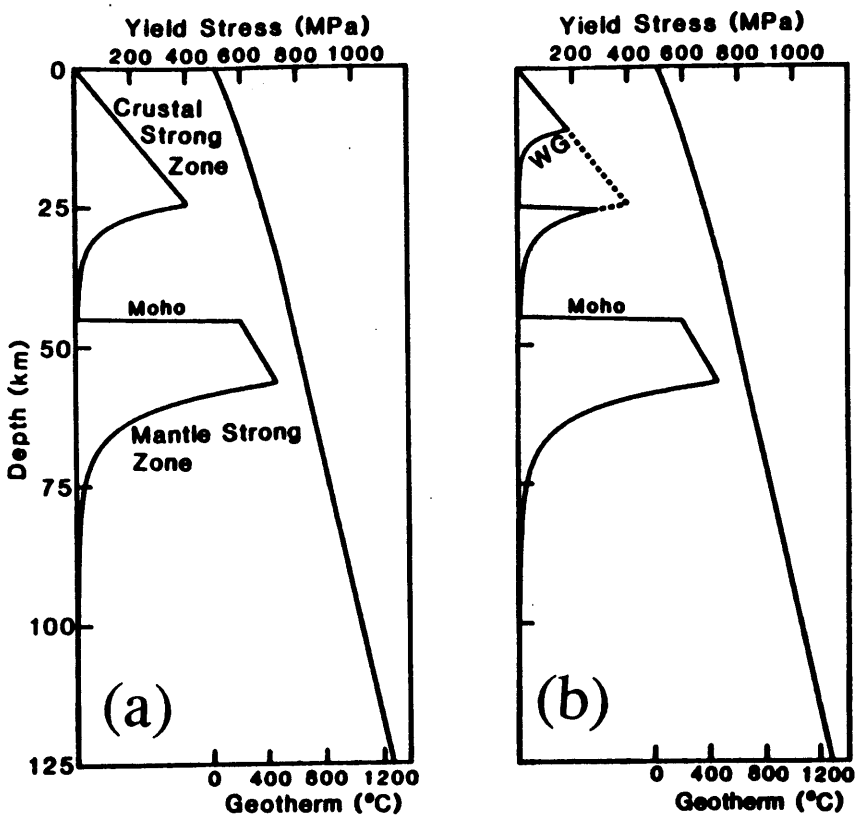
Yield Stress (MPa)
200 400 600 800 1000
0
25
50
75
100
125
Depth (km)
Crustal Strong Zone
Moho
Mantle Strong Zone
(a)
0 400 800 1200
Geotherm (°C)
Yield Stress (MPa)
200 400 600 800 1000
WG
Moho
(b)
0 400 800 1200
Geotherm (°C)

Figure 7

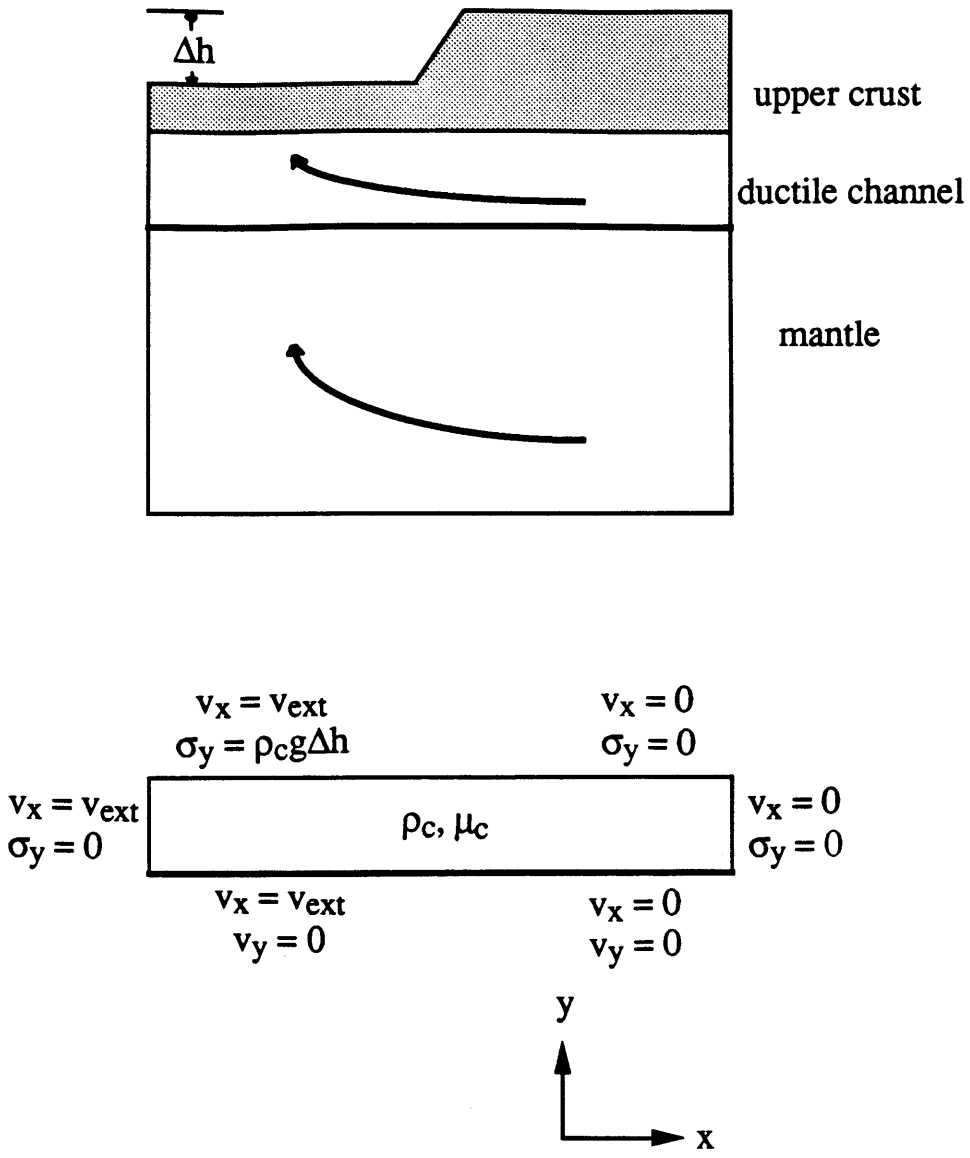
Δh
upper crust
ductile channel
mantle
$v_x = v_{ext}$
$\sigma_y = \rho_c g \Delta h$
$v_x = 0$
$\sigma_y = 0$
$v_x = v_{ext}$
$\sigma_y = 0$
ρ_c, μ_c
$v_x = 0$
$\sigma_y = 0$
$v_x = v_{ext}$
$v_y = 0$
$v_x = 0$
$v_y = 0$
y
x

Figure 8(a,b)

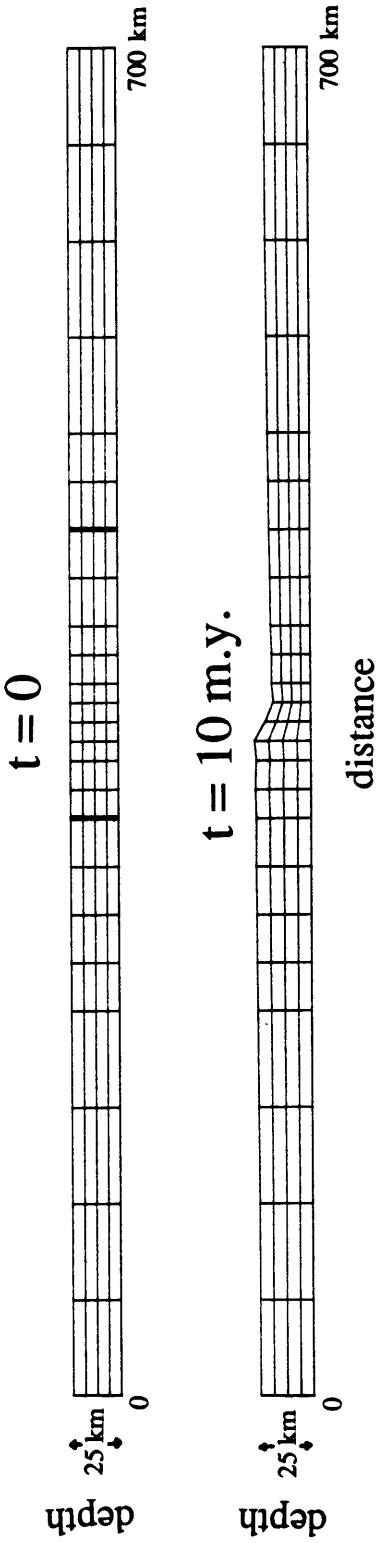

Figure 9

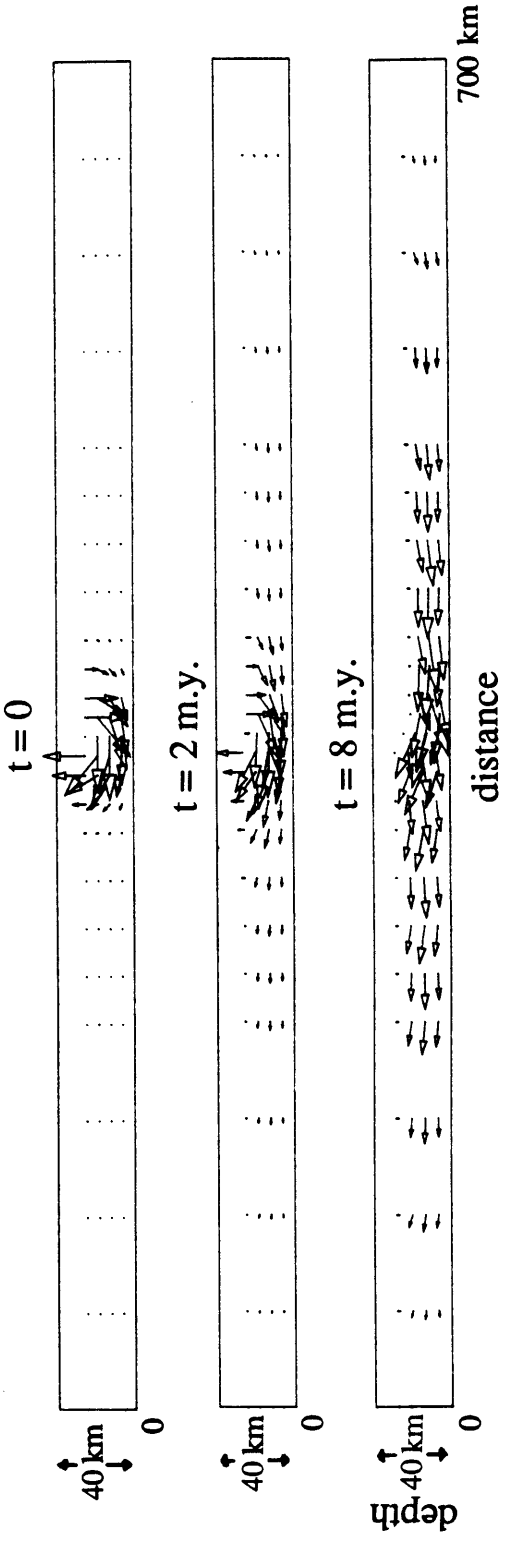

Figure 10

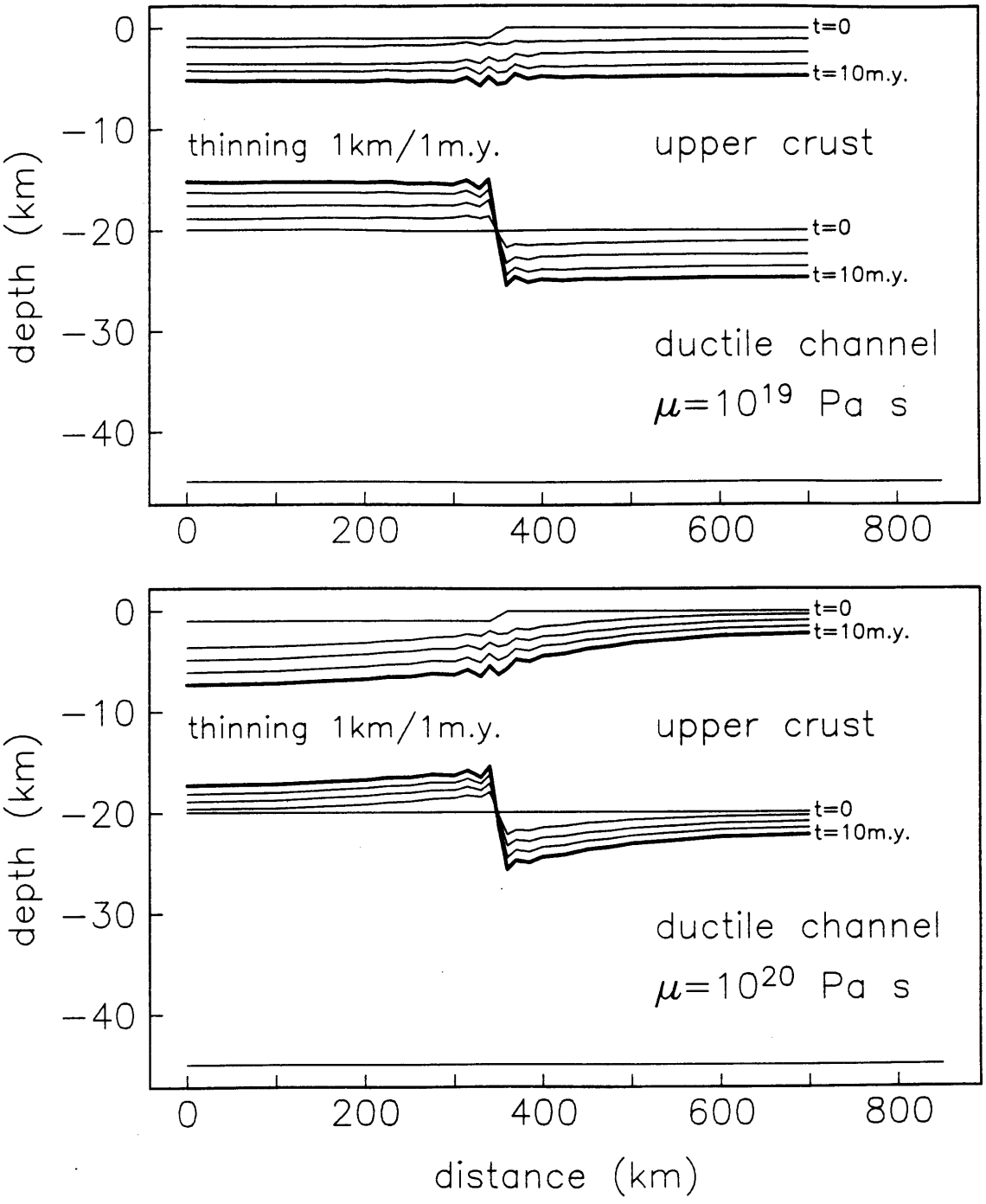
0
−10
−20
−30
−40
depth (km)
t=0
t=10m.y.
thinning 1km/1m.y.
upper crust
t=0
t=10m.y.
ductile channel
μ=10^19 Pa s
0
200
400
600
800
0
−10
−20
−30
−40
depth (km)
t=0
t=10m.y.
thinning 1km/1m.y.
upper crust
t=0
t=10m.y.
ductile channel
μ=10^20 Pa s
0
200
400
600
800
distance (km)

Figure 11

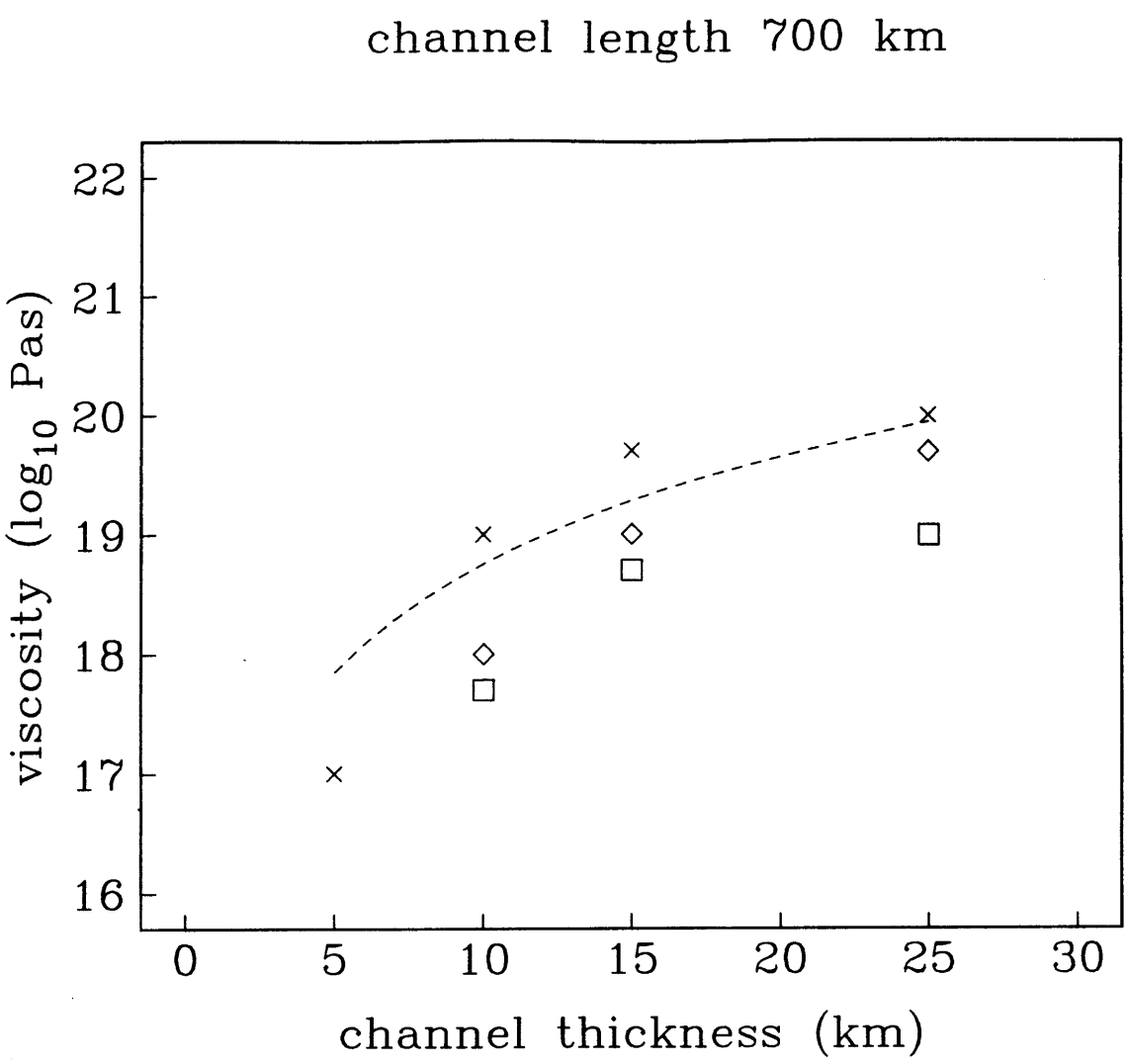
channel length 700 km
viscosity ($\log_{10}$ Pas)
22
21
20
19
18
17
16
0
5
10
15
20
25
30
channel thickness (km)

Figure 12

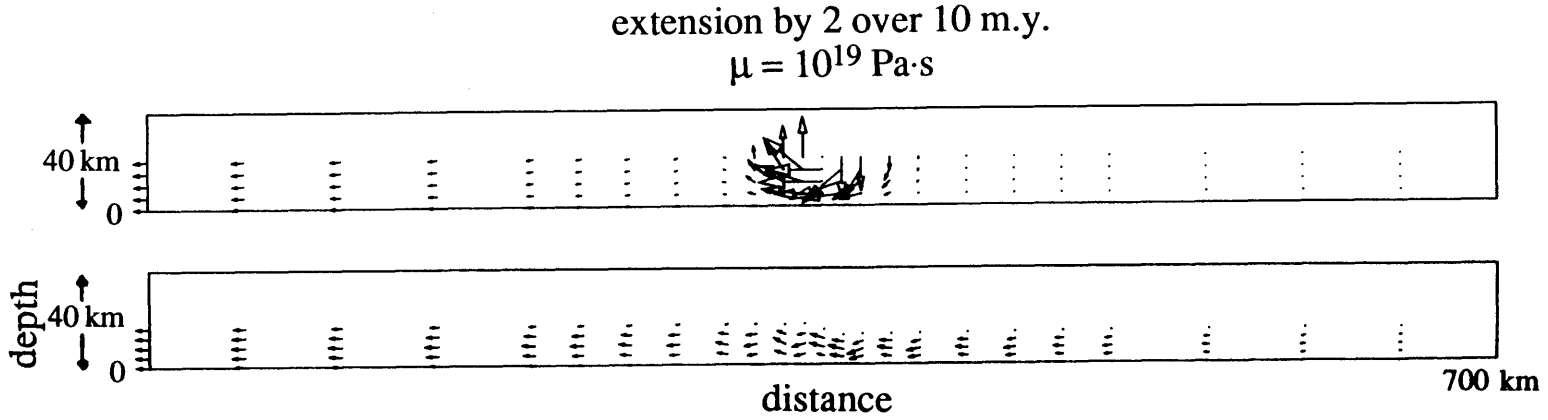
extension by 2 over 10 m.y.
μ = 10^19 Pa·s
40 km
0
depth
40 km
0
700 km
distance

Figure 13

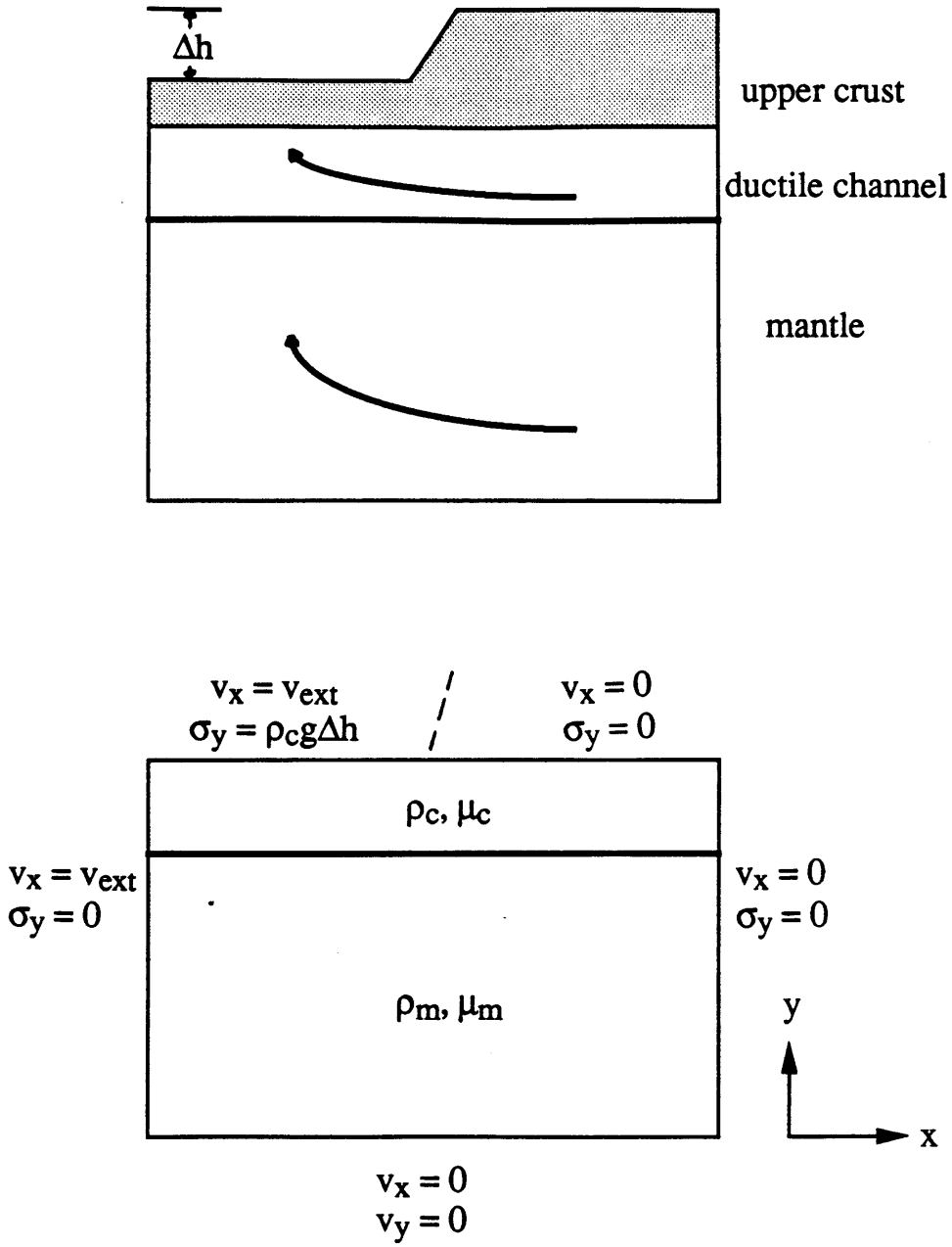
Δh
upper crust
ductile channel
mantle
$v_x = v_{ext}$
$\sigma_y = \rho_c g \Delta h$
$v_x = 0$
$\sigma_y = 0$
ρ_c, μ_c
$v_x = v_{ext}$
$\sigma_y = 0$
$v_x = 0$
$\sigma_y = 0$
ρ_m, μ_m
y
x
$v_x = 0$
$v_y = 0$

Figure 14(a)

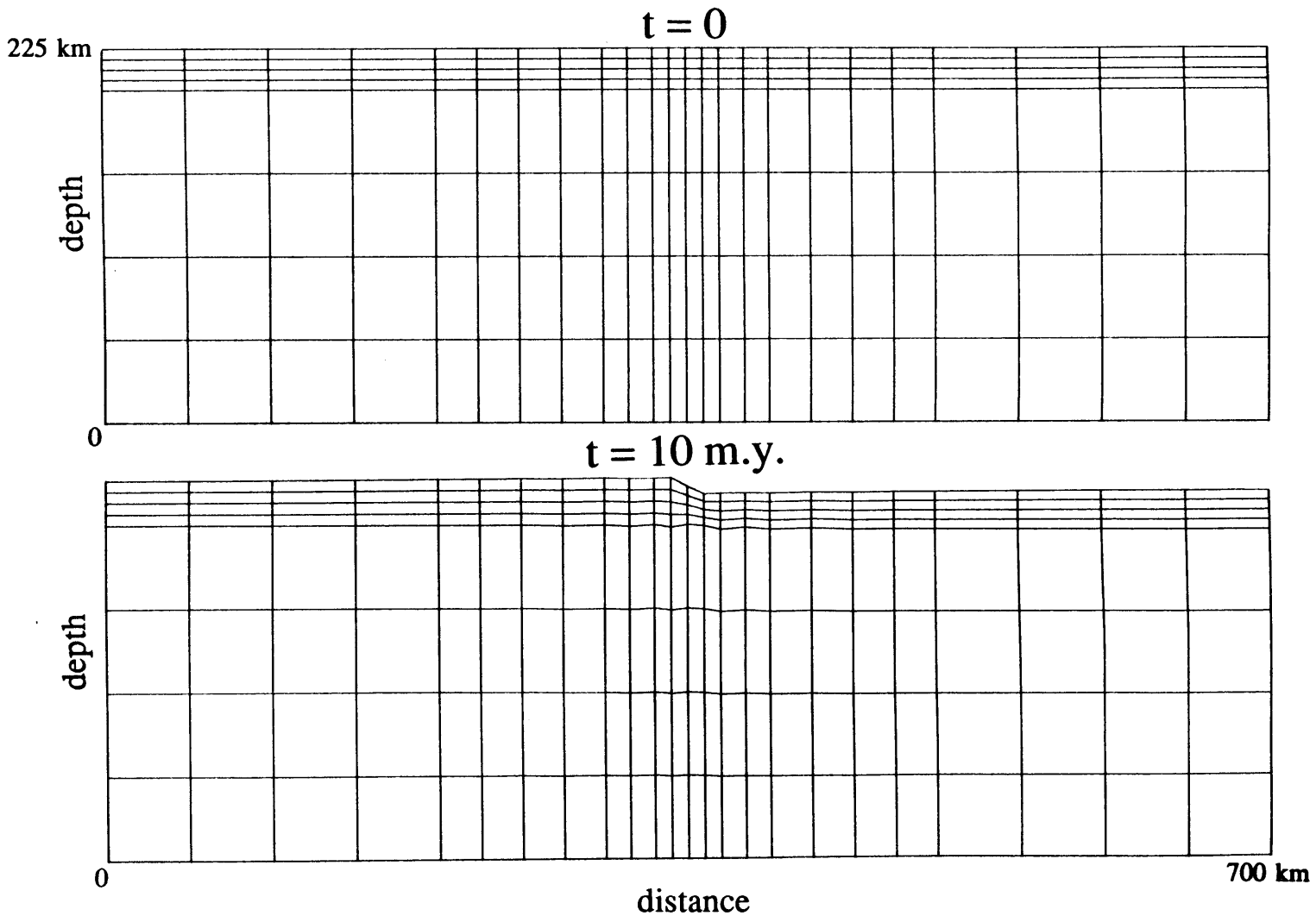

Figure 14(b)

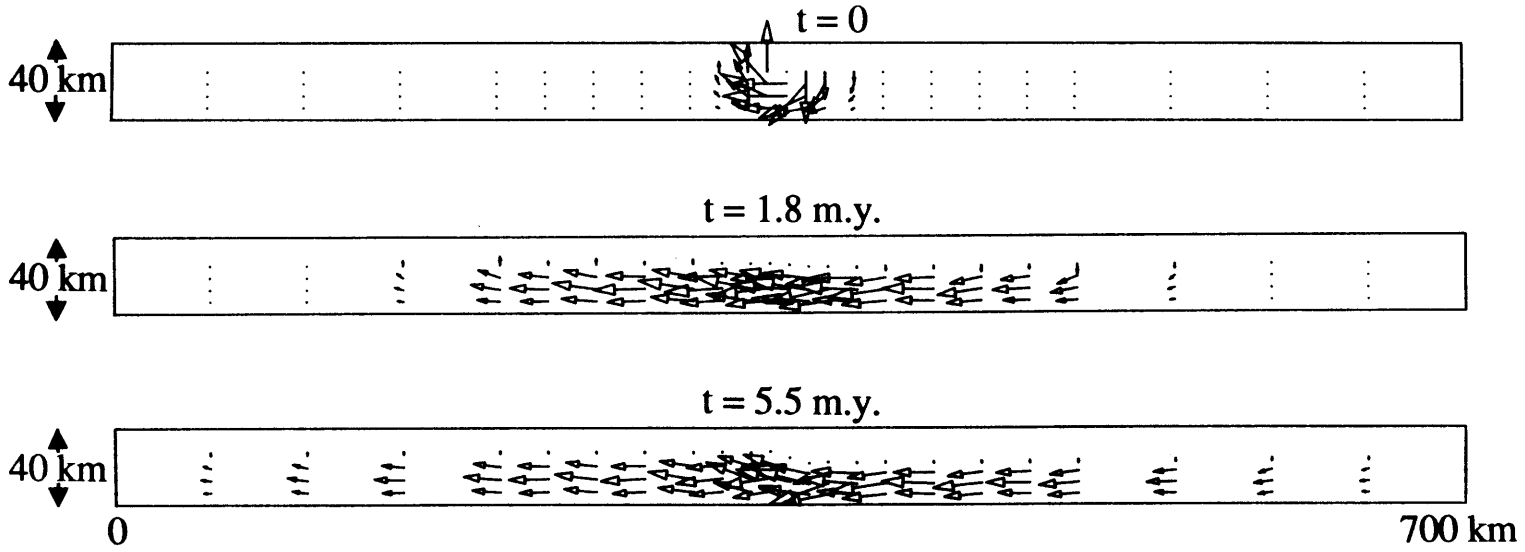

Figure 15(a)

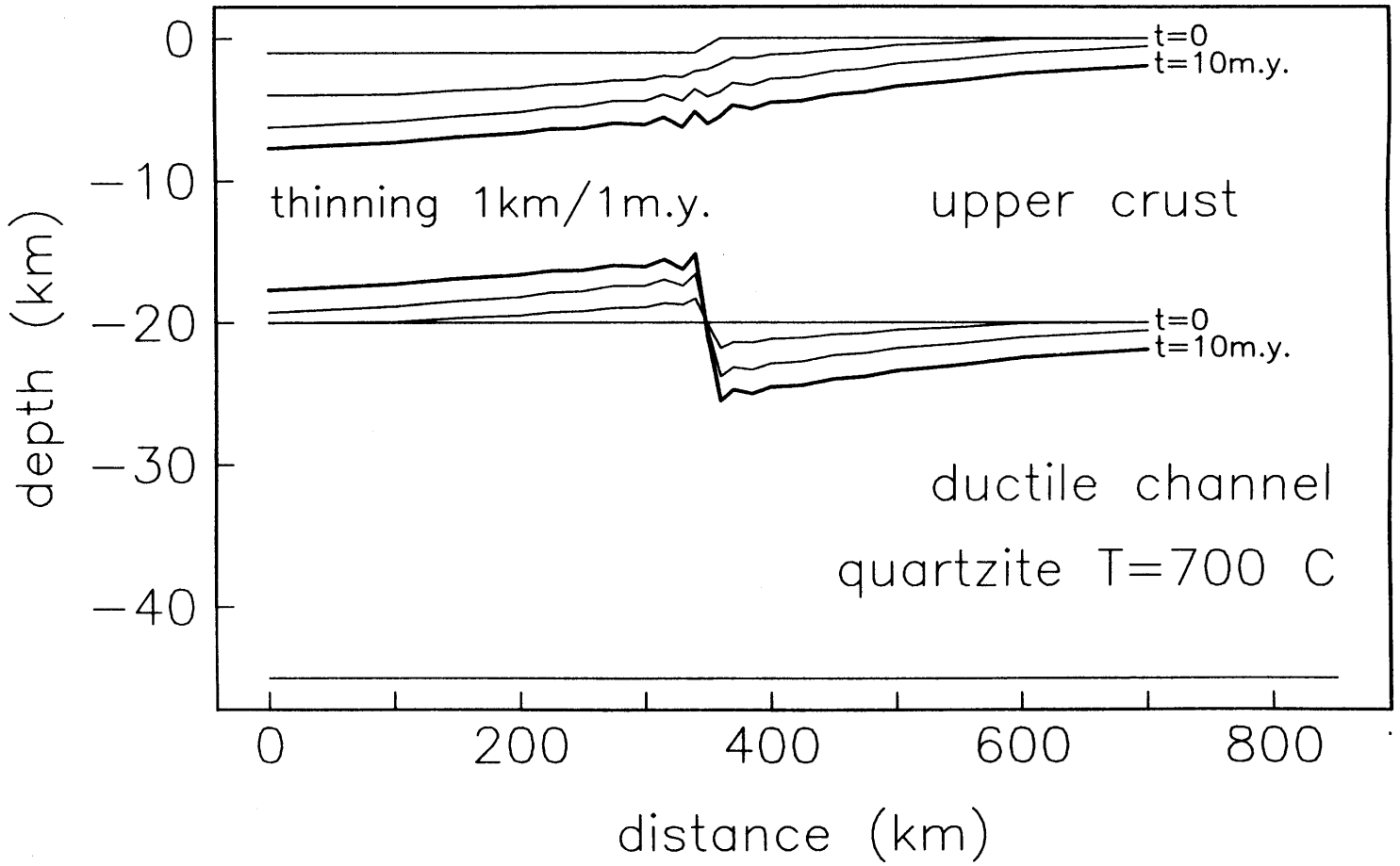
0
−10
−20
−30
−40
depth (km)
t=0
t=10m.y.
thinning 1km/1m.y.
upper crust
t=0
t=10m.y.
ductile channel
quartzite T=700 C
0
200
400
600
800
distance (km)

Figure 15(b)

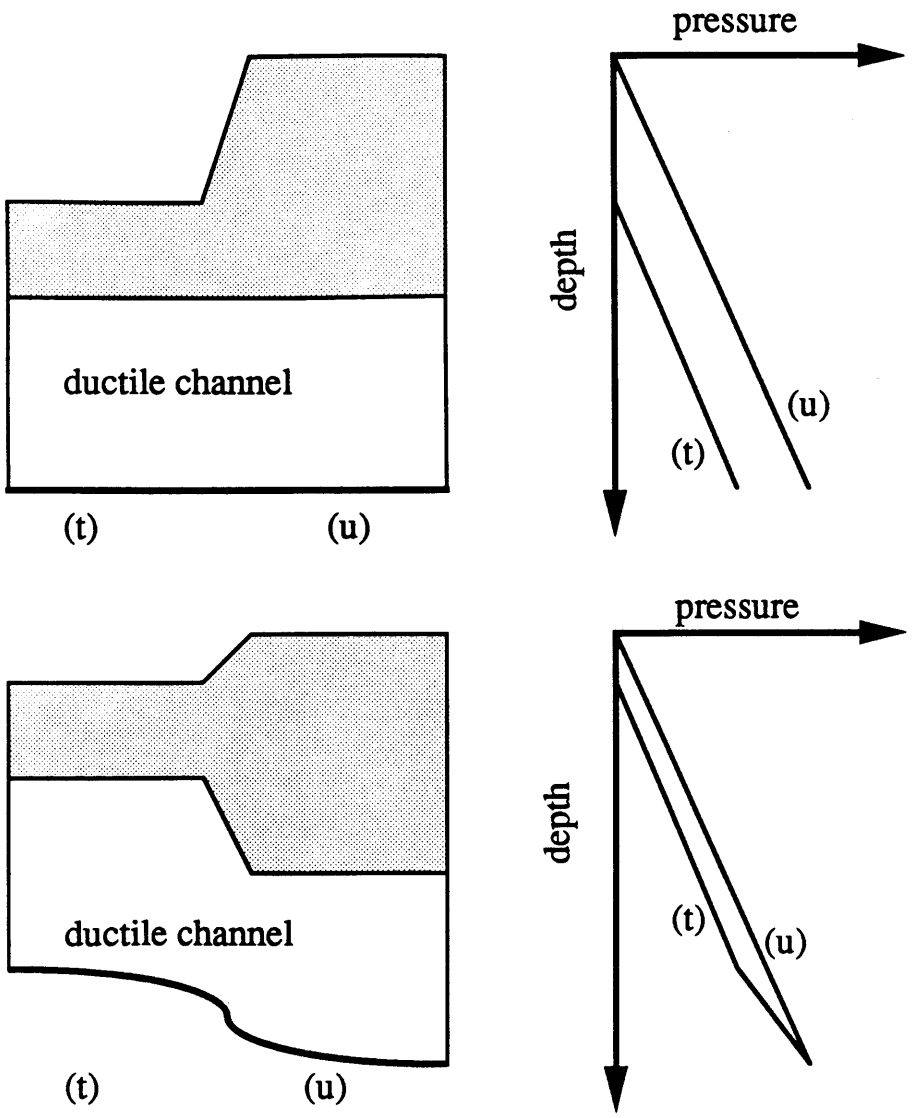
pressure
depth
ductile channel
(t)
(u)
(t)
(u)
pressure
depth
ductile channel
(t)
(u)
(t)
(u)

Figure 16

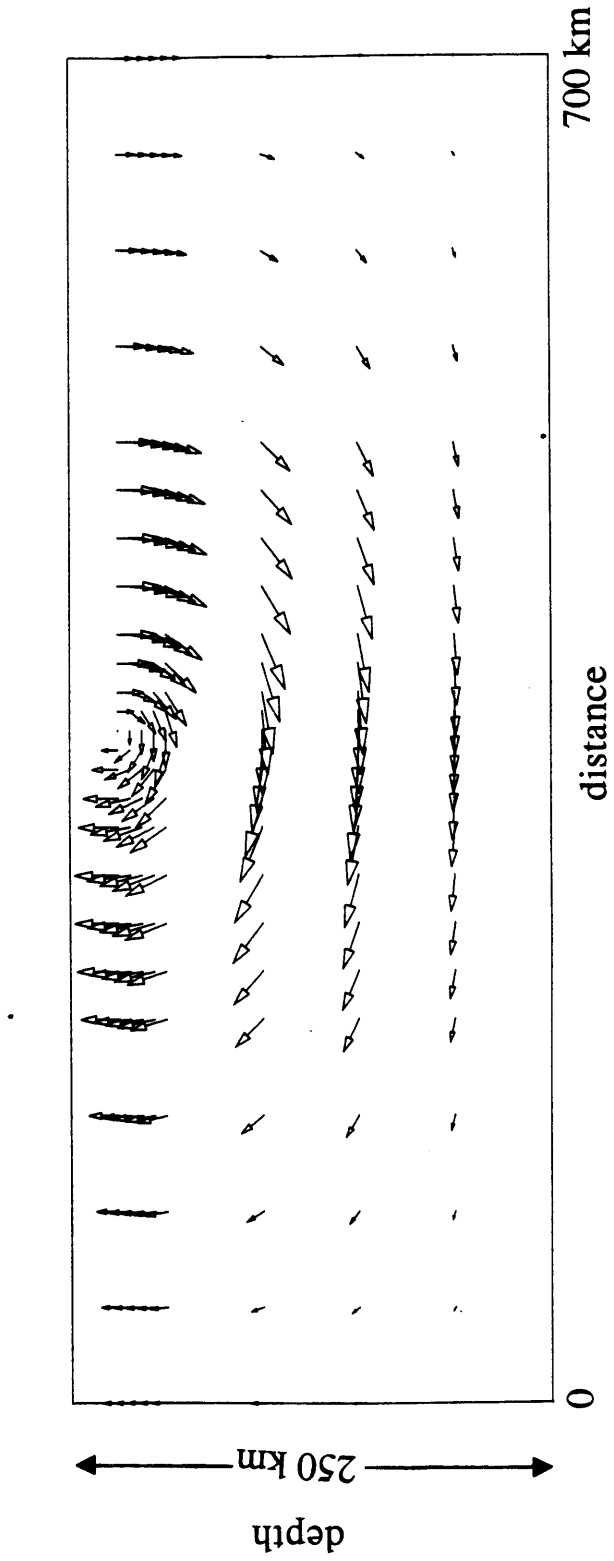

Figure 17

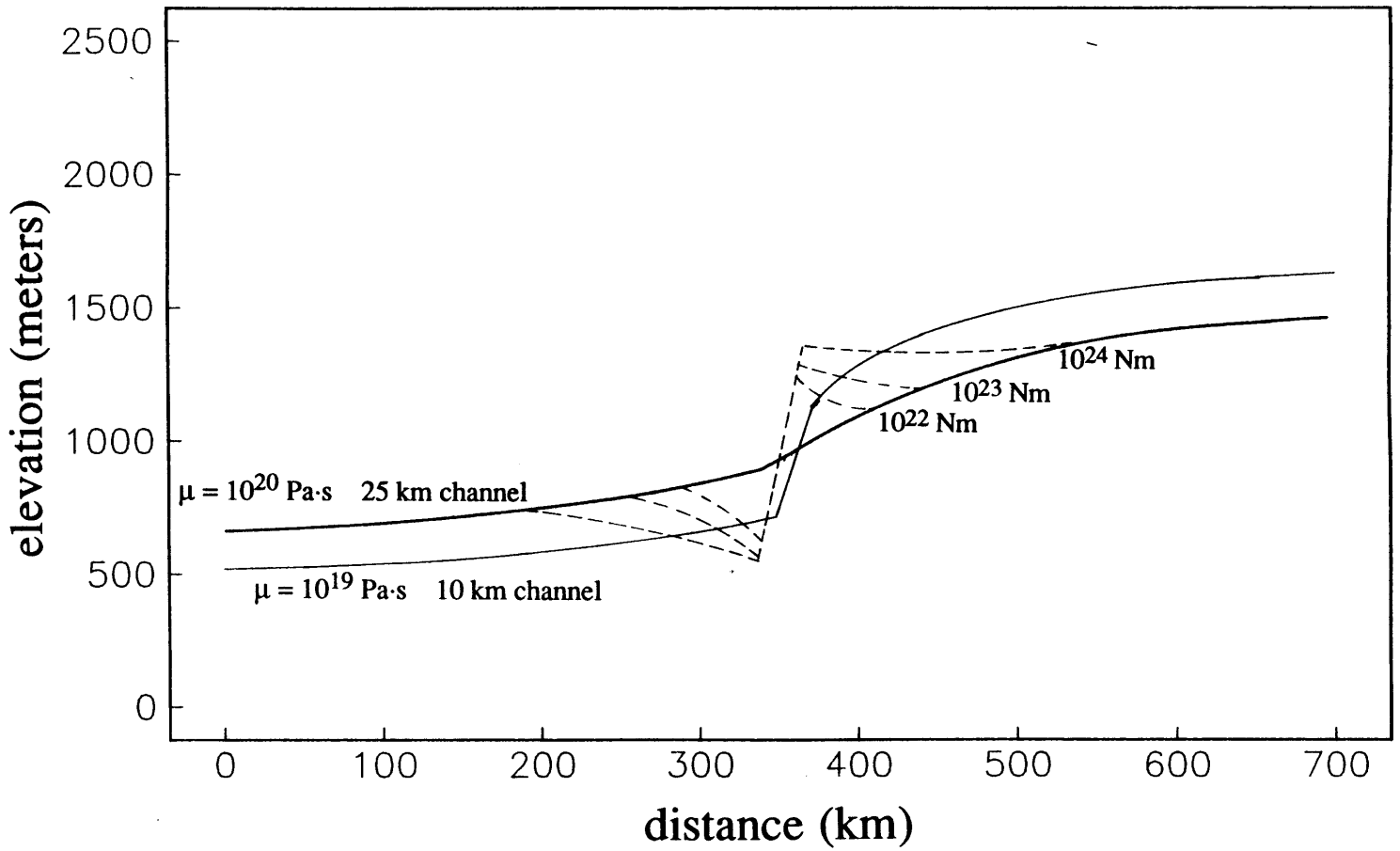
2500
2000
1500
1000
500
0
elevation (meters)
0
100
200
300
400
500
600
700
distance (km)
μ = 10^20 Pa·s 25 km channel
μ = 10^19 Pa·s 10 km channel
10^24 Nm
10^23 Nm
10^22 Nm

Figure 18

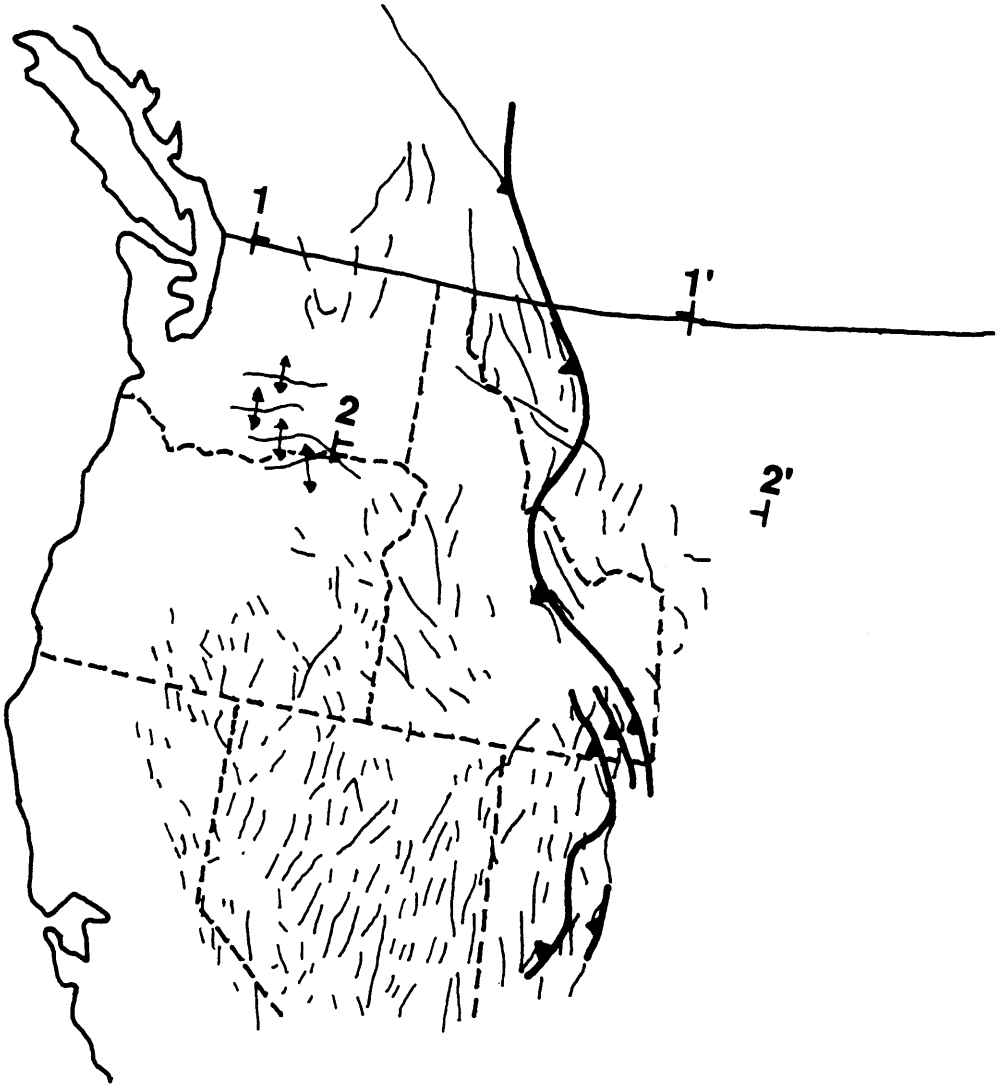

Figure 19

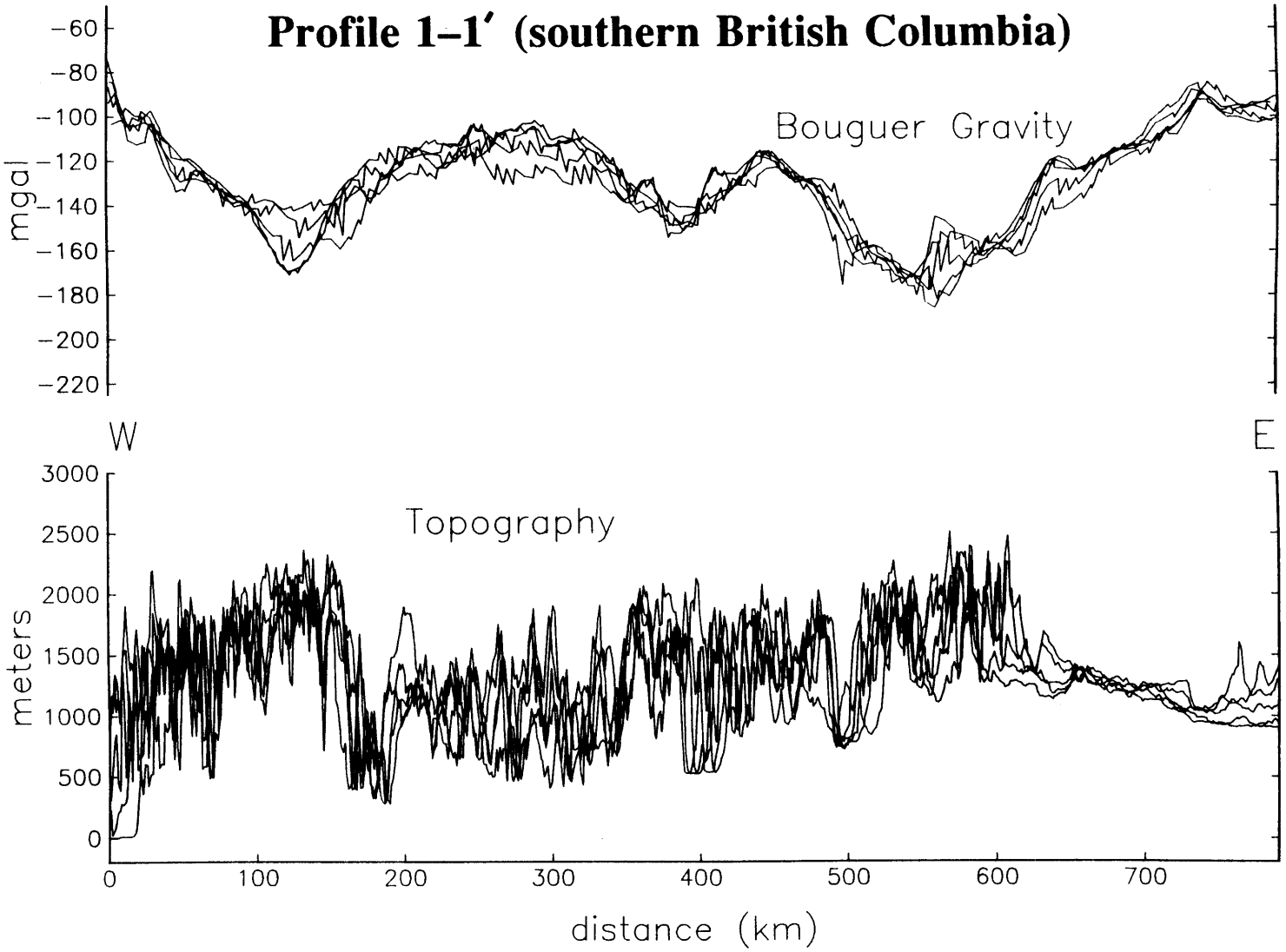
Profile 1–1′ (southern British Columbia)
Bouguer Gravity
mgal
−60
−80
−100
−120
−140
−160
−180
−200
−220
W
E
Topography
meters
3000
2500
2000
1500
1000
500
0
0
100
200
300
400
500
600
700
distance (km)

Figure 20(a)

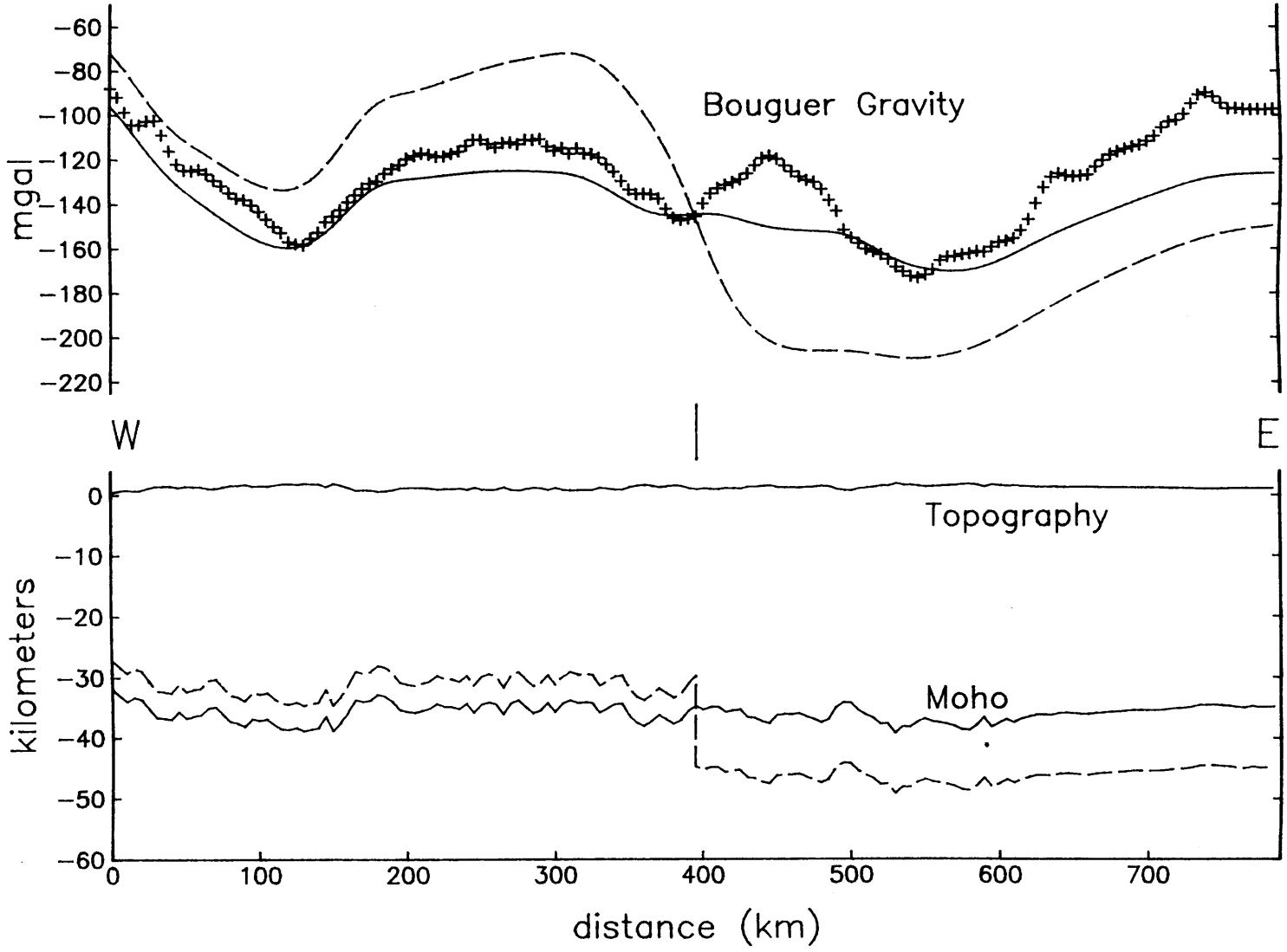
Bouguer Gravity
mgal
-60
-80
-100
-120
-140
-160
-180
-200
-220
W
E
Topography
Moho
kilometers
0
-10
-20
-30
-40
-50
-60
0
100
200
300
400
500
600
700
distance (km)

Figure 20(b)

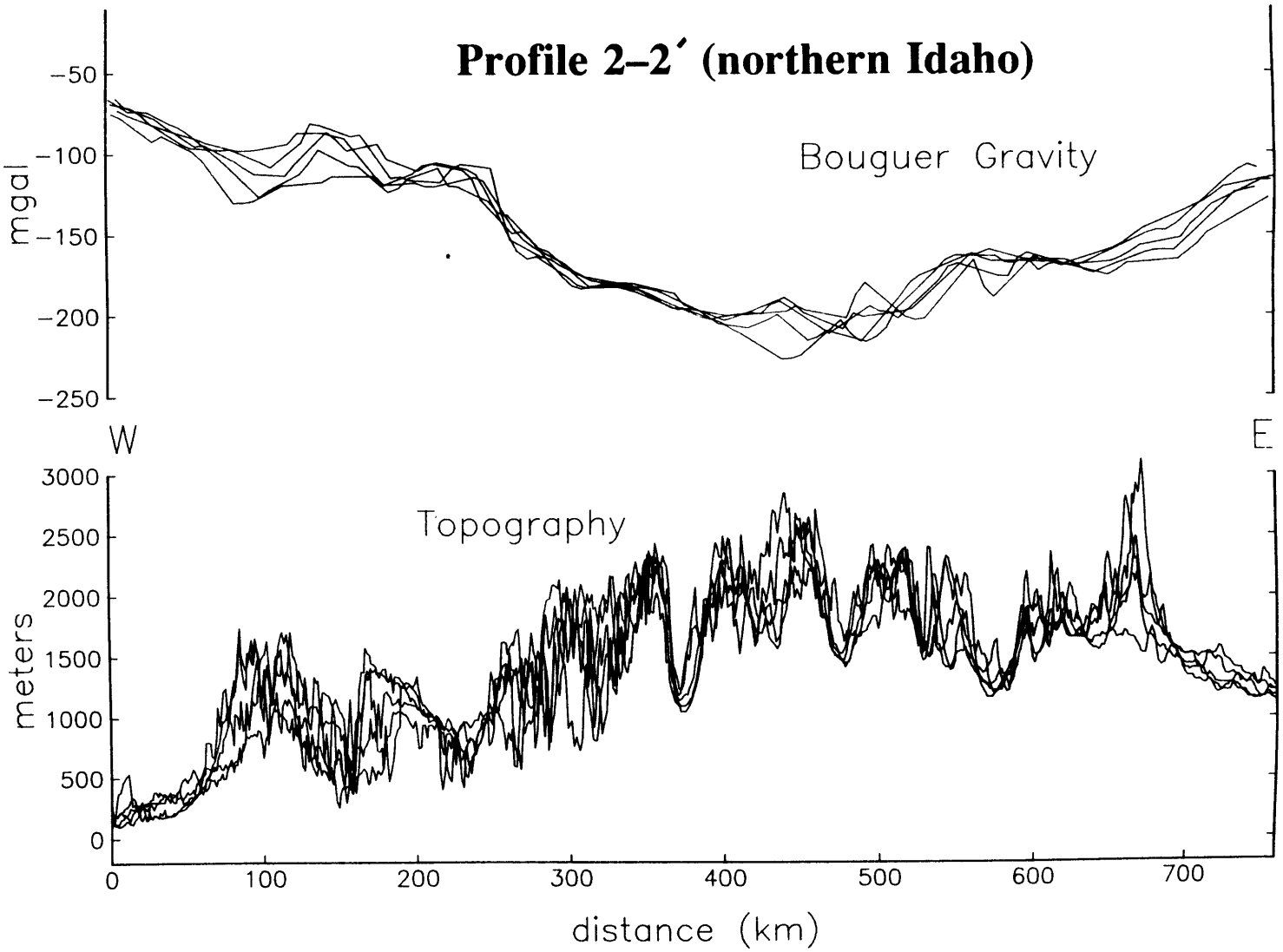
Profile 2–2′ (northern Idaho)
Bouguer Gravity
mgal
−50
−100
−150
−200
−250
W
E
Topography
meters
3000
2500
2000
1500
1000
500
0
0
100
200
300
400
500
600
700
distance (km)

Figure 21(a)

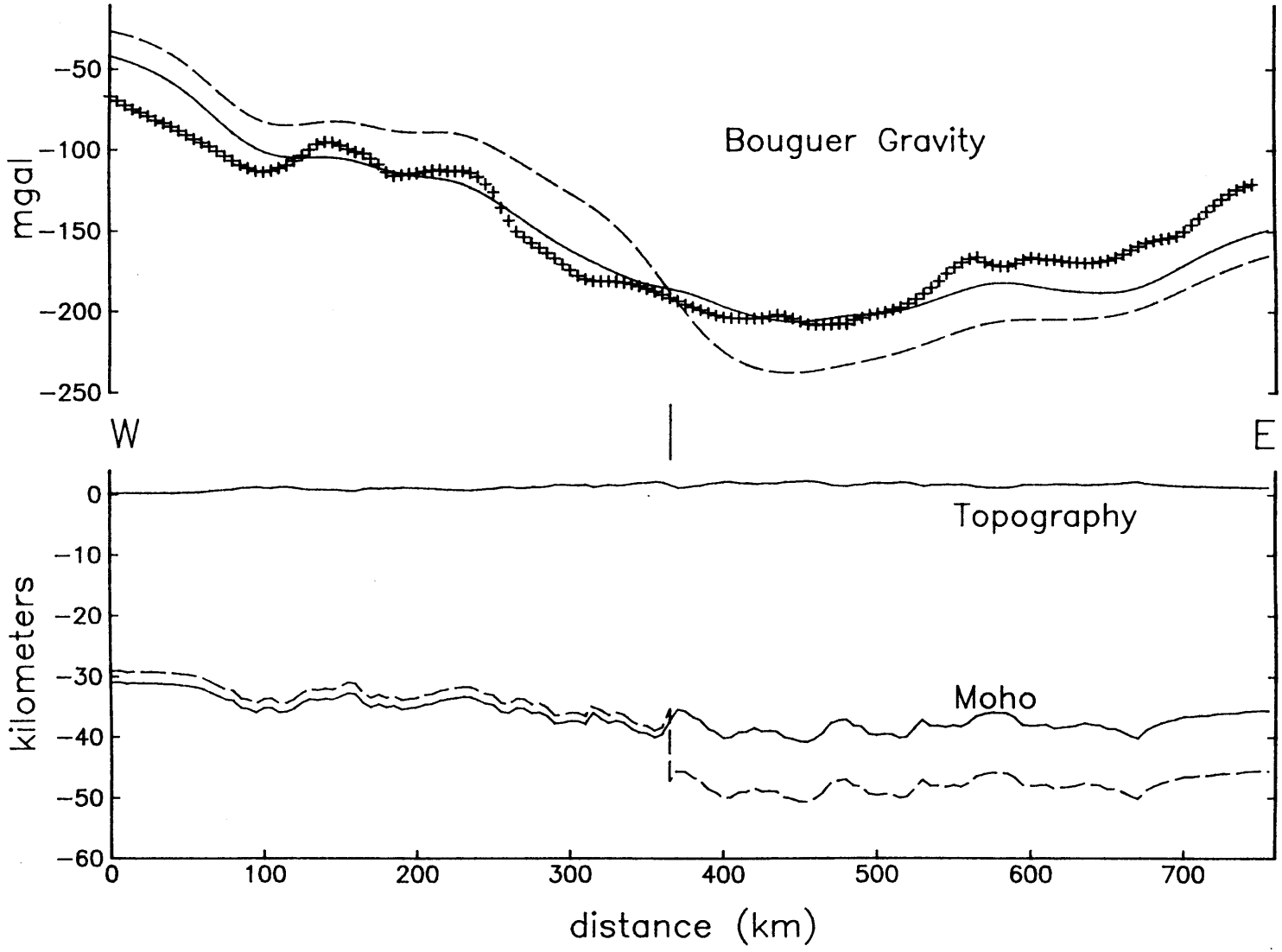
Bouguer Gravity
mgal
-50
-100
-150
-200
-250
W
E
Topography
Moho
kilometers
0
-10
-20
-30
-40
-50
-60
0
100
200
300
400
500
600
700
distance (km)

Figure 21(b)

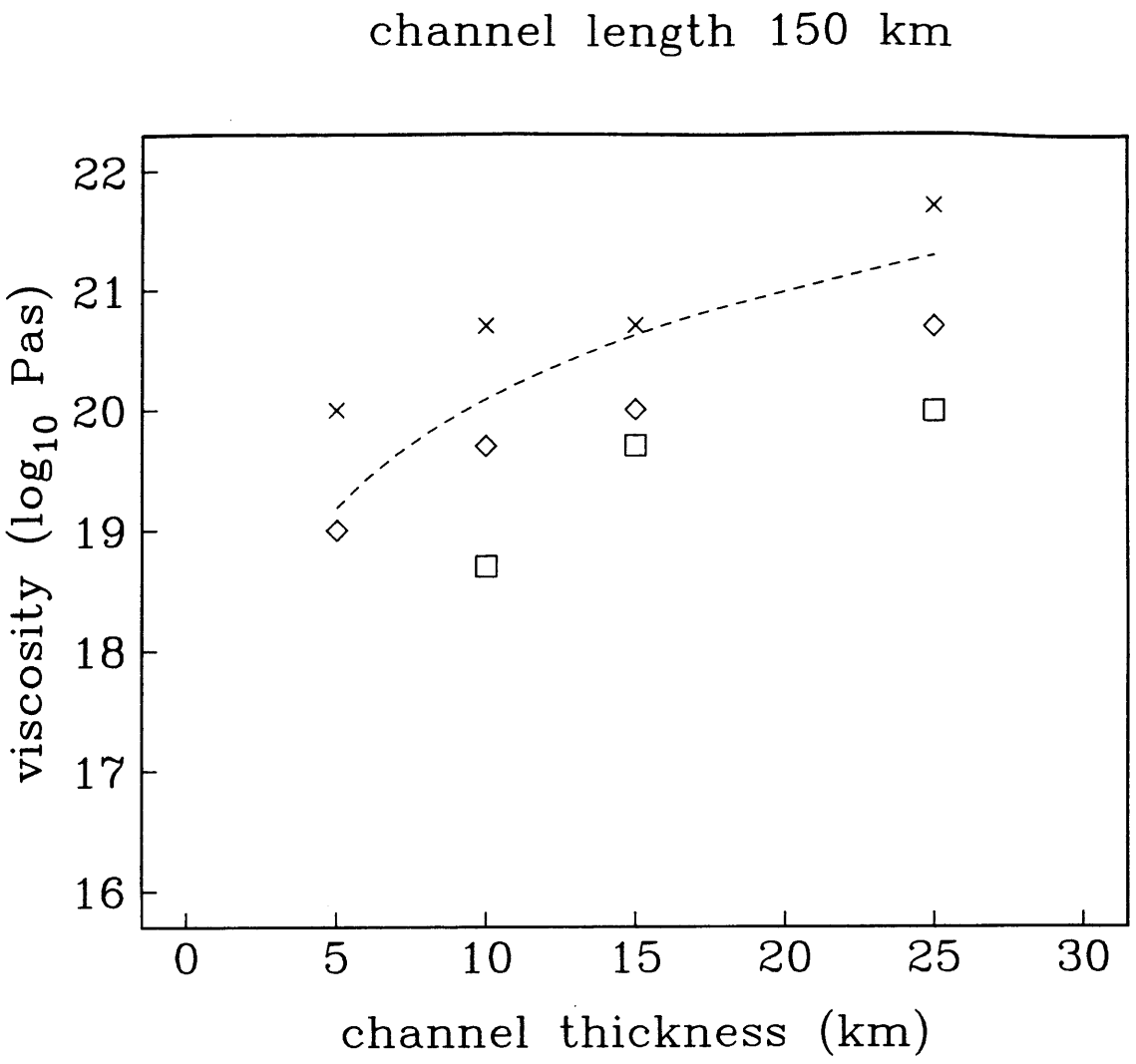
channel length 150 km
viscosity ($\log_{10}$ Pas)
22
21
20
19
18
17
16
0
5
10
15
20
25
30
channel thickness (km)

Figure 22